Online evaluation of weld quality for Friction Stir Welding process

Kartikey Mathur

School of Engineering

Lancaster University

A thesis submitted for the degree of Doctor of Philosophy

March 2024

Declaration

This thesis has not been submitted in support of an application for another degree at this or any other university. It is the result of my own work and includes nothing that is the outcome of the work done in collaboration except where specifically indicated. I have adequately cited and referenced the original. I also declare that the content of this thesis has not been published anywhere.

Kartikey Mathur   20/03/2024

<u>Acknowledgements</u>

<u>Dedication</u>

This thesis is dedicated to my family, whose love, patience, and unwavering belief in me have been my greatest source of strength. To my parents, for their constant encouragement and sacrifices, and for always reminding me of the importance of perseverance and passion.

To my partner, whose support, understanding, and love have made every challenge easier to face, and who has stood by me through every moment of this journey.

On-Line Evaluation of Weld Quality for Friction Stir Welding Process

Kartikey Mathur, B.Tech, M.Tech

School of Engineering, Lancaster University

A thesis submitted for the degree of Doctor of Philosophy, March 2024

Abstract

Friction stir welding (FSW) and Friction stir processing (FSP) have been widely accepted by different manufacturing industries ranging from semiconductor to the shipbuilding industry. With advanced manufacturing capabilities, there is an increased demand to weld parts with complex geometry and curved surfaces through the FSW process. The single process parameter-based weld monitoring systems are limited by their dependence on prerequisite data and type of type of defect. This limits the applicability of the existing weld monitoring systems for different FSW platforms and setups. The existing literature highlights the potential of multi-process parameter monitoring for the detection of commonly occurring FSW defects and flaws.

The presented study explores continuous acoustic emission monitoring methods for determining the weld quality for FSW joints. The novel acoustic emission (AE) based FSW monitoring system utilizes the ability of AE signals to capture the first level parameter of the FSW process yielding higher sensitivity to commonly observed FSW defects. The objective of this thesis is to develop a novel online weld monitoring system to detect the presence of commonly observed FSW defects and mitigate the need time time-consuming post weld inspections. The proposed AE-based FSW monitoring gives evidence of the detection of sub-surface voids, lack of penetration and lack of tool pressure from the tool shoulder. The defects and flaws are identified through patterns observed on the spectrograms obtained from the recorded AE signals of the FSW process. For the classification of welds according to the type of defects and flaws, convolutional neural networks (CNN) are utilized with spectrograms and mel-spectrograms as the input to the classification model. To obtain the optimized classification model, three parent CNN architectures are considered. This thesis presents a bespoke FSW CNN classification architecture that attained classification accuracy of 98% which highlights the potential of an integrated machine learning-AE online weld classification system for FSW.

Contents

Nomenclature

$a_{i,j,k}^{L}$	Activation term for forward propagation
b_k^L	Bias term for feature map
ΔX	Discretization interval
DF	Distribution Factor
F_P	Probe/Pin material flow zone
F_{SH}	Shoulder material flow zone
F_X	Force recorded on the tool in X direction
F_Y	Force recorded on the tool in Y direction
F_Z	Force recorded on the tool in the Z direction
IF	Intensity Factor
m	Mel-scale
R_H	Horizontal component of rotational velocity of material flow
R_V	Vertical component of rotational velocity of material flow
μ	Mean of the dataset
$F(x)$	Output of the weighted layer of Resnet architecture
Xij	Input patch for CNN at location
$Y(x)$	Interpolated continuous signal
f	Frequency scale
$f(n)$	Centre frequency estimated for
n	Population size
W_k^l	Weight vector for feature map at layer L for k[th] element
$x(n)$	Weighted frequency value for considered frequency bin
$\bar{X}$	Mean of X dataset
X_i	Sample value in a given dataset

$\bar{Y}$	Mean of Y dataset
Y_{WN}	White noise augmented AE signal
Y_{ae}	AE signal for augmentation
$Y_{i,j,k}^{L}$	Pooling function for CNNs
$Z_{i,j,k}^{L}$	Feature Map for CNNs

Abbreviations

AD	Analog to digital
AE	Acoustic Emission
ANN	Artificial Neural Network
BPNN	Back Propagation Neural Network
CNC	Computer numerical control
CNN	Convolutional Neural Network
CUDA	Compute Unified Device Architecture
CWT	Continuous Wavelet Transform
DFT	Discreet Fourier Transform
DWT	Discreet Wavelet Transform
FFT	Fast Fourier Transform
FSW	Friction Stir Welding
GA	Genetic Algorithms
HAZ	Heat Affected Zone
IR	Infra-red
KNN	K-Nearest Neighbour
LOP	Lack of Penetration
ML	Machine Learning
NDE	Non-Destructive Evaluation
PSD	Power Spectral Density
RMS	Root Mean Square
SBC	Single Board Computers
SVM	Support Vector Machine
SZ	Stir Zone
TMAZ	Thermo-Mechanical Affected Zone

TTA	Tool tilt angle
TWT	Tool Workpiece Thermocouple
UTS	Ultimate tensile strength
WNZ	Weld Nugget Zone
WP	Work-Package
YS	Yield strength

List of Figures

List of tables

1. Introduction

Industry 4.0 refers to the fourth industrial revolution, characterized by the integration of automation and data exchange to transform traditional manufacturing and industrial processes. Industry 4.0 has undergone a vast expansion in the past decade, manufacturers have been moving to manufacturing methods that offer greater flexibility for achieving higher efficiency and reduced lead times. Directed by the trend of Industry 4.0, Friction Stir Welding (FSW) has been adopted by multiple industries in the past decade as it provides a solution to commonly observed defects and flaws observed in conventional welding methods. FSW was invented at The Welding Institute (TWI) in 1991 as a solid-state joining method primarily for aluminium alloys. It is a solid-state joining method where a non-consumable tool is dwelled and traversed along the seam of a butt or lap joint [1]. The friction between the tool and base material generates heat approaching the solidus temperature to make the material plastic. The probe/pin of the tool promotes the plastic material to flow along the depth of the material and the shoulder results in surface-bound material flow with a forging force from the trailing side of the tool[1].

The FSW industry has experienced a vast number of variants and patents in the past decade. Owing to its advantages of low distortion, low energy, and ability to join dissimilar alloys; the shipbuilding, automobile and aerospace industries are rapidly adapting the Friction Stir Welding (FSW) process. Despite the numerous advantages of FSW over conventional welding processes, FSW is prone to defects and flaws caused by irregular heat generation, poor selection of process parameters and unsuitable tool geometry. The most common defects and flaws observed in FSW are surface and internal voids, root flaws and joint line remnants (which are discussed in Section 2.8). For the current state of the technology, the selection of optimum weld parameters for FSW is an iterative process which is inefficient and results in large waste material being generated. The requirement of post-weld inspection also increases the lead time for the entire process. Previous research in the domain of optimization of the FSW process has been focused on optimizing the tool design and changing the process parameters offline to make a sound weld. An online process monitoring system for FSW would significantly reduce the lead time for parts and enable changing to optimized process parameters in real time.

This thesis is focused on the early detection and identification of weld defects or flaws as the basis of an online weld quality monitoring system for FSW. The novelty of the

research is defined by the implementation of a continuous acoustic emission and force monitoring-based system for the classification and identification of defects and flaws. The acoustic emission signals obtained during the welding process are visualized and co-related with different weld parameters, flaws and defects. Spectrograms give data-rich time-frequency domain plots which are widely used for understanding the dynamic behaviour of a process.

To understand the correlation between the acoustic emission and the axial force on the tool, the standard deviation for the centroid of the spectrograms and the axial forces is also explored. The sensitivity of AE signals to detect changes material flow during the welding process and to the creation of defects was explored. Three conventional CNN (Convolutional Neural Network) architectures are compared to obtain a suitable architecture that can determine anomalies during the welding process visualized by the spectrograms. Based on the stability and accuracy of the proposed CNN models, the optimum CNN architecture for the classification of weld quality was explored.

1.1 Thesis Structure

Following the background and aim of the thesis discussed in Chapter 1, the second chapter presents a detailed explanation of the FSW process. Chapter 2 of this thesis presents a comprehensive literature review highlighting the control methodologies, weld monitoring methods & implementation of machine learning in the domain of FSW. Chapter 3 of this thesis gives details of the FSW platform and the sensor setup used to record process parameters (i.e.- AE signals and forces observed on the FSW tool). This chapter also lists the welds performed with the weld parameters explained and the material welded.

Chapter 4 describes the weld classification approach through Discrete Fourier Transform (DFT). The chapter also explains the results and discussion of the proposed continuous acoustic emission monitoring system for FSW and its ability to detect the presence of flaws and defects addressing the knowledge gaps present. In Chapter 5 the Convolutional Neural Network (CNN) approach for a weld classification system is discussed. A hybrid spectrogram-mel spectrogram variant of a conventional CNN-inspired model is also presented highlighting the benefits of reduced memory usage and higher accuracy.

The final chapter of this thesis outlines the effectiveness of the proposed weld monitoring system by answering the research questions. The proposed future work is themed to aid the development of a continuous AE monitoring-based closed loop weld

monitoring and control system and the potential of the integrated closed loop system is further discussed in section 5.8.

1.2 Research aims & objectives

Current weld monitoring systems are highly dependent on the force and torque data measured during the welding process. The existing control methodologies are focused on force and torque data to maintain the process stability. The existing models lack the transferability to different grades and types of material which limits the use of control systems. After the FSW process, the welded part needs to undergo an inspection process to determine the quality of the weld. This post-process inspection increases the overall lead time of the FSWed part and limits the flexibility of the manufacturing process. To aid state-of-the-art weld monitoring systems, this thesis discusses the potential for AE- data to be used to support a multisensory weld assessment system that can address the limitations of current weld monitoring systems. In order to demonstrate the capabilities of the proposed weld monitoring method; this thesis aims to address the following objectives:

    a.   To develop an open loop non-destructive evaluation system which could be used to monitor and qualify the welds by detecting the presence of defects.

    b.   Implementation of machine learning for the identification of defects through online process parameter monitoring.

1.3 Research methodology & contributions

This thesis discusses the tests performed for the development of an online weld monitoring system for the FSW process. To address the aims of the project, the complex thermo-mechanical phenomenon involved in the process is correlated with the AE signature of the FSW process. The experimental plan discussed in this thesis is based on inductive reasoning addressing the key research questions. The block diagram for a typical inductive reasoning case is presented in Figure 1. Inductive reasoning enables the development of theories based on prior and new observations.

Figure 1: Inductive reasoning flow diagram

The development of theories is based on existing literature and further explored and extended using inductive reasoning from the results of experiments. The experimental plan is divided into 5 work packages (WP) and each work package is built on the observations from the literature and previous WPs. Based on observed features of the acoustic emission data, the welds are classified according to their acceptability discussed in Chapter 2 of this thesis. The classified AE data from the welds is used by the convolutional neural networks(CNN) to automate the process of classification of welds online. The knowledge-based flow between the work packages and the development of the CNN model is presented in Figure 2 below. The experimental setup and the results for the presented workflow are explained in Chapter 3 and Chapter 4 of this thesis.
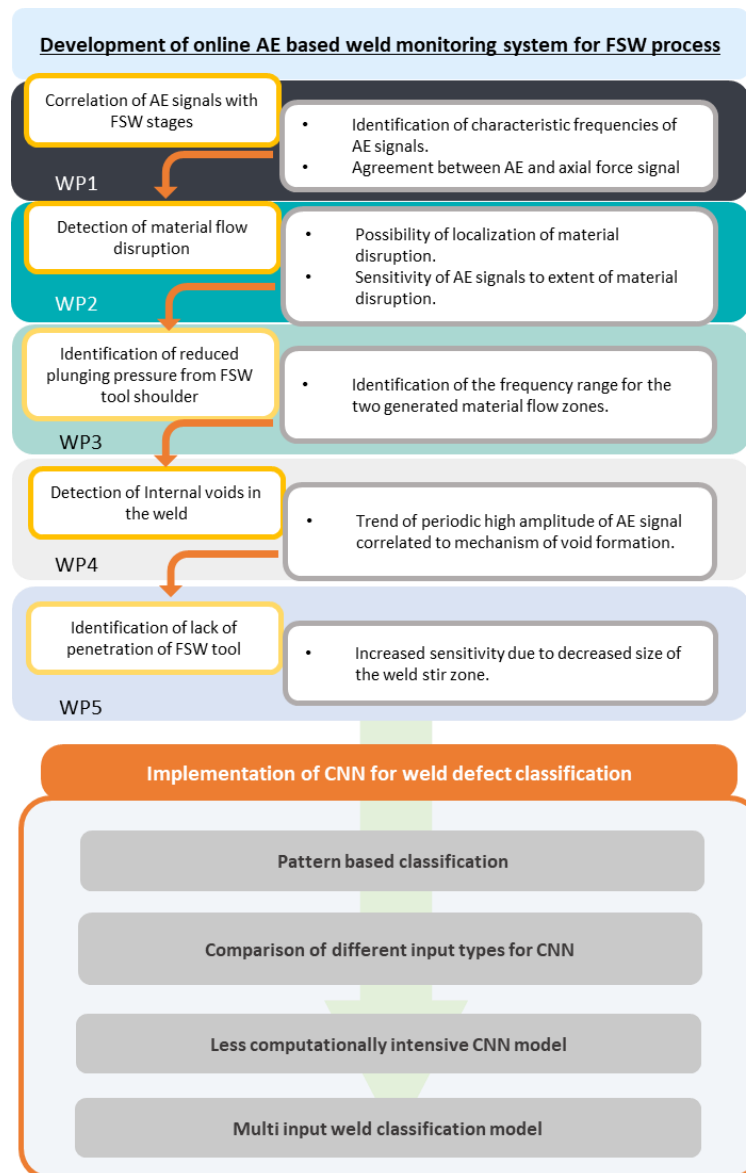
Figure 2: Knowledge flow between work packages and development of convolutional neural network (CNN)

The knowledge gap present in the domain of online weld monitoring for the FSW process is identified and addressed in Chapters 2 and 4 of this thesis. The key research questions (RQ) focused on weld defect and flaw detection, along with system integration are highlighted and discussed below.

RQ1: Can AE signals be correlated to FSW stages and observed forces?

RQ2: How does the placement of the AE sensor affect the recorded AE signature of the FSW process?

RQ3: Can material flow disruption be measured through AE monitoring?

RQ4: How sensitive is continuous AE monitoring to changes in process parameters for the FSW process?

RQ5: Can continuous AE monitoring detect the presence of FSW defects & flaws.?

RQ6: How reproducible and reliable is the proposed AE monitoring method?

RQ7: How best might machine learning models be integrated with AE monitoring of the FSW process?

RQ8: Can machine learning be used to aid weld quality-based decision making by FSW machine users?

1.4 Scope & limitations

To meet the aims of the project, knowledge in the domain of friction welding, automation and measurement is required, as illustrated in Figure 3. The need for knowledge in the illustrated areas is also outlined by the detailed sub-objectives stated in section 1.2. The AE-based weld monitoring system presented in the thesis aims to reduce the lead time for a part with an FSW joint. The welds discussed in this thesis are performed using the same tool and two grades of aluminium alloys were used to understand the weld response for medium and high strength grades. For this thesis, the AE data is recorded with wide-band sensors piezoelectric sensors to understand the characteristic frequencies of the FSW process. The use of CNNs is explored for the online weld classification system to aid a faster decision-making process and reduce lead time.
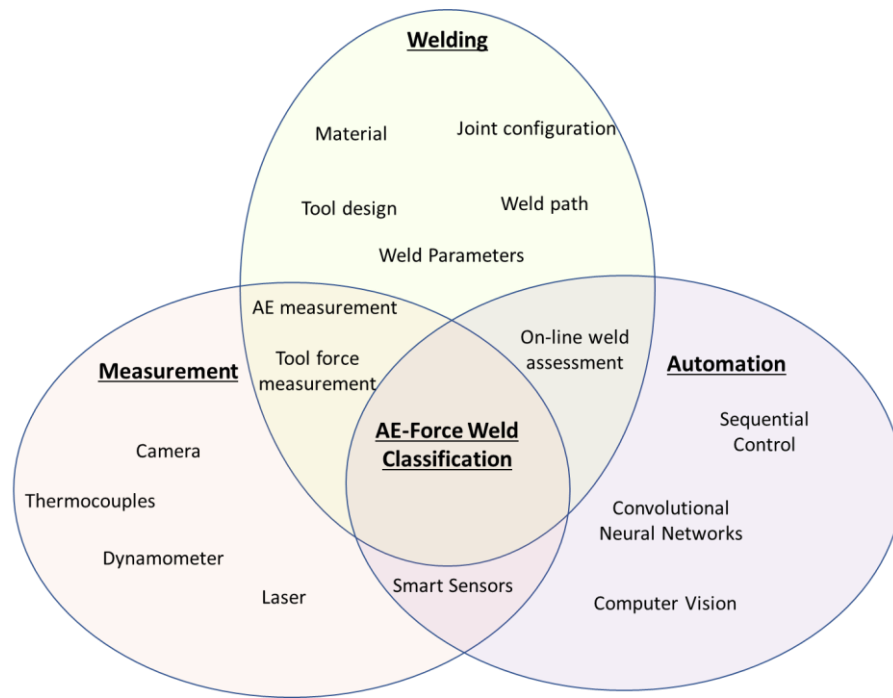
Figure 3- Main research focus with surrounding research area

Following the inductive reasoning approach to the project the welding experiments discussed in this thesis are limited to butt joint configuration and the same welding tool is used for all the welds performed and discussed in this thesis. The control strategy used for the FSW experimental setup has been limited to reduce the variability in interpreting the data. For online decision making, the research is limited to the use of CNNs in the domain of machine learning. CNN models are dependent on image data making the usability of the model limited to the computational capability of the computers. The data capturing methods of this thesis are limited to the computational and measurement abilities of the sensors and data acquisition systems. The knowledge transfer between the different grades of the same material is limited to AA6082-T6 precipitate hardened and AA5083-H111 non-hardenable aluminium alloy. The variability of the proposed analysis for different materials is not explored in this thesis. The weld parameters discussed in this thesis are selected based on existing literature and the variability analysis for the proposed method this not performed in this thesis. It should also be highlighted that the validation welds performed to address the variance in AE signals due to material properties and heat input are limited to a specific set of weld parameters discussed in the thesis.

2. Literature Review

2.1 Application of FSW

Multiple joint configurations can be welded using the FSW process with low distortion and high repeatability compared to conventional welding processes. Apart from various metallurgical benefits, FSW also offers energy and environmental benefits as well. It results in reduced overall weight of the joined part as no filler metal is used. Emphasizing the energy consumption of the FSW process, it uses 2.5% of the energy used for laser welding a part with the same material and size. The reduction in the weight of the overall part allows for reduced consumption of fuel in automotive, shipbuilding and aerospace applications [2]. Boeing implemented the FSW process in the manufacturing of inter-stage modules of Delta II rockets [3]. Space X also implemented the FSW process for circumferential and longitudinal welds of Falcon 9 rockets [4]. Due to the ability to join dissimilar metals, FSW is also widely used in the shipbuilding industry due to the ability to weld aluminium with low distortion, Nichols Brothers in Washington used FSW for the bow section of the US Navy X-Craft [5]. Helipads for offshore platform Oseberg Sør were made from marine grade aluminium joined together by FSW. Due to the high strength characteristics of FSW, Mazda used friction stir spot welding for the bonnets and rear doors of the Mazda RX-8 [6]. Manufacturers have been interested in FSW due to significantly low processing time, low tool consumable cost and high quality joints[7]. To attain high strength with the reduction in overall weight of the part, there is a high demand for parts where steel is welded with aluminium alloys. There were numerous studies performed which concluded that FSW is favourable for joining dissimilar metals [8],[1]. It was also stated that FSW steel joints resulted in higher joint strength, fewer defects and lower distortion of the workpiece compared to conventional welding methods. The advantages of FSW have also been recognized in the computer industry, as Apple used FSW to join the back panels of the iMac Intel 21.5" EMC 2544. A FS welded back panel enabled the housing to be thinner, by 5mm, which made it significantly thinner than its predecessors [9].

2.2 Principle of operation

Similar to the conventional welding process, the weld quality for FSW is determined by the heat input. As the probe of the non-consumable tool dwells into the base metal, the frictional heat generated by the tool shoulder and probe plasticizes the material [10][11]. Apart from heating the base metal with frictional heat, the tool also moves the material in the weld seam. The three phases or the weld cycle of conventional FSW

are defined in Figure 4, known as plunging, welding, and retracting. The tool probe enhances the flow of plasticized material below the shoulder to aid efficient stirring of the material. During the plunging phase, the tool is rotated at the desired RPM and dwelled in the joint line of base metal. The frictional heat generated by the rotating tool plasticizes the material around it before the process moves to the welding phase[12].
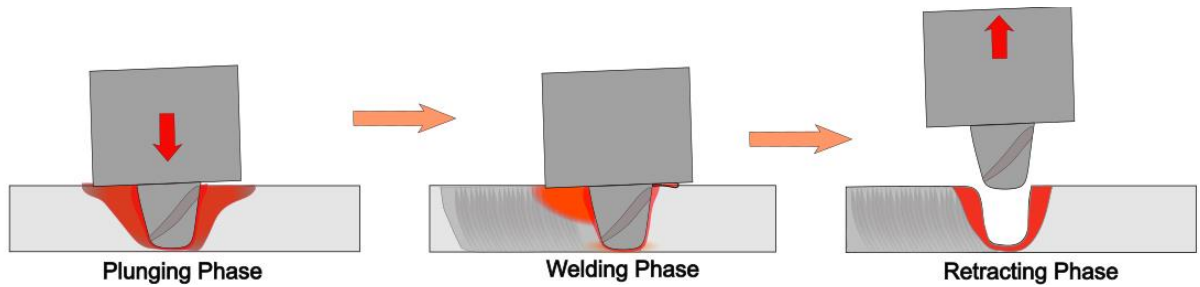
Figure 4- Three phases of the FSW process performed with an angled tool

The tool shoulder creates higher heat compared to the tool probe and keeps the material from being extruded out of the weld. With a tilt angle in the plane of the welding direction, the tool is moved along the seam, joining the material in the wake of the tool. At the end of the weld, the tool is withdrawn from the material leaving a keyhole in the welded joint line. The tool geometry and weld parameters influence the mechanical properties of the weld. The tool geometry is varied concerning the thickness of the base metal and the type of joint. The keyhole flaw at the end of the weld can be eliminated with the use of a retracting probe tool providing excess area at the end of the weld (i.e.-

Runoff region)[13]. The cross-sectional side view of the process is illustrated in Figure 5 below.
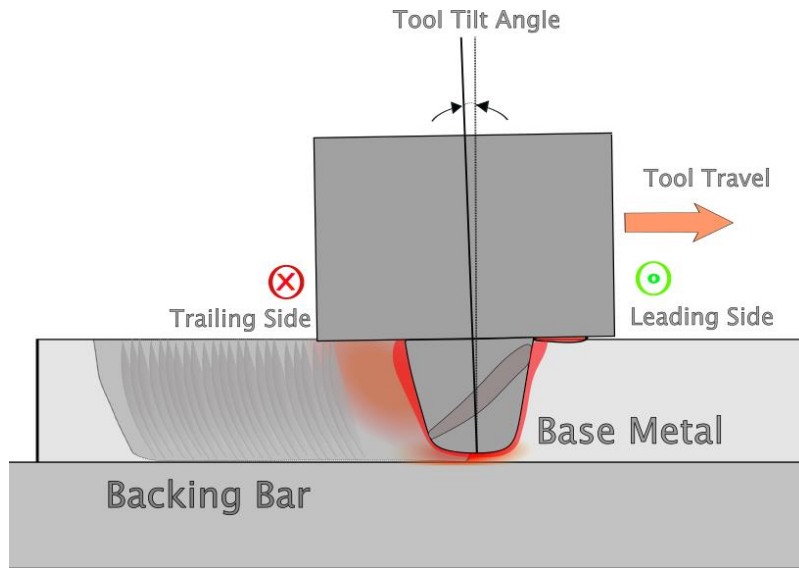
Figure 5- Schematic of tool dwelled inside the workpiece

Three regions can be identified in a typical cross-section of the FSW joint; stir zone (SZ), thermo-mechanical affected zone (TMAZ) and heat affected zone (HAZ). Different FSW zones are discussed later in the thesis in detail in section 3.1. To provide resistance to the axial force provided by the tool, the base metal is supported with a backing bar. To prevent the workpiece from deformation due to the high axial force, the backing bar is made of a harder material, commonly steel. As the backing bar is the closest to the stir zone after the base metal, it contributes to the majority of the heat dissipation caused during the welding process. The thermal conductivity of the backing bar has a significant impact on the quality of the performed weld [14]. During the welding process, the tool experiences forces in the axial direction and the lateral plane. To resist the forces exerted by the tool, the workpiece is clamped according to the workpiece geometry and type of FSW process, the clamping setup discussed in this thesis is further explained in section 3.3.

2.3   Friction stir welding parameters

The welding parameters govern the material flow & heat generation which consequently determine the peak temperature and weld quality. The frictional heat generated between the tool and workpiece material due to tool rotation and traversing of the tool combined with the adiabatic shearing of the stirred material, contributes the majority of the heat generation for the weld. Heat generation is also supported by the

axial force acting on the tool which causes increases in contact area and pressure at the shoulder & material interface [15]. The increase in the tool rotation speed increases weld heat input while increasing the tool traverse/travel rate decreases the heat input of the weld. Traversing the tool forward promotes the material flow along with the rotational motion of the tool. As the tool traverses, the material moves from the leading to the trailing side of the tool, this affects the weld thermal cycle [16]. The tilt angle of the tool increases the shoulder plunge depth at the trailing side of the tool, increasing the pressure exerted by the tool. The increased pressure results in higher temperature due to increased shearing forces, the material flow around the tool is not symmetrical because of the rotational and traversing motion of the tool following the joint line [17].

The amount of material stirred by the tool is dependent on the weld parameters and the tool geometry. The amount of heat generated during the welding process also depends on the thickness and geometry of the workpiece/base metal being welded. With suitable machine tools, FSW can be easily implemented, but during the process, the base material and welding tool undergo a complex thermomechanical process. Plastic flow, plastic deformation, dynamic recrystallization, cooling rate & material emissivity phenomena are interlinked which determine the integrity of the FSW joint. Different theories for process modelling exist in the literature but the intertwined phenomena increase the complexity of the process [18]. For a better understanding of weld parameters and process parameters, the FSW process can be explained by process inputs and outputs in Figure 6*(Adapted from* [19]).
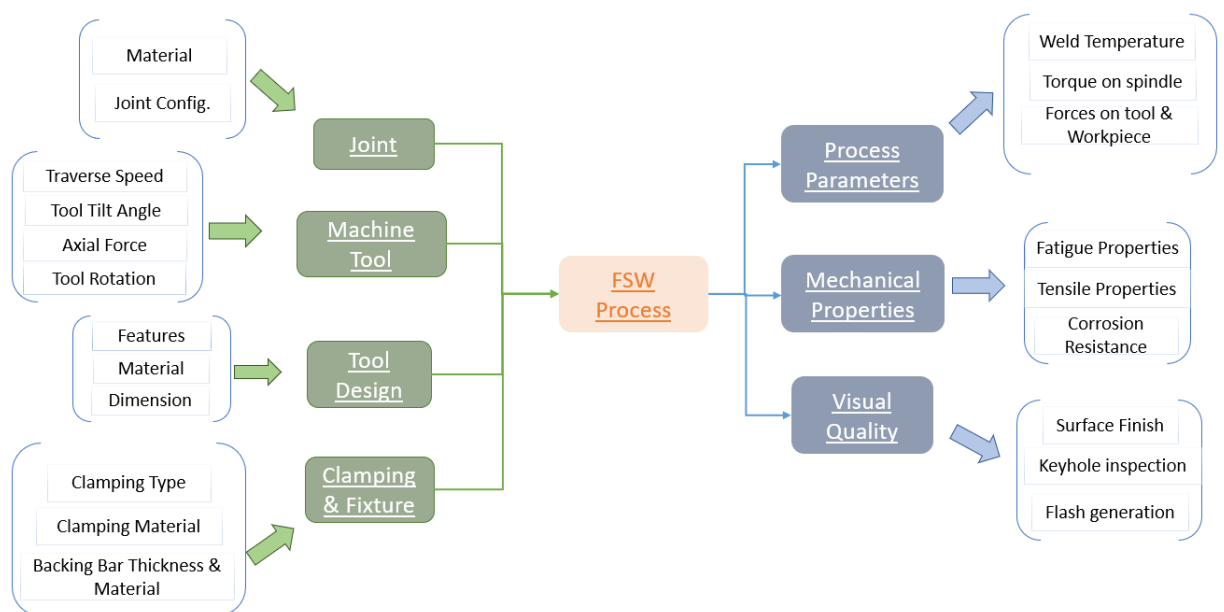
Figure 6- Input and output parameters affecting the weld quality of FSW joint [19]

The process parameters can be further divided into two levels depending on the source of parameters. *Figure 7* presents the two degrees of process parameters for the tool and workpiece interaction. The 1st level parameters are governed directly by the interaction while 2nd level parameters are dependent primarily on the 1st level process parameters.

Contact between tool & workpiece

1st Level	Frictional Heat	Shearing and stirring of material	Shearing Heat
2nd Level	Reaction forces on FSW tool	Torque on FSW tool	
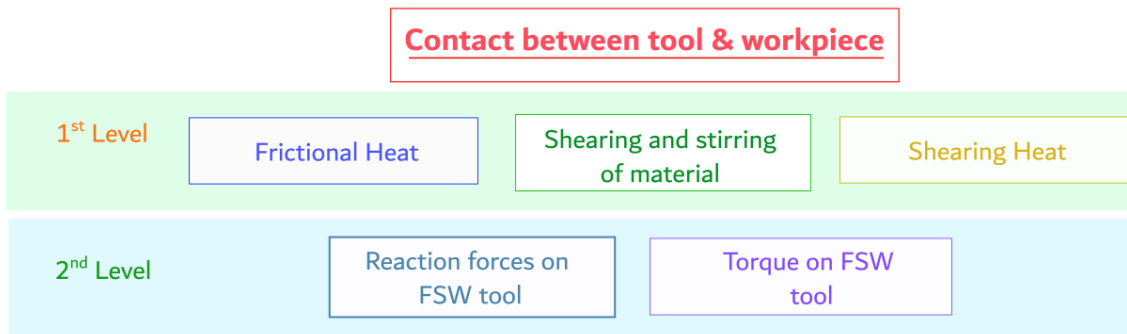
Figure 7- 1st & 2nd level process parameters for the FSW process

Forces observed on the tool during the process depend on the heat generated during the welding process which is inter-twined with three key weld parameters (i.e.- tool RPM, axial force & tool travel rate). The forces involved in the FSW process for a butt joint configuration, discussed in this thesis, can be visualized in *Figure 8.* The experimental setup for the work discussed in this thesis is explained in detail in Chapter 4 of this thesis.
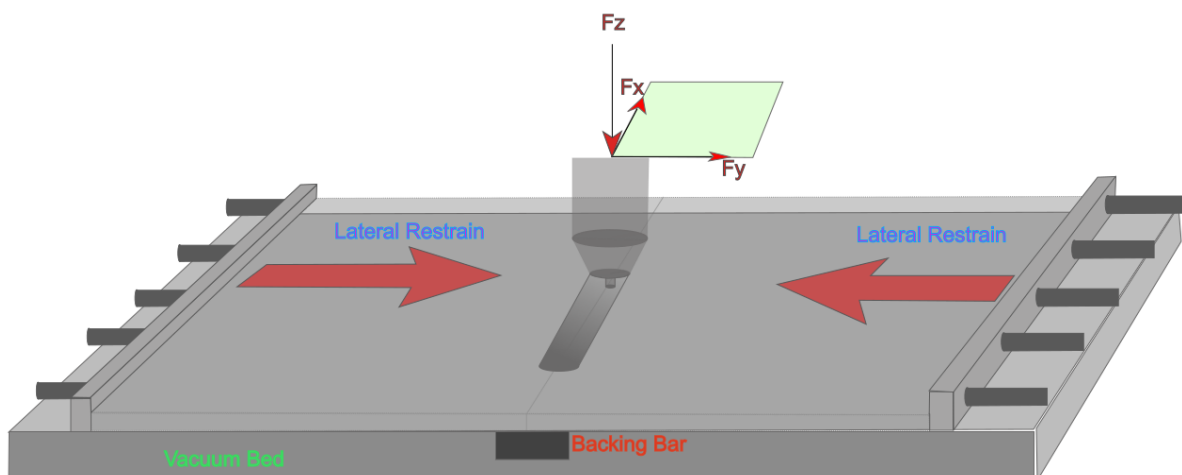
Figure 8- Forces and restraints for FSW process (Fx, Fy & Fz are forces in traverse, lateral and axial direction)

2.4 FSW Tool

The tool geometry has two key components, tool shoulder and tool pin. The tool shoulder is responsible for heat generation and prevents the expulsion of stirred material out of the weld. The probe of the tool is the first point of contact with the base metal, and it is responsible for heat generation during the plunging phase. During the welding phase, the tool probe is responsible for deforming the material and moving it around the tool. The three parts of the FSW tool are illustrated in *Figure 9 below.*
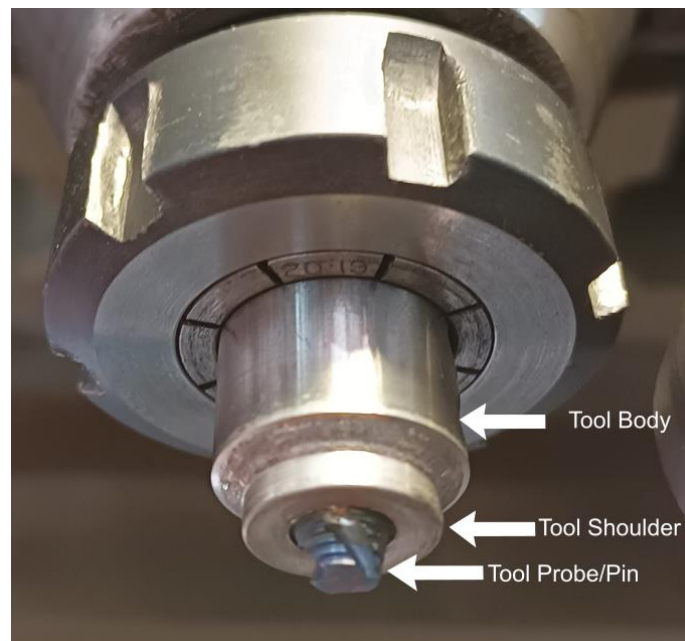
Figure 9- MX Tri-Flute Probe with featureless concave shoulder

Past research has shown that tool geometry has a significant impact on the weld quality as the tool shoulder is responsible for the majority of the heat generation [20]. The concave profile of the tool acts as a reservoir for the plasticized material by the probe. To enhance the shearing and friction with the workpiece, features are added to the tool shoulder. Most typical features added to the tool shoulder are shown in Figure 10. To control the material movement around the tool and increase the shearing of the material, features on the probe like threads, flutes and flats are added. Depending on the direction of the threads the material movement in the axial direction is controlled while flutes and flats are added to increase radial material moment. Depending on the material and type of joint, the combination of features on the tool probe and shoulder are selected.

Shoulder Features

Probe/ Pin Pofiles

Ridges

Scrolls

Unthreaded

Threaded

Groove

Knurling

Fluted

Taper with flat
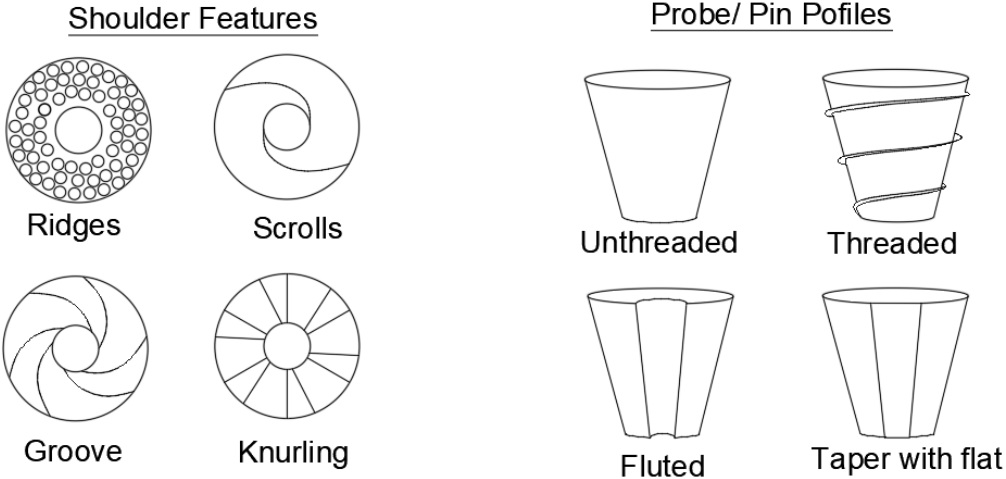
Figure 10- Shoulder features and tool probe profiles for tapered pin[21]

2.5 Temperature fields and microstructure

During the FSW process material undergoes a thermal cycle reaching solidus temperature caused by the frictional heat generated. The weld zone of an FSW joint is classified into three regions depending on microstructural features (i.e.- WNZ (Weld Nugget Zone), TMAZ (Thermomechanically Affected Zone) & HAZ (Heat Affected Zone)). The three regions are highlighted in Figure 11 for better visualization.

(1) Weld Nugget Zone(WNZ)- Region located at the centre of the weld experiencing high stain rates 10^0-10^2 s^{-1} undergoing severe plastic deformation(SPD) [22]. In the WNZ the peak temperature was reported to reach 80% to 90% of the melting temperature of the base metal [23]. The severe plastic deformation caused by the FSW tool and exposure to high temperatures results in dynamic recrystallization and finer grain size reaching to size of 5µm [24].

(2) Thermomechanically affected zone (TMAZ)- Located next to the WNZ region of the weld, experiences lesser strain and significantly lower temperatures compared to the WNZ. Dynamic recrystallization is not observed in this region. Flow patterns (i.e.-Onion rings) are observed in this region as the weld temperature transitions from hot to cold laterally in the weld [25]. Elongated grains are characteristic of this region of the weld.

(3) Heat affected zone (HAZ)- Adjacent to the TMAZ, this region of the weld experiences a thermal cycle but no plastic deformation occurs in this region.
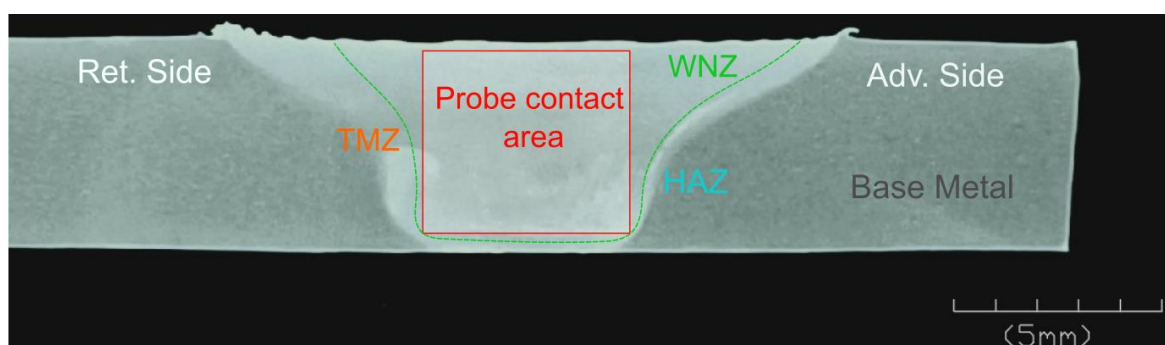
Figure 11-Macrograph of FSWed joint cross-section with three weld regions

Similar to conventional welding processes, the quality of the welded joints is dependent on the heat input to the weld. Primarily two temperature measurement methods have been explored by researchers in the past namely, thermocouple measurement and infra-red (IR) camera measurements [26][27]. The difference in the temperature between the advancing and retreating sides of the weld is also explored in the literature

[28]. The advancing side of the weld on average experiences a greater extent of the highest temperature field while a significantly lesser area is covered by the same temperature field line on the retreating side of the weld. During the FSW process, the highest temperature is reported at the interface of the tool and workpiece, varying from 500°C to 600°C (for different grades of aluminium). The workpiece temperature outside has been reported to drop significantly by 25% within the span of 2mm from the shoulder edge [29]. The temperature attained for the FSW of steel is significantly higher compared to aluminium. The temperature map for FSW of DH36 steel can be visualized in Figure 12 where the temperature below the solidus point is reported. The variation of the temperature along the width of the weld as a result of the difference in material flow around the tool is visualized. The existing literature highlights the usage of thermocouples placed in different positions within the tool and the workpiece. Due to the limitations of applications conventional thermocouple measurement methods lack continuous weld temperature capabilities [26][30]. The use of (IR) cameras for monitoring is limited due to the emissivity and no direct sight to the interface region[26]. In the above-discussed literature, the Tool Workpiece Thermocouple (TWT) measurement method has proven to provide the most accurate measurement at the tool-workpiece interface [31].
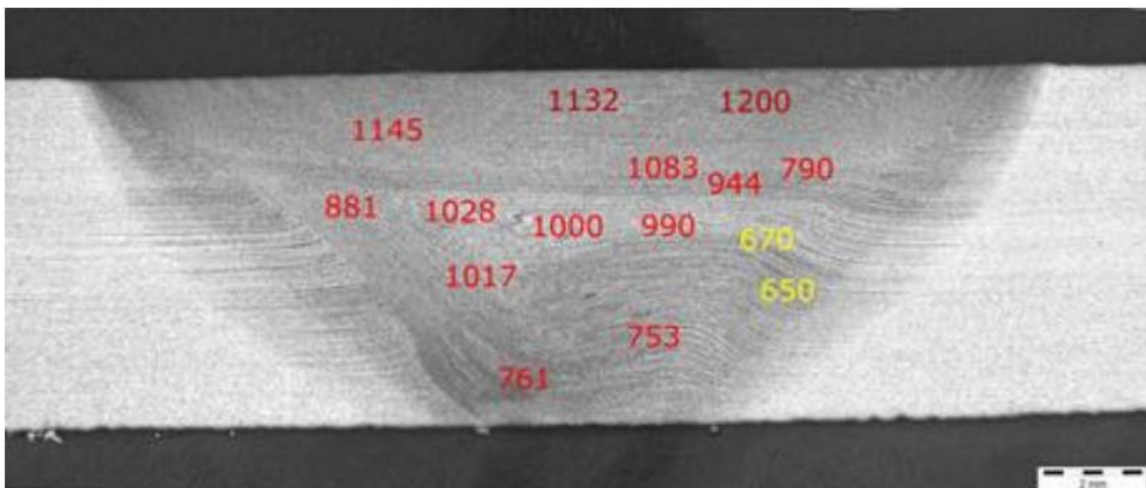
Figure 12- Composite temperature map for 6mm FSWed DH36 plates[32]

The development of microstructure and the size of the weld zones are greatly dependent on the tool geometry and the welding parameters used for welding. In the past two decades, there has been significant literature published understanding the influence of welding parameters on the microstructure and grain size of the FSW joints. Early studies in this domain were focused on assessing the transition of grain size from

coarse to fine, highlighting the complex precipitation phenomenon [33]. A. Ali et al. [34] presented a study exploring the residual stresses and cyclic behaviour of samples extracted from WNZ, TMAZ, HAZ and parent metal, understanding the influence of welding parameters on the microstructure and grain size of AA2024-T351. Asymmetry in grain size, hardness and residual stress within each region of a typical FSW cross-section is reported. Through the cyclic testing, HAZ reported a yielding point of (448 MPa) and TMAZ had the lowest yielding point of (272 MPa) highlighting TMAZ as the region of fatigue failure. The abovementioned literature highlights the influence of tool geometry on the weld quality and outlines the temperature ranges in different regions of the weld.

The effect of tool design on microstructure development and mechanical response has also been studied [35]. Performing the FSW welds for AA7020-T6 using a featureless tool with two probe and shoulder profiles was used. A more gradual transformation from the stir zone to TMAZ was observed for the frustum-shaped rounded probe profile. H.A Derazkola et al. [36] explored the viscosity changes, thermal history and material velocity of FSWed T joints. A range of tool tilt angles (TTA) from 0.5°- 4° was used to perform the welds. With an increase in the TTA, the higher temperature at the WNZ was reported and a gradual reduction in the grain size with an increase in the tool tilt angle was highlighted. With the increase in the TTA, the size of WNZ increased sharply to 2.5° while a significant decrease in the size of WNZ was observed from 2.5° to 4° of TTA.

There exists a large volume of literature focusing on welding dissimilar metals by the FSW process. To obtain acceptable weld quality for FSWed dissimilar metals, the harder materials are placed on the advancing side of the weld. The requirement of high heat input to weld dissimilar metals has also been highlighted in the existing literature [37]. The support the stirring and increase the heat input for softer material, tool offset perpendicular to the welding direction is also introduced and reported in the literature [38], [39]. One of the key advantages for FSW underlined by manufacturers is the process's ability to weld casted parts. Y.G Kim et. al [40] explored three commonly occurring defects for FSWed aluminium die-casted alloys. Different weld zones & defects observed for FSWed ADC12 alloy are co-related with the weld parameters. Abnormal stirring action is correlated with the presence of the void on the advancing side of the weld. Reduction in the size of the sub-surface void by high plunging force / axial force has also been reported. Joining Al to Cu has also been widely explored by researchers and manufacturers in the past and has been a theme for highlighting FSW advantages [41],[42],[43],[44]. C.W Tan explored [45] explored the mechanism of

composite like structures formed during welding 5A02 aluminium alloy and copper by the FSW process. At the interface Al/Cu joint, the broken fragments at the nano-scale from copper mixed with Al form Inter Metallic Compounds (IMCs) resulting in distinctively high hardness.

Researchers have also focused on analysing weld regions for different FSW variants, W.S Chang et al. [46] explored the effect of laser exposure on AA6061 & AZ31 Mg laser assisted FSWed joints. For visualization of flow zones, a Ni foil was added at the interface of two metals. Defects of a significant scale were observed for lesser laser power and the defect was mitigated by increasing the laser power by 20%. The mass concentration of Mg-Kα was higher than Al-Kα in the stir zone (SZ) of the weld while the opposite trend was observed for the first 10% of the starting distance of SZ or WNZ. A. Tamadon et. al [47] explored the flow behaviour for Bobbin-FSW process for AA1100 and AA3003. Utilizing the macrographs obtained from the welds with different tool rpm and weld speeds, the size of the stir zone and heat affected zone are compared. The extent of grain refinement was also explored using the Electron Backscatter Diffraction (EBSD). Through the recrystallization fraction analysis, a 13% higher percentage of fully recrystallized material for AA3003 is observed at the centre of the stir zone of the weld. The abovementioned literature highlights the effect of weld parameters on the mechanical and microstructural properties of FSWed joints. It also highlights the strong intercorrelation of the different phenomena discussed.

2.6 Tool design and material flow

FSW tool selection plays a vital role in determining weld quality. The frictional heat generated by the tool shoulder majorly contributes to the weld temperature. In the past, several studies have demonstrated that the mechanical properties of FSW joints are greatly dependent on the tool design. For efficient material flow around the tool and effective stirring of plasticized material, features are introduced to the tool probe and shoulder [48]. Depending upon the material thickness and the orientation of the joint, optimal tool geometry and material are selected. For FSW of aluminium alloys, Cobalt MP159 (Nickel-cobalt-based superalloy) and AISI H13 are the most commonly used materials for FSW tooling. For welding harder metals like different grades of steel and titanium, more wear-resistant materials like tungsten carbide and polycrystalline boron nitride (PCBN) are used for tooling [49][50].

A concave tool shoulder profile has proven to be the most effective as it prevents the extrusion of material out of the weld [51]. Tool tilt angle promotes the forging action from the tool and the mixing of material expelled from the tool pin. Due to increased

heel plunge depth, more material is removed from the weld promoting flash generation. The material at the edge of the concave shoulder is pushed down reducing the flash generated [52]. The shoulder design can be carefully selected based on weld parameters and the tool probe geometry. Studies for complex shoulder features like ridges, grooves & knurling have not been reported, whereas the use of scrolls has been widely reported. Scrolls are used to redirect the material displaced by the shoulder towards the probe which promotes the downward material movement of the probe. The need for tilt angle can also be mitigated by using a scroll shoulder design [53]. Since the scroll grooves increase the material engagement, the formation of undercut at the edge of the tool and workpiece is greatly reduced. In the past convex scrolled shoulder have been used to induce more flexibility to the contact area for the shoulder and workpiece [54].

The commonly used FSW tool probe outer surface geometries were discussed briefly in section 2.4. From the past research, it was observed that the rounded probe base helped reduce the tool wear and improve the weld quality. The round base promotes gradual temperature change during the plunging phase, which reduces the local stress concentrations [2]. During the initial development of the FSW tools, it was observed that by adding flats the material flow can be controlled [55]. To promote the stirring action by the tool and control the material flow, threads were added with the flats which reduced the possibility of void formation [56].

The left-hand threaded probe promotes the stirring action by pushing the material towards the root of the weld. This vertical movement of the plasticized material ensures the merger of the probe and shoulder-generated material flow. A tool with a combination of flats and threads has also been proven to be effective for joining stringer-skin joints (lap joints) [57]. It was observed that a tool with three flats and a neutral thread allowed an increase in rotational speed without promoting vertical flow to decrease the hooking effect. The material flow zones can be visualized in *Figure 13*. For welding harder metals, threads on the tool are avoided due to the tool wear caused by the base metal [49],[58].
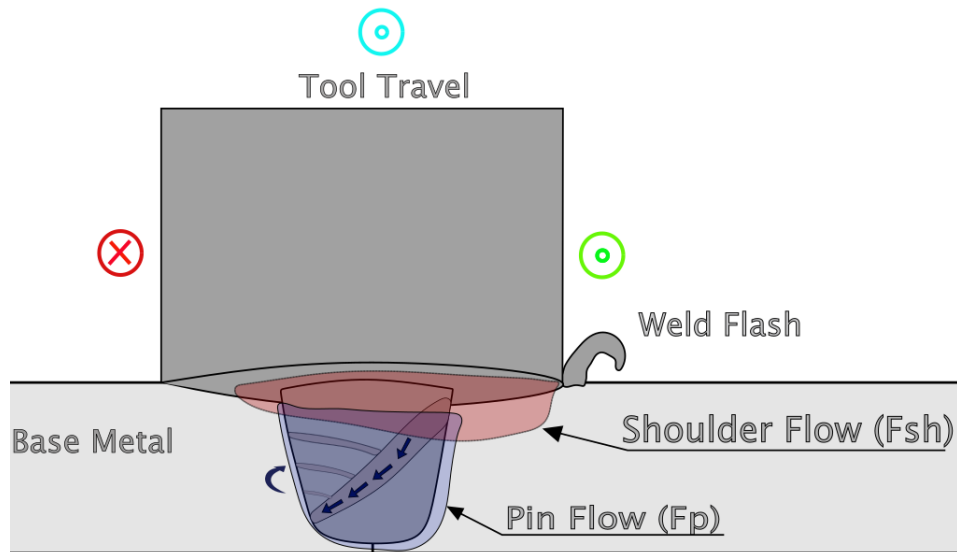
Figure 13- Probe & shoulder flow zone for butt joint orientation.

Material flow for FSW has been vastly studied using marker studies and simulations. Early studies on joining dissimilar metals reported a pattern in the material deposited by the tool in the wake [59], [60]. The marker studies were performed by embedding harder material shots within the joint line [61]. During the study, it was observed that the stirred material originates from the top of the weld and is pushed down by the probe threads. Following the pattern observation in the stir zone of the weld, researchers developed different flow theories. The current around the probe was classified into two, straight through and maelstrom [62]. It was stated that periodic oscillations in both currents result in periodic interleaving from residues shed by the tool in both flow regions. The most commonly observed pattern in the weld cross section is banding of varying thickness and is termed "Onion Rings" [25].

Based on the flow theories, researchers have tried modelling the flow zones on the FSW process [63], [64]. In the early works dealing with flow modelling for FSW, a toric velocity field around the tool has been discussed [65]. The work also illustrates the decreasing amplitude of the torsional vector field along the length of the tool. In the past, weld temperature and the torque of FSW have been predicted and validated using by using analytical coefficients [66]. During the validation of the predicted process parameters, a variance of up to 15% was observed for different grades of aluminium. It was observed that the tool geometry and rotational speed highly influence the predicted weld parameters. The numerical modelling can be extended to simulating the flow around the tool and the defect generation mechanism can be simulated using a coupled thermo-mechanical 3D FE model [67]. Early FEA studies stated that the

frictional models do not account for the non-linear friction phenomena like temperature, particle velocity and pressure exerted by the tool [68]. X. Deng and S. Xu [69] presented a two-dimensional simulation procedure for the FSW process. The simulation also underlines the variation of tangential force along the radial direction of the tool.

From the significant volume present for optimization of tool design, it can be stated that the tools used to perform FSW can be optimized to attain the desired weld quality. The process of optimizing the tool geometry is extensive and often involves non-destructive testing and NDE. Through the simulation-based approach, researchers have attempted to mitigate and reduce the time and cost involved with physical testing. Due to the limitation of conventional models & solvers to address the interdependent complex phenomenon involved in FSW, predictions from simulations are time-intensive and lack accuracy. Considering the state of art computer technology, the simulation-based approach of optimizing the FSW is time-consuming and cannot provide online input to the process.

2.7   Control methodology and use of robots for FSW

Researchers and manufacturers have used machine tools, industrial robots and dedicated FSW machines to perform friction stir processes. The flexibility of the FSW plant to adapt to the corrective signals generated by the weld monitoring system is greatly dependent on the type of control system. The control methodologies commonly used while performing FSW can be majorly classified into two, force control & position control. As the name suggests for the force control method, the axial force exerted on the tool is controlled to ensure maximum tool engagement, while in position control a set weld path is maintained. To study the effects of various control methodologies, researchers have used industrial robots over conventional machine tools for welding complex geometries. Industrial robots give the user more flexibility and control compared to dedicated FSW machines and conventional machine tools. The feedback loop for the control system of FSW environment/plant is majorly classified into two; direct control and indirect control.

The axial force experienced by the tool is also dependent on the rotational speed and the traverse rate of the tool during the weld. Travel axis load controllers have also been proven to be effective in controlling the weld quality by regularizing the heat input into the weld seam [70]. Longhurst et al.[71] compared the axial force models based on varying spindle rotational speed, traverse speed and plunge depth control. It was stated that force control by varying rotation speed is attained by continuously varying power which in turn governs the heat input to the weld. Significant emphasis

on welding of 3D surfaces has been given in the literature. Soron and Kalaykov [72] used an industrial robot to perform FSW for straight lines and 3D curved paths. An outer force control loop was coupled with an internal position control loop while welding, which resulted in successful force control of FSW. It was also stated that the curved path experienced oscillations and limited force control was attained. Due to the positional error of the robot, the penetration depth was also difficult to predict. Other researchers have also followed a similar approach to controlling the axial force. C. Smith [73] used a PID controller on an industrial robot to perform FSW. The presented study was concluded by outlining the limitations of industrial robots. It was stated the force control update rate of 2Hz was too slow to have adequate control during the plunge phase.

In the past, researchers have measured the torque at the tool and workpiece interface with a dynamometer and by monitoring the current flowing to the spindle motor [74][75]. Similar to axial force control by monitoring traverse speed, the plunge depth can also be altered by controlling the torque on the FSW tool [75]. It was observed that torque is a more representative measure of the load acting on the FSW tool. The flexibility in measuring the torque also supports the cause of having a torque-based weld monitoring system. The torque at the surface of the shear interface boundary was represented as the summation of torque on the shoulder, torque on the probe sides and torque on the bottom of the tool pin. For the visualization of the torque control system, the block diagram for torque control by plunge depth is shown in Figure 14. The torque PID controller is connected in series with the position PID controller in the nested loop configuration. This nested loop configuration allows torque control through varying positions.
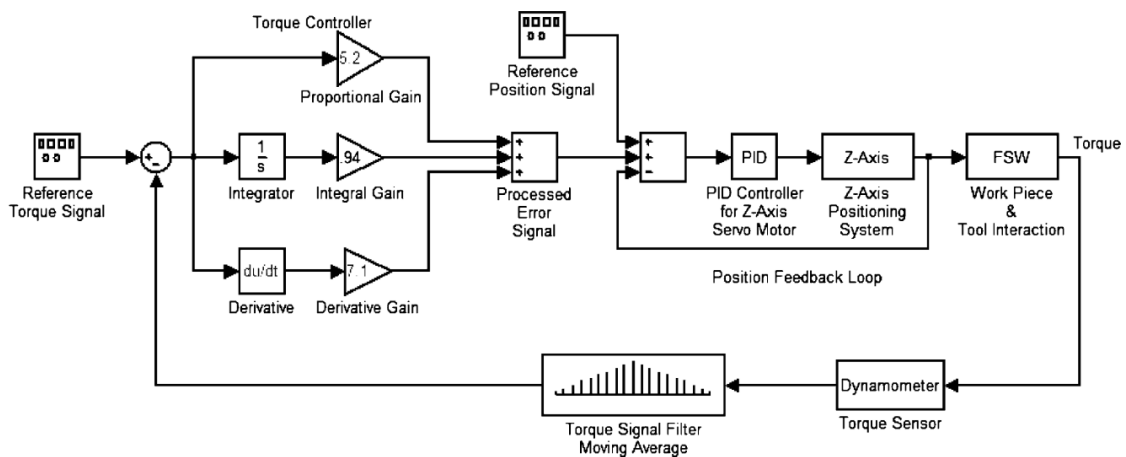
Figure 14: Block diagram of torque control by variable plunge depth [75]

The FSW with industrial serial robots has been limited to a material thickness of less than 3mm due to the lack of stiffness of the arm. The lack of stiffness also induces positional error which is compensated by the force monitoring method to attain the desired trajectory [76]. J.D Backer & Bolmsjo [77] presented the deflection model for an FSW robot focusing on compensation for positional error induced due to forces observed on the welding tool. The weld path compensation model was verified by comparing the case with and without engaging a compensator. It was also observed that the FSW robot yielded three times higher static force compared to the dynamic case. The discussed study was further explained in the thesis of J.D Backer [31].

To overcome the limitation of the stiffness faced by serial industrial robots, researchers have also compared the benefits of parallel kinematic robots for friction stir processing applications. Compared to other FSW control methods on serial robots, a limited amount of research work has been done for analysing FSW control on parallel robots. Jing Shi et al. [78] presented an optimal design of a 3-PRS parallel mechanism for FSW with the design of a tool head. The kinematic performance analysis of the zero-torsion mechanism was done using the new Jacobian matrix formulation. Qinchuan Li et al. [79] presented a five-axis hybrid robot for FSW where he analysed the mobility. The singularities of the parallel component have been analysed using the Jacobian analysis. Based on the link lengths and rotation angles a regular workspace was obtained which is suitable for FSW applications.

2.8   Defect detection and weld quality prediction for FSW

Despite FSW's high stability and advantages over conventional welding processes, FSW is still prone to flaws and defects. A flaw is defined as an unintentional imperfection in the weld, whereas a weld defect is defined as an imperfection whose presence adversely affects the weld performance and its presence cannot be accepted. The defects or weld flaws are mostly caused by inappropriate weld parameters or geometric properties of the tool & workpiece. The commonly occurring defects and their causes are listed in Table 1 with the acceptance level according to the ISO 25239-5 standards [80]. While the welding flaws can be accepted with certain flexibility, welding defects are not accepted and resulting in higher lead time and waste material. As mentioned in the previous sections, a major volume of literature is focused on monitoring FSW process parameters for the detection of defects and flaws. These monitoring methods are developed in the theme of Industry 4.0 for the development of an optimized FSW system.

Defect/Flaw Type	Location	Reason	Acceptance level (EN ISO 25239-5)[81]
Excess flash	Interface of tool shoulder and workpiece	• (For force-controlled machines) Axial force is more than required. • The tool position is set too deep into the base metal. • High tool tilt angle causes the tool heel to plunge into the base metal.	The acceptable size of the imperfection established in accordance with separate regulations or the designer's requirements
Surface lack of fill	On the surface of the weld	• Longitudinal defect caused by low traverse speed combined with high RPM. (Hot welds)	1% of thickness or 0.5mm
Voids/Cavities	Subsurface at the interface of flow zones.	• Longitudinal defects caused by low RPM and high traverse speed. (Cold Welds)	5% of thickness or 0.5mm
Hooking	Interface of two workpieces	• Upward or downward curving of the material interface of two base metals	The acceptable size of the imperfection established in accordance with separate regulations or the designer's requirements
Root Flaw	The bottom part of the weld	• Incorrect tool plunge depth • Poor joint tool alignment • Unsuitable workpiece/tool geometry.	Not acceptable

Table 1- Typical defects observed for FSW processes [80]

Apart from the defects generated because of unsuitable weld parameters, fit-up defects are the other most commonly occurring defects. The joint fit-up issues are further divided into seam gap, thickness mismatch and offset to the joint line. Previous research has established that the tool offset direction affects the joint strength and elongation change [82]. Imani & Guillot [83] presented a study analysing the effect of

joint fix-up issues on the mechanical properties of the weld. Along with the development of control methodology, researchers have also focused on the weld monitoring and defect detection methods for FSW. Early defect detection methods utilized force monitoring methods and offline data analysis for the prediction of defects. Using the process parameters and weld temperature correlation, the welds were classified into good and bad welds.

The literature on force monitoring for FSW has highlighted the ability of online gap detection in the weld seam. Y. Yang et al. [84] presented a power spectral density (PSD) based on a gap monitoring algorithm validated with experimental results. It has also been observed that due to the misalignment, the probability of the gap was observed before the probe came in contact because of the reduced material interaction from the shoulder. Since the approach is based on a sudden variation of axial force, the study fails to demonstrate the model's effectiveness with a gap along the seam. Tool misalignment has also been correlated with variation in axial force observed during the weld. Fleming et al. [85] presented an axial force measurement-based tool offset estimator for T-joints. Compared to either end of the joint, higher axial forces were reported at the centre of the joint. The results from the estimator had an absolute error of 0.42mm and a standard deviation of 0.508mm relative to the true offset. The presented study fails to present the tool misalignment in the axial direction and the effect of the axial forces on the tool.

The variation in the forces has been analysed to detect the presence of disruption in the material flow leading to weld defects and flaws. Several studies have focused on the implementation of frequency domain and frequency-time domain analysis. Discreet Fourier Transform (DFT) and Fast-Fourier Transform (FFT) have been widely used for the identification of surface defects and understanding tool workpiece interaction through frequency domain analysis. T.Jene et al.[86] presented a study to analyse the effect of process parameters on the joint quality of FSW joints. Coupled with a high sampling rate of 200kHz using STFT, the study highlighted the ability to detect cavities in the weld by measuring the force encountered by the tool. Parameter optimization windows have also been defined mathematically considering torque, axial force and the tool rotation speed [87]. A physics-based model explored the possibility of detecting the sub-surface voids by analysing the forces perpendicular to the weld direction. It was highlighted the interaction of the discontinuities with the flats of the FSW tool resulted in higher harmonics of force oscillations. In the thesis, the interaction of the flutes with the walls of the subsurface cavities is further explored.

The Discreet Wavelet Transform (DWT) is widely used in FSW literature as a tool to decompose the force, vibration and acoustic emission signals. The FFT, STFT & DFT analysis of data gathered from multiple sources has been widely used to relate the presence of the defect with higher amplitude of lower frequencies. The signal with a high sample rate/frequency is decomposed into approximate coefficient and detail coefficient by convoluting a mother wavelet. From a family of wavelets, the best wavelet is selected by calculating the energy-to-entropy ratio for each wavelet in each wavelet family. By using DWT & CWT, researchers have tried to localize the presence of defects in a weld. U. Kumar et al.[88] presented a study illustrating the capability of DWT to localize the defect by analysing the variance of the decomposed signals. In the study, a featureless flat shoulder with a featureless probe was used to perform the welds at a 0° tilt angle. These unsuitable weld parameters and tool design choices increased the probability of defect formation. The squared errors of the defect coefficients were related to the top and underside of the weld. Another study with similar tools and materials used CWT to relate the weld perturbations with decomposed signals [89]. Different scales of the CWT coefficients were plotted against the length of the weld. Based on the variance calculated from the CWT coefficients, it was also concluded that CWT was more sensitive to minor perturbations.
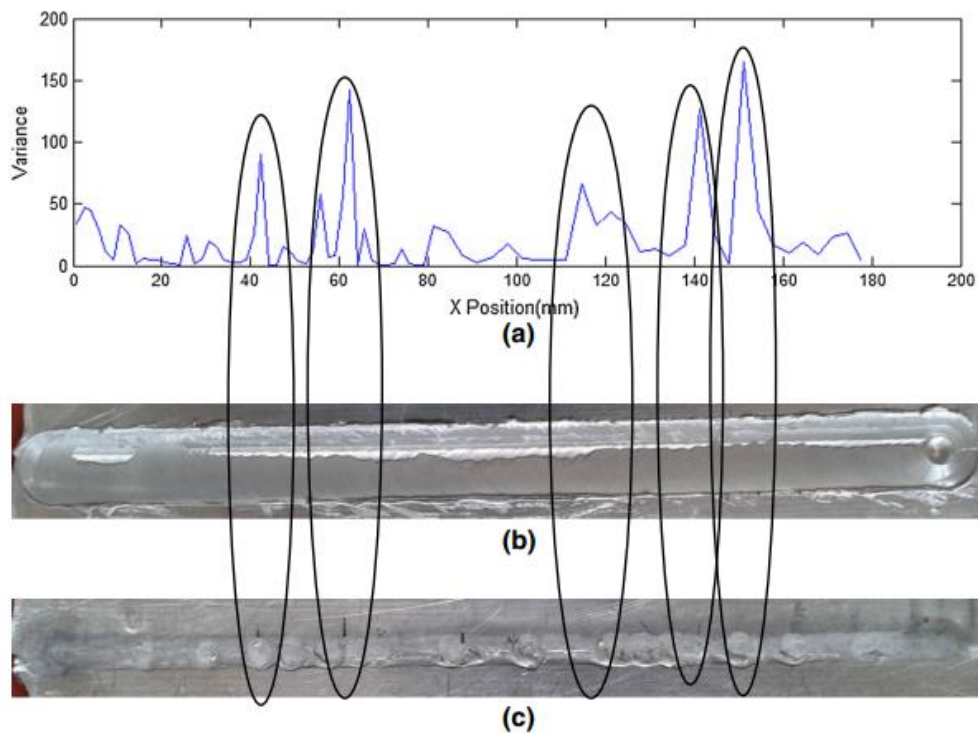
Figure 15: (a) Plot of variance of CWT coefficients at scale 1; (b) Upper surface of the weld seam; (c) Underside of the weld seam [88]

The axial and lateral force monitoring method is the most widely used methodology for preliminary online weld quality assessment. The amount of literature exploring the size of subsurface cavities is significantly lesser compared to others. The key paper for exploring the behaviour of void generation was presented by A. Shrivastava et.al [90]. The presented study utilized 1st and 3rd harmonics of the force in the direction of travel observed on the tool. Discrepancies in the predicted and the experimental values of void volume were observed. It was concluded that with the proper choice of data acquisition system and frequency analyser, the size of the subsurface voids can be detected in real-time. The proposed study was also repeated and presented by D. Franke et al [91]. It was highlighted that for soft metals, the disruption in the force signal was less pronounced. For harder metals, a significant disruption was observed for consolidated welds as well. The discrepancy in the results from the two studies demonstrates high confidence for the proposed model and thus requires more confident void monitoring models.

Overall, a major volume of literature in the domain of the FSW process focuses on understanding the weld properties and process techniques. Force monitoring has been the most widely used method to detect the presence of a defect. By frequency domain analysis of the recorded forces in the axial direction, a trend of higher amplitude at low frequencies was observed. The higher amplitude of axial forces also results in poor surface quality due to excess plunging of the tool in the material. This can be visually seen on the surface of the weld in the form of flash and irregular tool marks on the joint line which makes the approach redundant. A smaller volume of literature deals with the ability of force & torque monitoring methods to detect sub-surface voids. While the ability to determine tool engagement through torque monitoring is highlighted, the aspect of detecting a lack of penetration is also not reported in the literature mentioned above.

2.9 Acoustic emissions of FSW

Acoustic emission (AE) waves are generated due to the release of energy due to the deformation and breaking of material bonds caused by external force [92]. The wave characteristics are dependent on material properties which define the constitutive behaviour of the material. To understand wave propagation, the elastic wave can be further classified into two, P-wave and S-wave based on the particle motion and the direction of the wave. The generation source can be further classified by physical processes (i.e.- dislocation, friction, impact, fibre breakage, delamination, etc.). The elastic waves are captured using electrostatic, piezoelectric, and piezoresistive-based

transducers [93]. AE monitoring has been widely used in the industry due to its ability to detect early failures of structures. The AE signals can be classified into two types; burst signals and continuous emission signals [94]. The waveforms for burst and continuous AE signals are shown in Figure 16 below

A) Burst AE Signal

B) Continuous AE Signal
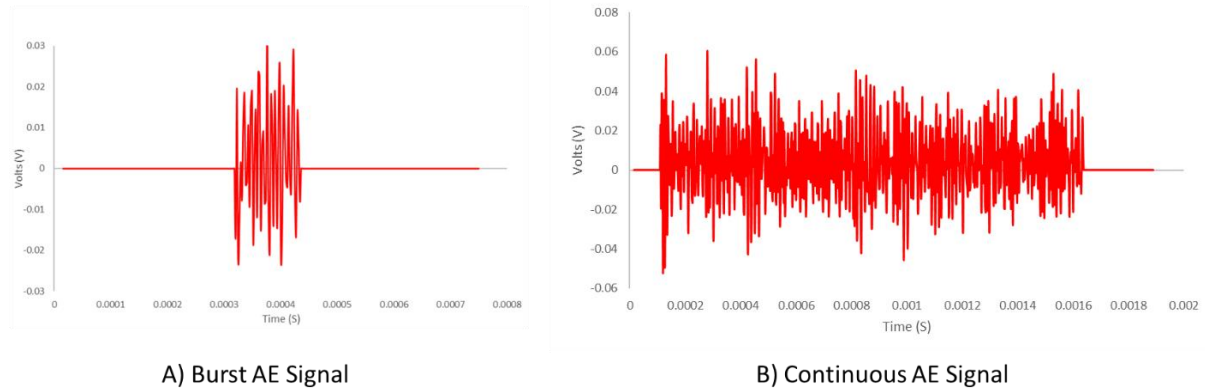
Figure 16: A) Burst AE signal on a time scale; B) Continuous AE signal on the time scale

For burst type AE signals, parametric analysis is preferred to obtain the characteristics of the signal while for continuous AE signals, waveform analysis is preferred to get wave characteristics observed for a longer period. The data analysis method for processing the AE is further discussed in section 3.5.

Researchers have also monitored the acoustic emission of the FSW process to predict and localize defects. The acoustic emission monitoring methods can be categorized into two, continuous monitoring and transient monitoring. Through the transient AE monitoring method, the parameters like rise time, no. of hits, wave energy & threshold frequency are correlated with the presence of defects. V.Soundararajan et al. [95] explored the ability of the AE monitoring system to determine the tool-workpiece and shoulder interaction. By varying the process parameters (i.e.- rotational speed and traverse speed) the difference in PSD trend is highlighted. For higher thermal stress and workpiece temperature, the PSD in the frequency band of 100-170 kHz increases. Implementing STFT with DWT, it was stated that an AE monitoring system is capable of providing real-time feedback. Weld parameters and tool profiles have also been linked to the vibroacoustic data obtained from the FSW process [96]. Conventional accelerometers were used to measure the vibrations observed at the machine tool bed. Similar to past research, the AE signal was decomposed using the DWT up to the 8th decomposition level, reaching a maximum of 25kHz. Characteristic frequency ranges from 3.2kHz – 6.4kHz were identified. Similar to the literature on force monitoring for detecting gaps, researchers have also explored the ability to detect disruption by

monitoring the AE of the weld [97]. Based on the wave energy estimated for different welding parameters, welds with weld gaps were identified. The ability of online monitoring of the FSW process through the AE monitoring method is also highlighted. Researchers have also focused on the transient AE monitoring for FSW, different AE signal parameters were correlated with tensile strength [98]. High repeatability and correlation between the AE parameters and tensile strength were observed for the performed welds.

While there exists a large volume of literature on the usage of AE monitoring of machining processes (i.e.- milling, turning & drilling), there is relatively little literature present in the field of AE-based monitoring of FSW. The existing literature focusing on transient AE monitoring lacks justification for the ability to quantify process stability. A large portion of the literature highlights the advantages of online and real-time AE monitoring of FSW to aid the state-of-the-art weld monitoring system. The existing literature for monitoring FSW through AE highlights the capabilities of transient monitoring methods for AE but does not discuss the potential of continuous AE monitoring for FSW. While transient monitoring methods are limited to a fixed band of frequencies the continuous AE monitoring method enables to observation wider band of frequencies resulting in data rich process monitoring source. The latest existing literature is also limited to the static welding process (spot welding) and does not account for the development of material flow along the welding process. The experiments performed in this thesis address the above-mentioned limitations by using continuous AE monitoring methods for a range of weld parameters with different combinations of sensors. This thesis also elaborates on the ability to detect standard FSW defects and flaws through continuous AE monitoring.

2.10 Application of Machine Learning to FSW

Machine learning (ML) has become an integral part of Industry 4.0, manufacturers and researchers have employed ML algorithms for optimizing and behaviour prediction of advanced manufacturing processes. The wide extent of the usage of ML algorithms can be observed in machining, additive manufacturing and welding processes. The machine learning methods can be classified into three categories according to the learning processes[99].

- Supervised learning: Learning method where labelled data is used for training the model and offers high accuracy for real-world applications.
- Unsupervised learning: It utilizes non-labelled data for the training process and the inference is relatively less accurate for practical applications.

- Reinforcement learning: This learning method utilizes the positive and negative feedback from the environment for modification of the model parameters to achieve desired accuracy.

The supervised learning method is used for tasks involving classification and regression that require high accuracy. An artificial neural network(ANN) is a type of ML algorithm that imitates the function of a biological neuron to perform computational tasks. It is a weight-based learning algorithm that was first introduced in the field of neurobiology [100]. The concept of deep learning was later developed with ANNs as the building blocks for deep neural networks (DNNs) for performing regression and classification tasks. The concept of a self-organizing Neural Network for recognizing visual patterns was presented by Kunihiko Fukushima [101] which is the core of the development of CNNs. The ability of CNNs to classify the images was first illustrated by LeCun et.al through the identification of handwritten MNIST digits through the proposed LeNet-5 architecture [102].

There exists a substantial amount of literature focusing on the implementation of machine learning for manufacturing processes. In the past, two-decade researchers have intensively used machine learning as a tool to optimize and monitor machining processes. The application of CNNs for condition monitoring has been the most accepted in the domain of machining processes. A study focusing on the implementation of CNN for tool wear monitoring for the milling process was presented by X.Wu et.al [103]. The presented model utilized the images of the milling tool after milling Nickel-based superalloy Inconel 718 and it was observed that the proposed ToolWearnet model had an average recognition precision rate of 96.20%. The use of spectrograms as input to CNN determining the tool wear during the milling process has also been reported [104]. S Su et. al presented CNN CNN-based cutting force prediction model for the end milling process. The presented CNN model utilized input from the mechanist force model and geometric simulation and it was concluded the model could predict the cutting forces with an accuracy of 99% with a prediction time of 0.057s. The abovementioned literature highlights the potential of the implementation of CNNs for the FSW process.

Early research in force monitoring and control of the FSW process has proven to be effective. In the past decade, researchers and manufacturers have focused on predicting and optimizing weld parameters and mechanical properties of the weld. Early research into the implantation of neural networks in the FSW process has been focused on probabilistic interpretation to binary classify the welds [105]. E. Boldsaikhan

et al [106] presented a one-layer Back Propagation Neural Network (BPNN) for binary weld classification. The presented took advantage of a frequency pattern observed for forging force for sound and defective welds. With a significantly high density of the dataset, the proposed model classified the weld with 95% accuracy. Despite high accuracy, the authors highlighted FSW machine variation, tool geometry and the gap between the workpieces as the major limiting factors for the proposed model.

A similar approach was presented by A. Baraka et al. [64] utilizing DFT, RBF-NN & linguistic rules. The proposed model defined process parameters and feedback forces as the input to the data-driven model to predict the weld quality threshold for DFT analysis in real time. The defective welds produced had large-scale surface defects which can be identified with a higher amplitude of forging force/ axial force. In the past, the process parameters have also been optimized using Genetic Algorithms (GA) to attain the desired mechanical properties of the welded joint (i.e.- ultimate tensile strength, yield strength, elongation & hardness) [74]. The study compared Binary GA, Real-coded GA, Differential Evaluation (DE) and particle Swarm Optimization (PSO). It was concluded that PSO & DE are suitable algorithms to apply for optimizing the weld parameters to achieve the desired mechanical properties of the weld. The study also describes the percentage contribution of input parameters on the mechanical properties. It was observed that tool geometry and RPM had the highest contribution in determining the mechanical properties of the weld.

Researchers have also explored other process parameters of FSW to predict the weld quality of joints. B.Das et al.[107] explored DWT to decompose spindle motor current signal and feed motor current signal for weld quality prediction using an artificial neural network (ANN). The study highlights the method for the selection of a mother wavelet and discusses the three major wavelet families. The accuracy of the two ANN models for predicting the ultimate tensile strength (UTS) & yield strength (YS) is compared. From the presented models, the Radial Bias Function Neural Network (RBFNN) was reported to have higher accuracy. The presented study also states the methods for finding the optimum decomposition level and the best mother wavelet function mentioning the computational cost of a high decomposition level. Support Vector Machine(SVM) has also been applied for the classification of FSW joints [108]. The methodology implemented wavelet analysis to extract features from the captured weld images. A Gaussian and 2nd-degree polynomial kernel have been used to classify the defective and sound welds. Following a similar theme for image processing, histograms extracted from the weld images have been combined with acoustic emission analysis for binary classification of the weld [109]. Through the AE transient analysis, a

reduction in the count with an increase in amplitude and RMS was observed and using the statistical features from image processing, the welds were classified binarily.

Compared to the literature in the domain of tool optimization and parameter optimization, a relatively small body of literature focuses on the application of the machine learning model to the FSW process. Researchers have employed a diverse range of machine learning models utilizing different data sources and features for predicting the optimized weld parameters and weld quality. Existing literature highlights the accuracy of the models, but does not account for transferability to different grades of similar material. The experiments discussed in this thesis were performed on AA5083-H111 and AA6082-T6 with good transferability. A major volume of the existing literature in this domain follows the trend of quantifying the weld quality with the mechanical property of the weld from a sample extracted out of a part of the weld. As discussed in section 2.6, the mechanical properties are greatly dependent on the material flow around the tool, discrepancies in this approach may arise considering the complex geometries and welding path with curvatures. The existing literature also does not discuss the time consumed by the ML models to produce the output. The work presented in this thesis also addresses the ability of deployment of the discussed ML models.

The spectrograms enable easier visualization and interpretation of high sampling rate AE signals on a time scale which can also be used for image-based classification. This section of the thesis discusses the potential for implementing a Convolutional Neural Network (CNN) for weld classification and defect identification from the recorded AE signal. Convolutional neural networks are a sub-category of deep learning models with significant advantages such as the ability to utilize spatial correlation in the data. Data processing through CNN is divided into 3 sub-processes; convolution, sub-sampling\pooling and connection with fully connected layers. The convolution process through the data can be further divided into two; 1-dimensional convolution and 2-dimensional convolution. For the classification and recognition of image data, convolutional neural networks are preferred over other classification models like KNN & SVM due its ability to learn from hierarchical features from images. Figure 17 illustrates the layer layout of the conventional CNN with the example of spectrograms as the input for the binary classification of the weld into the good and defective weld. The feature map from the input image is estimated from the feature kernel propagated through the image forming the convolution layer. The feature map is then subjected to an element-wise activation function to obtain the new feature kernel to be fed to another layer. The feature map for the kth number at the Lth layer $Z_{i,j,k}^{L}$ is represented in Eq.(1) below where

X_{ij} is the input patch at location (i, j) with W_k^l and b_k^L being the weight vector and bias term respectively [110].

$$Z_{i,j,k}^L = W_k^{l^T} X_{ij} + b_k^L \qquad [1]$$

The activation of each feature map is explained in Eq.(2) below where a is the activation and $a_{i,j,k}^L$ is the activation value obtained. The pooling layer is introduced for the reduction of feature map resolution to reduce the computational cost and introduce shift-invariance The pooling function performed on the activation value is shown in Eq.(3) below where $Y_{i,j,k}^L$.is the pooled value and $\mathcal{R}(i, j)$ is the local neighbourhood value [110].

$$a_{i,j,k}^L = a(Z_{i,j,k}^L) \qquad [2]$$

$$Y_{i,j,k}^L = pool(a_{i,j,k}^L), \forall (m, n) \in \mathcal{R}(i, j) \qquad [3]$$
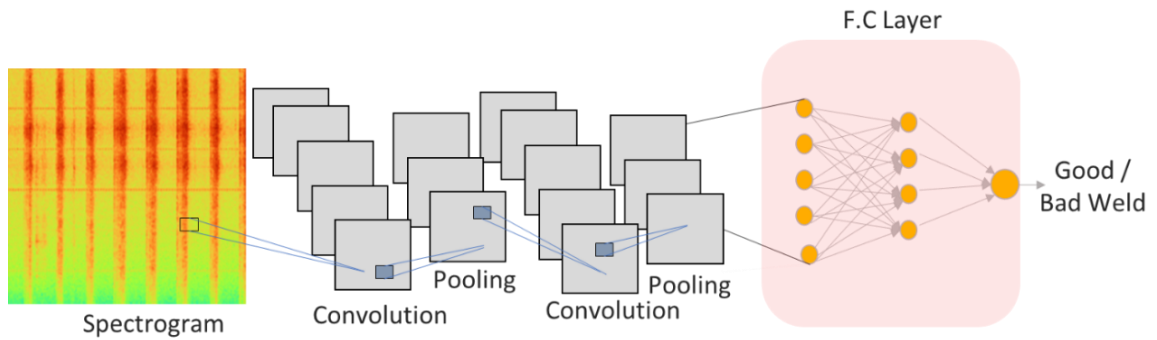
Figure 17: Layers of typical CNN architecture for binary weld classification with spectrogram as input

In this thesis, three CNN architectures are considered based on the time scale of their development and improvements addressing the applicability. Each architecture has addressed different aspects of image recognition. The three CNN architectures discussed are:

- **VGG-16 CNN architecture** [111]**:** It is the one of initial models proposed for image data classification and recognition. The model utilizes convolutional and sub-sampling/ pooling layers in series reducing the size of the image through sub-sampling. A typical VGG-16 model has 16 weighted layers with a total of 13 convolutional, 5 max pooling, and 3 dense (fully connected) layers. Fully connected layers have softmax or softargmax activation (normalized exponential function to convert a vector of real number into probability

distribution) as the last layer. The number of filters for individual layers of conventional CNN is 64 for convolutional layer 1, 128 for convolutional layer 2, 256 for convolutional layer 3 and 512 for layers 4 & 5 respectively. The architecture for the conventional VGG16 CNN model can be visualized in Figure 18 below.
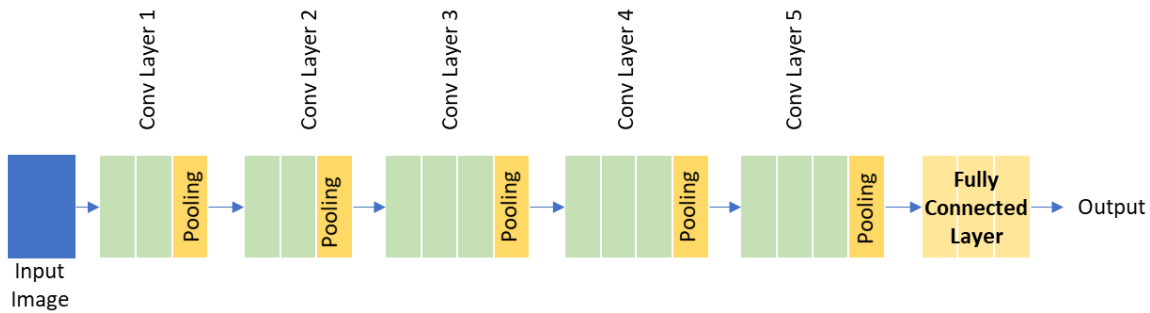
Figure 18: Architecture of conventional VGG-16 model[111]

- **Google Le Net (Inception) CNN Architecture:** In the theme of the development of a deeper convolutional model modern version of conventional Le Net- 5 was proposed by Google[112]. This model was developed focusing on capturing the sparse features present in the image that can have greater variation in size. Unlike the sequential dataflow of the VGG-16 model, the Inception model processes the image parallelly with three convolutional blocks and a pooling block. The output from four blocks is concatenated before connecting the following layer. The two versions of an elemental block of the Inception module can be visualized in Figure 19 below.
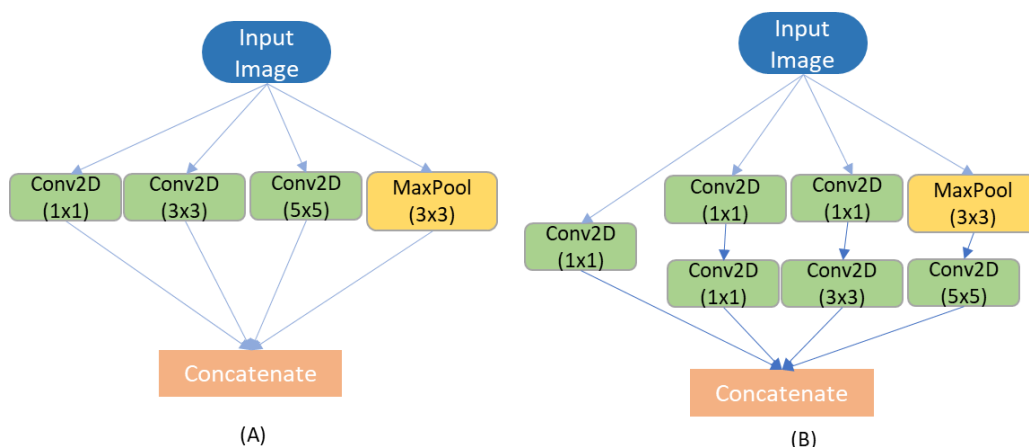
Figure 19: (A) Elemental block for inception module, Naive version; (B) Inception module with dimension reduction [112]

- **<u>Residual convolutional neural network:</u>** To pick up the complex features from the images, deeper neural networks were needed. With an increase in the depth of the neural networks, the accuracy of the model was reduced. To mitigate the loss in accuracy while maintaining the depth of the network, residual networks were introduced [113]. The residual network aimed to maintain high accuracy and mitigate the degradation problem for the deep learning framework. The constitutional block for a typical residual learning block with a convolutional residual block is illustrated in Figure 20(A) below, where $F(x)$ is the output of feed forward operation x is the input to the network. For residual CNNs, a typical residual block consists of a convolutional layer followed by batch normalization and activation units. Researchers have found 34 and 50-block residual architectures to have higher accuracy for common image-based applications [114].
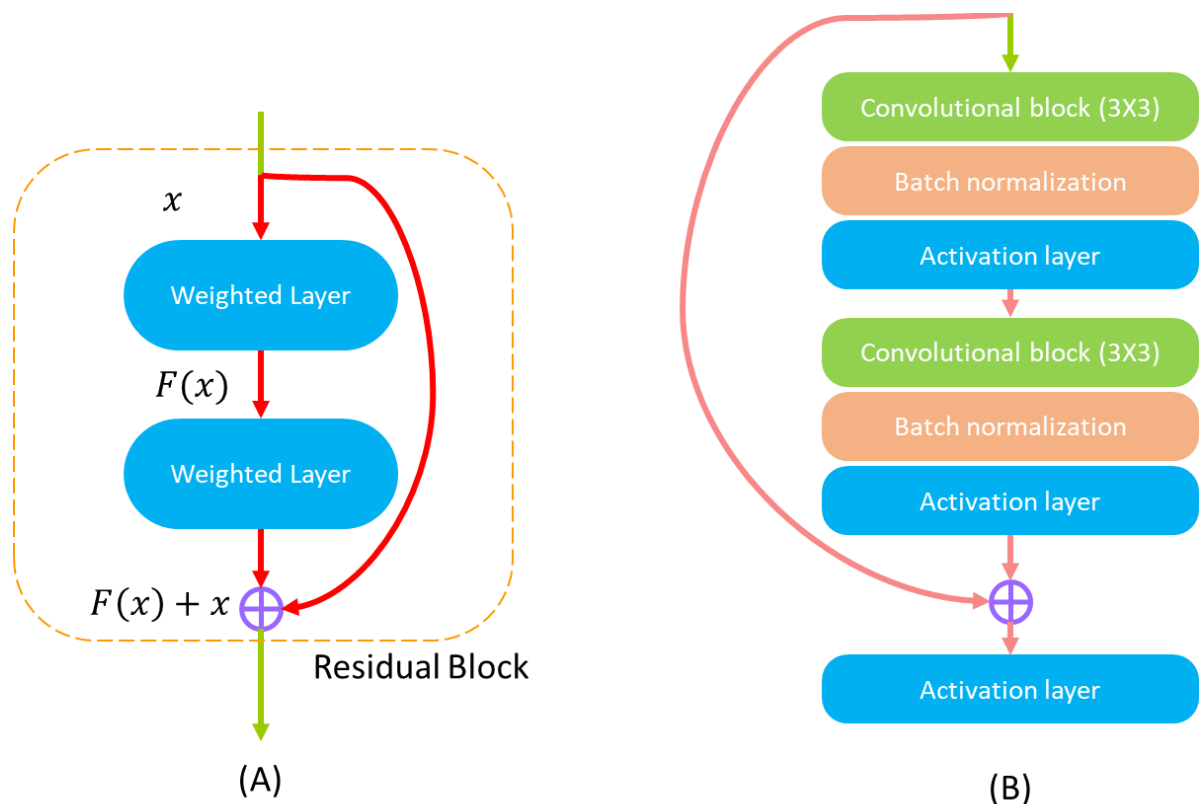
Figure 20: (A)Unit building block for typical residual learning; (B) Convolutional neural network-based residual learning block [113]

3. Experimental Platform

3.1 ESAB Super Stir FSW machine & material

The welds discussed in this thesis were performed on a dedicated FSW machine (ESAB Super-Stir) located at TWI Ltd. Cambridge. ESAB Super-Stir has a stiffened gantry design allowing high accuracy with the least positional distortion. The FSW platform also offers a large working envelope of 8x5m. Welds with high thickness (up to 25mm) can also be performed using this platform. The FSW platform in the standby position before welding is shown in Figure 21 below.
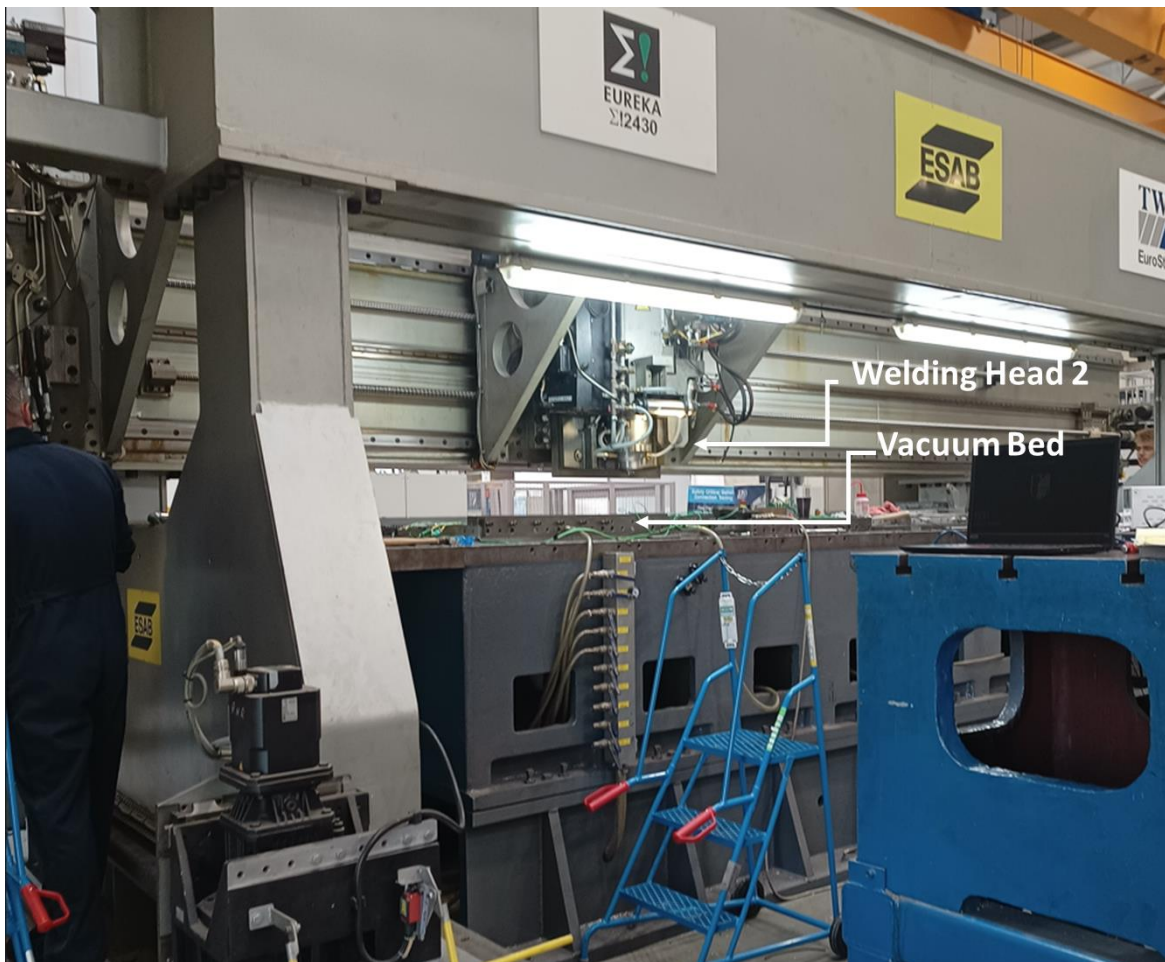
Figure 21- ESAB Super-Stir FSW Platform at TWI Cambridge

With two welding heads on the gantry, each welding head is designed for high speed and high torque individually. For the welding head with high torque specification, the maximum axial loading is 100kN. For welds discussed in this thesis, the welding head with high torque specification is used. The specifications for each head are defined in Table 2. Large parts and curved surfaces such as EV battery trays, wing ribs &

canisters have been successfully welded in the past using ESAB Super-Stir. During the welding phase, the traverse speed, tool tilt angle (TTA) and the spindle speed cannot be varied. Compared to CNC machine tools and FSW robots, the ESAB Super-Stir offers significantly higher maximum traverse & axial/vertical loading conditions. As the high welding speed (traverse speed) is not a consideration for the research, a welding head with high torque-delivering capability was selected for performing the welds.

	Welding Head 1	**Welding Head 2**
Spindle Speed (RPM)	0-3000	3000-5000
Max. Traverse Loading	20kN	5kN
Max. Vertical Loading	100kN	60kN
Head Tilt Angle/ Tool Tilt Angle	2.5° (X-Axis) & 5° (Y-Axis)	
Spindle Torque (Nm)	340Nm at 100–500RPM/ 100Nm at 2000RPM/50Nm at 3000 RPM	60Nm at 3000RPM/ 30Nm at 5000RPM/50Nm at 1500 RPM

Table 2- Specifications for the two welding heads of the ESAB Super-Stir FSW machine

Considering the approach of the experimental design, softer and harder aluminium grades AA6082-T6 (precipitation hardened) and AA5083-H111 (non-hardenable) were used to perform FSW for butt joints of the same material. The material composition for both the aluminium alloys is mentioned in Table 3 & Table 4 of this thesis [115][116].

	Mn	**Fe**	**Mg**	**Si**	**Cu**	**Zn**	**Ti**	**Cr**	**Al**
Min	0.40	-	0.60	0.7	-	-	-	-	Bal
Max	1.00	0.50	1.20	1.3	0.10	0.2	0.1	0.2	

Table 3- Material composition for AA6082-T6

	Mn	**Fe**	**Mg**	**Si**	**Cu**	**Zn**	**Ti**	**Cr**	**Al**
Min	0.40	-	4.00	0	-	0	-	0.05	Bal
Max	1.00	0.40	4.90	0.40	0.10	0.10	0.15	0.25	

Table 4- Material composition for AA5083-H111

3.2 Coordinate & Control System

The ESAB Super-Stir system uses position and force control methods to perform the welds. The dynamometer positioned at the top of the welding head is used to monitor and record the forces in all three directions. From the traverse & axial force control methods, the machine uses axial force control to ensure proper tool contact under force control. In position control, the machine performs the weld with initial and final coordinates defined using the positioning pendant. The coordinate system for the platform is illustrated in Figure 22
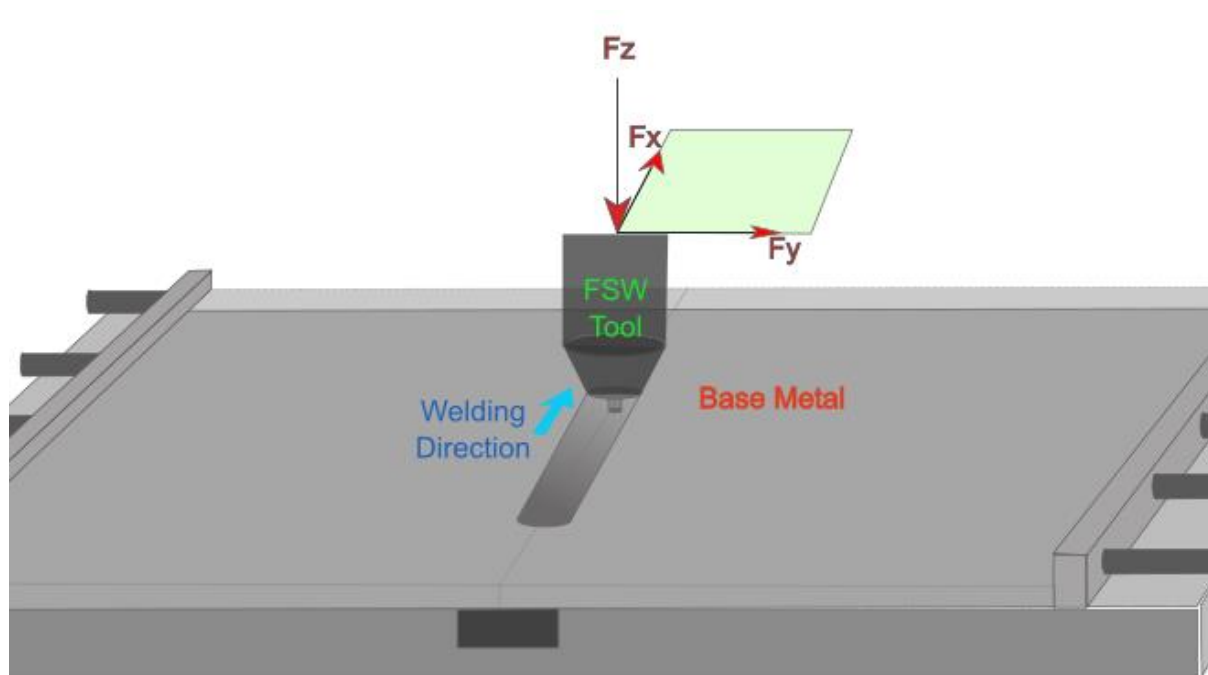
Figure 22- Weld direction and forces involved in the FSW process

3.3 Clamping Jig & Backing Bar

To ensure no movement of the base metal, clamping forces in all three directions (i.e.- X, Y & Z) are needed. The vacuum bed creates a uniform pressure along the surface of the plate, mitigating the deformation caused by the point clamping force. To restrain the plate's movement in the Y axis, restraining bars are used and the clamping force is controlled by tightening the screws of the threaded bar. Two clamping blocks at the end of each plate are placed to restrict the motion of the plate in the weld direction. The forces experienced by the base metal while performing FSW are illustrated in Figure 23 below.
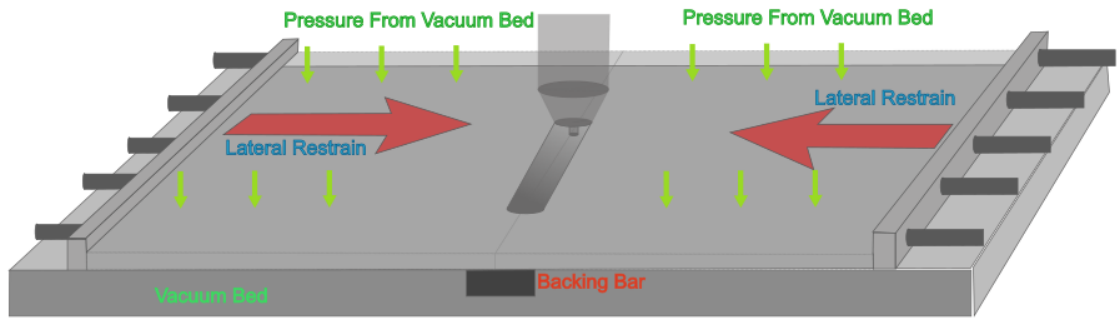
Figure 23- Clamping forces experienced by the based metal while performing FSW

While performing conventional FSW, the probe length is kept slightly above the rear face of the plate to ensure the tool does not pass through the plate. For the welds discussed in this thesis, a fixed probe length of 4.8mm was used. To mitigate the deformation by the axial force exerted by the tool, the backing bar is placed on the opposite side of the plate. The backing bar is made of a harder material to resist the forces. The setup used bright-drawn mild steel as the backing bar due to its higher strength and smoother surface finish. In the discussed setup, a backing bar of 1000mm in length,10mm in height and 30mm in width was used.
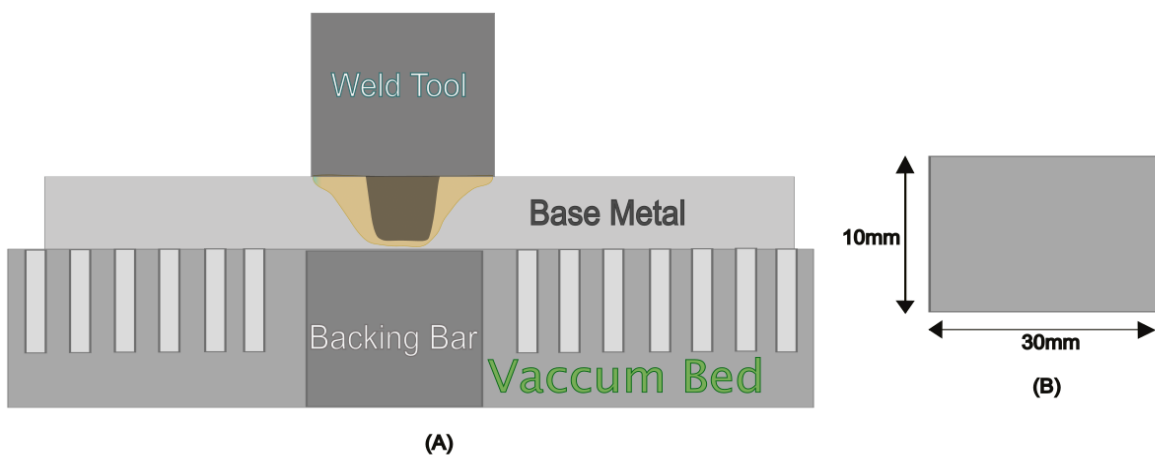
Figure 24- (A) Position of the backing bar in the welding platform; (B) Cross-sectional dimension of the backing bar

3.4 FSW tool design

The welds discussed in this thesis were performed using the same tool (inspected for tool wear through surface profilometry discussed in section 4.2) keeping the probe/pin length constant at 4.8mm. This two-part tool consisted of a separate tool shoulder and tool probe. A combination of a featureless concave shoulder with a threaded tri-flute probe was selected because of its high efficiency and ability to weld different grades of aluminium alloys reported during the welds performed in the past (based on the discussion with TWI staff). The tool shoulder is made of H13 tool steel and the tool probe is made of nickel-cobalt alloy MP159 respectively. With a higher tensile and yield strength for MP159 compared to H13 at an elevated temperature of 480°C, MP159 is better suited for the FSW tool probe. The schematics for tool geometry for the tool probe and tool shoulder are shown in Figure 25 below.
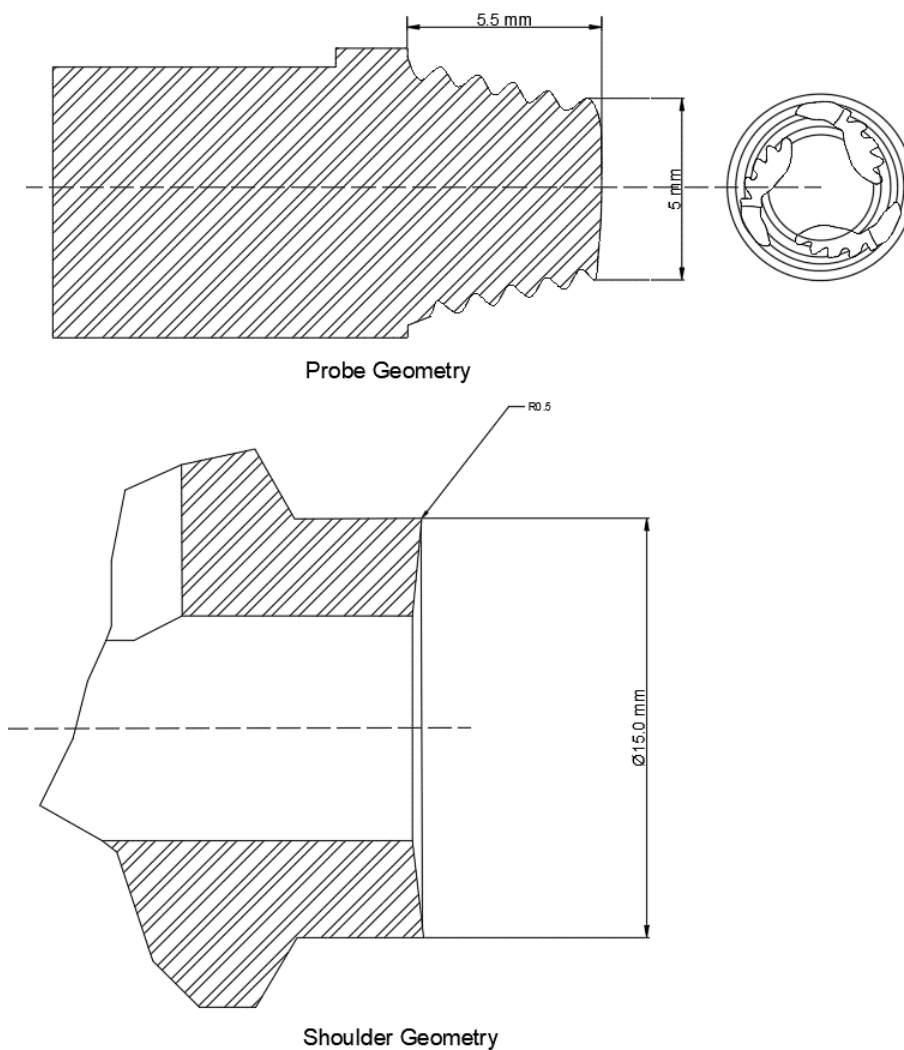
Figure 25- Schematic for two-part FSW tool with probe and shoulder geometry [117], [118]

3.5 Acoustic Emission Monitoring Setup

The experimental setup used commercially available piezoelectric-based VS-900 RIC wide-band acoustic sensors from Vallen System which were tested for sensitivity by facilities at TWI Ltd. The sensitivity of the sensor over a range of frequencies is presented in the datasheet of the sensor provided by Vallen System on their website [119]. The sensitivity plot from the datasheet is provided in Figure 26 below.

(A)   **(B)**
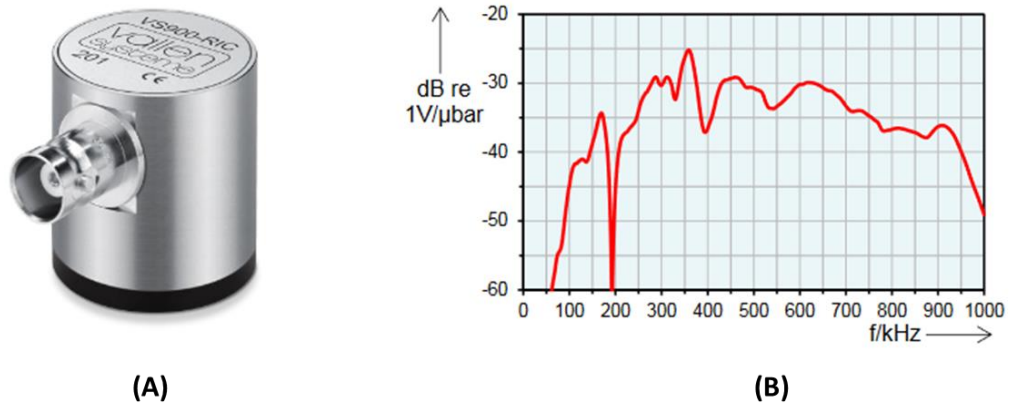
Figure 26: (A) VS-900RIC sensor with the BNC connector; (B)Sensitivity plot for the VS-900 RIC sensor over the frequency (0 - 1000 kHz) [119]

The sensor-enabled measurement of frequency within the range of 100kHz to 900kHz with a peak sensitivity of 350kHz. For maintaining uniform pressure on the surface and ensuring good contact, magnetic holders/mounts from Vallen System (MAG4R) were used along with the screw brackets to ensure even contact. In the discussed experiments, the sensors are mounted with and without the couplants. With the built-in pre-amplifiers, the complexity of the experimental setup is reduced. For the power supply for the sensors, a variable bench power supply set to an output of 28.8V was used. The high-frequency data obtained from the VS-900 RIC sensors was recorded using a 4-channel Picoscope 5442d (USB PC oscilloscope) powered by the USB connection. Picoscope offers the flexibility of measuring sensor signals with a high sampling rate with multi-channel data recording. With the limited memory capacity of the Picoscope device, data at a 62.5 MS/s sampling rate at 16-bit resolution can be stored on the onboard memory distributed in 32 memory bins. The connection of the setup is illustrated in Figure 27 below. The data flow of the AE signals for plotting spectrograms is explained in Figure 28 below
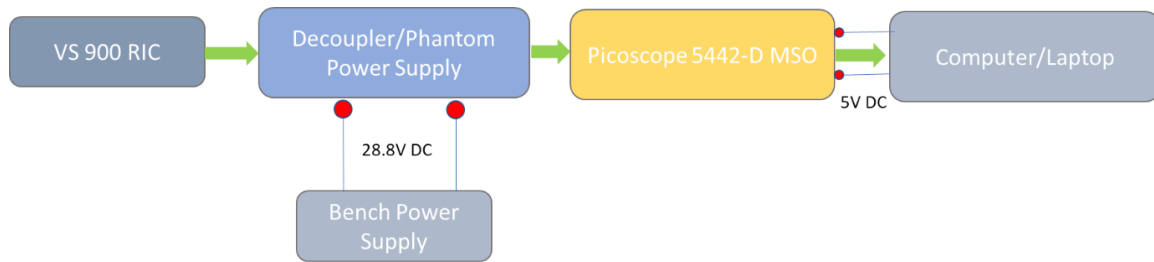
Figure 27- Connection diagram for measuring Acoustic Emissions (AE) for the FSW process
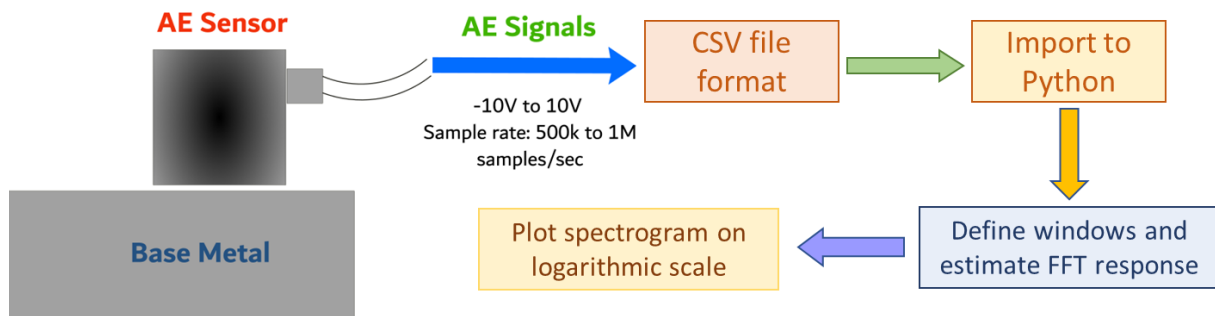
Figure 28: Data flow for visualizing recorded AE data

Considering the Nyquist frequency theorem [120], the recording parameters were selected to maintain the sampling frequency at 1MHz or 1MS/ s or 500kHz for longer welds. The recording parameters are defined in Table 5. The measured voltages at the defined sampling rate were exported to .CSV format after the weld was complete. A pair of sensors were placed in three different combinations for the comparison of the AE signal recorded at different positions. The location of sensors for each combination is illustrated in Figure 29 where the location of the two base metal plates, joint line, backing bar and advancing & retreating side AE sensor. When the sensors are placed on the plate, the middle section on the outer edge region of the plate away from the joint line is used for placing the sensors. While placing the sensor on the backing bar, the sensors are placed at the centreline of the backing bar touching with clearance of 2mm-3mm from the edge of the plate. Sensors placed on the support bed were placed in with a clearance of 100mm from the plates.
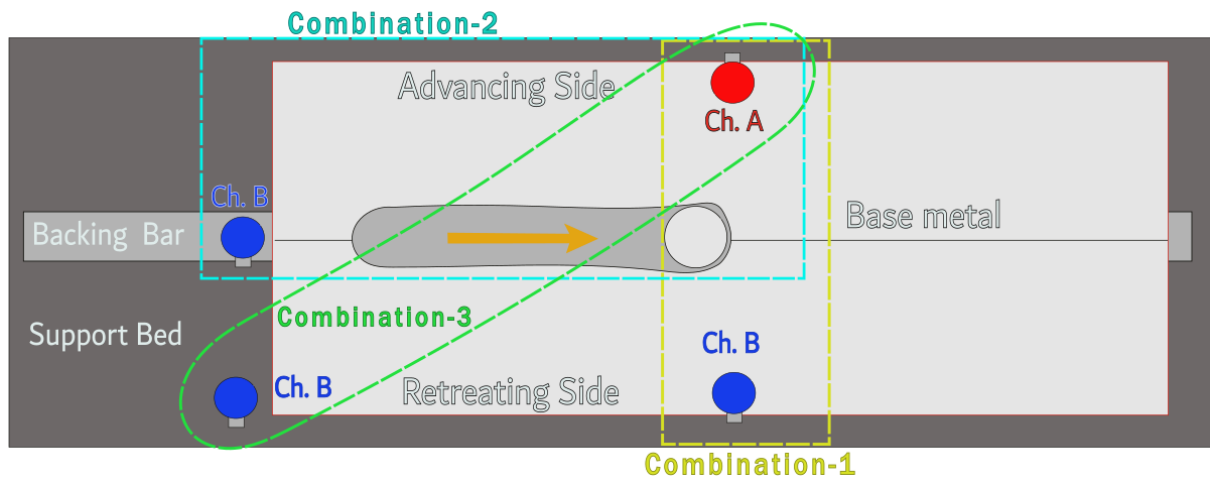
Figure 29- Three combinations of position for a pair of VS-900 RIC sensors.

Case	Peak Voltage(V)	Resolution(bit)	Ms/div	Memory Bins/ Waveforms
1	+/- 10V	16(2 Ch.)	100	32
2	+/- 10V	16(2 Ch.)	200	32

Table 5- Picoscope waveform recording configuration

3.5.1 Data analysis approach

The data analysis approach can be divided into two, parametric analysis and waveform analysis, the two analysis methods and the features are illustrated in Figure 30 below. Depending on the requirements of the features that need to be extracted from the AE data the signal processing approach can be selected. As mentioned earlier, this thesis uses a continuous acoustic emission monitoring method for monitoring the FSW process. Using the waveform analysis, the correlation between the AE features for different weld parameters is obtained and discussed in chapter 4 of this thesis.
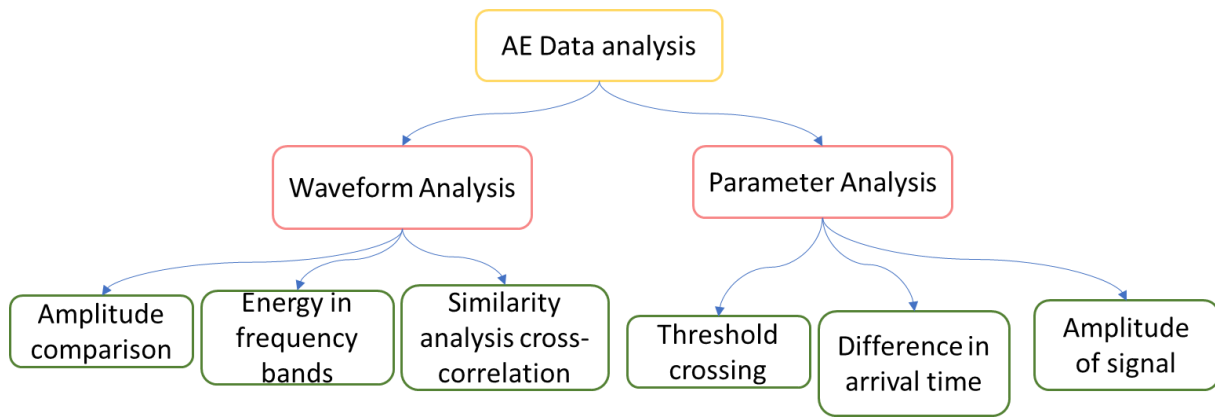
Figure 30: Signal processing approach for AE data

To visualize the AE data and for training the neural network for weld classification, spectrograms using the AE data are plotted. Spectrograms are widely used for visualization of the constituent frequencies of a signal. The spectrograms are plotted on a logarithmic scale illustrating the distribution of frequencies on a time scale with the intensity in decibels (dB). The third axis illustrates a colour bar representing the intensity of the frequency on a logarithmic scale. The spectrogram plotting process for AE data can be divided into 4 steps below. The Python script for plotting spectrogram is mentioned in Appendix 1 of this thesis.

- Framing: The dataset obtained for the AE of the process is sliced using windows performing a short time.
- STFT/FFT: To obtain the frequency features of the signal, the Fourier transform is used to deconstruct the signal and extract amplitudes of the constituting waves.
- Log transformation: The data obtained after the STFT/FFT is normalized by estimating the logarithmic values of the dataset.
- Plotting spectrogram: The normalized amplitude of each window is plotted to correspond to the frequency bins to obtain a time-frequency spectrogram.

3.6   Introducing the point of material disruption

The material disruption in the weld is caused by introducing holes with different diameters from 3.5 mm to 4.5 mm with a constant depth of 4.5 mm. The two welds with material disruption points discussed in section 3.8. are D2 and D3. Weld D2 with a length of 220mm, the hole is positioned at the centre of the weld. For weld D3, performed for a greater length of 470mm, the holes of 3mm, 3,5mm and 4.5mm diameter were drilled in the joint line. While the material disruption regions have a higher probability of having defects and flaws, material disruption cannot be directly stated as analogous to the presence of defects.
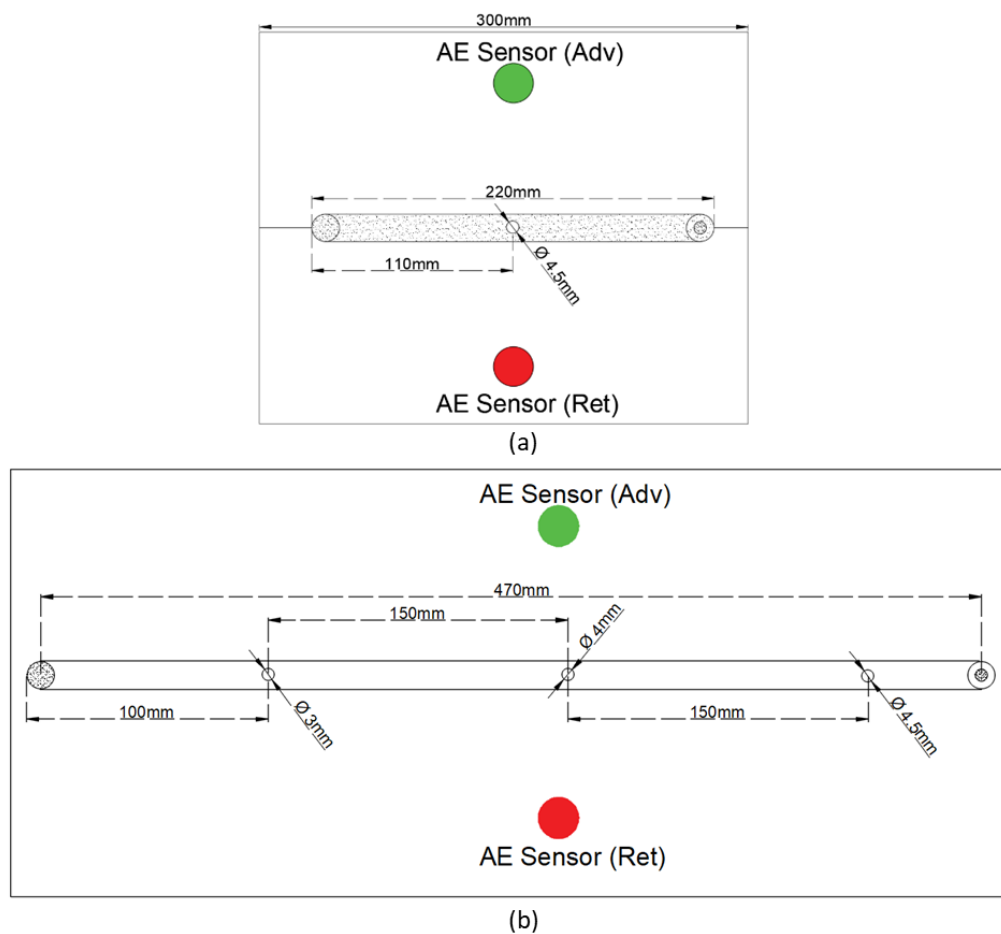
Figure 31- Position of the holes for inducing material disruption in the welds D2 & D3

3.7   Weld temperature measurement setup

To determine the correlation between the acoustic emissions and the welding temperature, 8 K-type thermocouples and two VS900-RIC AE sensors were used in the setup. The schematic for the setup is shown in Figure 32, illustrating the position

of thermocouples and AE sensors. Four thermocouples of specification mentioned in *Table.6.* were placed on both the advancing & retreating sides of the weld. The AE data was captured using the two VS-900RIC sensors (discussed in *Section 4.6*) placed on either side of the weld. As the tool-shoulder engagement also needs to be quantified (discussed in sections 4.4 & 4.5), the Picoscope was configured to record with a sampling frequency of 998KS/Sec. With a core diameter of 0.711mm, the thermocouple probe has an effective diameter of 1.3mm at the tip of the spot-welded twister pair. The thermocouples are placed 22mm away from the joint line considering the roller clearance. To ensure proper contact of the thermocouple with the weld plate, holes of 1.3mm diameter and depth are drilled on the plates using a CNC machine.
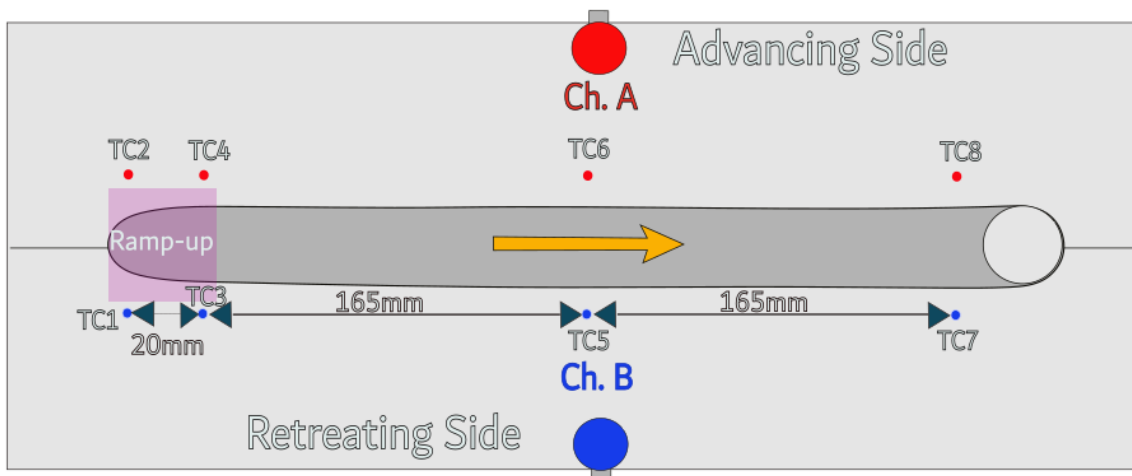
Figure 32- Weld temperature measurement setup

Conduct or type	Conductor Diameter	Length	Insulation Material	Min-Max Operating Temperature	Calibration
K	0.711mm	300mm	High Temp Fiberglass	-10ºC to +400ºC	UKAS Batch Calibrated (+/-1.1 ºC)

Table 6- Specifications for the thermocouple used in the study[121]

The weld direction is marked with the yellow arrow from left to right with the clockwise rotation of the tool making the top half the advancing and the lower half the retreating side of the weld. Thermocouples on both sides were placed into the holes drilled by the CNC machine and secured by thermal reflective tape. The position of the thermocouples TC3 and TC4 was kept closer to the starting position of the weld to

capture the temperature difference in the ramp-up phase of the weld. TC5 & TC6 thermocouple probes were positioned at the centre of the weld to measure the temperature in the steady zone. TC7 and TC8 were placed 20mm before the tool was retracted.

3.8 Welding trial phases & parameters

The welding trials were conducted in 7 phases focused on inducing or enhancing a particular weld thermomechanical phenomenon. Based on previous welds (mentioned in existing literature in Chapter 3) performed for similar materials, the weld parameter range was selected. The welding trial phases, with the aim for each phase, are defined in Table 7. For ease of referencing and understanding, the weld numbers have a prefix of the phase under which they were performed. Following Table 7 below, the weld parameters for the discussed welding trials are mentioned in Table 8. All the welds discussed in this thesis were performed with position control with a constant plunge rate.

Phase	Motivation	Weld reference.	AE Setup Combination
1st	Correlating the measured AE with axial forces	C1 to C6	Combination 3
2nd	Effect of material disruption on AE signals	D1 to D6	Combination 1
3rd	Effect of lack of shoulder engagement	SE1 to SE4	Combination 1
4th	Detection of Lack of Penetration (LOP) by AE signals	LOP1 to LOP12	Combination 2
5th	Validation welds for the presence of internal defects & lack of penetration	V1 & V2	Combination 1 & 2
6th	Co-relation of AE with weld temperature	T1 to T4	Combination 1
7th	Repeatability analysis for AE measurement method	R1 to R4	Combination 1

Table 7- Welding trial phases and referencing nomenclature

Weld reference	Tool rotation rate (RPM)	Tool Traverse speed (mm/min)	Tool Tilt Angle	Plunge depth (mm)	Plate Thickness (mm)	Weld Length (mm)	Base Material
C1	800	500	1.5°	4.8	5	100	AA6082
C2	1000	500	1.5°	4.8	5	100	AA6082
C3	1200	500	1.5°	4.8	5	100	AA6082
C4	800	500	1.5°	4.8	5	100	AA6082
C5	1000	500	1.5°	4.8	5	100	AA6082
C6	1200	500	1.5°	4.8	5	100	AA6082
D1	1200	550	3°	4.8	5	225	AA6082
D2	1200	550	3°	4.8	5	220	AA6082
D3	1200	550	3°	4.8	5	470	AA6082
D4	800	1000	3°	4.8	5	230	AA6082
D5	600	1000	3°	4.8	5	230	AA6082
D6	1200	550	1.5°	4.8	5	200	AA6082
SE1	800	500	1.5°	4.8	5	200	AA5083
SE2	800	500	1.5°	4.6	5	200	AA5083
SE3	700	500	1.5°	4.6	5	200	AA5083
SE4	900	500	1.5°	4.6	5	200	AA5083
LOP1	500	300	1.5°	4.8	5	140	AA5083
LOP2	500	300	1.5°	4.8	6	140	AA5083
LOP3	600	300	1.5°	4.8	5	140	AA5083
LOP4	700	300	1.5°	4.8	5	140	AA5083
LOP5	600	300	1.5°	4.8	6	140	AA5083
LOP6	700	300	1.5°	4.8	6	140	AA5083
LOP7	800	300	1.5°	4.8	5	140	AA5083

LOP8	900	300	1.5°	4.8	5	140	AA5083
LOP9	1000	300	1.5°	4.8	5	140	AA5083
LOP10	800	300	1.5°	4.8	6	140	AA5083
LOP11	900	300	1.5°	4.8	6	140	AA5083
LOP12	1000	300	1.5°	4.8	6	140	AA5083
V1	620	1100	3°	4.8	5	370	AA6082
V2	720	950	3°	4.8	5	370	AA6082
T1	500	550	3°	4.8	5	370	AA6082
T2	800	550	3°	4.8	5	370	AA6082
T3	500	550	1.5°	4.8	5	370	AA6082
T4	800	550	1.5°	4.8	5	370	AA6082
R1	800	550	1.5°	4.8	5	360	AA6082
R2	500	300	1.5°	4.8	5	250	AA5083
R3	800	300	1.5°	4.8	6	250	AA5083
R4	1200	550	3°	4.8	5	250	AA6082

Table 8- Weld parameters for six phases of welding trials

3.9 Dataset augmentation method for ML

Since the spectrograms obtained from the AE signals of the welding process are limited by the number of welds performed, dataset-widening methods need to be used. The conventional dataset-widening methods for image data use flipping, rotating, zooming, translating and adding Gaussian noise (increasing the granularity of the image) to images. The abovementioned data augmentation methods are not suitable for augmenting spectrograms obtained from AE signals as the characteristic features of the spectrograms would be not accounted for. Unlike the conventional image-based inputs, the integrity of the spectrograms is dependent on the frequency and the time scales.

To prevent the model from overfitting the number of trainable parameters is reduced. To further prevent the model to overfit the training data augmentation is focused on increasing the variance of the input data. A threshold of 10% of coefficient of variance

is selected as the threshold to control the spread of the data without losing the essential information. To assess the effectiveness of the training process and to prevent overfitting of the model the exploration vs exploitation aspect is quantified through plotting the coefficient of variance for the classified data of the training dataset.

For augmentation of spectrograms of AE signals, mel-spectrograms are introduced to the dataset for training and testing the deep learning networks. mel referring to 'Melody' is a scale that was developed to scale high and low frequencies and differentiate distinct frequencies as stated in a book by O'Shaughnessy [122]. Using Eq. (4) below, the AE signal is converted from frequency scale to mel-scale.

$$m = 2595 * \log\left(1 + \frac{f}{700}\right) \qquad [4]$$

Where m is a perceptual frequency in mel-scale & f is the actual frequency of the data in Hertz. Furthermore, the dataset is augmented using pitch scaling, inducing random gain and adding white noise to the data set which is a novel method developed for application to CNN. Through the introduction of the abovementioned factors into the dataset, the robustness of the deep learning model can be increased without altering the characteristic features of the AE signals observed through spectrograms. This is validated through visual inspection of the spectrogram which clearly shows the events discussed in this thesis after undergoing the augmentation process.

By using the Librosa library [123] for audio engineering available for Python, the AE signals are augmented for different combinations of parameters of augmentation methods mentioned above. The process for generating the training dataset using the augmentation dataset can be better visualized in Figure 33.
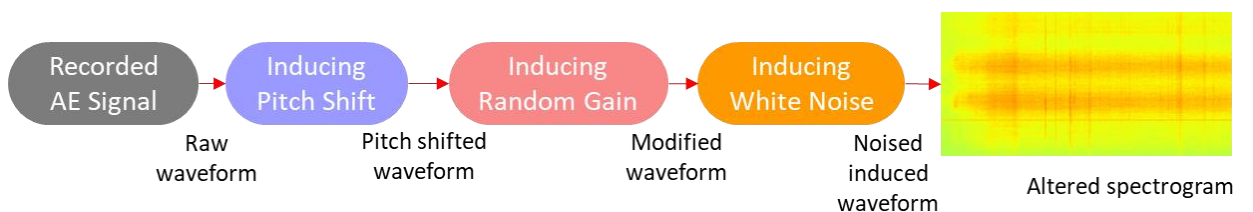
Figure 33: AE data processing for augmentation of the training dataset

Pitch shift or pitch scaling is introduced by finding the octave scale defined in Eq.(5) [124], where F1 and F2 are the frequencies of the two signals The signal is then resampled to the desired frequency using the Sinc interpolation or Whittaker–Shannon

interpolation defined in Eq. (6) [125]. In the equation the interpolated continuous signal $Y(x)$ is resampled from original samples Y_n with the discretization interval of Δx. For introducing random gain to the AE signal, the sample is discretized and multiplied with a gain factor (presented in Eq.(7)) estimated randomly from a range presented in Table 9.

$$Octave\ number = \log_2 \frac{F_1}{F_2} \tag{5}$$

$$Y(x) = \sum_{n=-\infty}^{n=\infty} Y_n\ Sinc\left(\pi\left(\frac{x}{\Delta x} - n\right)\right) \tag{6}$$

$$Y(x) = \sum_{n=0}^{n=N} Y_n * Gain \tag{7}$$

As the last step of the augmentation, white noise is added to the AE signal by estimating a random distribution factor (DF) from the gaussian distribution of signal obtained though the standard deviation of the signal. The mathematical expression of the white noise is presented in the Eq.(8) below where Y_{wn} is the white noise added AE signal and Y_{ae} is the original AE signal. The intensity factor (IF) is defined to scale the distribution factor (DF).

$$Y_{wn} = Y_{ae} + (DF * IF) \tag{8}$$

The above-mentioned augmentation methods are performed with two Python scripts using Matplotlib and Librosa library. The first script is developed for file handling while the second script is focused on plotting the spectrograms. The first script "Weld_Data_Gen.py" which is responsible for file handling and denoising AE data is presented in Appendix 1. The second script "audaug.py" deals with the augmentation of AE data with spectrogram plotting and saving the spectrograms (mentioned in Appendix 1). The flow of data from reading AE signals to plotting them is presented in Figure 34 below.
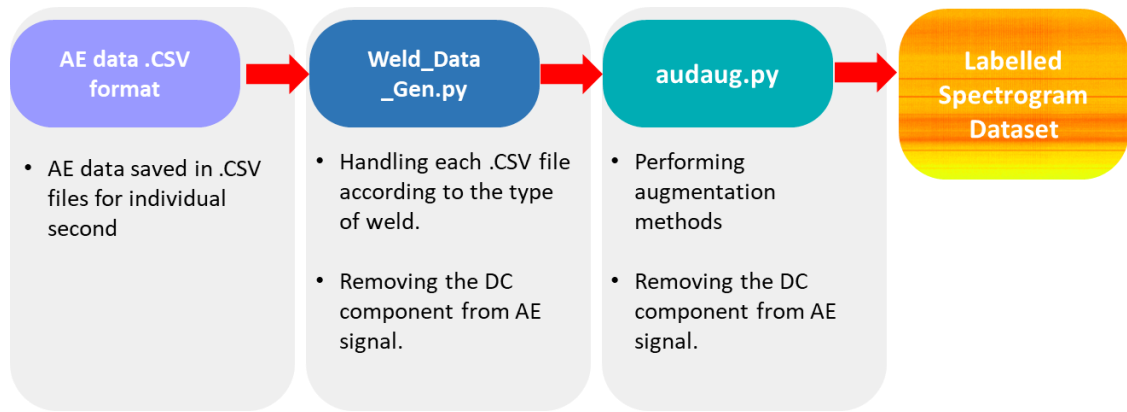
Figure 34: Data flow for augmentation of AE signal and creation of labelled dataset for the ML training process.

Table 9 presents the abovementioned parameters of augmentation methods used for the generation of validation and training datasets. The starting parameters of the augmentation methods are selected through an iterative process where the augmentation was most observable through visual inspection. For a generation of the training dataset, a wider range of augmentation parameters with higher resolution is selected resulting in a higher number of generated spectrograms. The validation dataset has a 70% lesser number of spectrograms due to a smaller range of augmentation parameters with lower resolution between the parameters.

Dataset	Sparse classification labels /Binary Classification	Pitch Shift Scale	Random Gain	White Noise Scale	Total Spectrograms
Validation Dataset	Internal Void/Bad	1.3-2.5	23-30	0.5-1.0	270
	Lack of shoulder pressure/Good	1.3-2.5	23-30	0.5-1.0	270
	Material Disruption/Bad	1.7-2.3	23-30	0.5-1.0	256
	Sound welds/Good	1.6-2.0	23-30	0.5-1.0	297
Training Dataset	Internal Void/Bad	0.3-1.5	12-24	0.2-0.6	840
	Lack of shoulder pressure/Good	0.3-1.5	12-24	0.2-0.6	840

	Material Disruption/Bad	0.3-1.8	12-25	0.2-0.5	960
	Sound welds/Good	0.3-1.5	10-25	0.2-0.8	1100

Table 9: Dataset augmentation parameters used for generating training and validation datasets

Material
Disruption/Bad   0.3-1.8   12-25   0.2-0.5   960

3.10 CNN architectures and training platform

The development and testing of the CNN architectures discussed in this thesis are performed using the TensorFlow library for Python along with the other supporting libraries like Matplotlib for visualization of the plots from the training process. To assess the performance of the proposed parent architecture-inspired models, the Keras library is used to generate classification reports and a confusion matrix.

The classification report uses true and false values of positive and negative classification from the model. The classification report utilizes recall factor, precision factor and F1 score to assess the model's performance. Recall and precision are defined based on positives and negative results classified by the model in the two Eq.(9) & Eq.(10) below. Support defines the number of occurrences in the dataset or the number of events predicted or classified by the model.

$$Recall = \frac{True\ Positive}{True\ Positive + False\ Negative} \tag{9}$$

$$Precision = \frac{True\ Positive}{False\ Positive + True\ Positive} \tag{10}$$

$$F1\ Score = \frac{True\ Positive}{\frac{1}{2}(False\ Positive + False\ Negative) + True\ Positive} \tag{11}$$

A confusion matrix is used to visualize the classification performance of the algorithm using criteria of true and false values of positive and negative classification as a classification report [126]. The performance of a sparse classification model can be best visualized using a confusion matrix. Confusion matrix is utilized in sections 5.4 and 5.5 to assess the classification performance of the proposed models.

3.10.1 VGG-16 CNN Architecture

The architecture of the CNN models can be altered according to the application and to reduce the computational cost. This section of the thesis discusses a less computationally intensive version of the VGG-16 model (discussed in section 2.10) with a reduced number of filters and layers. The modified architecture of the VGG16-inspired CNN is illustrated in Figure 35 below. The Python script for the proposed VGG-16 architecture can be found in Appendix: 2.
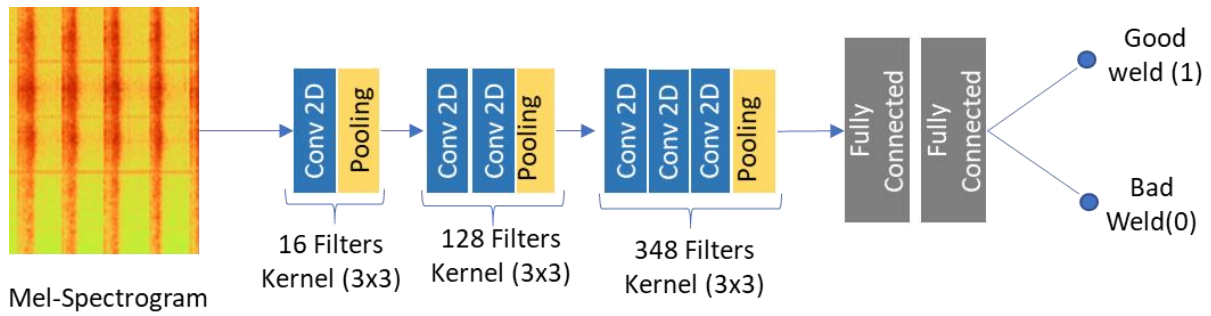
Figure 35: VGG16 inspired CNN architecture for binary classification of welds

Unlike the parent VGG-16 architecture with 5 layers, the proposed VGG-16 inspired network has 3 layers with an increasing number of filters reducing the number of trainable parameters. The proposed inspired model performs binary and sparse classification of the welds using one input (i.e-mel-spectrograms). Chapter 5 of this thesis will discuss the training and testing results obtained for the abovementioned CNN architecture.

3.10.2 Google Le Net (Inception) CNN Architecture

To overcome the limitations of mel-spectrogram, two inputs (i.e.- Spectrogram & mel Spectrogram) CNN architecture is proposed. To reduce the complexity of the network and accommodate two inputs, the number of layers is reduced and two Inception-inspired architectures are proposed in this thesis. The two Inception-inspired networks for sparse classification of weld quality are shown in Figure 36 below with the colours representing the acceptability of the weld for an application following the standards discussed in section 2.8.
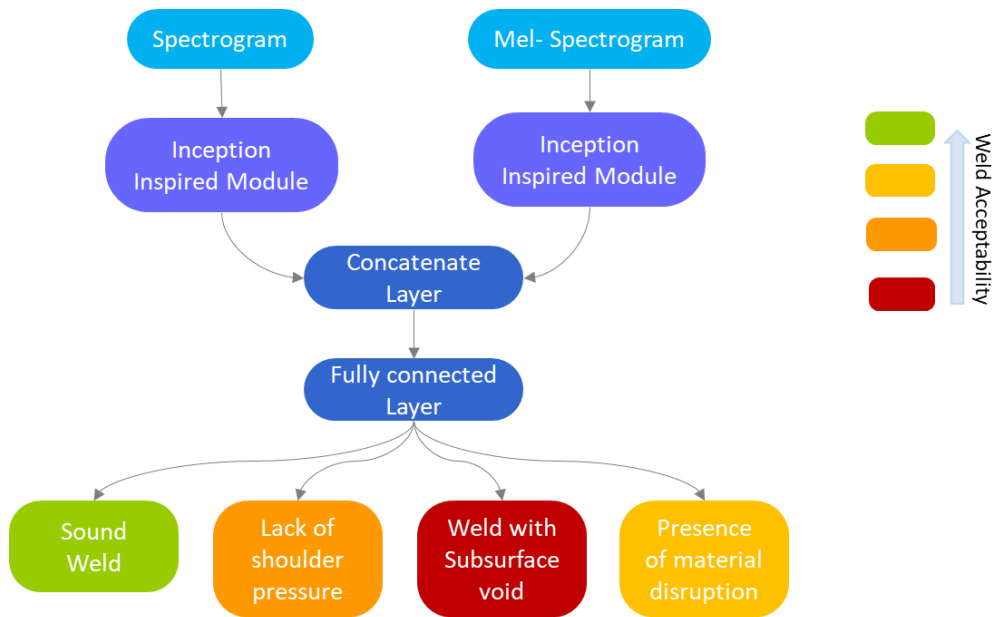
Figure 36: Inception-inspired sparse weld classification model version-1
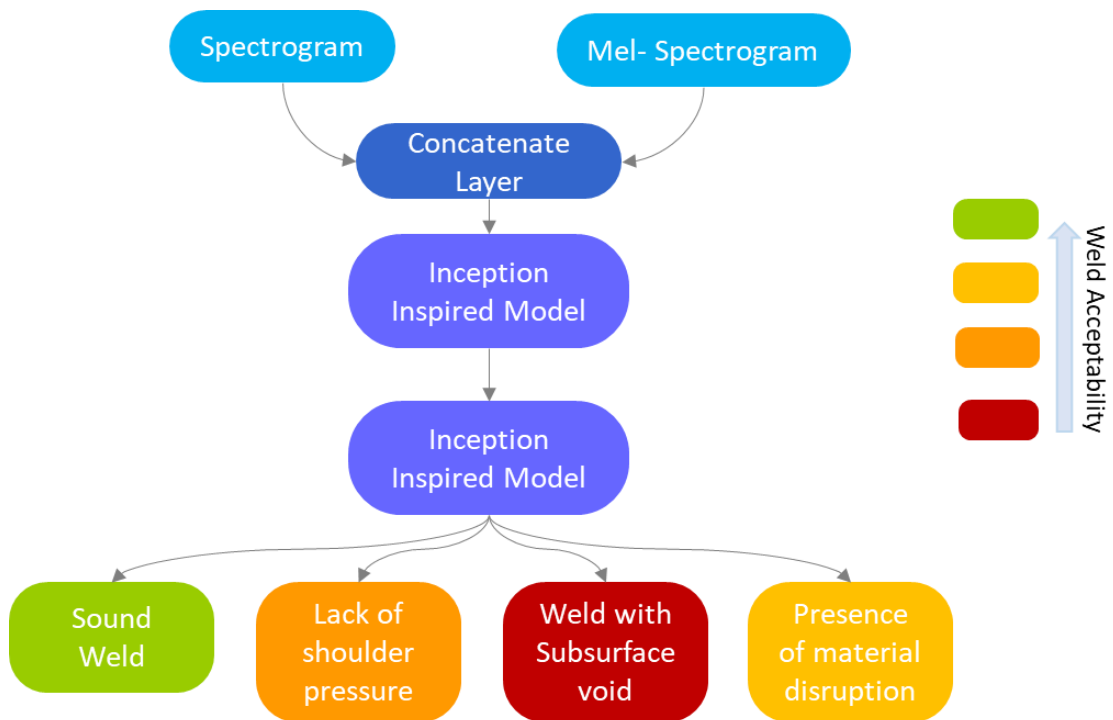
Figure 37: Inception-inspired sparse weld classification model version-2

Unlike the conventional inception model, the proposed architecture takes two images simultaneously and processes them. Figure 36 and Figure 37 are the two variants of the proposed architecture utilizing hybrid input and concatenating before and after the inception-inspired module. The last layer of the model is sparsely categorized using

56

the weld defects as the labels of the categories (discussed in section 3.9). The training plots with the model accuracy from the test data are discussed in section 5.4 of this thesis.

3.10.3 Residual convolutional neural network

The elemental block for the residual learning model is discussed in section 2.10. This section discusses a less memory-intensive model to reduce the computational cost of training the model. Similar to the abovementioned inception model, the proposed model accommodates dual input (i.e.- mel-spectrogram, Spectrogram) through a concatenation layer. Figure 38 illustrates the residual learning-based model for the classification of weld quality through AE data.
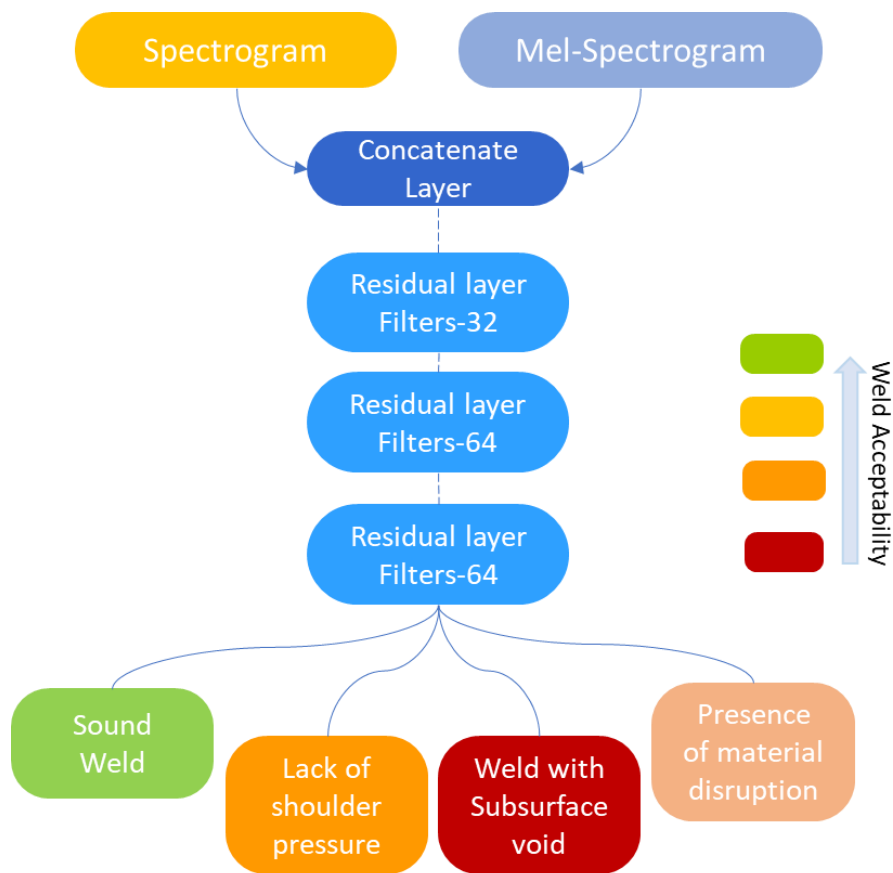
Figure 38: Resnet-inspired sparse weld classification model following the classification colours for acceptability

Similar to the models discussed earlier in sections 3.10.1 and 3.10.2, the proposed model sparsely classifies the welds into four categories based on the acceptability of the defects according to the standards. The proposed model resulted in 80% fewer parameters compared to the parent Resnet-50 architecture. The details about kernel size, stride length and the libraries used for the network development can be found in the Python script in Appendix 2.

3.10.4 Training parameters and the platform

The selection of hyperparameters during the training process is based on the existing literature and iterative trial and error method. The proposed model uses stochastic gradient descent (SGD) as an optimizer and categorical cross-entropy to estimate model loss, which is used in the literature dealing with image classification [127][128]. An epoch limit of 60 was selected by an iterative process aiming for steady training plots. The models are trained on a computer with configurations presented in Table 10. For utilizing the Compute Unified Device Architecture (CUDA) cores present on the GPU, a GPU-compatible version of TensorFlow was installed.

Component	Specification
CPU	12th Generation Intel® Core™ i7-12700H
GPU	Nvidia® GeForce® RTX™ 3050 Ti, 4 GB, GDDR6
RAM	16 GB, 2 x 8 GB, Dual-Channel DDR5, 4800 MHz

Table 10: Technical specification of the computer used for training the ML model

4.   Results & Discussion

4.1   Validation of weld classification method by DFT

The database from TWI's Friction & Forging Processes Department for FSW of 15mm DH36 steel sections was used to validate the methodology of weld classification through resultant force measurement. As discussed in section Figure 39, the presence of the defect was identified using the Discreet Fourier Transform (DFT) for frequency domain analysis of axial force. The database consisted of forces in all three directions (X, Y & Z Direction) measured with a sampling frequency of 10hz. The resultant forces in the plane perpendicular to the tool axis are estimated by Eq (11). Where F_x & F_y are the forces recorded in the X and Y directions. The lateral plane for the welding platform is illustrated in Figure 39.

$$F_{Resultant} = \sqrt{F_X{}^2 + F_y{}^2} \qquad [11]$$
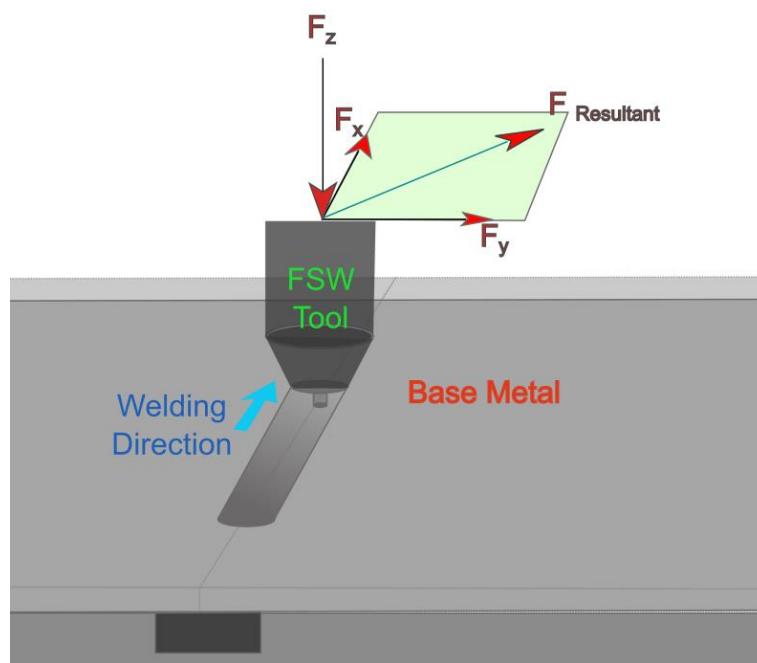
Figure 39: Resultant forces observed in the lateral plane of the FSW platform

The recorded data of 9 welds (i.e.- Weld 1-Weld 9) performed in the series with the same tool and FSW platform with varying weld parameters (i.e.- traverse speed, tool RPM and plunge depth) for the same weld length. The tool traverse rate and tool

rotation speed for weld 1 to weld 9 is varied from 19mm/min to 54mm/min and 120 to 230. The welds with the corresponding weld parameters are presented in Table 11 below.

Weld Name	Tool Rotation Speed (RPM)	Tool Traverse Rate (mm/min)
W1	120	19
W2	200	17
W3	120	17
W4	120	17
W5	170	17
W6	230	37
W7	230	48
W8	230	42
W9	230	54

Table 11: Weld parameters for welding DH36 with 15mm thickness

With the probe length of 12mm, welds are performed on 15mm thick DH36 steel sheets resulting in partial penetration. The welding phase can be identified from the recorded force data illustrated in Figure 40. While the forces in the Z direction have minimal variance in the signal, forces in the X and Y direction are observed to have higher variance with lower amplitude. As the welds are performed with different travel rates, the force data is plotted against the number of samples for better visualization of data collectively in Figure 41. From the presented dataset it is observed that welds W2 and W5 have lower amplitudes compared to the other welds. It is also observed that with the lower amplitude, the resultant forces for welds W5 and W2 resulted in 60% higher variance than the welds with a higher amplitude of resultant forces. This highlights that even with higher heat input the material flow around the tool experiences events of instability. The use of Fast Fourier Transform (FFT) is further explored to classify the welds in this section.
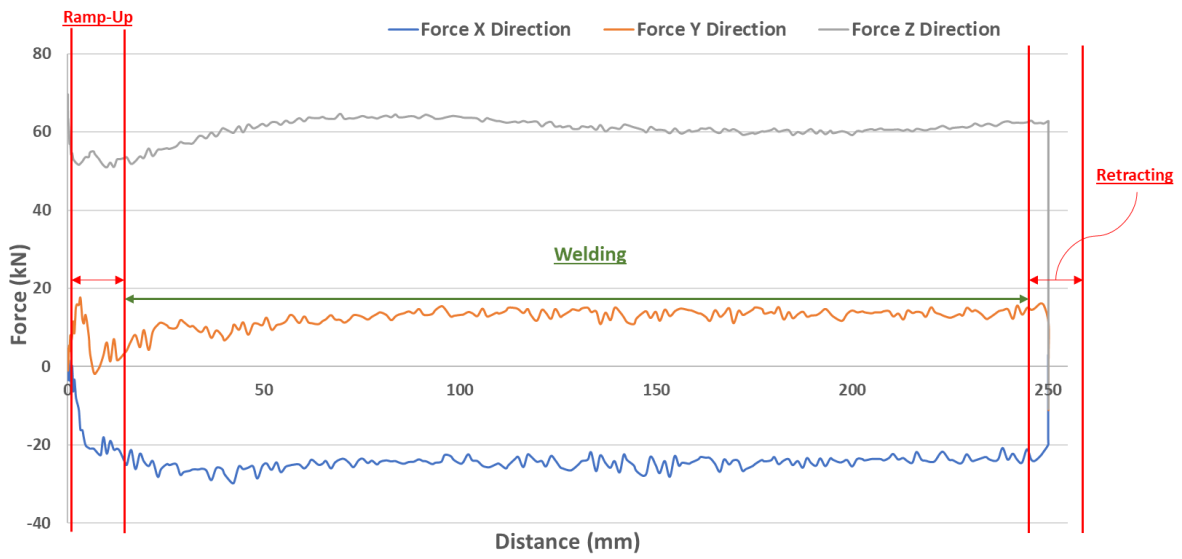
Figure 40: Visualization of welding phases through the force data recorded in X, Y and Z direction
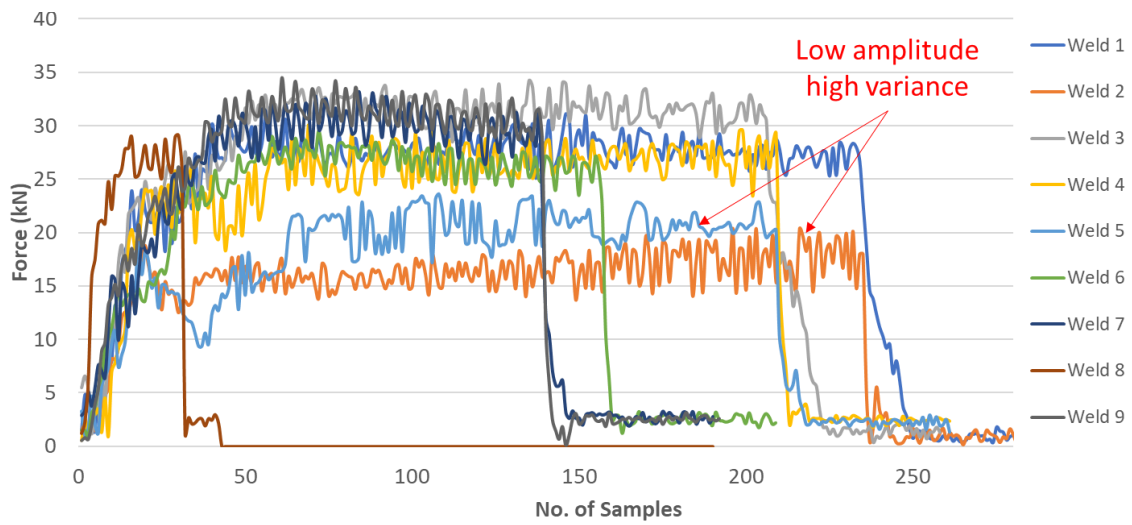
Figure 41: Resultant forces in the lateral plane (XY plane) observed for each weld performed
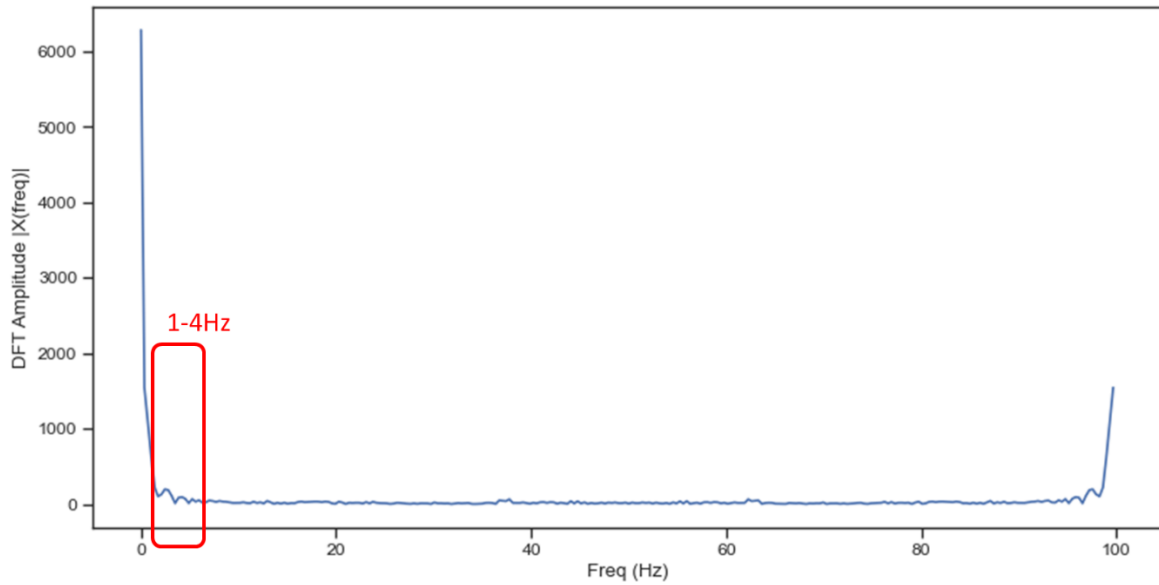
Figure 42- DFT obtained for resultant force signal of weld W1

The constituent frequencies of the resultant forces can be studied through Discrete Fourier Transform (DFT). As highlighted in section 2.8, frequency domain analysis through Fourier Transforms has been reported to have a good correlation with weld quality. To determine the weld quality without visual inspection, the DFT of the resultant forces is estimated and the maximum amplitude is plotted. The DFT amplitudes corresponding to the frequencies obtained from axial forces of weld W1 are plotted in Figure 42 with a window highlighting the low frequencies under consideration. Neglecting the peak at 0Hz, which is essentially the mean of the signal, the sample averaged DFT amplitude of frequencies from 1Hz to 4Hz is plotted for different welds with the upper and bottom threshold limits in Figure 43.
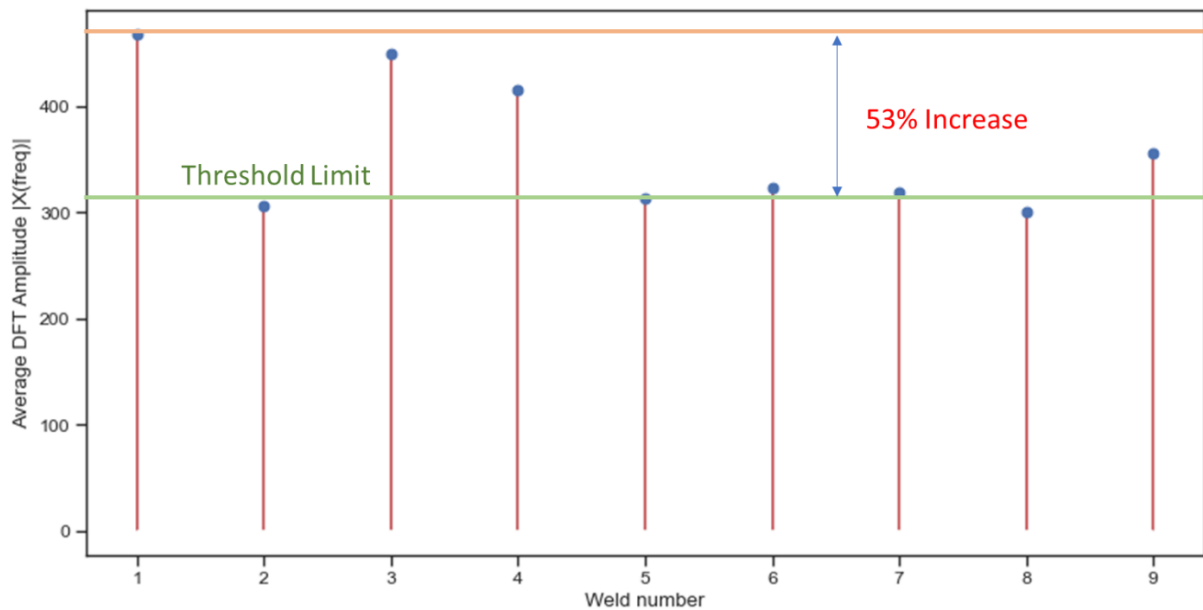
Figure 43- Average DFT amplitudes obtained between 1Hz to 4Hz for welds 1 to 9

Based on the DFT amplitudes a threshold line for the weld quality can be established (correlating to minimal disruption in the process). In Figure 43, the threshold line for weld classification is defined at 306 N. The maximum amplitude observed for the series of the weld was 53% higher than the threshold at 480N. For the welds with higher average DFT amplitude than the threshold, weld defects were observed at the root and the surface of the weld. The macrograph for Weld 1 with cavities on the advancing side wall is shown in Figure 44 with a maximum cavity size of 0.8 mm. Welds 3, 4, & 9 were reported to have surface defects because of higher plunge depth resulting in high plunging pressure. This shows a good correlation between the maximum amplitude of DFT(observed between 1-4Hz) and the presence of defects in the discussed welds.
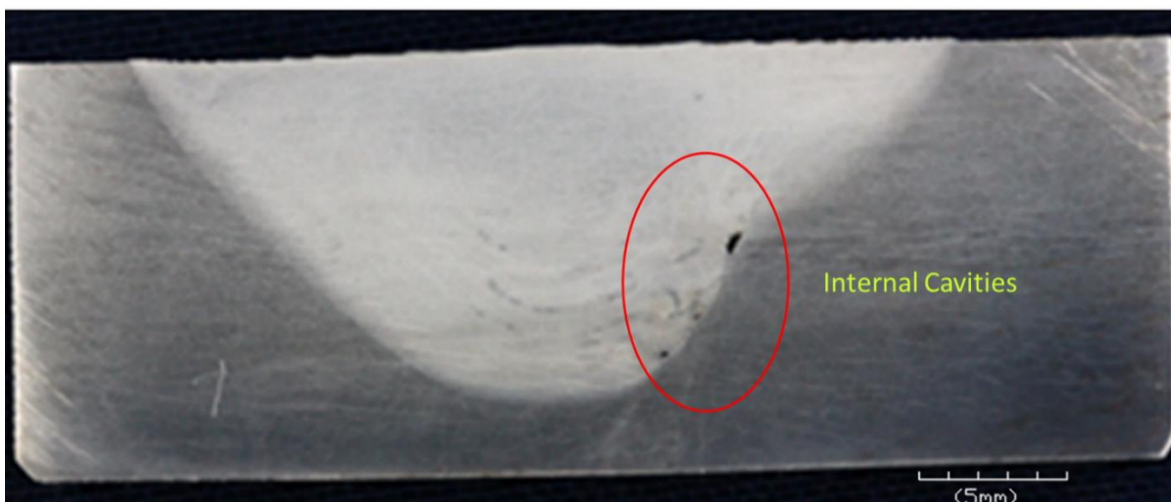
Figure 44- Cavities observed on the advancing side wall of the weld (W1)
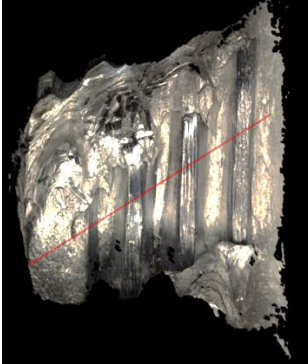
As discussed, and highlighted in the existing literature (section 2.6), the amount of lateral and axial forces generated during the weld are greatly dependent on the type of material welded. The force monitoring-based threshold method discussed in the literature and in this section for the classification of the weld quality is material and tool-specific and cannot be transferred to welds performed with different grades and tools. The results obtained from this section also underline similar limitations for the application of DFT-based weld classification systems. In the existing literature, different methods of force analysis are utilized, directed towards the development of online weld monitoring methods. The limitations of the force monitoring methods for defect detection and localization are further summarized below.

- The defective welds identified through performing DFT on the resultant signal have characteristic high forces which may also be caused due to a different tool or the base material. This makes the defect detection process specific to the welding platform and material.

- Through DFT analysis the welds can only be classified as with or without defects (i.e.- Binarily). The method also fails to relate the extent of the defect with the observed amplitude from DFT analysis. Apart from the quantifying extent of defect the DFT analysis also fails to localize the defect in the weld.

- Discreet wavelet transforms (DWT) solve the issue of localizing the defects in the weld but the applicability of the method is limited by the pre-requisite information for the decomposition level. While the sampling rate for the presented welds was 10Hz, the existing literature uses sampling rates in the magnitudes of kHz[129]. This highlights the limitation of the DWT method in terms of the applicability of real-time weld monitoring systems.

- The selection of level and mother wavelet for decomposition is dependent on the energy-to-entropy ratio estimated for each wavelet family [107]. With the increase in the decomposition level, the time needed to estimate the detail and approximation coefficient also increases exponentially, limiting the applicability of the method for online and real-time applications.

- As highlighted in the previous sections of this thesis, the force observed on the tool is defined under 2nd-level process parameters. As the 2nd level parameters are the resultant of the 1st level parameters, it can be stated that the 2nd level parameter would have significant feature loss and would be comparatively less sensitive.

Considering the abovementioned limitations and the observations, the uncertainties of a force-based weld monitoring method are highlighted. This underlines the requirement for a multi-parameter process monitoring system to have better confidence in the decision-making for online weld quality assessment.

4.2 Measuring wear for the FSW tool

The tool used to perform the welds is discussed in section 3.4 of this thesis. The two-part tool consists of a tool shoulder and probe. Before performing the welds, the minimum and maximum diameters were measured using the digital callipers to ensure that there was no major tool wear. To further ensure that the tool did not go through major wear during the welding process, the optical profilometry on the tool is performed after the completion of welds discussed in the following sub-sections. The depth of the probe threads is measured and compared with the designed depth according to drawings. The threaded surface of the tool probe is divided into three segments by the spiral flutes (i.e.-P1, P2 & P3) illustrated in Figure 25 of Section 3.4. Table 12 shows the three scanned segments of the threaded surface of the tool probe.

Surface Name	Scanned surface
Threaded surface P1	
Threaded surface P2	

Threaded surface P3	
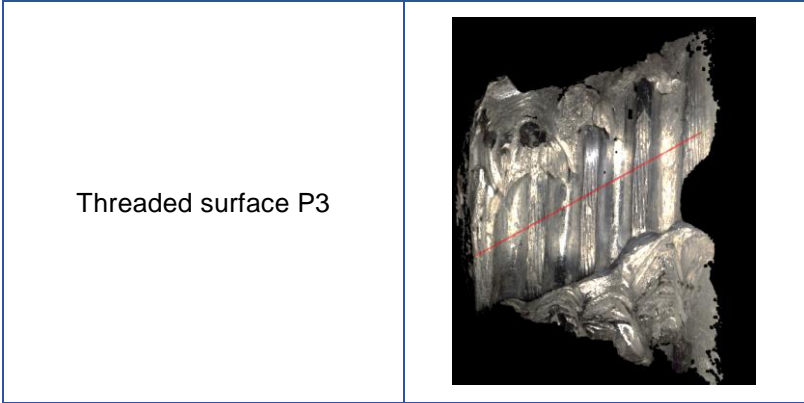
Table 12: Threaded surfaces of tool probe with measurement lines

The depth measurement is performed using an Alicona Infinite Focus optical profilometer with a 5x lens giving the observable area with width and height of 50mm. Before measuring depth, a form removal process was carried out to flatten the conical form of the tool probe. Figure 45 illustrates the variation of the depth across the measurement line for surfaces P1, P2 and P3 compared with the designed depth. Comparing the designed depth and measured depth through surface profilometry, it is concluded that after performing all the welds discussed in this thesis, the tool went through negligible wear and would have a negligible effect on the material flow of the welded material. This aids the repeatability of the experimental setup
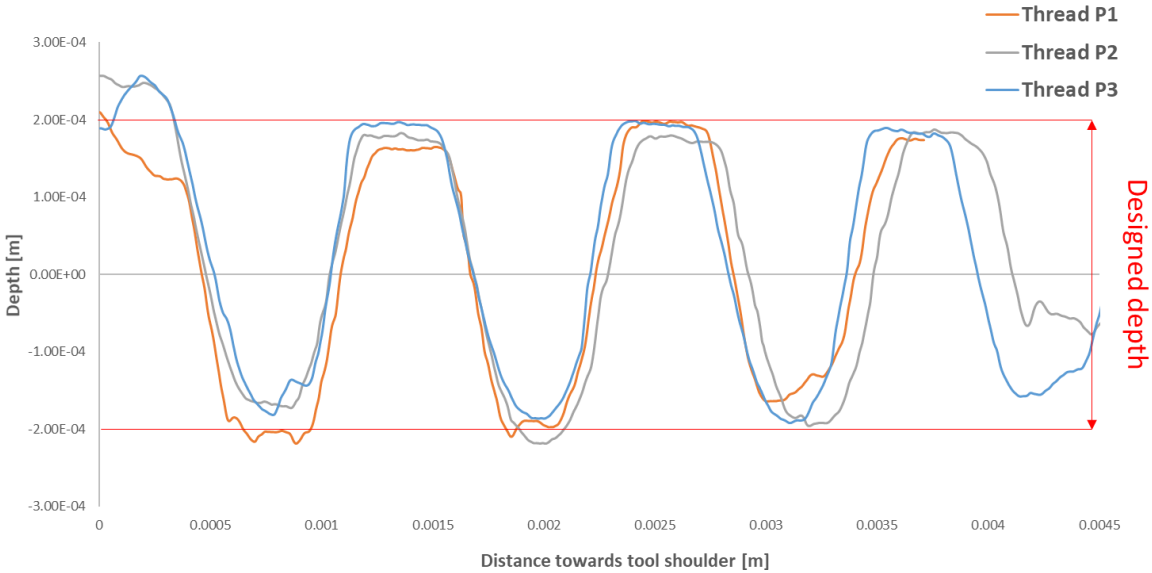
Figure 45: Depth profilometry of threaded surfaces for measuring tool wear

4.3 Correlation between AE signals and tool forces for FSW

4.3.1 Effect of AE sensor placement on features of AE signal

Using the AE sensor setup with *combination-3* (explained in section 3.5) accompanied by the on-plant force monitoring system of the ESAB FSW machine, the forces and acoustic emission for the welds C1-C6 are recorded. The constant weld parameters are defined in *Table.10*. The plates are fixed on a vacuum bed in a butt joint configuration and held by the clamps as discussed and illustrated in section 3.3. The constant weld parameters for the welds discussed in this section are shown in Table 13. The list of varying weld parameters for welds C1-C6 is shown in Table 14 below. For capturing the acoustic emission signals from the weld, a single channel was used to record the signals. For welds C1, C2 and C3 the AE signals were recorded using Channel A and the remaining welds were recorded by Channel B using a 16-bit single-channel mode configuration. This configuration for recording the AE signal is used to maximize the recording time/buffer memory for each run. The increase in the data recording capacity allowed to capture of AE signals of welds with longer lengths.

Tilt angle	Tool Traverse Rate (mm/min)	Probe Length (mm)	Plate Thickness (mm)	Weld Length (mm)
1°	500	4.8	5	100

Table 13- Constant weld parameters for 1st phase of welding trials

Weld Name	Tool Rotation Speed (RPM)
C1	800
C2	1000
C3	1200
C4	800
C5	1000
C6	1200

Table 14- Weld parameters for the 1st phase of welding trials

Since the welds are performed with constant feed rate and dwell time, the average amplitudes and Root Mean Square (RMS) amplitudes for AE signals can be compared. To determine the spread of the data, the standard deviation for each weld is also calculated. Before estimating the RMS and variance for the collected AE data, the mean removal of the data is carried out to remove the DC component of the signal. The typical AE data with mean and RMS values is shown in Figure 46. The RMS and variance are estimated using Eq.(12) & Eq.(13).
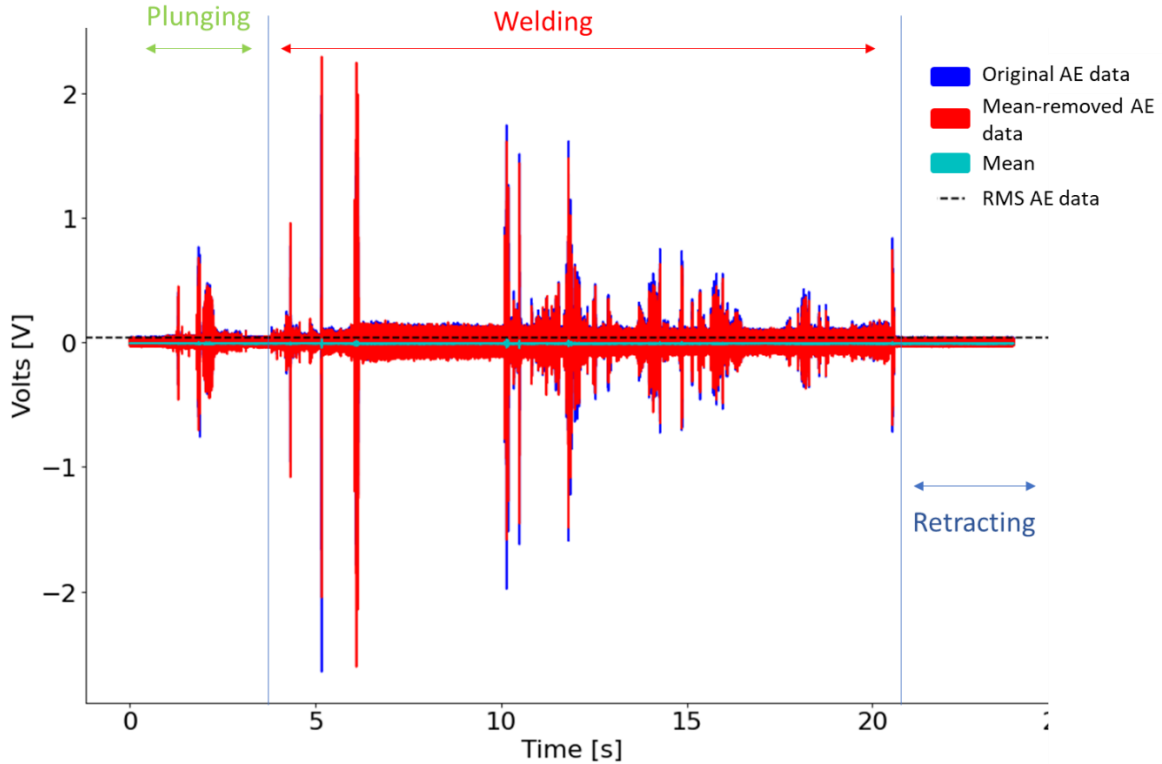
Figure 46: Typical AE data with the RMS and mean-removed data for different welding phases

$$RMS = \sqrt{\frac{1}{n}\sum_i X_i^2} \tag{12}$$

$$Variance = \frac{\sum(X_i - \mu)^2}{n} \tag{13}$$

Where, X_i is each measurement in the signal with mean (μ) with the population size (n) elements. The RMS values and standard deviation for the AE signals recorded during the weld C1 to C6 are plotted in Figure 47 to correlate and visualize the trend.
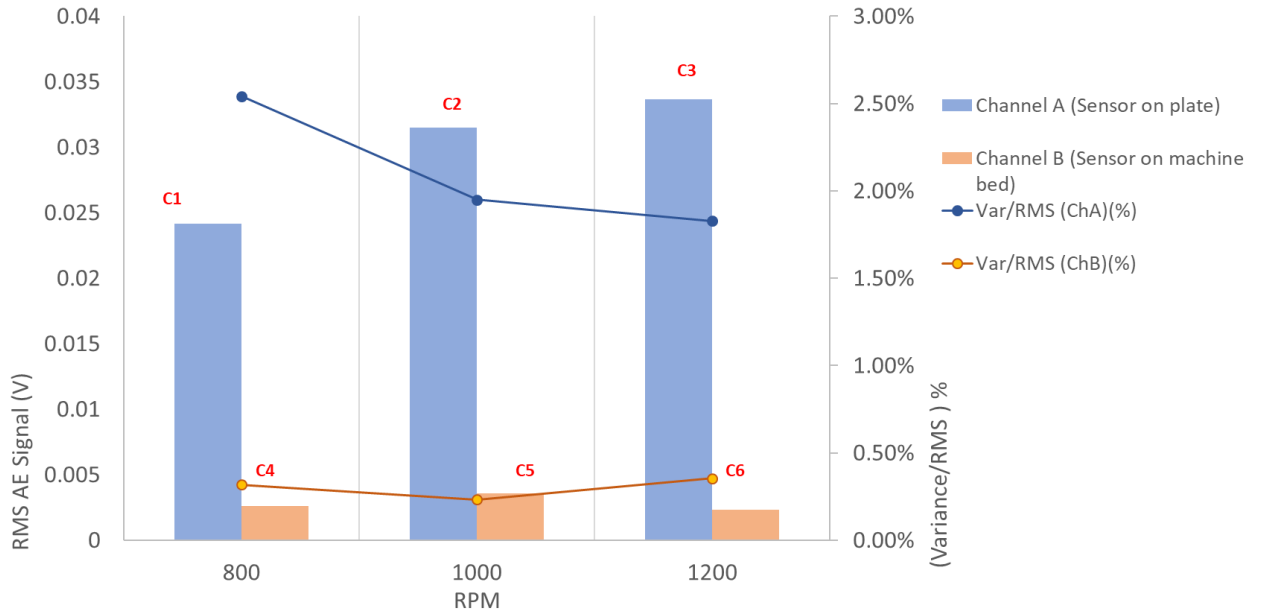
Figure 47- Comparison of RMS and Std. Deviation of AE signals for two sensor positions

The bar plot is divided into three sections for RPM between 800 & 1200 with two vertical axes for the RMS value and the variance percentage of the AE signal. Increasing the RPM from 800 to 1000 increased the RMS amplitude by 30%, while the increase in the RPM from 1000 to 1200 resulted in increased RMS by 7% for the AE signal recorded with the sensor on the plate. An opposite trend is observed in the case when the sensor is placed on the machine bed. With an increase in the tool RPM from 800 to 1000, the RMS of the AE signal is increased by 35% while increasing RPM from 1000 to 1200 the RMS amplitude is reduced by 33%. The trend of increasing RMS amplitude is complimented with a decreasing variance percentage in the case of when the sensor is placed on the plate. Similar to the difference in trend for RPM for different sensor positions, the variance percentage also shows a different trend for when the sensor is placed on the machine bed.

As the highest sampling frequency is limited by the recording capabilities of the Picoscope (recording time of approximately 32 sec at a sampling rate of 900k samples per second), following the Nyquist- Shannon sampling theorem, a maximum frequency spectrum up to 450kHz can be obtained. It was observed that FSW performed on AA6082 resulted in the generation of AE signals in the range of 100kHz to 430kHz. Through the short-time Fourier transforms spectrograms, the time-frequency analysis for the AE signal can be done and the frequencies generated during the welds can be visualized. The spectrograms for welds C3 & C6 are illustrated in Figure 48.
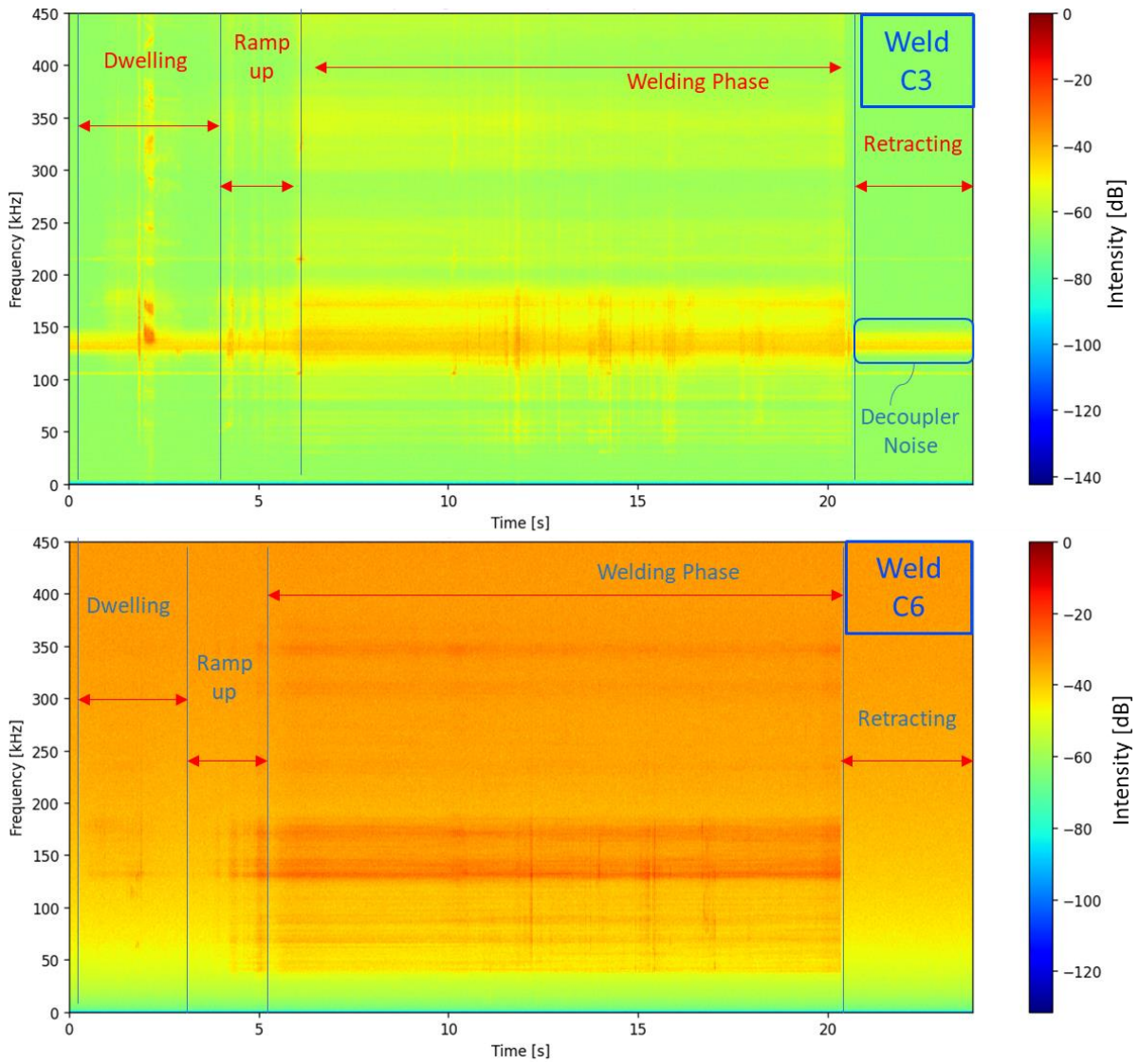
Figure 48: Spectrograms obtained from AE signals of welds C3 and C6

From the spectrogram obtained for both welds, the frequency bandwidth for the observed peaks in the spectrogram is comparable. More defined peaks are obtained in the range of 50kHz to 180kHz while less profound peaks are distinguished from 300kHz to 380 kHz. Overall the spectrogram for weld C3 has a higher variance in the peaks (demonstrated by a higher shift in frequency intensity) while C6 has relatively shallower peaks compared to C3. The centroid of the spectrogram /spectral centroid is estimated by aggregating the frequencies present at a particular time period. It can be mathematically expressed using Eq. (14).

$$Centroid = \frac{\sum_{n=0}^{N-1} f(n)x(n)}{\sum_{n=0}^{N-1} x(n)} \qquad [14]$$

Where $f(n)$ is the centre frequency and $x(n)$ is the weighted frequency value for the bin [130]. To understand the variation process forces and spectrogram, the standard

deviation of spectral centroid and axial forces is plotted in Figure 49. Due to the difference in the sampling rate for both datasets, two x-axes are plotted representing the number of samples for each dataset. The sampling rate for the dynamometer is 10Hz while the AE signals are recorded at a greater sampling rate of 900kHz.
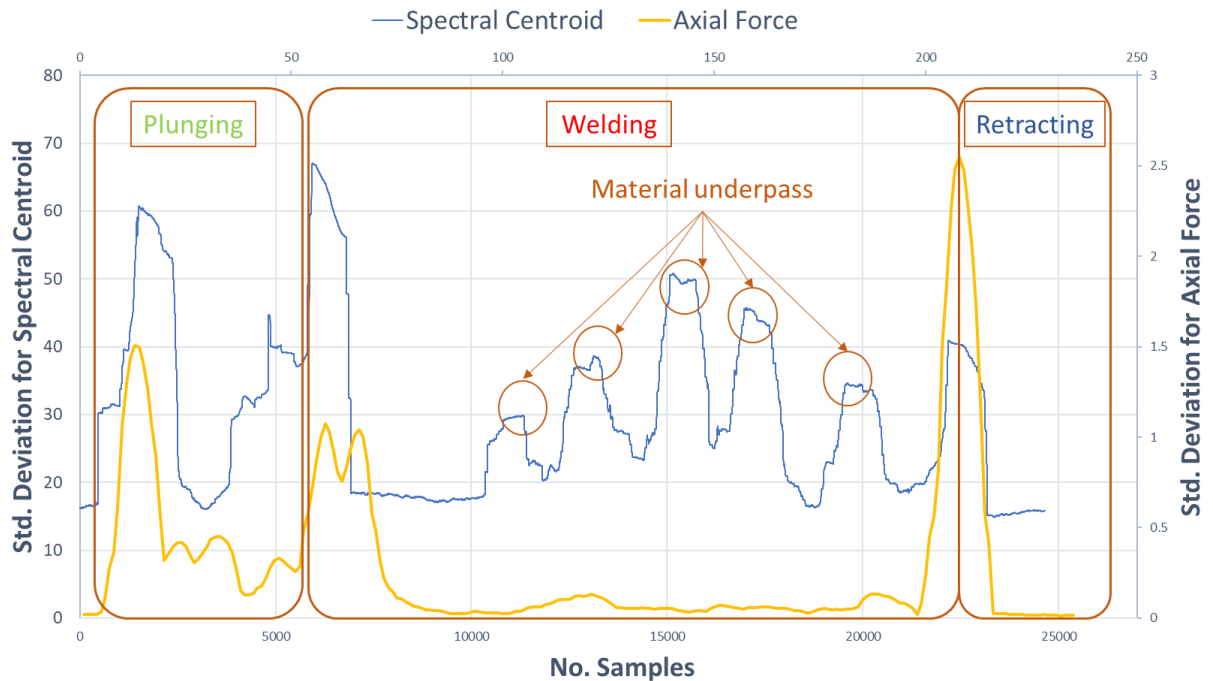
Figure 49: Standard deviation of axial force and spectral centroid for weld C6

In Figure 49, during the plunging phase both the AE signal and axial force signal show two peaks, the two peaks correspond to the tool probe contact and tool shoulder contact. The AE signal shows a higher standard deviation at the beginning of the welding phase. During the welding phase, five peaks with an amplitude range of min 30Hz to 50 Hz are also observed. During the transition from the welding phase to the retracting phase, a peak of 40Hz is also reported which can also be observed in the axial force data recorded. The leading side of the tool shoulder experiences periodic accumulation of material which is carried to a certain distance before it passes under the tool shoulder. This passing of accumulated material under the tool shoulder increases the material being sheared and causes periodic peaks in the AE signal. While the AE signals recorded a standard deviation of 30Hz up to 50Hz, axial force data fails to capture this phenomenon. This observation highlights the sensitivity of AE signals over the observed forces on the FSW tool.

The effect of sensor position is analysed by varying the RPM and keeping the traverse rate and tool tilt angle constant. Using the centroids obtained from the spectrograms,

the standard deviation of the centroid and force is compared along the length of the weld. A similar nature of AE for static welds/spot welds is reported in the literature discussed in section 2.9 [131]. The shear waves generated during the FSW process are transmitted through the base metal and reach the sensor. In the case when the sensor is placed on the machine bed, the shear waves are transmitted through the viscous plastic stir zone before it reaches the sensor. With the increase in heat input by the increased RPM, the size of the stir zone/nugget zone increases. This increase is directly correlated with the dampening effect, which in turn reduces the amplitude of the signal. The AE signal transmission mechanism can be further explained using Figure 50.
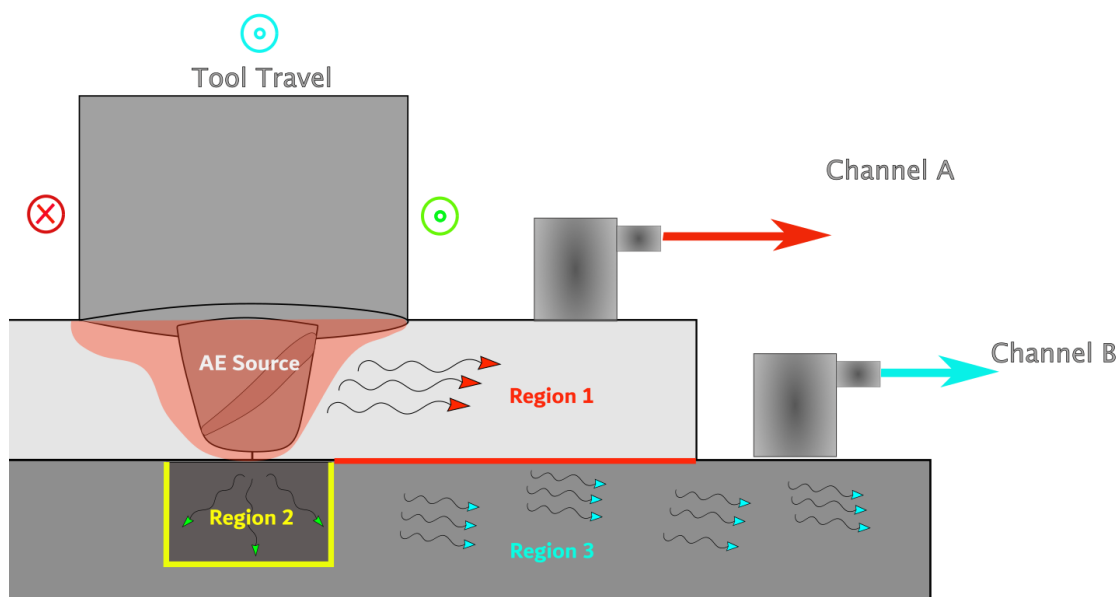
Figure 50- Cross-sectional view of the transmission of AE for two sensor locations

Three regions for AE transmission can be defined considering the material and the interface. The edge contact between the material and the tool acts as the source for shear wave generation. The second source of shear wave generation is the shearing of material away from the tool. The amplitude of the shearing action reduces along the circumferential direction. Region 1 can be defined as the region closest to the source within the welded material and has no interface. Since there is no loss due to the interface, this region has the highest amplitude. Region 2 experiences the second highest amplitude as the shear waves have to pass the interface between the base metal and the backing bar. For Region 3, the shear waves are propagated through the backing bar and the base metal before it reaches the Channel B sensor. Due to the increased size of the nugget zone, the amplitude of the shear waves travelling in Region 3 reduces as it is directly affected by the size of the stir zone.

4.4   Effect of tool tilt angle and material disruption on AE signal

For the welds discussed in this section, combination-1 of the sensor layout plan discussed in *section 3.5* is used for welding AA6082 5mm thick plates. The clamping setup discussed in section *3.3* is used to keep the plates in position while performing the welds. The welds are performed with a constant probe length of 4.8mm. The varying weld parameters are defined in Table 15 below.

Weld Name	Tool RPM	Tool Traverse rate (mm/min)	Weld Length (mm)	Tool Tilt Angle
D1	1200	550	220	3°
D2	1200	550	220	3°
D3	1200	550	470	3°
D4	800	1000	230	3°
D5	600	1050	230	3°
D6	1200	550	200	1.5°

Table 15 - Varying weld parameters for phase 2nd of welding trials

The material disruption is induced by introducing holes in the joint line. The position and the size of the holes are explained earlier in section 3.6. Weld D2 is performed with a single hole in the joint line while weld D3 is performed with multiple holes in the joint line with different diameters and constant depths. Weld D1 was performed with no holes in the joint line to set the reference for the welds with induced material disruption.

Weld #	Root Mean Square (RMS)		
	Channel A (V) (Advancing)	Channel B (V)(Retreating)	Amplitude ratio
D1	0.047	0.019	2.513
D2	0.080	0.028	2.852
D3	0.107	0.046	2.320
D4	0.056	0.037	1.524
D5	0.121	0.089	1.361
D6	0.028	0.039	0.717

Table 16- RMS amplitude obtained from welds performed for phase 2 trials

The AE signals for material shearing on either side of the weld are correlated by comparing the RMS of the AE signal (defined in Table 16).To observe the trend between the welds, the bar graph of the amplitude ratio of signals from the advancing and retreating sides is plotted in Figure 51. For the welds, D1 to D5 the amplitude of the AE signal on the advancing side was observed higher than the retreating side of the weld. Welds D1 to D3 were performed with higher heat input from D4 & D5 with different RPM and tool traverse rates. Higher RPM coupled with high tilt angle results in increased high shearing due to plunging shoulder on the advancing side.
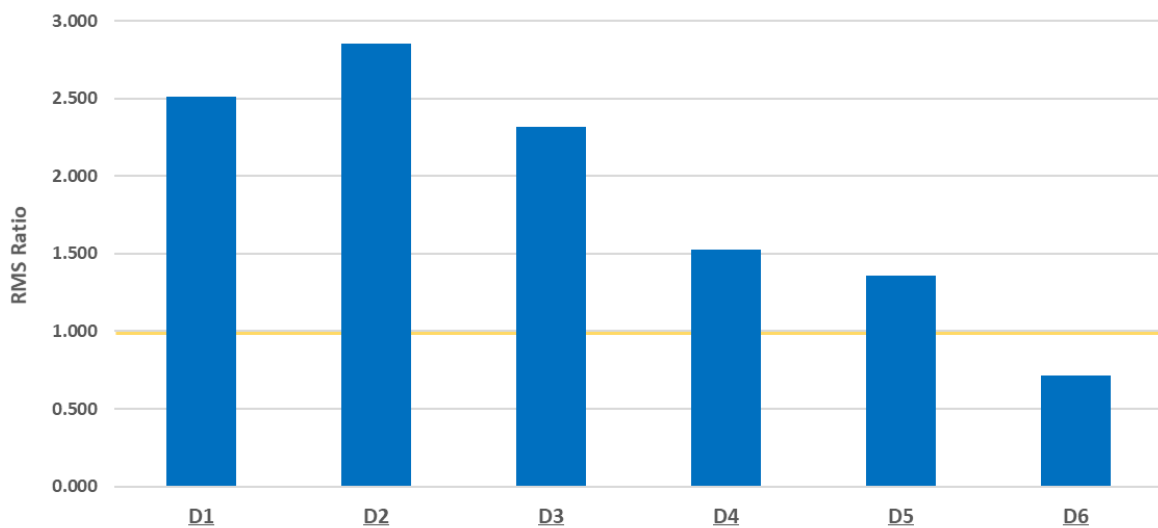
Figure 51- RMS amplitude ratio for the advancing and the retreating side of the welds

Figure 52 illustrates the material flow directions observed for FSW with high tool tilt angles. On the advancing side of the, the direction of material flow is opposite to the direction of the direction of the oncoming material. While on the retreating side of the weld, the direction of the oncoming material is the same as the direction of material flow. This results in asymmetric material flow around the tool. Due to the increased tool tilt angle, the shoulder engagement at the leading side of the tool reduces while the plunging/forging action of the shoulder on the trailing side of the tool increases. The shearing action on both sides during the welding phase is defined by the direction of the material flow. On the advancing side, the shearing action is majorly caused by the dislocation of the material by the tool while on the retreating side, the shearing action is dominated by dislocation and deposition. The material removed from the excess plunging of the trailing side of the tool shoulder induces underfill in the weld.
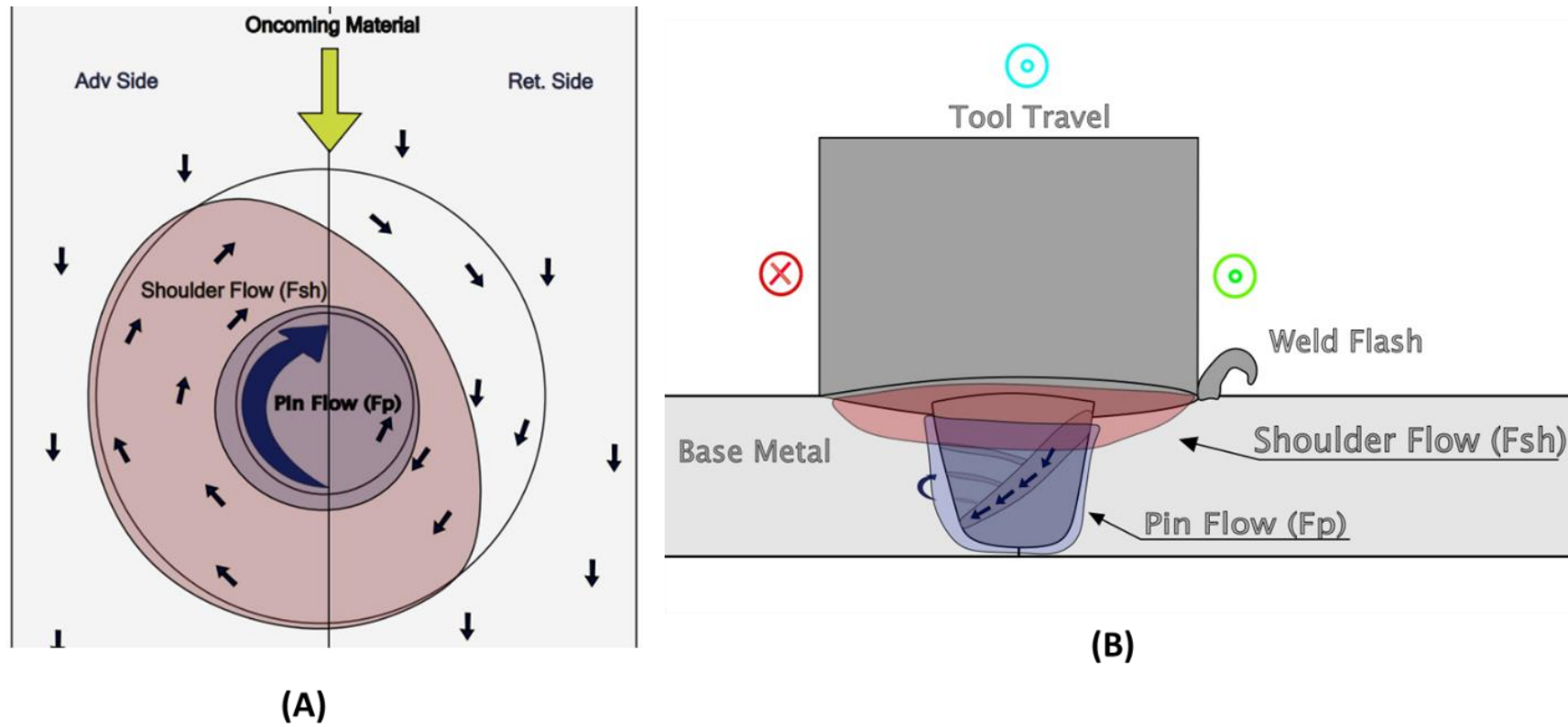
Figure 52- (A) Axial view of the material flow for FSW; (B) Cross-sectional view of material flow for FSW joint

Due to the high heel plunging action of the tool, traces of excess weld flash are also observed in the spectrogram obtained for weld D1 with no holes in the joint line. The periodic vertical lines are observed in the spectrogram in the frequency range of 100kHz to 400kHz. The flash segments observed on the top side of the weld are correlated with the vertical lines on the spectrograms illustrated in Figure 53(A). The top side of the weld can be further co-related with the spectral centroid in Figure 53(B). The peaks observed in the spectral centroid plot are observed to be in correlation with the length of flash segments. The generation of flash can be understood as the periodic movement of the plasticized material due to excess heel plunging action observed at the trailing side. The excess plunging pressure increases the heat generated at the trailing side of the tool shoulder which experiences a periodic behaviour due to the colder oncoming material. From the abovementioned results, it is concluded that through cont. AE monitoring method, the effect of tool tilt angle on material flow around the FSW tool can be monitored and quantified. The following sub-sections explore the material disruption caused by different material disruption sources.

(A)

(B)
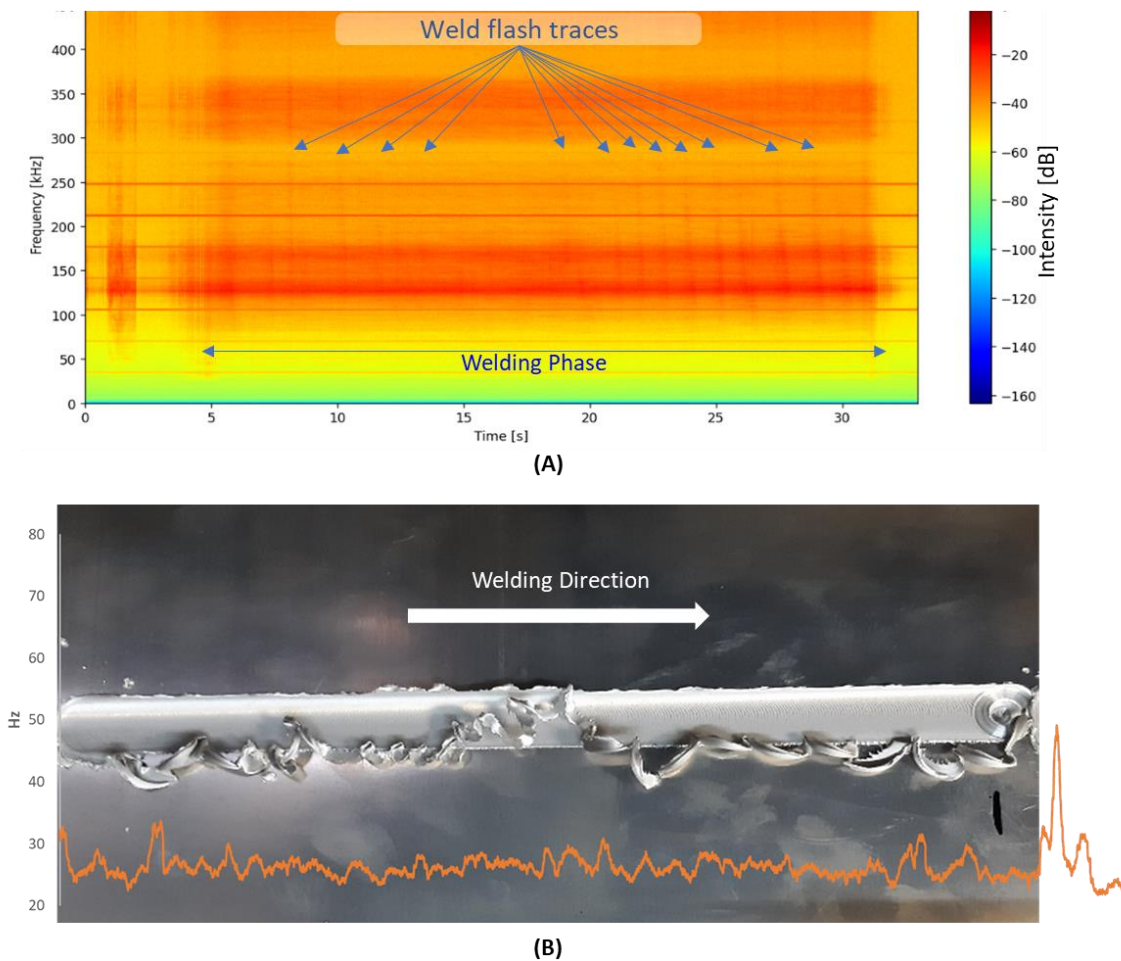
Figure 53: (A) Weld flash traces observed in the spectrogram for weld D1 (B) Correlation of the top side of the weld plotted with standard deviation of spectral centroid

4.4.1 Effect of material flow disruption on force and AE signals

As discussed in section 3.6, the material disruption for the material flow around the tool is introduced by drilling holes of different diameters along the joint line. For weld D2 a hole of 4.5mm diameter is drilled at a distance of 110mm from the start. To corelate the axial force and the AE signal for the performed welds, the standard deviation of both data is plotted in Figure 54 below. The AE signals for the weld D2 are recorded using the 1st configuration of Picoscope resulting in a maximum observed frequency of 450kHz. The standard deviation for the AE signal and axial force on the Y axis is plotted with the number of samples on the top and bottom horizontal axis. At the point of interaction of the tool with the hole, a standard deviation peak of 130Hz is observed at the centre of the welding phase. A peak amplitude of 1.6kN is observed for the monitored axial force during the interaction of the tool and the hole in the joint line. The lack of material around the tool causes disruption in the reaction forces and the amount of material sheared by the tool.
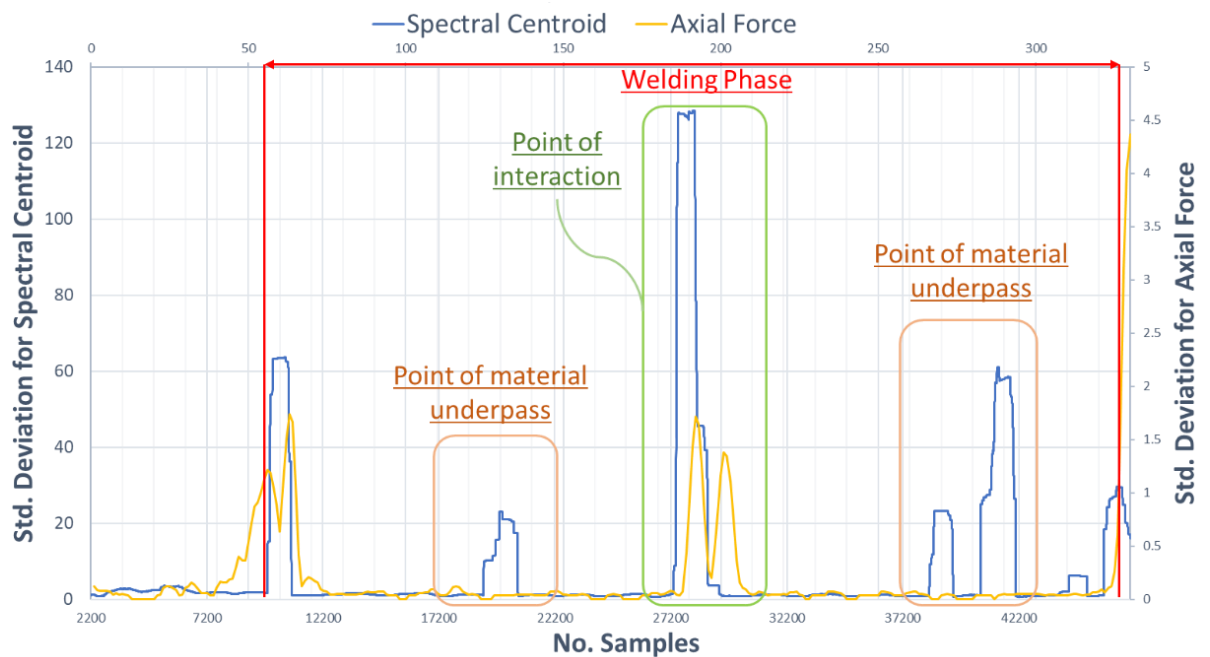
Figure 54- Standard deviation for AE signal and axial forces observed for weld D2

Two instances of leading-edge material accumulation underpass were also observed before and after the peak for hole interaction. High tool rotation speed with a high tilt angle promotes the accumulation of the material at the clearance on the leading side of the tool. The periodic nature of the material underpass can also be observed in Figure 54. The first peak of material underpass occurs at the 17200-sample point and the second peak is observed at 37300 sample number. It can be observed that both

peaks are observed at similar distances from the start and point of interaction of the tool. The lack of material due to the presence of a hole is evident on the top surface of the weld in Figure 55(A). Figure 55(B) shows the underside of the weld with the narrowing of heat affected zone caused due to the reduction in the stirred material. The narrowing of the HAZ underside starts after the reduction of material flow around the tool. As the tool enters back into the base metal after the hole, the HAZ on the underside of the weld regains the original width of 14mm. From the radiography of the weld D2, it was observed that there were no internal voids in the weld but evidence of underfill around the region of interest.
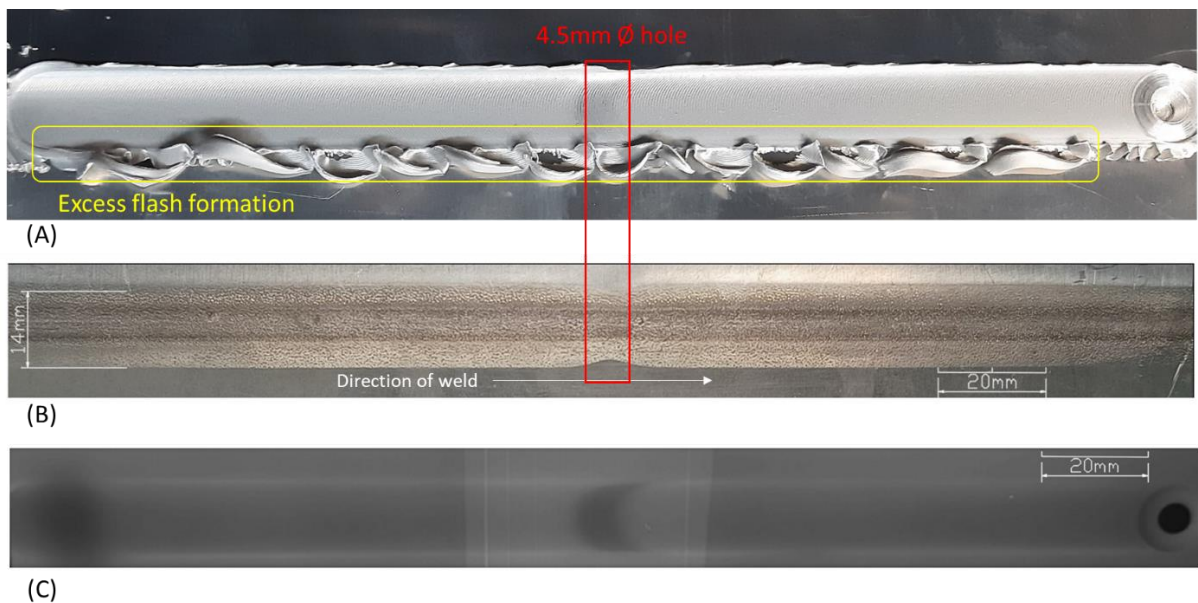
Figure 55: (A) Top surface of the weld D2 with excess flash generation (B) Underside of the weld D2 with narrowing of the heat affected zone, (C) Radiography for the weld D2 with evident density change at the centre of the weld.

To understand the influence of the diameter of the holes, a longer weld of 470mm with multiple holes of 3mm, 4mm and 4.5mm at a distance of 150mm was performed. Using the standard deviation of spectral centroid and axial force, the position of the holes in the joint line is correlated. The effect of material disruption on the top surface can be visualized in Figure 56.
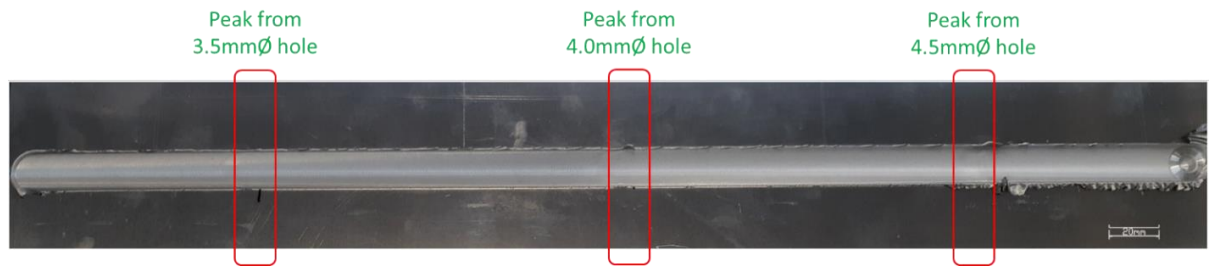
Figure 56: Top surface of the weld D3 performed with the same parameters as D2 with the location of material disruption points caused
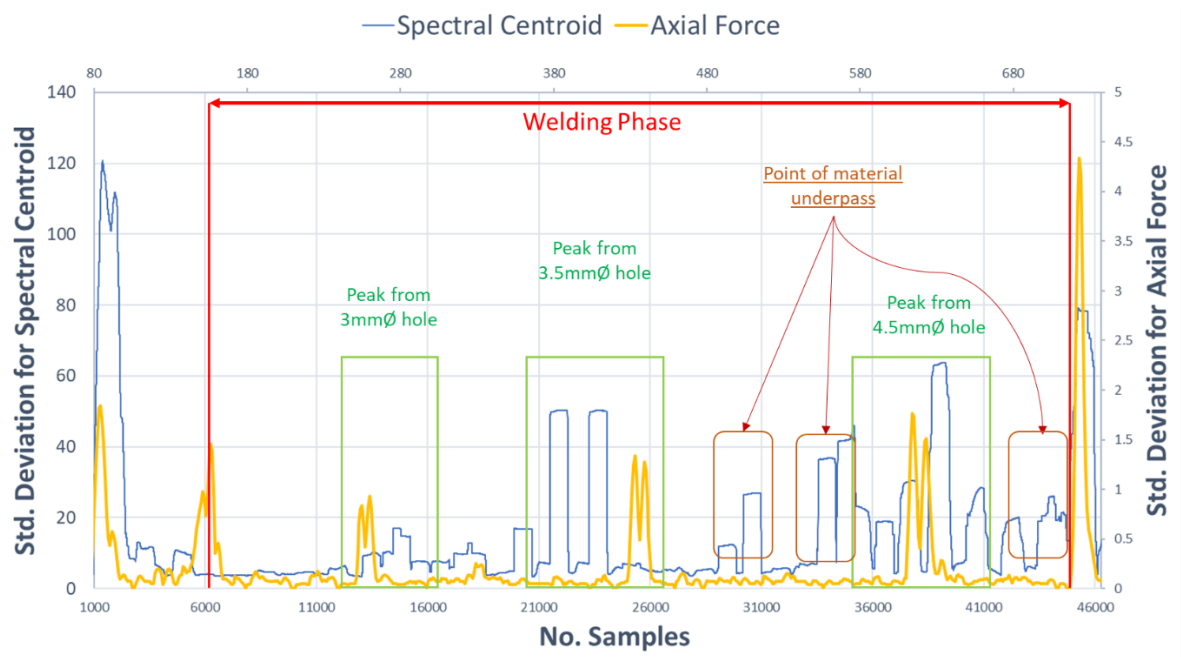
Figure 57: Standard deviation of AE signal and axial forces observed for weld D3

Since the longer welds cannot be recorded using 1st configuration for Picoscope (discussed in section 3.5), 2nd configuration with a lower sampling rate is selected to monitor weld D3 which reduces the maximum observable frequency to 225Hz. Similar to weld D2, the standard deviation of the axial force and spectral centroid observed for weld D3 is plotted in Figure 57. Comparing the peaks due to the material disruption, it can be observed that the peaks for AE signals while encountering the hole are significantly reduced. For the first hole, the standard deviation of axial force data reports a higher peak compared to their respective scales to the standard deviation of the AE signal. For the second hole, the peaks in standard deviation are disrupted by the event of the material underpass. Similar peaks of the material underpass are observed after the 2nd point of material disruption. A more prominent peak is observed when the tool encounters the 3rd hole. This discrepancy in the behaviour can be correlated to the logarithmic nature of the spectrogram and the reduction in the maximum observed frequency. The disruption in shear waves is caused due to the

incomplete merger of the probe flow zone to the shoulder flow zone. From the abovementioned observations, it can be observed that, with a reduction in observed frequency the sensitivity of AE signals to material disruption is reduced.

The underfill observed as a result of material loss in the weld due to the hole resulted in the unacceptable weld flaw. Underfill in the welds may also be introduced by excess plunging of the tool shoulder or tool heel plunge at high TTA. As highlighted in section 2.8 of this thesis, the defect in FSW could form gradually and could result in no material disruption around the tool (e.g.- lack of penetration, tool offset). Based on the findings from the literature discussed in section 2.8, the presence of commonly occurring defects cannot be stated as analogous to the presence of artificially-induced material disruption through holes in the joint line. Even though the material disruption cannot be directly correlated with defects, it can be correlated with process breakdown and unusual material flow around the tool in the case of welding complex geometry. The reduction in increase in the tool engagement for the case of joint lines with curvature can be illustrated in Figure 58 & Figure 59 below. As the tool moves towards inward curvature the tool shoulder would experience a higher amount of material interaction with the tool shoulder. From Figure 59, it can be visualized that as the tool leaves the trajectory for the joint line, the material flow around the tool reduces which alters the AE signals. Similar to the case with the higher tool shoulder-material interaction, the decrease in material interaction due to the outward curve in the joint line can also be detected. The effect of tool shoulder interaction on AE signal is further explored in the following sub-sections of this chapter. This section gives evidence proving the ability of AE monitoring to detect the change in tool-workpiece engagement. The section also highlights the limitations of the force monitoring method to detect the presence of underfill caused by tool tilt angle. From the evidence discussed earlier in this section, it can be stated that this increase in excess material shearing can be detected through the AE monitoring method
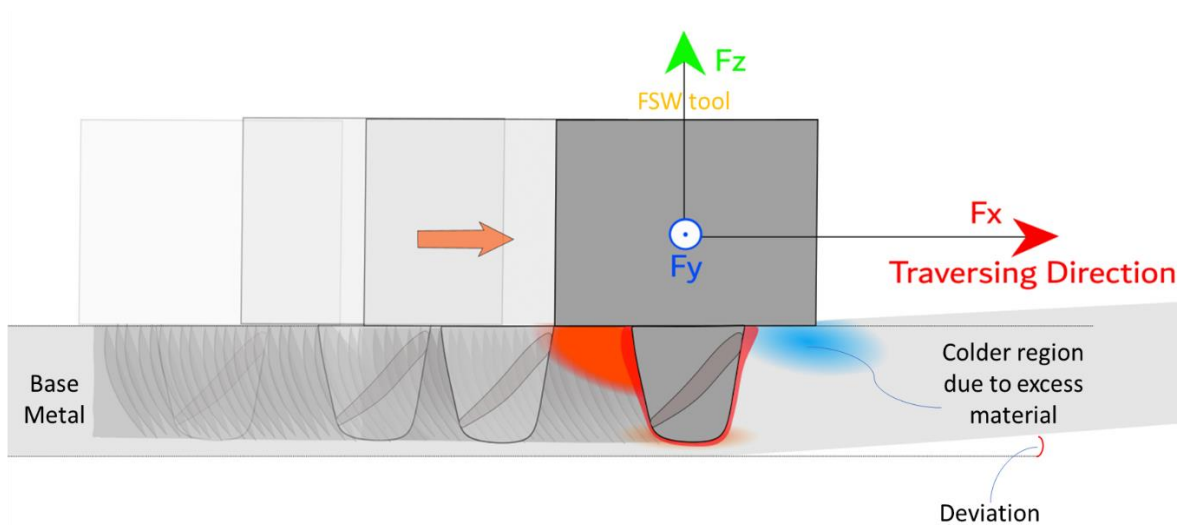
Figure 58:Change in temperature fields around the tool in case performing welds for irregular surface
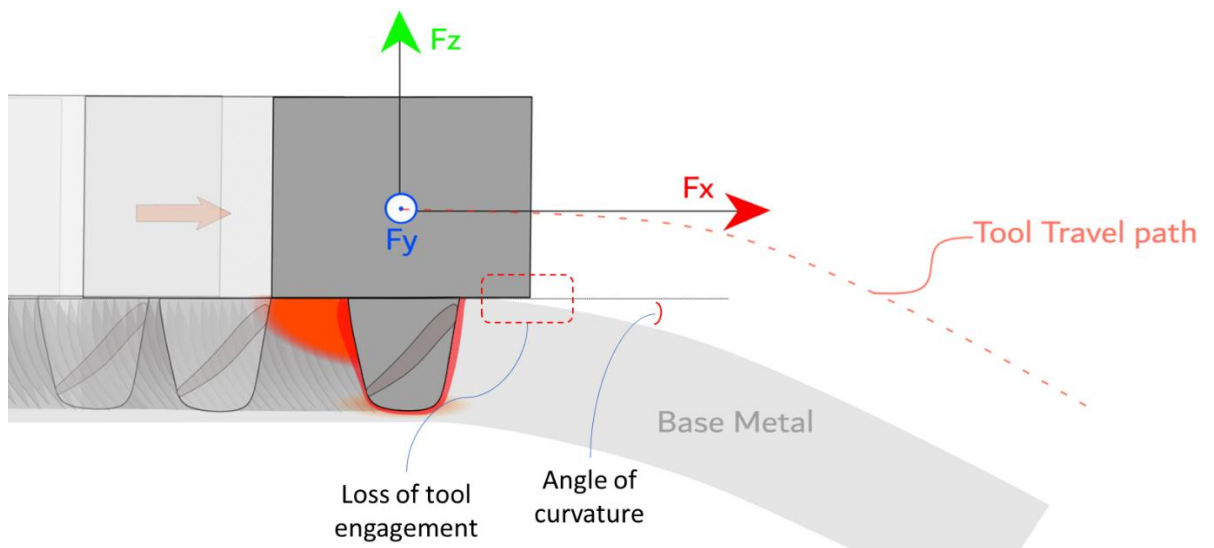
Figure 59: Loss of tool engagement while welding surfaces with curvature inwards to a straight line

4.4.2   Detection of internal cavities through AE signal

Welds D4 and D5 of equal length are performed with a higher tool traverse rate (1000mm/min & 1050mm/min) and nominal tool RPM (800 & 600). These parameters reduce the heat input of the weld. Figure 60 compares the radiographs obtained for welds D4 and D5. It was observed that Weld D4 had density changes along the stir zone observed in a darker gradient. The radiograph obtained for weld D5 showed a long continuous cavity along the joint line. The radiographs for both the welds (i.e.- D4 & D5) are shown in Figure 60. For visualizing the size and position of the defect in the weld, a section of the weld from the centre of the weld with the joint line is mounted and etched using Keller's reagent. The macrograph for the section is shown in Figure 61 below. To analyse the root of weld D5, a 10x zoomed image is presented in Figure 62. The delaminated material along the joint remnant line is also observed.
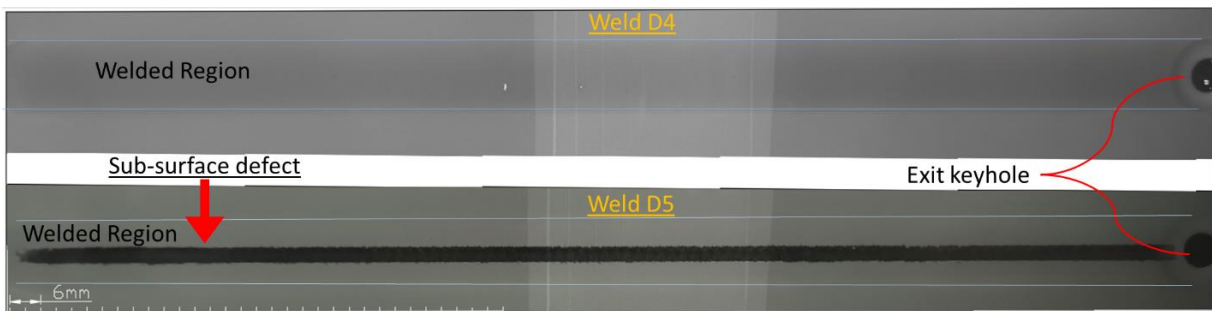
Figure 60: Radiographs for the welds D4 & D5 performed with high tool traverse rate
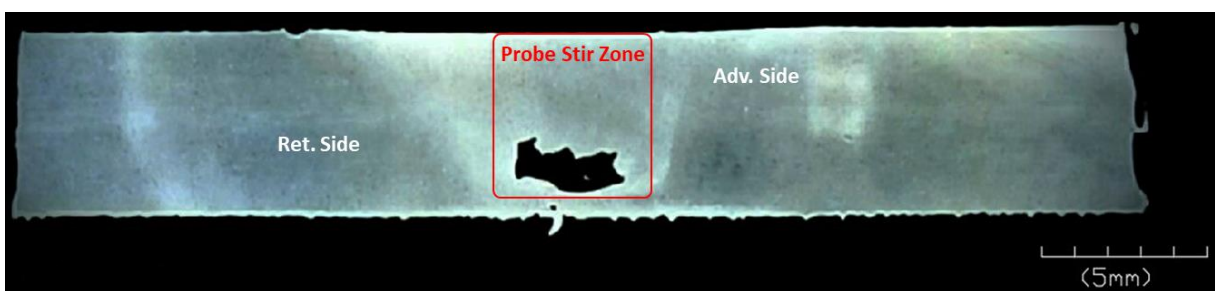
Figure 61: Position of the internal cavity formed while performing weld D5
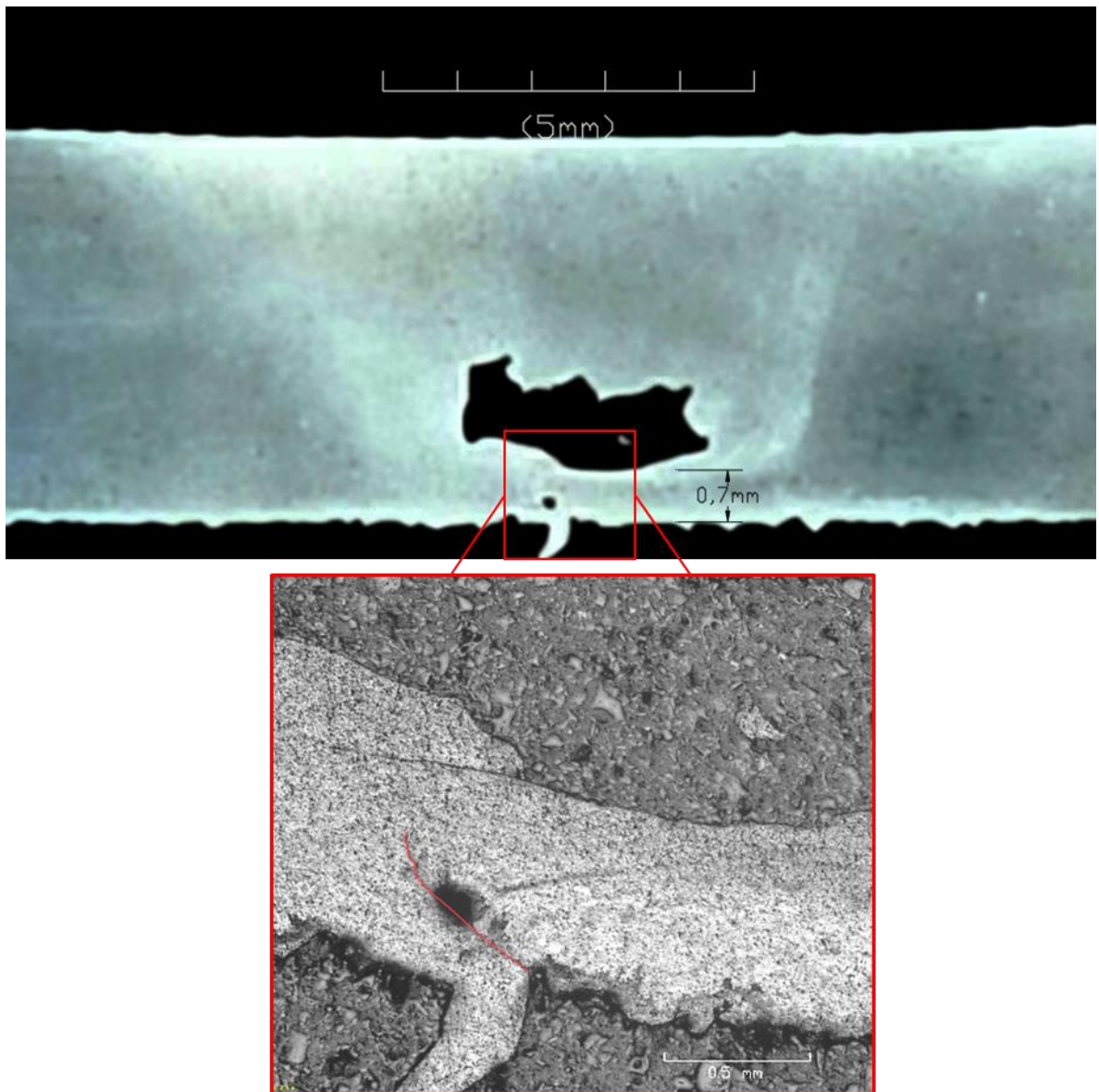
Figure 62: Delamination observed at the joint remnant line towards the underside of the weld

In Figure 61, the position and the size of the internal cavity formed for the weld D5 are visualized in the macrograph. With 3.8mm maximum width and 1mm maximum height, the cavity covered an area of 2.9 mm^2. The cavity was formed due to the colder temperature at the trailing side of the tool probe resulting in a lack of plasticized material to fill the material stagnation point. The same mechanism was followed through the joint line leaving a continuous void behind the tool.

The axial forces observed on the tool for welds D4 and D5 are plotted in Figure 63. Since the tool rotation speed is lower by 25% for weld D5, the forces observed on the tool while welding are observed to be higher. A difference of 10kN is observed during

the welding forces with an 85% higher amplitude observed for the peak during the dwelling phase.
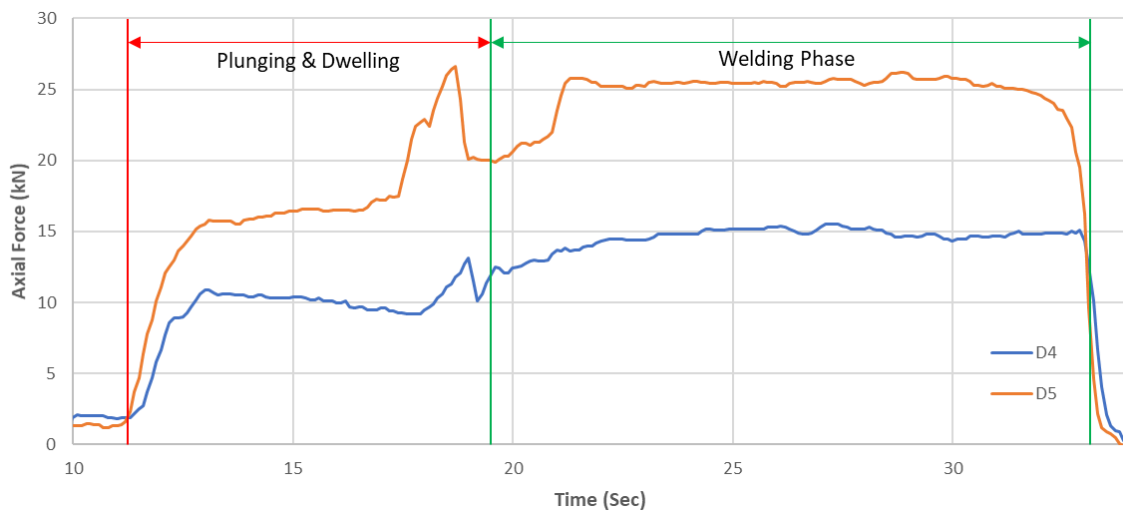
Figure 63: Axial force observed on the welding tool recorded during weld D4 & D5

By plotting the moving window standard deviation for the monitored axial forces, the correlation between the welds is established. Since both welds are performed with the same traverse rate, the stability of the welding process can be estimated using the rolling standard deviation for 5 samples in Figure 64 below.
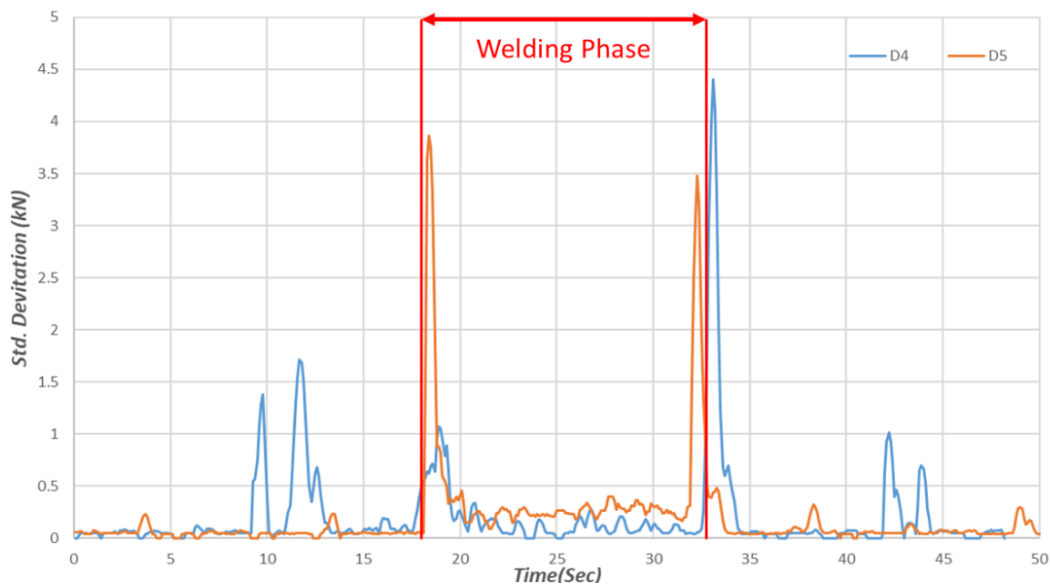
Figure 64: Standard deviation for axial forces recorded for welds D4 & D5

During the welding phase, weld D4 resulted in irregular peaks of 250N of sample standard deviation while weld D5 resulted in more uniformly dispersed data with a

maximum sample standard deviation of 400N. This highlights the effect of the difference in the amplitude of the recorded forces on standard deviation, the higher amplitude of the axial forces may also result in a higher variance. Considering the trend of force monitoring methods mentioned in the literature review, the higher variation of axial forces is related to the presence of the defect. An opposite trend is observed in the abovementioned case promoting inconclusiveness and inducing a lack of confidence in observing weld defects through the monitoring of forces.

The AE signals from both welds were collected using the 2nd configuration of Picoscope. Since both welds were performed with a similar traverse speed, AE signals for 12 seconds were captured for each weld. Illustrated in Figure 65 & Figure 66 below, the spectrograms with a maximum frequency of 225kHz for welds D4 and D5 are plotted. The spectrogram for weld D4 illustrates smoother peaks while weld D5 had sharper periodic peaks from 100kHz to 225kHz during the welding phase. From the abovementioned observations, the lack of sensitivity of axial forces to detect sub-surface defects is underlined. It was also observed that despite of reduced range of frequency bandwidth of the AE signal, the spectrograms obtained are distinguishable and the presence of sub-surface voids can be detected.
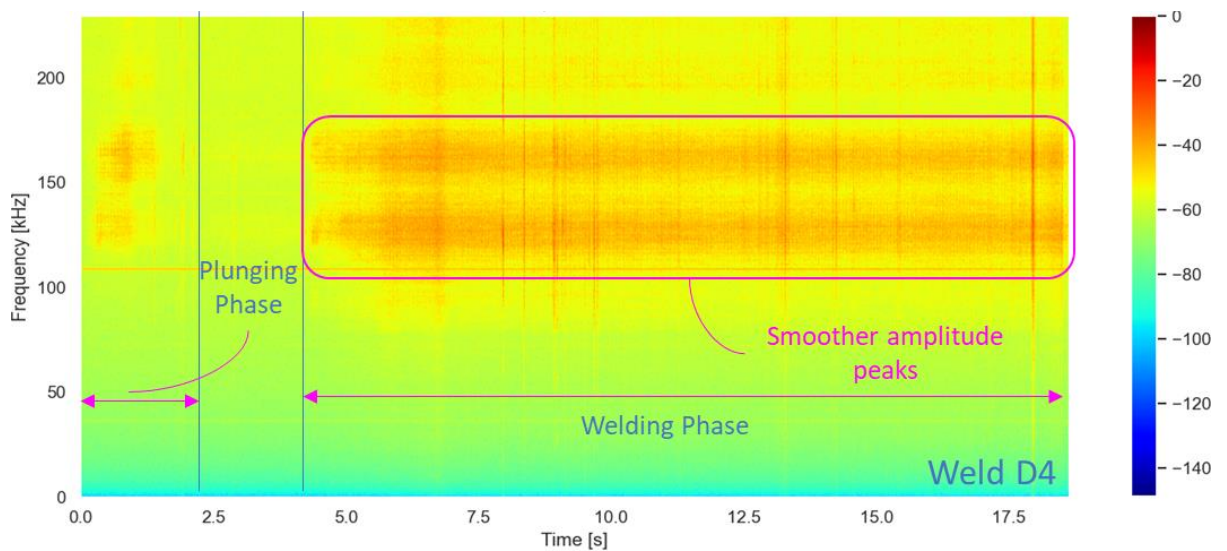
Figure 65: Spectrograms obtained for AE signals captured for welds D4
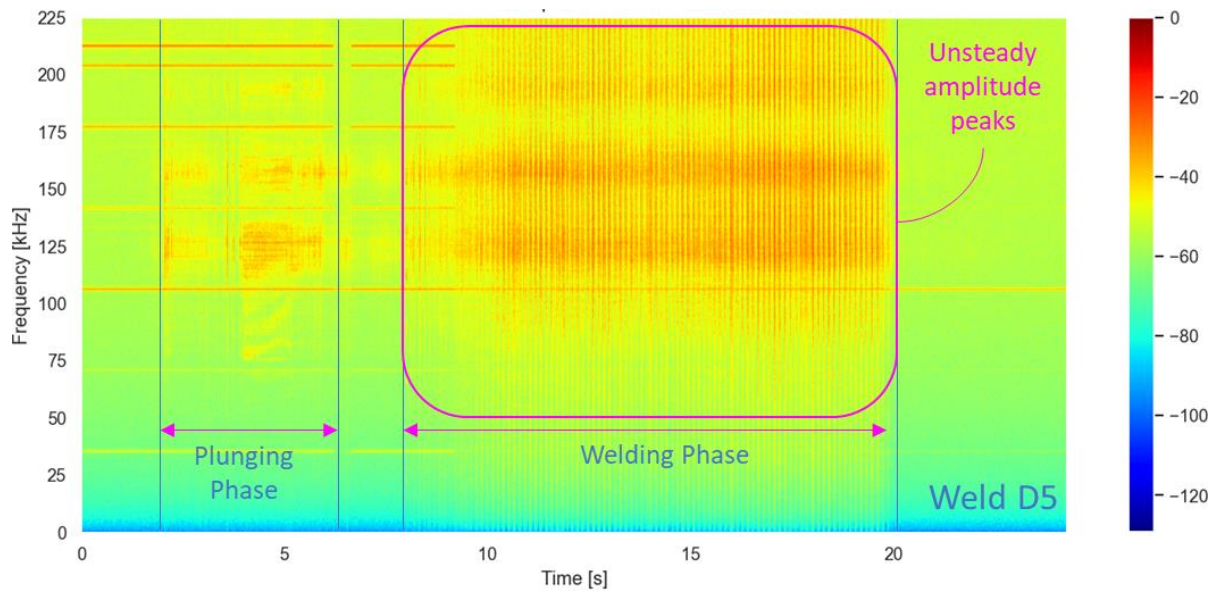
Figure 66- Spectrograms obtained for AE signals captured for welds D5

The defect formation mechanism can be explained using the material flow theories discussed in section 2.6 and illustrated in Figure 52 earlier in this thesis. Figure 67 shows the lateral view of void formation as the tool traverses through 5mm thick plates. As observed from the material flow theory in the case of a tool traversing at a high tool tilt angle, a stagnation point for material flow is observed at the trailing side of the pin. As the bottom part of the tool probe contributes to lower frictional heat generation due to lower surface area, the material around the tool is not plasticized enough to compensate for the material required at the trailing stagnation point. As the tool traverses the plasticized material from the leading side of the tool delaminates from the tool due to lower temperature, leaving a void behind. As the stir zone is not fully formed, a joint remnant line is observed towards the bottom of the void shown in Figure 62.
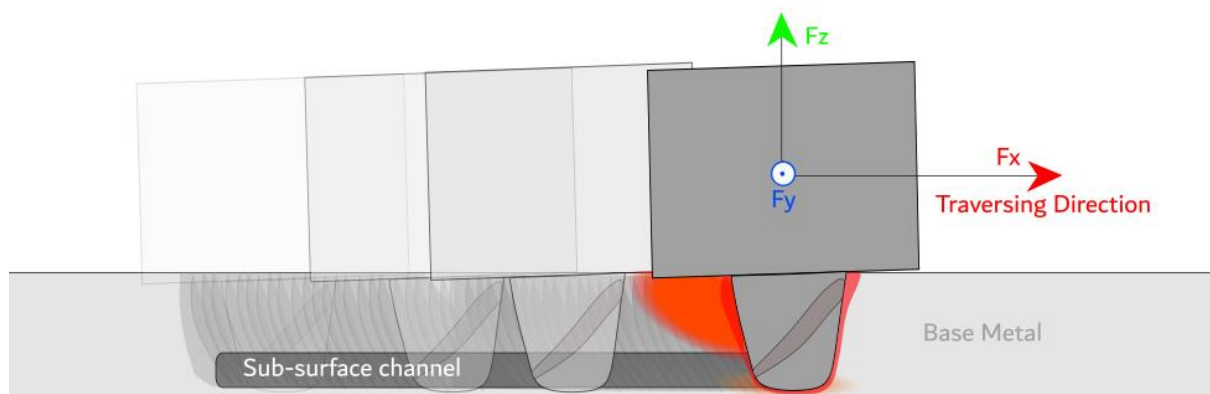
Figure 67: Position of void in the weld observed in traversing direction plane

4.4.3   Influence of tilt angle on high RPM welds

Welds D1 to D5 were performed with a high tool tilt angle of 3° while weld D6 was performed at a lower tilt angle of 1.5°. With the same sensor placement as discussed in section 3.5, AE signals on the advancing and retreating sides are measured. As highlighted in Table 17, the amplitude on the retreating side of the weld was higher than the advancing side reducing the amplitude ratio to below unity.

Weld #	Root Mean Square		
	Channel A (Advancing)	Channel B (Retreating)	Amplitude ratio
D1	0.047	0.019	2.51
D6	0.028	0.039	0.72

Table 17- RMS amplitude of AE signals on the advancing and retreating side of the weld

The influence of shoulder engagement through the tool tilt angle can also be visualized using the PSD for the welds D1 and D6. Figure 68 below shows the logarithmic PSD plot against the observed frequencies.
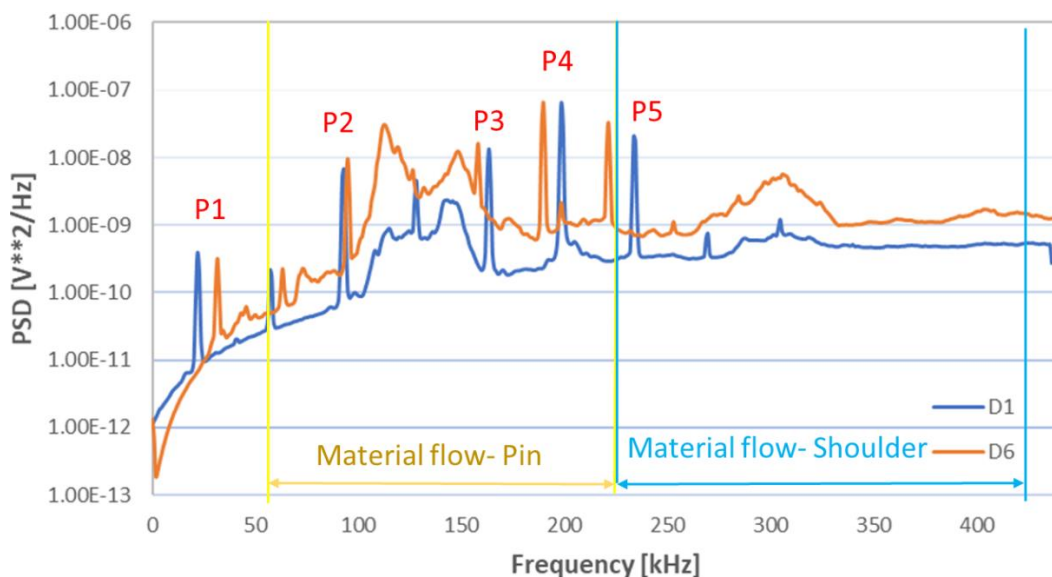
Figure 68: Power Spectrum Density (PSD) for AE signals observed for weld D1 & D6

From the PSD plot, the distinctive features of both welds from dominant frequencies are highlighted. Similar trends in both the PSD datasets are observed with two shallow peak regions observed from 100kHz to 200kHz & 270kHz to 340kHz. Based on the

abovementioned peaks, two regions for material flow and shoulder flow can be identified. Within the two datasets, five peaks with similar amplitudes (i.e.- P1 to P5) arise due to the electronic resonance caused by the decoupler/phantom power supply. Weld D1 performed with a high tool tilt angle of 3° reduced the tool-material engagement resulting in lower PSD amplitude. For weld D6 performed with a lower tilt angle of 1.5° the tool material engagement is increased by an increase in the contact surface resulting in higher PSD amplitudes. The slope of the shallower peaks between P2 and P3 are similar for both D6 and D1. An opposite trend is observed for the peak observed for D6 & D1. This behaviour is correlated to partial shoulder engagement affecting the frequencies from 250kHz to 400kHz.

This behaviour of the AE signals can be explained by elaborating on the relative velocity of the material movement and velocity of the oncoming material/ tool traverse. The velocity vectors can be visualized with the help of Figure 69 below, where Rh and Rv are the horizontal and rotational components of the rotational velocities with Vm the velocity of the oncoming material forming Rr, the resultant rotational velocity.
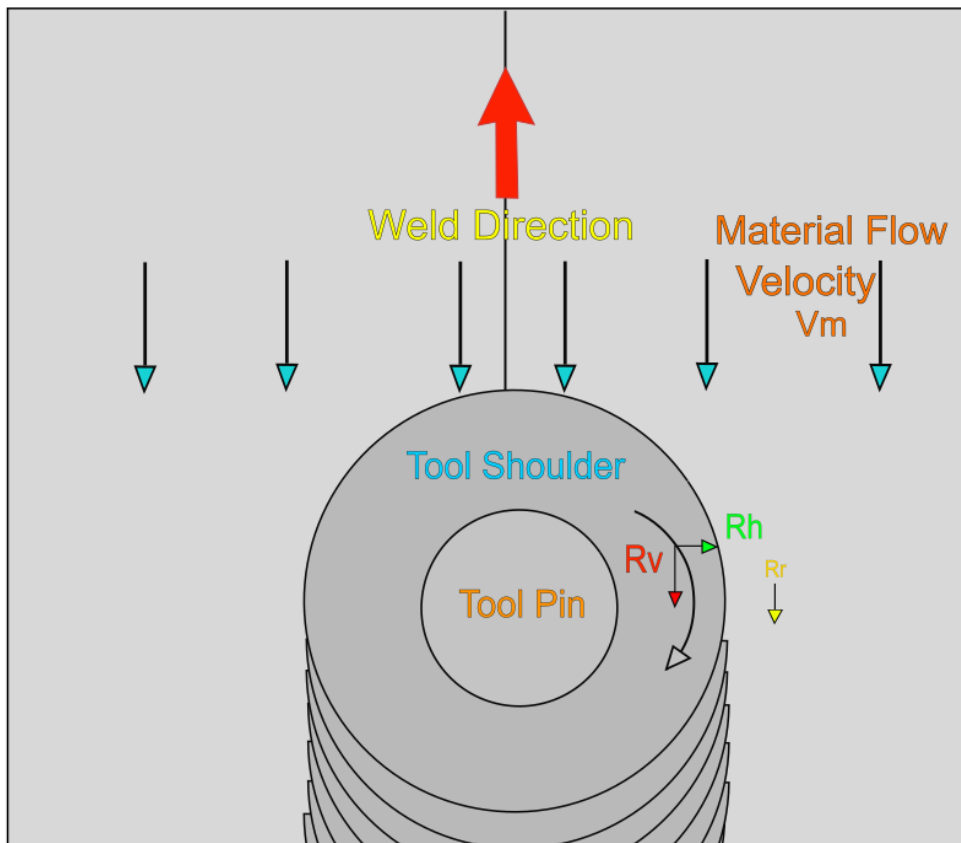
Figure 69- Material flow & oncoming material velocities

The amplitude of the AE signal on the advancing side of the weld is higher because of the opposite direction of material flow by the tool and the oncoming material. The opposite is observed on the retreating side as the direction of tool material flow and oncoming material flow are the same. The difference in amplitude is further increased with an increase in the tool tilt angle due to a lack of material engagement on the leading side of the tool. As the tool tilt angle is reduced, the material engagement on the leading side of the weld is increased resulting in higher rotational velocity on the trailing side. With the increase in the rotational velocity on the retreating side, the shearing of base metal would increase, resulting in a higher amplitude of the AE signal. From the results obtained in this chapter, it is concluded that change in the axial force cannot be directly related to material disruption. It is highlighted that the advantage of cont. AE monitoring method quantifies the material shearing on the advancing and retreating side of the weld and it can be used to support the detection of material flow for the FSW process.

4.5 Influence of plunging pressure on AE signal

4.5.1 Effect of shoulder engagement on tool forces and Ae signals

For this section of the thesis welds performed in the 3rd phase of experimental trials are discussed for welding 5mm thick AA5083 (i.e.- SE1-SE4) (section 3.8). AA5083 is preferred over AA6082 due to its higher hardness and tensile strength which is correlated to higher amplitudes of shear waves. Use AA5083 also validates the knowledge transferability between similar alloys. To reduce the engagement of the tool shoulder and material, an axial offset is introduced to the FSW tool. For measuring the AE signals generated during the weld, 2nd combination (discussed in section 3.5) of AE sensors is used along with the on-machine dynamometer for force measurement. The weld parameters for the discussed welds are presented in Table 18 & Table 19 below.

Tool Tilt Angle	Plate Thickness	Length
1.5°	5 mm	200mm

Table 18: Constant parameters for welds performed under Phase 3 trials

Weld #	SE1	SE2	SE3	SE4
Tool RPM	800	800	700	900
Tool Traverse Rate (mm/min)	440	440	460	330
Tool Plunge Depth (mm)	4.8	4.6	4.6	4.6

Table 19: Varying parameters for welds performed under Phase 3 trials
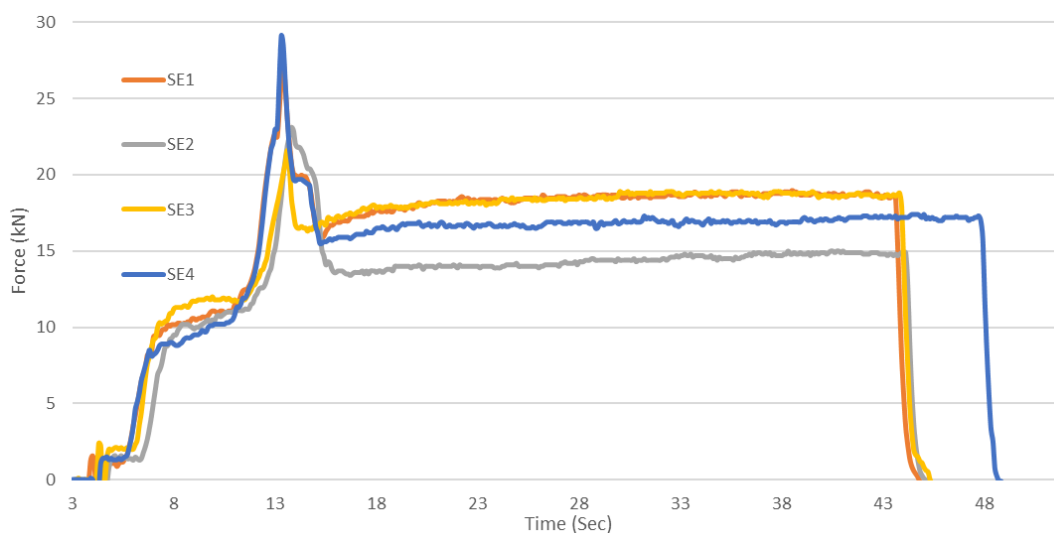
Figure 70: Axial forces observed for welds SE1 to SE4

91

SE1 was performed as a benchmark weld to assess the proper shoulder contact signal. Weld SE2 to SE4 was performed with a reduced plunge depth of 4.6 by introducing position offset. Weld SE3 was performed with a higher tool traverse rate to reduce the heat input to the weld, while SE4 was performed with high RPM and a lower tool traverse rate to increase the heat input. All the welds performed in this welding trial resulted in sound welds with no flaws or defects. The effect of plunge depth is seen on the axial forces while the observed lateral/ side forces (Y direction) did not show any correlation.

Figure 70 shows the variation of the axial forces with reduced plunge depth and varying weld parameters. The weld performed with ideal plunge depth resulted in an average axial force of 18kN during the welding phase while the axial force dropped to 14kN when the tool plunge depth was reduced by 0.2mm. This reduction in the forces is caused due to the reduced workpiece-tool contact area. Compared to weld SE1 performed with ideal plunge depth, weld SE3 was performed with a higher tool traverse rate which reduced the heat input to the weld and increased the axial force on the welding tool. For weld SE4 the axial force drops to an average of 17kN due to higher heat input to the weld by decreasing tool traverse rate and increased tool rotation rate.

While welds SE1 and SE 3 were performed with different weld parameters, they yielded close to identical force signatures. This observation underlines the limitations of monitoring the 2nd-degree process parameters (i.e.- forces observed on the FSW tool). Furthermore, the results obtained from monitoring of AE signals discussed in this section aid the reasoning for the development multi-process parameter monitoring system.
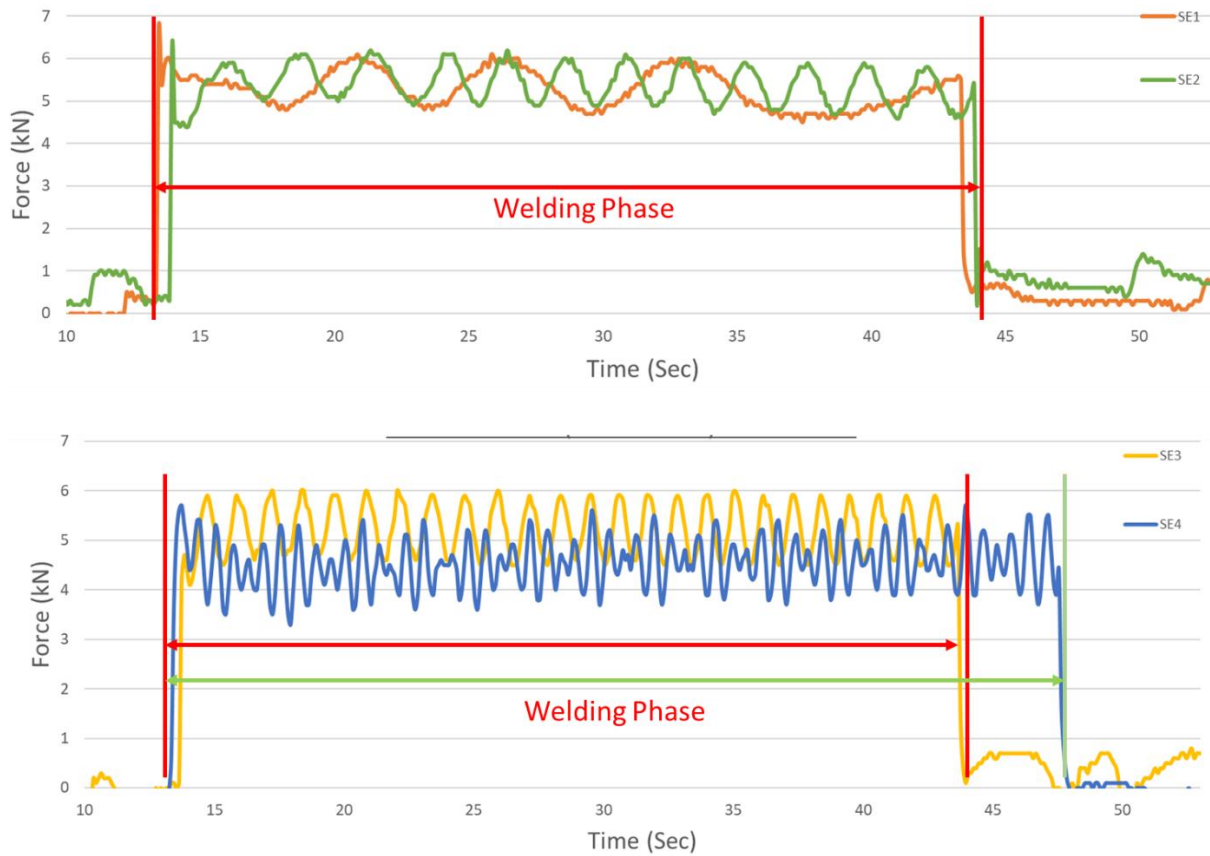
Figure71: Traverse forces (X-direction) observed for welds SE1, SE2, SE3 & SE4

In Figure, the influence of tool offset on the cyclic trend of traverse force is observed. For weld SE1 the force recorded consists of high-frequency low amplitude and low-frequency high amplitude waves. SE2 has uniform periodic cycles with consistent maximum and minimum amplitudes. Figure shows the traverse forces observed for welds SE3 and SE4. While the traverse forces for SE3 were uniform with consistent maximum and minimum amplitudes, SE4 resulted in lower forces with periodic waveform.
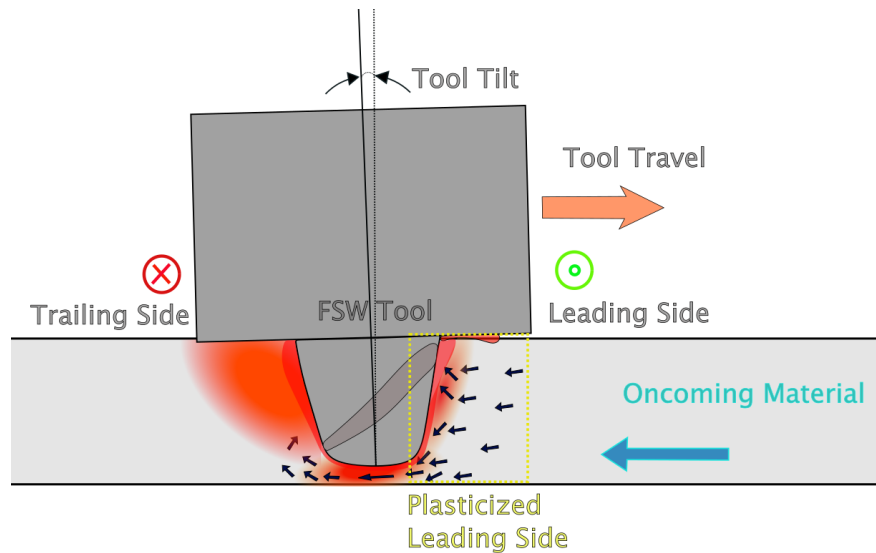
Figure 71: Region of plasticized material ahead of the tool (Leading side)

The forces in the traversing direction are greatly dependent on the plasticized material ahead of the weld. The amount of plasticized material on the leading side of the tool is illustrated in Figure 71. During the welding phase, the plasticized material ahead of the tool experiences a periodic increase and decrease. With the increase in the size of this region, the tool experiences less resistance traversing and reciprocally.

To analyse the abovementioned effect on the welds performed at a high tool tilt angle and the traverse forces, welds D4 and D5 from section 4.4 are discussed below. The traverse forces for welds D4 & D5 performed during the 2nd phase of welding trials are plotted in Figure 72. Due to the difference in the magnitude of forces, the two vertical scales are plotted for welds D4 and D5 respectively. As discussed in section 4.4 the recorded force data is not conclusive enough to determine the presence of internal voids in the weld.
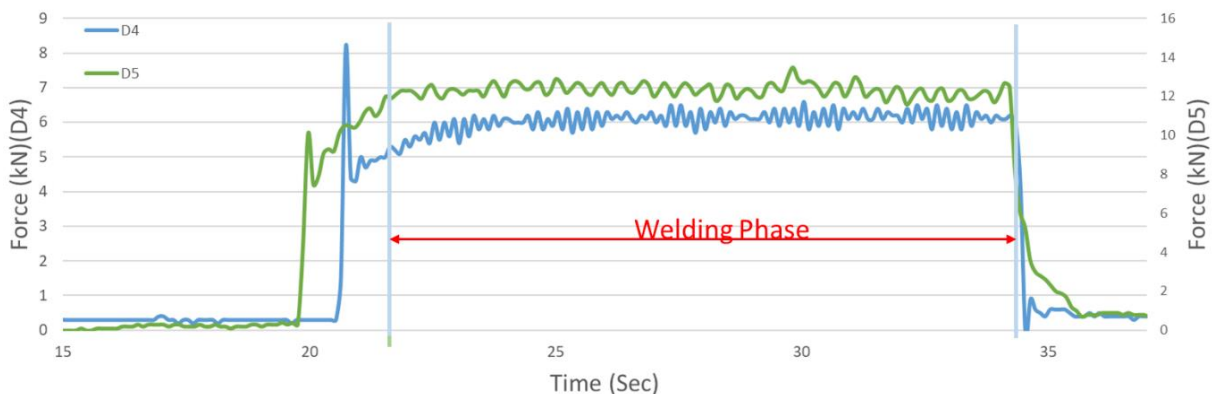
Figure 72: Traverse forces (X-direction) observed for welds D4 & D5

From the forces recorded in the traversing direction, the effect of the contact area on the leading side of the tool can be estimated. As the reduction in the size of the leading side contact area can also occur due to tilt angle or welding a curved part, the force signals cannot be directly correlated to the lack of shoulder engagement due to the tool offset.

Figure 73 shows the PSD comparison for welds SE1, SE2, SE3 & SE4 performed with different weld parameters mentioned in Table 19. Two flow zones (i.e. flow zone and shoulder flow zone) can be identified from the PSD originating from 10kHz to 225kHz and 225kHz to 450kHz respectively. Similar peaks of electrical resonance (explained in section 4.4.3) due to the phantom power supply are observed. Weld SE1, performed with full penetration depth, resulted in a higher amplitude of PSD for the observed spectrum compared to welds SE2, SE3, and SE4 performed with 0.2mm axial tool offset. The amplitudes of PSD observed for SE3 are lower compared to SE2 in the probe flow zone and of similar amplitudes in the shoulder flow zone. Weld SE4 performed with higher tool RPM and partial tool penetration has a lower amplitude of PSD in the probe flow region but a similar peak to SE1 with an amplitude higher than 1.00 E-8 V^2/Hz is observed in the shoulder flow region. The difference of 30kHz is also observed between the abovementioned peaks in the shoulder flow region.
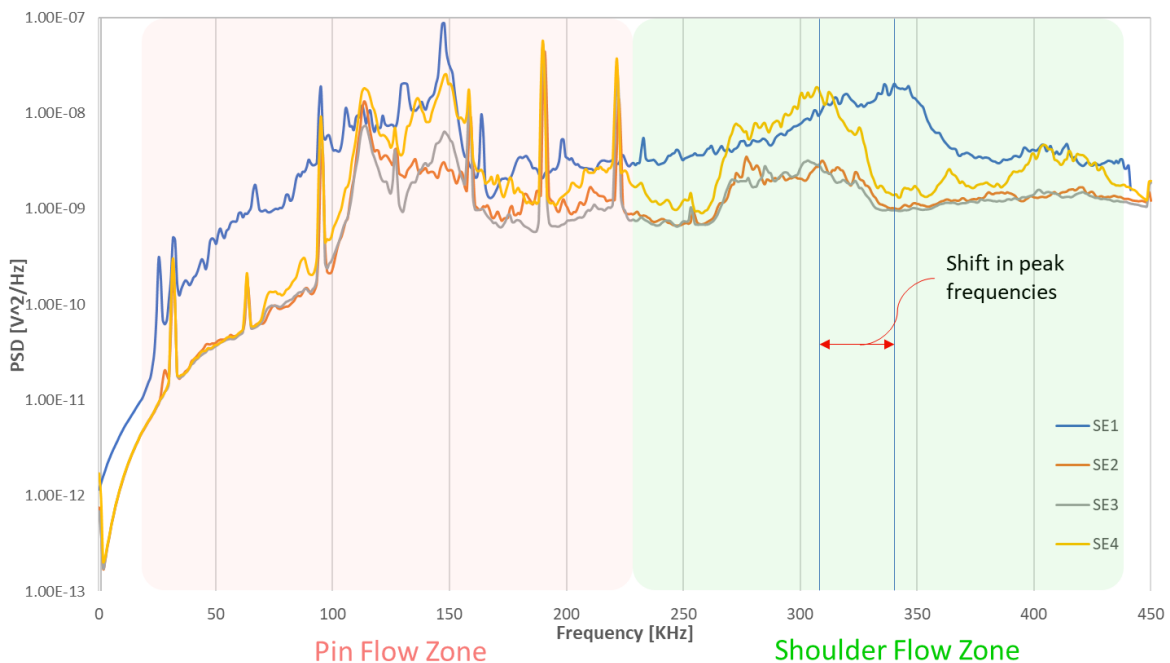
Figure 73- PSD obtained for welds SE1, SE2, SE3 and SE4

As discussed in the previous sections of this thesis, AE signals of the FSW process are majorly dependent on the material being sheared by the tool. From the above-mentioned trend in the PSD for welds SE1 to SE4, the effect of weld parameters can be observed. As the shoulder engagement increases, the PSD amplitudes for the shoulder flow region also increase. Welds S2 and S3 had a flatter peak compared to S4 due to lower plasticized material around the tool due to the low heat input to weld. Weld SE4 resulted in significantly higher PSD amplitude due to increased tool RPM, increased heat input and more plasticized material coming in contact with the shoulder. As the PSD gives the frequency domain information about the AE signals, the influence of shoulder interaction in the time domain can be better visualized using spectrograms. Figure 74 shows the spectrograms plotted for AE signals obtained from welds SE1 and SE3. Due to the limited monitoring window, the spectrogram for SE1 shows irregularities in the monitoring of welding phases.
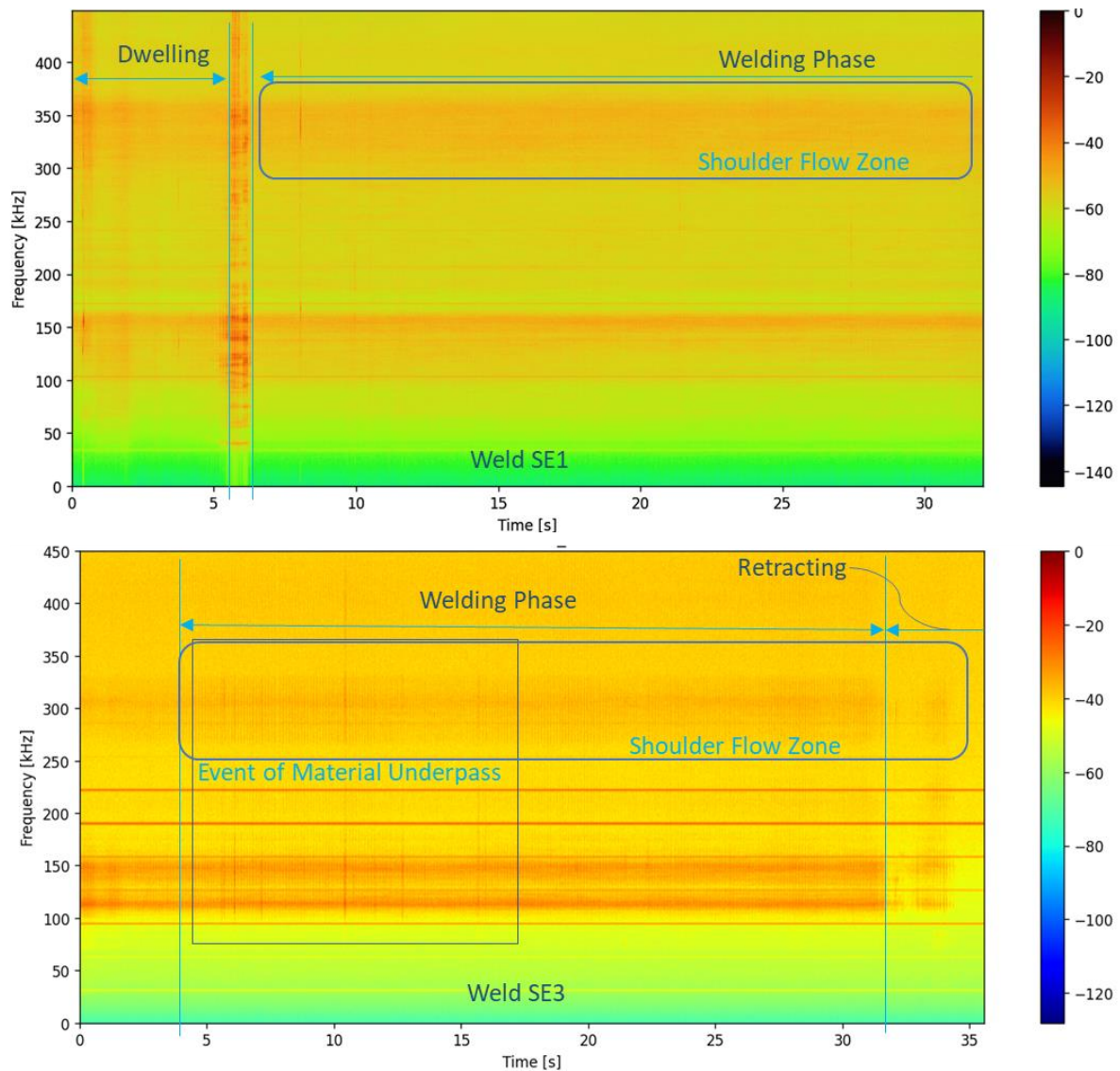
Figure 74- Spectrograms obtained from AE signals of weld SE1 & SE3

While the spectrogram for weld SE1 illustrates higher amplitudes of AE signal from 300kHz to 360kHz, the spectrogram obtained for SE3 shows less prominent peaks in the frequency range of 260kHz to 325kHz. The spectrogram for weld SE3 also illustrates the increased points of shoulder underpass for the accumulated material. The material underpass of accumulated material ahead is not gradual due to the clearance between the workpiece and the tool shoulder. This event is also promoted by a lack of heat input at the surface of the weld due to a lack of shoulder engagement. Weld SE4 is performed with a lower tool traverse rate results in greater heat input to the weld and contributes to more material interaction with the tool shoulder. The spectrogram obtained from the AE signal recorded for weld SE4 is plotted in Figure 75. Unlike the spectrogram for weld SE3, the spectrogram for weld SE4 shows a higher amplitude of frequencies observed for the tool shoulder flow region. The ambiguity of

axial and traverse force monitoring highlights the lack of confidence in weld classification. This illustrates the advantages of weld monitoring through AE by spectrograms over force-based monitoring and the ability to detect a lack of FSW tool engagement with the workpiece.
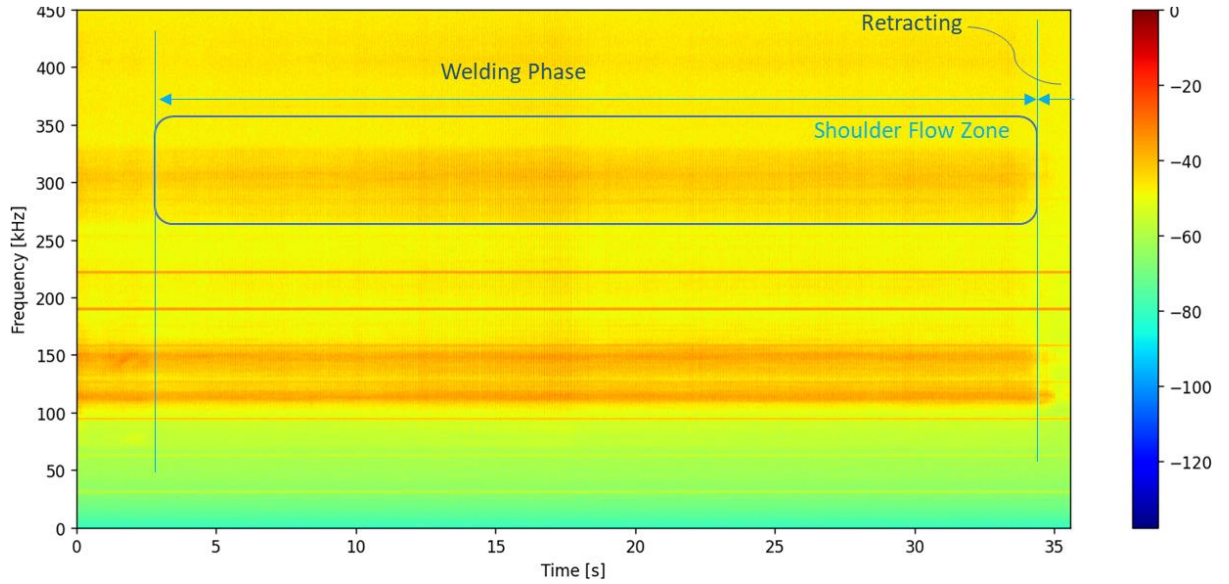
Figure 75- Spectrogram for AE signal recorded for weld SE4

4.6   Detection of lack of penetration by AE monitoring

This section of the thesis discusses the welds performed on AA5083 in the 4th phase discussed in section 3.8 (i.e.- LOP1 to LOP 12). Lack of penetration defect is induced by welding plates with different thicknesses (i.e.- 5mm & 6mm) with the same welding parameters. To understand the transferability of the knowledge for continuous AE monitoring between aluminium grades and analyse the effect of shearing of non heat treatable alloy, AA5083 is chosen for the welds discussed in this section. For monitoring the AE of the FSW process, two AE sensors are used in combination 3 layout (explained in section 3.5) illustrated in Figure 76. Since the welds are performed with a lower tool traverse rate the time duration of the welding phase, is the 2nd configuration of data recording for Picoscope (defined in section 3.5). The weld parameters for the performed welds are mentioned in Table 20 & Table 21 below.
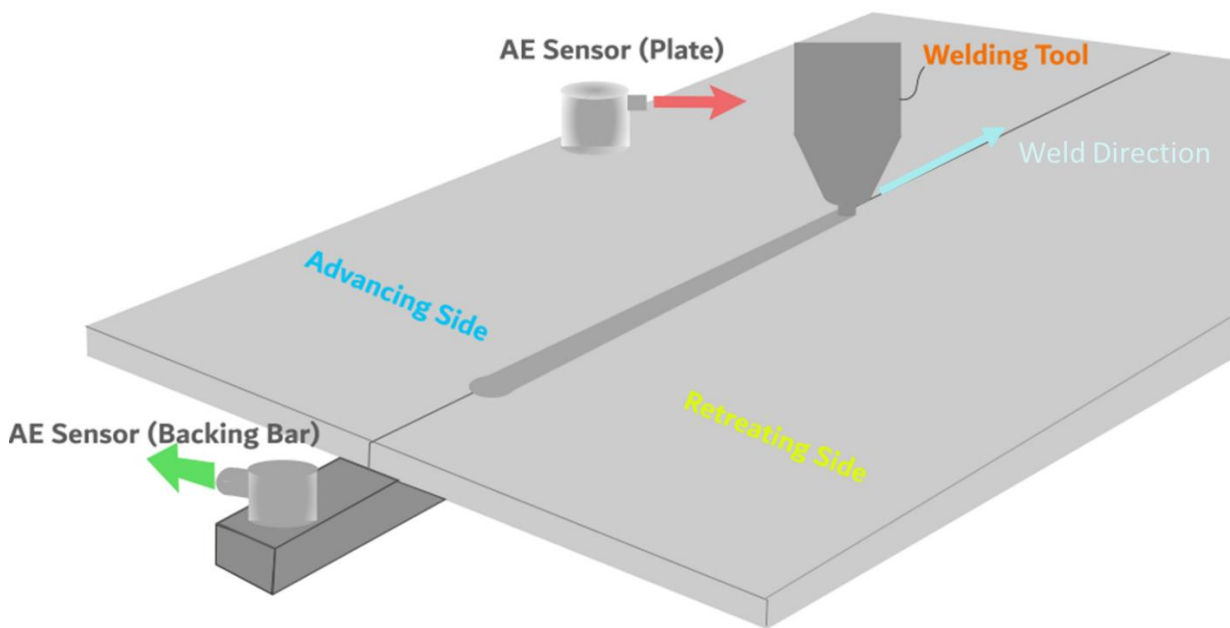
Figure 76: Schematic for the experimental setup for the 4th phase of the welding Trial

Plunge Depth	Feed Rate	Tilt Angle	Weld Length
4.8 mm	300 mm/min	1.5°	140 mm

Table 20- Constant weld parameters for 4th phase of welding trial

Weld #	Tool RPM	Thickness of plate
LOP1	500	5mm
LOP2	500	6mm
LOP3	600	5mm
LOP4	700	6mm
LOP5	600	6mm
LOP6	700	6mm
LOP7	800	5mm
LOP8	900	5mm
LOP9	1000	5mm
LOP10	800	6mm
LOP11	900	6mm
LOP12	1000	6mm

Table 21- Varying weld parameters for 4th phase of welding trial

Lack of penetration (LOP) defect is caused when there is an unwelded region at the bottom of the weld which acts as a point of failure for the welded joint. This may be caused by to partially penetrated tool, laterally offset tool position and fit-up defects. The detection of LOP through monitoring of force data is not reported in the literature. This section focuses on the ability of continuous AE monitoring to detect the presence of LOP.

4.6.1   Influence of plate thickness on size of stir zone

To understand the effect of tool RPM on the size of the stir zone, two sections from the centre of the weld for 5mm and 6mm thick plates are etched using Keller's reagent to analyse the stir zone. Figure 77 below compares the stir zone for 5mm and 6mm AA5083 welded plates (i.e.- Welds LOP1, LOP2) by overlaying the outline of the stir zone for LOP2 on LOP1. Since both the welds are performed using the same tool & weld parameters the size of the stir zone for different thickness can be compared.
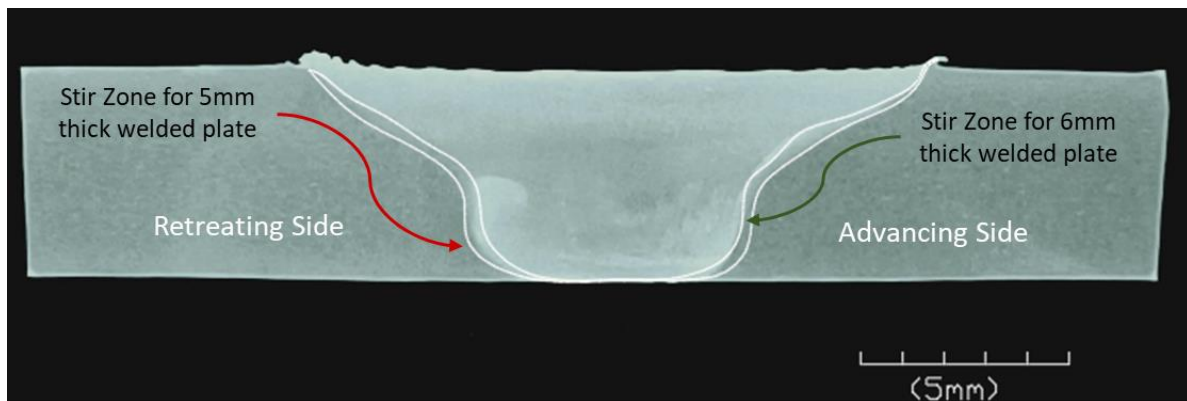
Figure 77: Comparison of stir zones for 5mm & 6mm thick AA5083 plates

The size of the stir zone for the weld performed on a 5mm thick plate resulted in a stir zone area of 43.8mm^2, while the weld performed on a 6mm thick plate with the same welding parameter yielded a lower area of 41.5mm^2. This reduction in the area of the stir zone can be explained by highlighting the heat input and heat dissipation caused during the welding process. As mentioned in the previous sections of this thesis, the heat input to the weld is governed by the welding parameters and the tool used while the amount of heat dissipated depends on the material around the stir zone. For welds performed with full penetration of tool for a 5mm thick plate, there is no unwelded material at the root of the weld which results in greater heat concentration in the weld. For welds performed with a partially penetrated tool, there remains an unwelded region at the bottom of the weld which acts as a heat sink, reducing the heat concentration and the size of the stir zone.

4.6.2 Time-frequency domain analysis for detecting LOP

Section 4.3 of this thesis discusses the damping of AE waves caused by increasing the heat concentration of the weld by increasing the tool RPM through parametric analysis. The previous section highlights the effect of material thickness on the size of the stir zone. Since one of the objectives of the project is to develop a deep learning-based classification model using spectrograms, this section aims to utilize the features from spectrograms to detect LOP. Using the 3rd combination of sensor setup (explained in section 3.5), spectrograms from data recorded by the two sensors are plotted. Similar to the previous sections, the spectrograms are simplified using the spectral centroid, explained earlier in Section 4.3 of this thesis. The effect damping caused by the stir zone is further explored through waveform analysis of the recorded AE signals from welds LOP1 to LOP12. As the CNNs are not sensitive to detect changes in spectrograms, the presence of lack of penetration is related to the size of the stir zone.

By estimating the sample standard deviation for the centroid of the spectrogram using the moving window of 1028 for 1 second, the spectrogram is simplified to analyse and present the spread of the centroid in the time scale for the duration of the weld. Through the sample standard deviation of the spectral centroid, the percentage variance coefficient is estimated as defined in Eq (15). The block diagram for signal processing is illustrated using Figure 78.

$$Percentage\ variance\ coefficient\ (PVC) = \frac{Standard\ Deviation}{Sample\ mean} \times 100 \qquad [15]$$

Figure 78: Flow chart for estimating the percentage variance offset values from the spectrogram
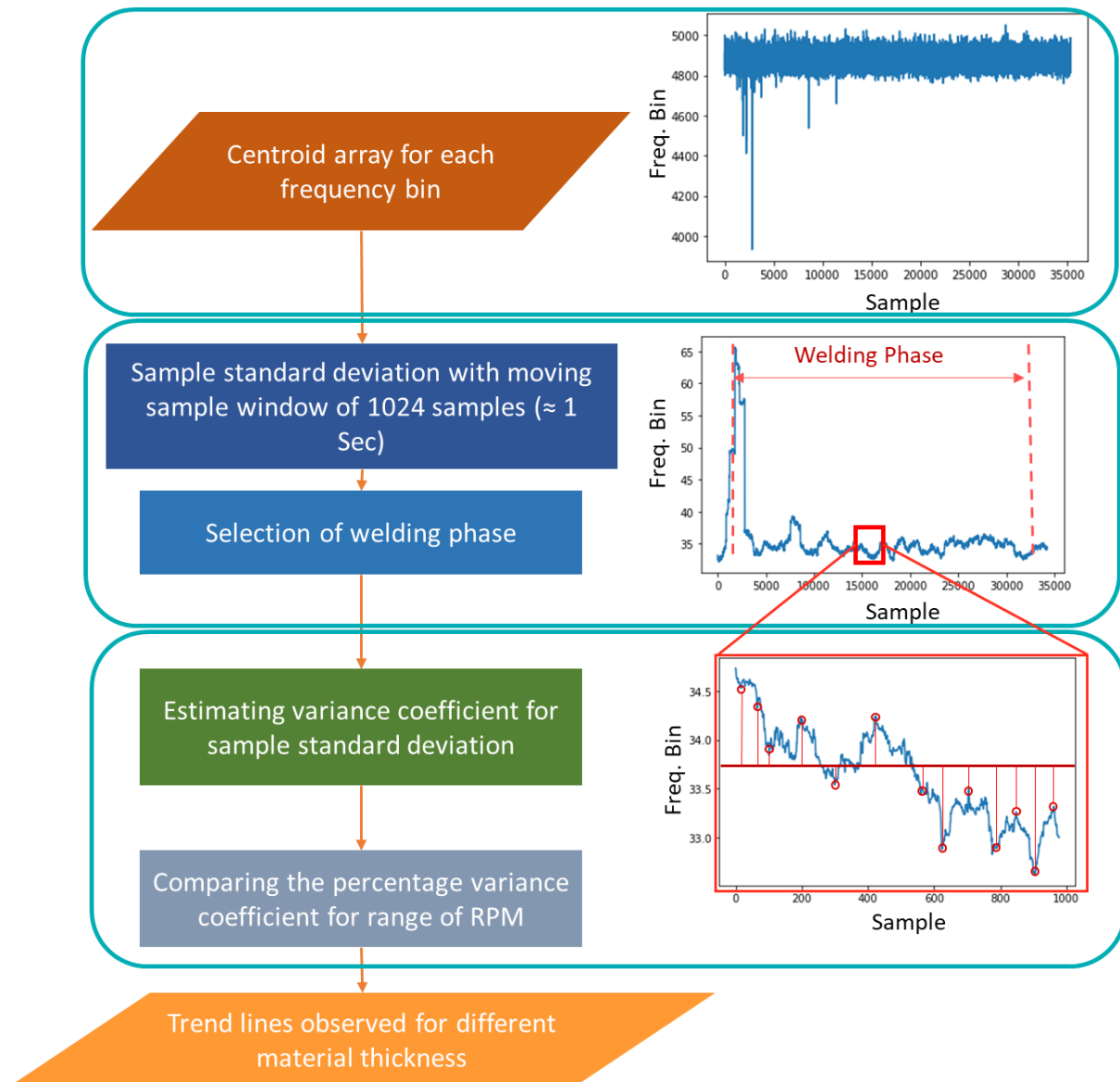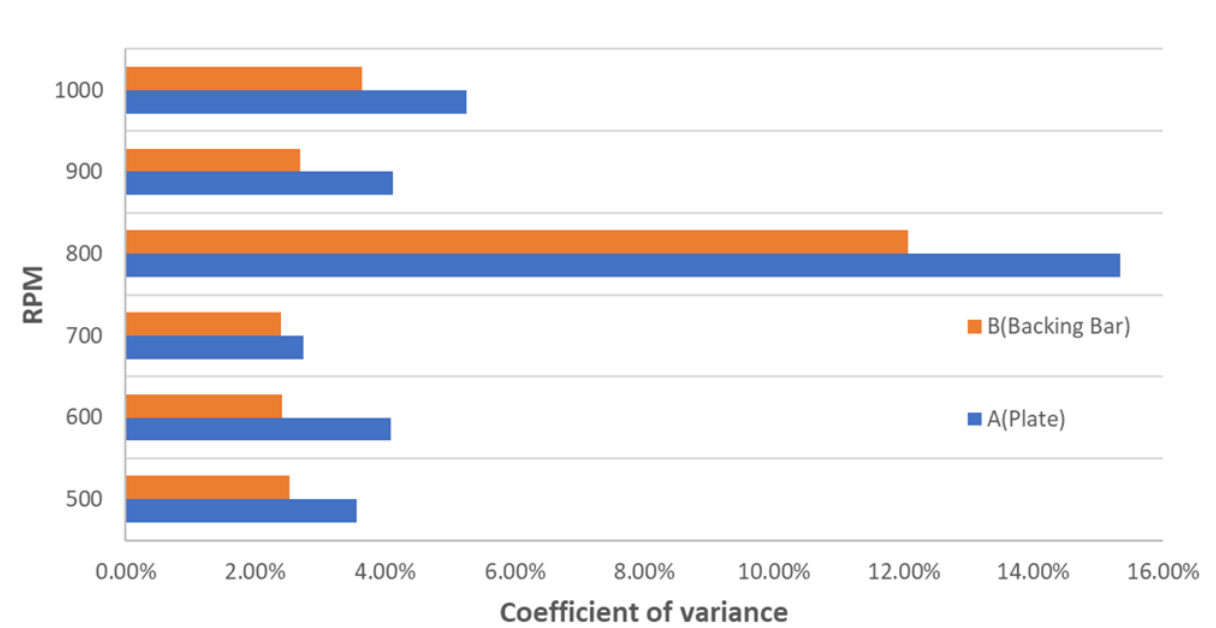
Figure 79: Percentage variance coefficient obtained from sample standard deviation of spectral centroid obtained from welding 5mm thick plates
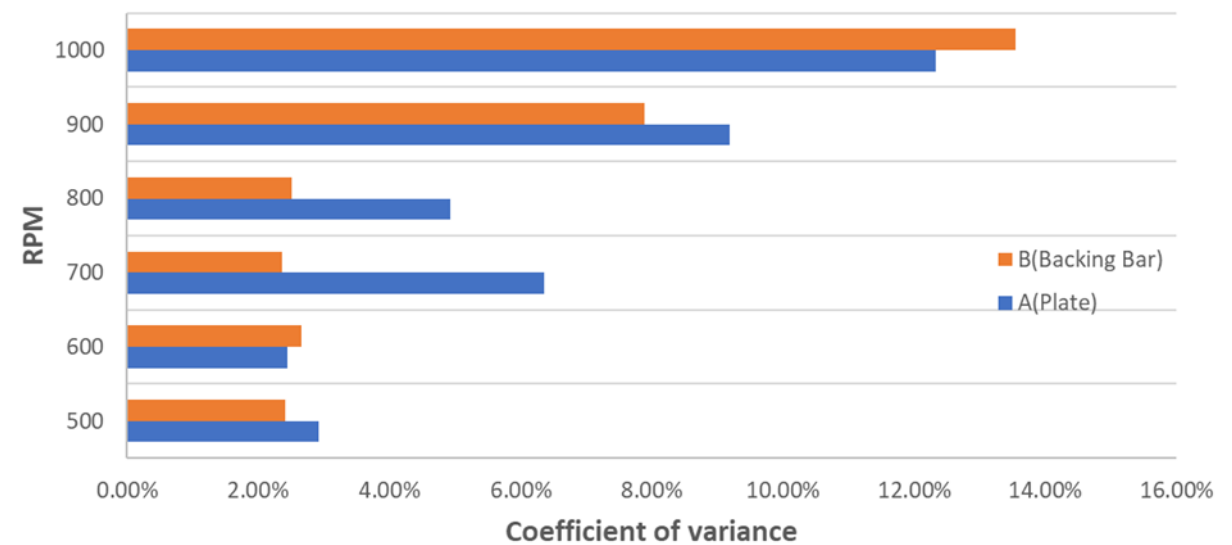
Figure 80: Percentage variance coefficient obtained from sample standard deviation of spectral centroid obtained from welding 6mm thick plates

To compare the coefficient of variance of the sample standard deviation for the spectral centroid for a range of tool RPM, bar plots are presented in Figure 79 & Figure 80 for 5mm and 6mm thick plates respectively. The bar plots are divided with RPM on the Y axis and coefficient of variance deduced from spectral centroid on the X axis obtained from sensors placed on the plate and backing bar. In *Figure 79* the coefficient of variance of the AE signals obtained from the sensor placed on the plate resulted

increase from 3.5% to 5.25% for RPM of 500 to 1000 with a maximum coefficient of variance observed at 800 RPM. The exponential coefficient observed for the trend line is 0.108. A similar trend was observed for the coefficient variance of the AE signals obtained from the sensor placed on the backing bar where the coefficient of variance increased from 2.5% to 3.6% following a flatter exponential trend with the exponential constant of 0.105. Figure 80 shows the variance coefficient obtained from AE signals recorded for the welds performed on 6mm thick plates with RPM ranging from 500 to 1000. The variance coefficient obtained from the AE signals recorded by the sensors placed on the plate resulted in an increase from 2.93% for 500 RPM to 12.33% for 1000 RPM. A similar trend was observed for 700, 800,900 and 1000RPM where the percentage coefficient of variance increased from 2.41% to 13.56%. The exponential constant for the percentage variance coefficient observed for the AE signal from the sensor placed on the backing bar was 10% higher when the sensor was placed on the plate. *Figure 79* shows no prominent exponential trend in the coefficient of variance for the AE signal. *Figure 80* shows an exponential trend in the percentage variance coefficient values for both sensor locations (i.e.- on the plate and the backing bar). The difference in the trend can be explained using *Figure 81* which illustrates the unwelded region and reduced heat concentration in the weld.
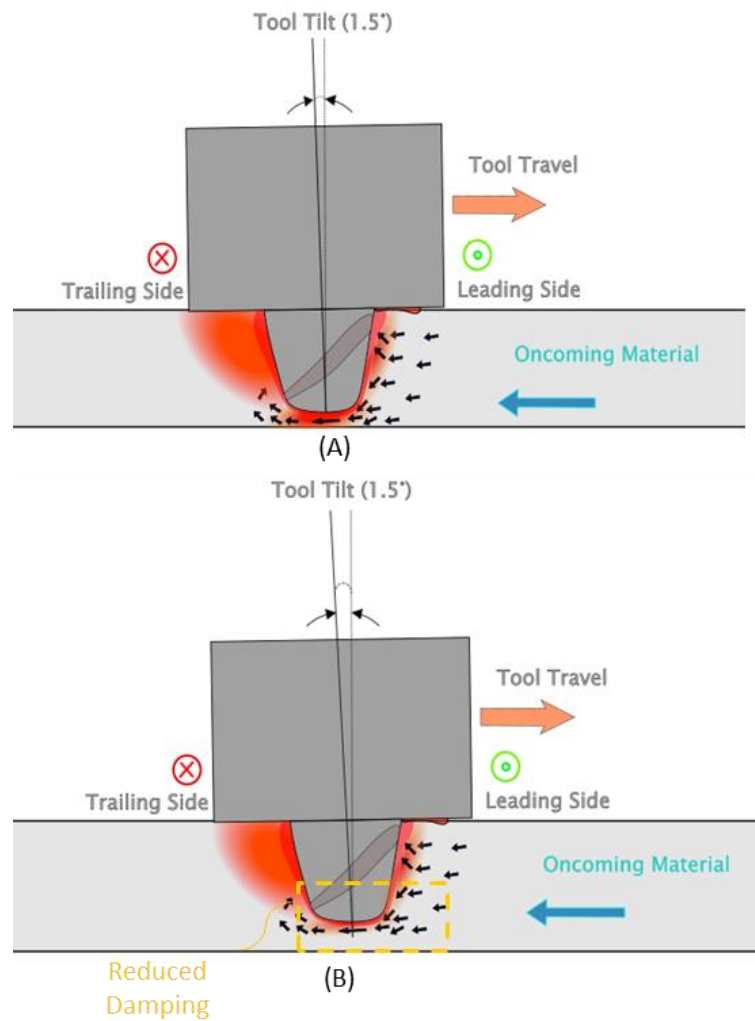
Figure 81: (A) Lateral cross-sectional view for full penetration weld with the material flow; (B) Lateral cross-sectional view for partially penetrated weld with the unwelded region

While the results from section 4.6.1 confirm that the size of the stir zone is reduced with increased plate thickness, section 4.3.1 highlights the ability AE monitoring system to detect the change in the size of the stir zone. Based on these observations the potential of detection of LOP through AE monitoring is highlighted. The abovementioned results illustrate the contrasting trend of the AE signals from welding plates with 5mm and 6mm thickness. This difference in the trend of AE signals can be explained with Figure 81 which illustrates the side cross-sectional view in the Z-X plane underlining the reduced stir zone size for a 6mm thick plate as the result of heat dissipation caused by excess material. As the tool RPM increases the size of the stir zone also increases, increasing the damping and reducing the variance of AE signal (caused by the generation of flash and events of tool material underpass) during the welding phase. This distinct behaviour of AE signals can be traced back to the thickness of welded plates and detecting the presence of LOP. The observations made from this section and section 4.3.1 highlight the ability of the advantages of the AE

monitoring method to detect the presence of LOP which can not be detected through the force monitoring method.

4.7   Validation of detection of internal voids

For validating the repeatability of the AE signal to detect the presence of internal voids, two welds with high tool traverse rate and high tilt angle are performed on AA6082. To measure the AE signal from the welds, combination 1 of the AE sensor setup (discussed in *section 3.5*) is used. The varying & constant weld parameters for the two welds performed are discussed in Table 22 & Table 23 below.

Weld Length	Tool tilt angle	Material thickness	Effective tool length
370mm	3°	5mm	4.8mm

Table 22: Constant weld parameters for phase 5 welds (V1 &V2)

Weld No.	Tool RPM	Tool traverse rate
V1	620	1100mm/min
V2	730	950mm/min

Table 23: Varying weld parameters for the weld V1 & V2

Weld V1 was performed with a 10% higher tool traverse rate and 22% tool RPM compared to weld D4 (performed with a high tool traverse rate) mentioned in *section 4.4.2*. Weld V2 was performed with higher heat input compared to V1 with a 17% higher tool RPM and 13.6% lower tool traverse rate. The axial and traverse forces observed during the weld are plotted in Figure 82 & Figure 83.
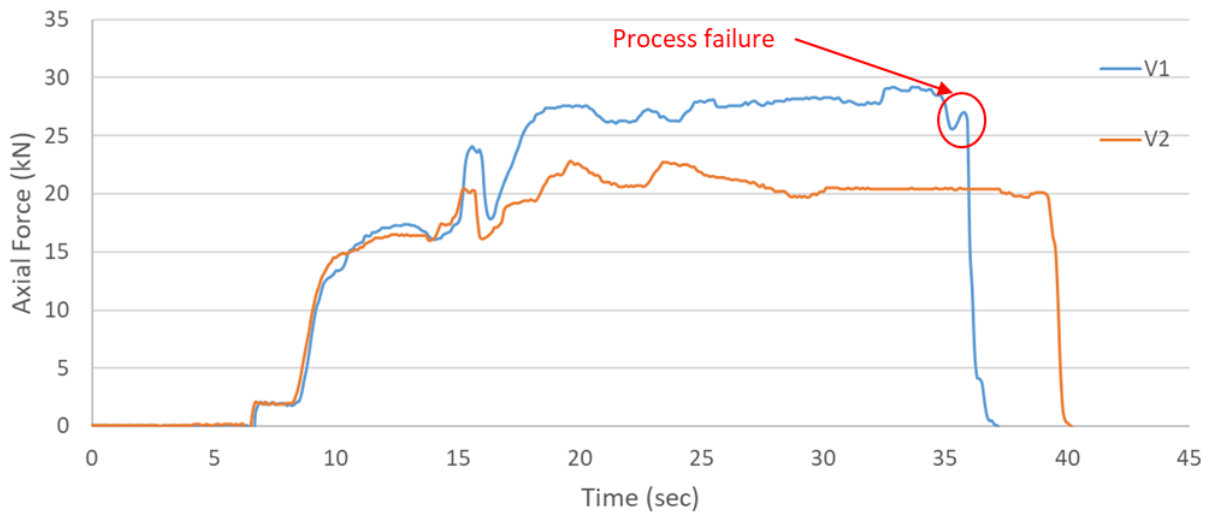
Figure 82: Axial forces observed on the FSW tool for performed welds V1 & V2
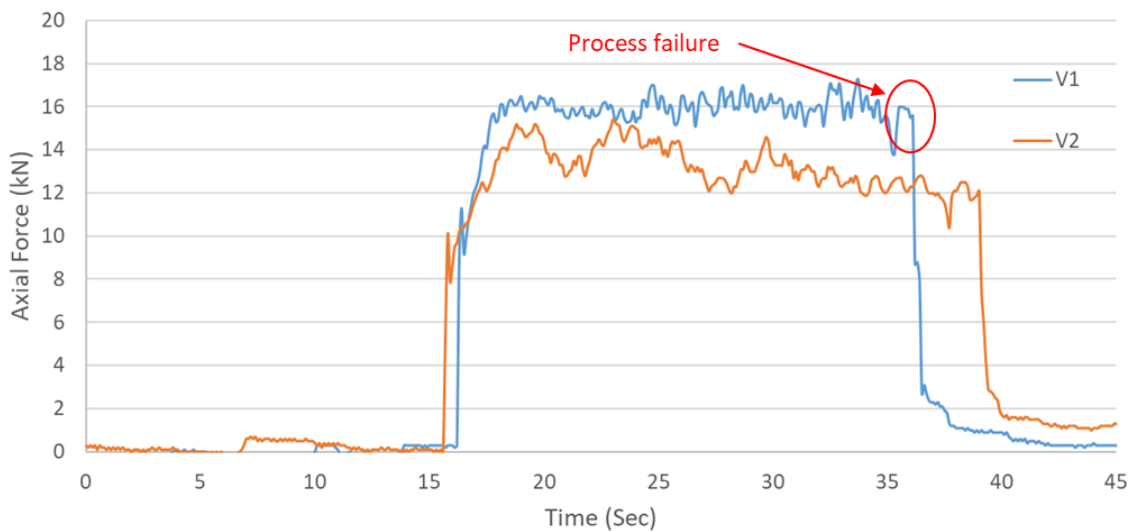
Figure 83- Traverse forces observed on the FSW tool during welds V1 &V2

The forces observed for V1 were higher than V2 for both directions (i.e.- axial and traverse) due to low heat input to the weld. The weld V1 experienced a failure during the transition from the welding phase to the retracting phase which was reflected in the recorded axial force data as a peak. Unlike the axial force signals, the forces observed in the X-direction (tool traverse direction) did not reflect a clear peak for process failure which distinguishes it from a sound weld (i.e.- Weld V2). The top side of the weld V1 with a lack of fill defect is shown in Figure 84 below.

Figure 84: Topside of the failed weld V1 due to insufficient heat input

Weld V2 performed with a lower tool traverse rate resulted in no surface defects and with lesser flash generated compared to weld V1. Figure 85 shows the top side of the weld V2 with no traces of lack of fill.
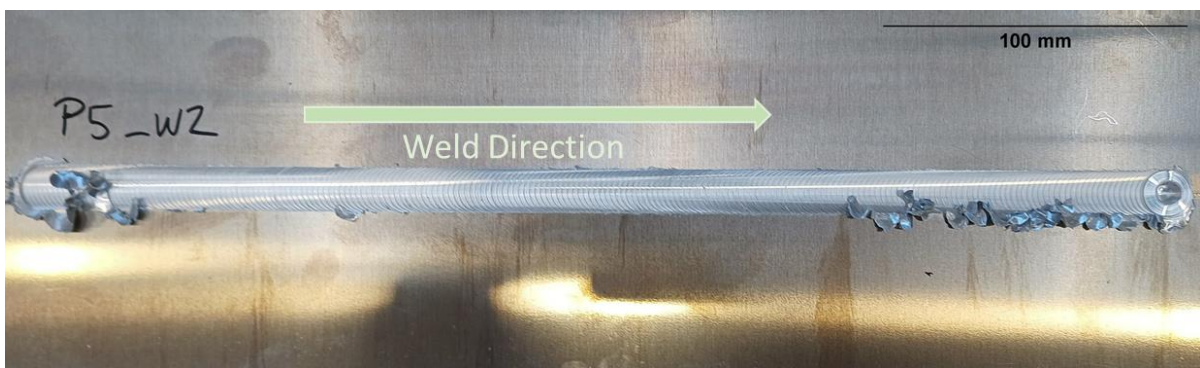
Figure 85: Topside of the weld V2 with flash generated during the weld

The spectrogram obtained from the AE signal recorded by the sensor on the advancing side is shown in Figure 87. A higher amplitude of AE was observed from 50kHz to 250kHz for the time period of 23 sec of the welding phase. A similar trend to weld D5 with internal voids of periodic high amplitudes was observed in the spectrogram highlighting the presence of a subsurface void in the weld across its length. Figure 88 shows the radiograph for the weld V2 with a sub-surface void running across its length. The void observed had an average width of 2.8mm and height of 1mm spanning over a length of 365mm. During the retracting of the tool at the end of the weld, the tool shoulder seals the void making it undetectable to visual inspection. The amplitude of the recorded AE signal varies across the weld and gives a good correlation with the depth of the void in the radiograph. The two sections of the sub-surface void are shown in Figure 88, (A) with a wider section of void and (B) with shallower void. A similar trend is observed from the spectrogram where the amplitude of the intermittent peaks reduces along the weld.
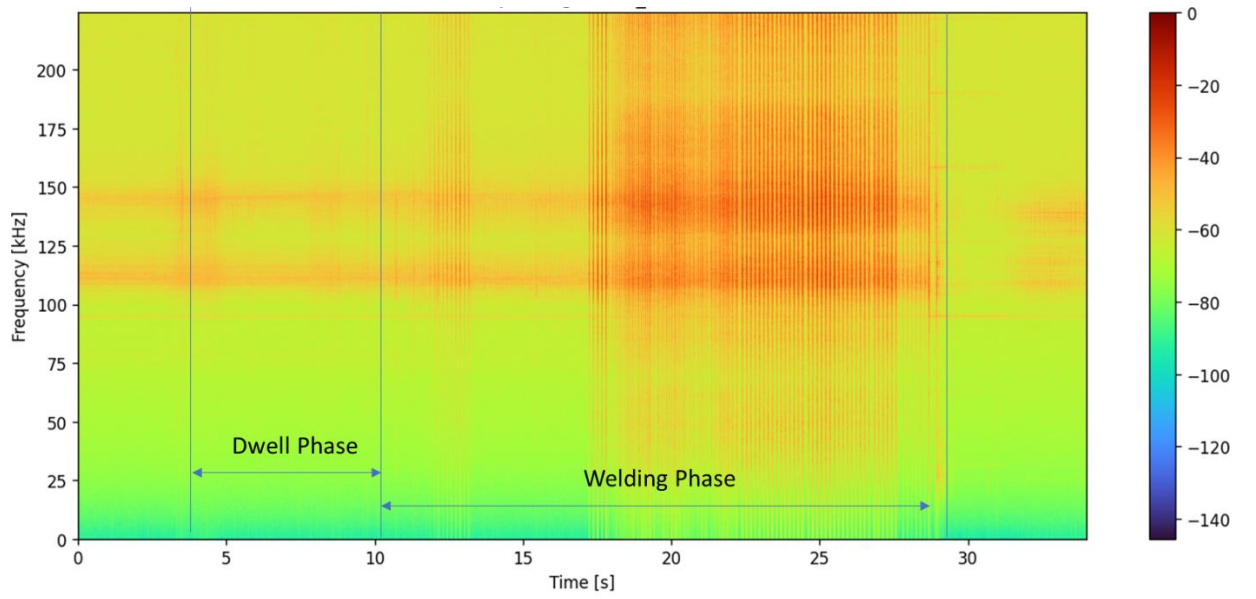
Figure 86: Spectrogram for AE signal recorded for weld V1
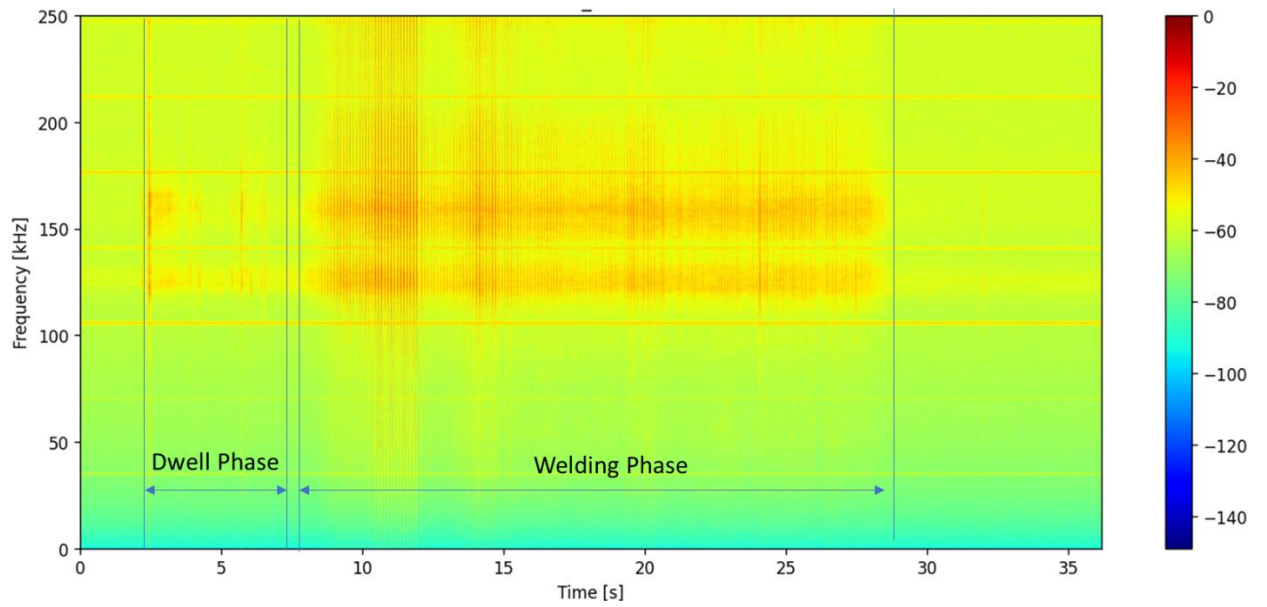
Figure 87: Spectrogram for AE signal recorded for weld V2
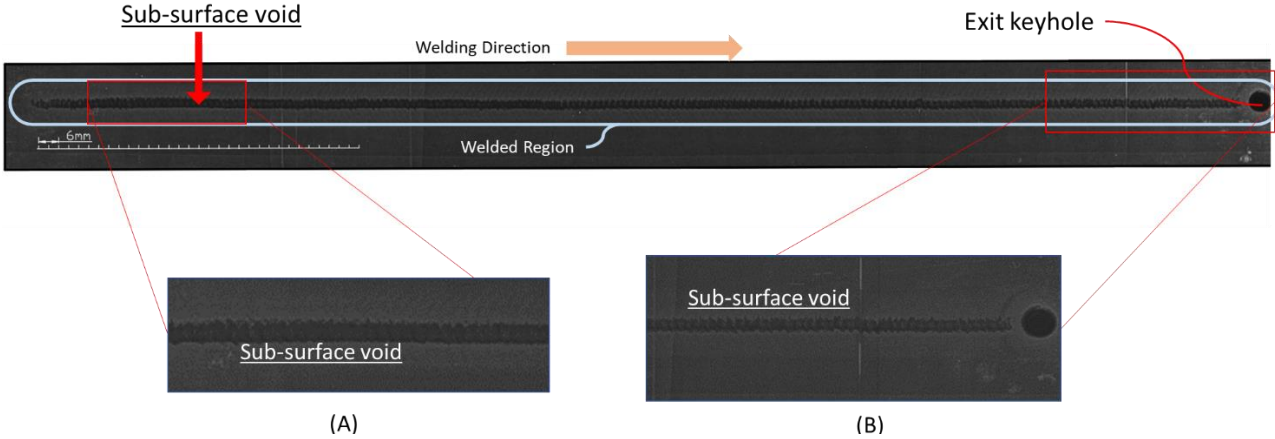
Figure 88: Radiograph obtained for the weld V2 with the sub-surface void

The effect of tool rotation on the side walls of the void can be observed. Figure 89 shows a scaled image of the void. The advancing side wall of the wall has more profound features compared to the retreating side of the weld. The difference in the features can be related to the tool rotation and traversing direction. On the advancing side of the weld, the direction of the tool rotation is opposite to the oncoming material and vice versa on the retreating side.
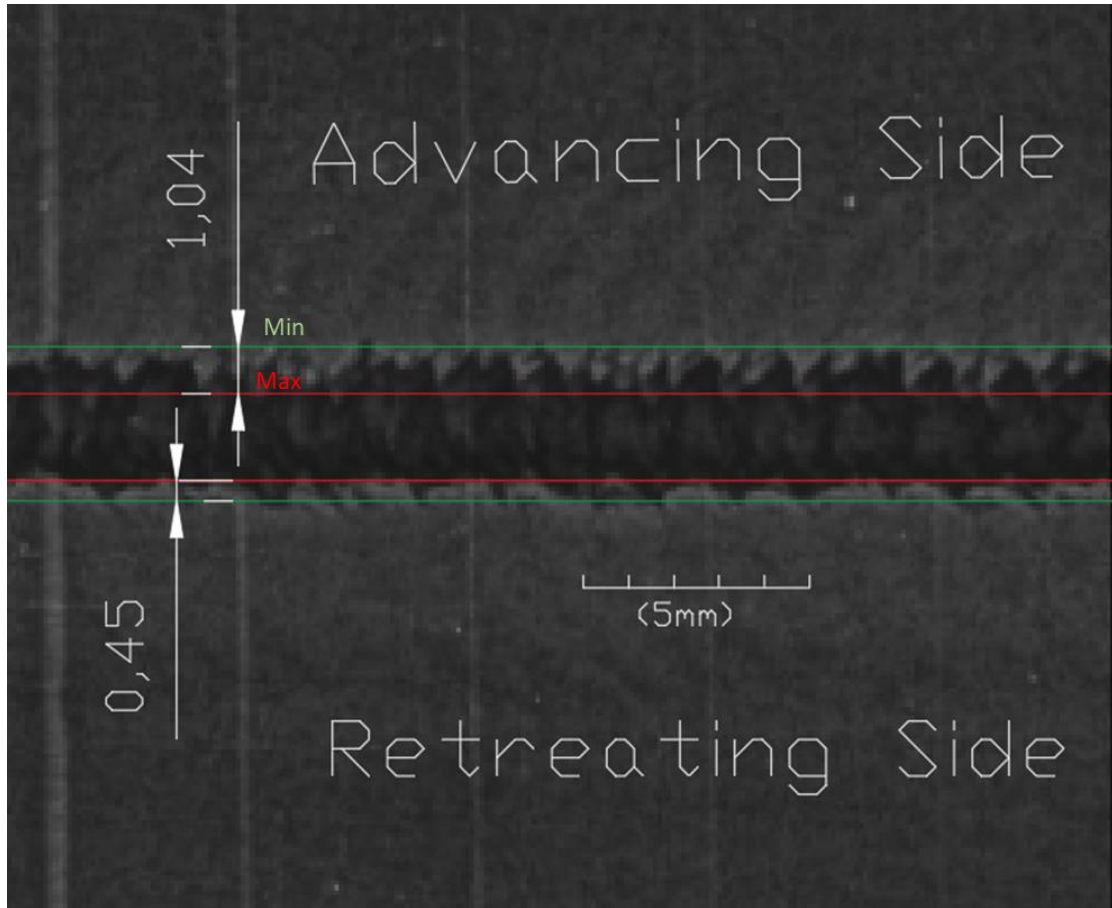
Figure 89: Variation in features on the advancing and retreating side walls of the void (all dimensions in mm)

Figure 90 illustrates the spectrogram and radiograph obtained for the 2-second window of the welding phase. The instances of intermittent material shearing leading to void formation can also be observed in the spectrogram with high amplitude peaks observed from 10kHz to 250kHz. A total of 17 high shearing instances were observed for both spectrogram and radiograph with a distance of 1.84mm and a time of 0.1162 seconds between them.
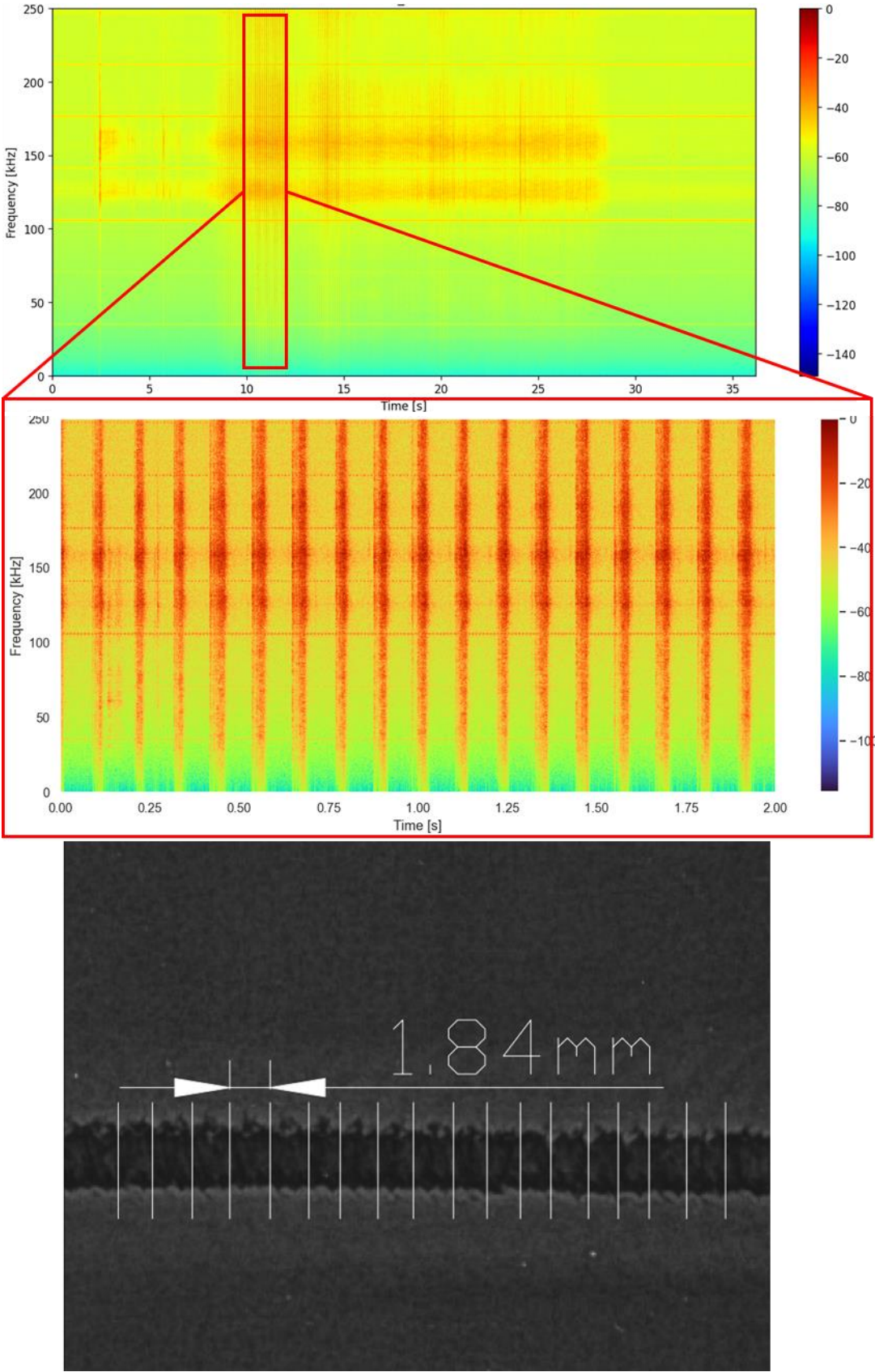
Figure 90: Instances of material shearing observed for the 2-second window for spectrogram and radiograph

From the spectrogram obtained for weld V2, the width of the sub-surface void is correlated with the amplitude of peaks observed in the spectrogram. Comparing the radiograph and spectrogram obtained for a 2-second window for the weld, it is observed the event of high shearing can be accurately tracked through the spectrogram. This highlights the ability of the AE monitoring-based system to monitor welds for process stability in real time. Section 4.4.2 of this thesis explains the mechanism for sub-surface void formation by reduced frictional heat generated at the trailing side of the tool probe. Based on the observations from section 4.4.2 and the results from the validation welds presented in this section, it is concluded that the continuous AE monitoring method is effective in distinguishing the high-shearing event of the FSW process resulting in a welding defect.

4.8 Weld temperature and AE correlation

To understand the correlation between the temperature and AE signals, two AE sensors are placed with 8 thermocouples positioned on the advancing and retreating side of the weld. (As discussed in the *Section 3.7*). To capture the interaction of the shoulder with the AE signal, 1st configuration of the Picoscope recording is mentioned in Table 5. The parameters for the welds performed in this phase of the experimental trial are mentioned in Table 24 & Table 25 below.

Weld Length	Effective probe length	Tool Traverse Speed	Material Type	Material Thickness
370mm	4.8	550mm/min	AA6082	5mm

Table 24: Constant weld parameters for the welds discussed in phase 6 of trials

Weld #	Tool tilt angle	Tool RPM
T1	3°	500
T2	3°	800
T3	1.5°	500
T4	1.5°	800

Table 25: Varying weld parameters for the welds performed in phase 6 of the experimental trial

To ensure that the process attains stability at the point measurement of temperature, point P3 is selected at the centre of the weld line. The location of point P3 is illustrated in Figure 91. The welding phase for each weld lasts for 40.3 seconds which is beyond the data recording capabilities. From the recorded AE signals during the welding phases, a window of 10 seconds with P3 as the centre is selected to analyse the correlation between the AE signals and the weld temperature.
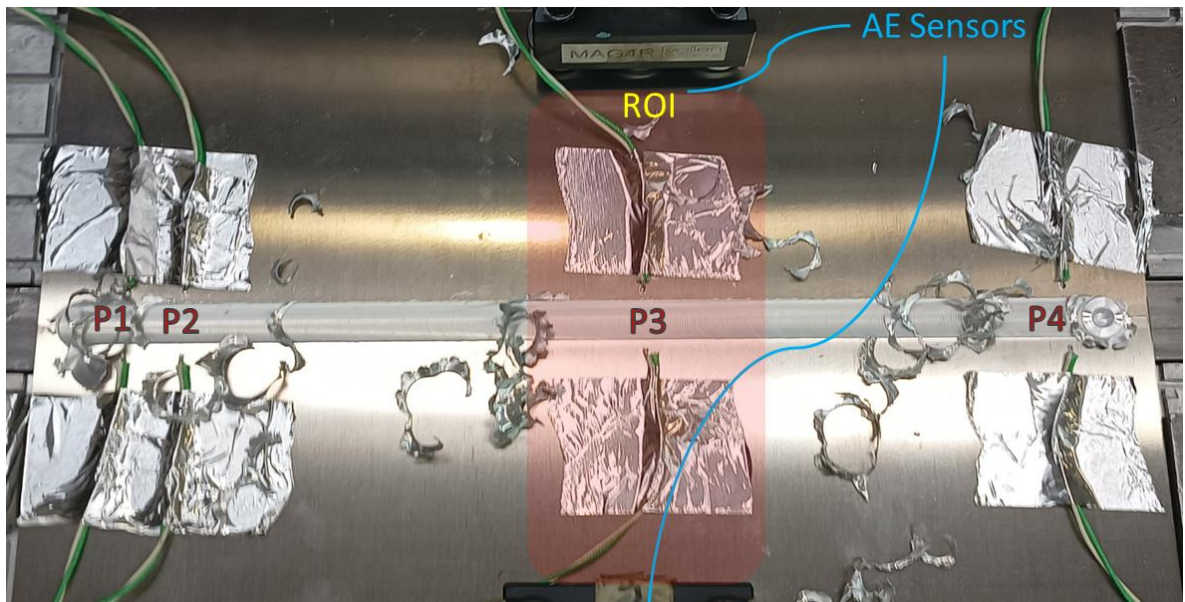
Figure 91: Region of interest (ROI)with temperature measurement points (P1, P2, P3 & P4)

The variation in the temperature through the transition from the dwell phase to the ramp-up phase is recorded by the thermocouples placed on the advancing and retreating sides of the weld. The temperature variation along the length of the weld T1 Figure 92 below.
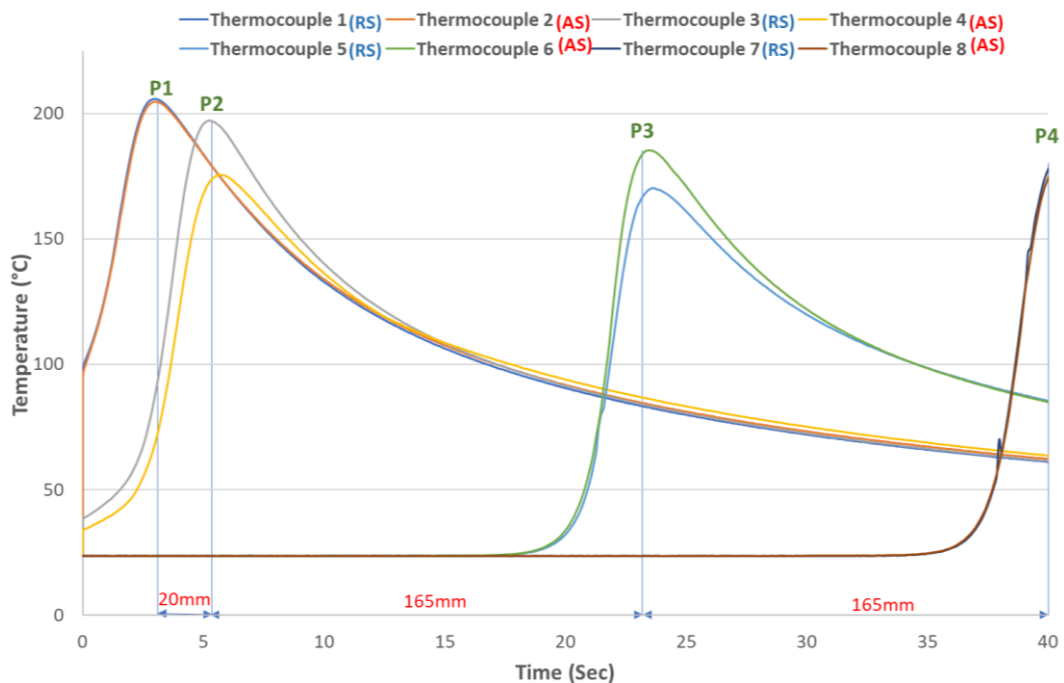
Figure 92: Temperature variation observed for advancing and retreating side of the weld T1

Figure 93 illustrates the peak temperature measured at points P1, P2, P3 and P4 from thermocouples placed on the advancing and retreating side of the weld. A downward trend of the temperatures can be observed moving from point P1 to P4.
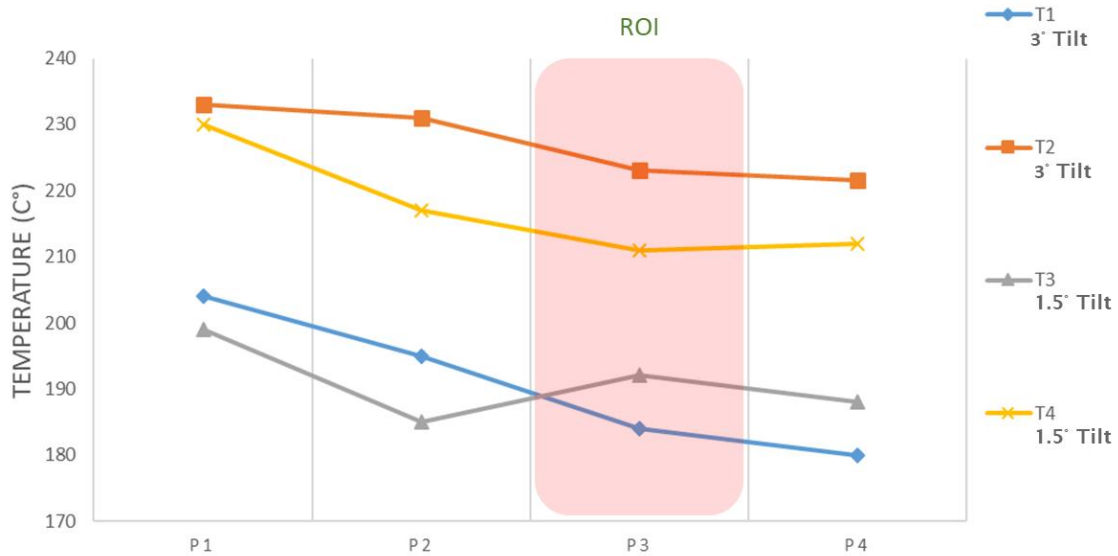
Figure 93: Peak temperature at points P1, P2, P3 & P4 for welds T1, T2, T3 &T4

Based on the plot, two groups of weld temperatures can be observed for the same tool RPM. Weld T1 and weld T3 performed with RPM of 500 results in similar temperatures. With an increase in RPM from 500 to 800 the observed temperatures increase by 11% on average. For the weld T3, the observed temperature at point P3 is higher than the weld T1 performed at a higher tilt angle. An opposite trend is observed for welds T2 & T4 performed at higher RPM where weld T4 with higher tool tilt angle recorded 4% lower temperatures along the points P2, P3 & P4.
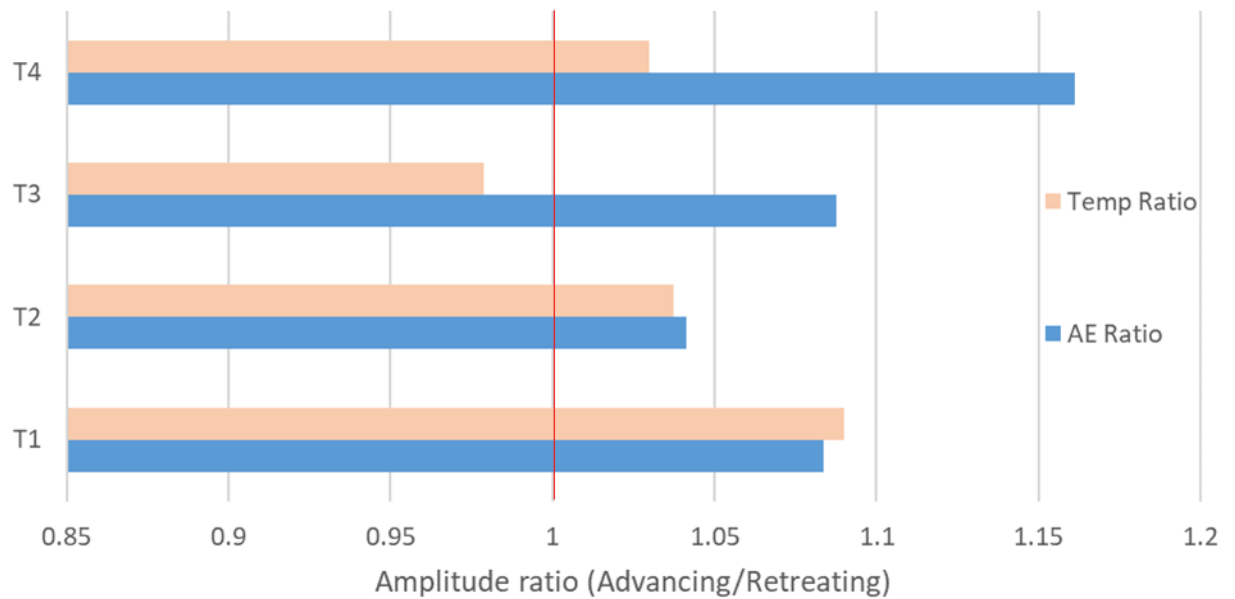
Figure 94: Ratio of RMS of AE signals and recorded temperature on advancing & retreating sides of the weld

To understand the effect of shearing on the temperatures recorded from the advancing and retreating side of the weld, Figure 94 shows the ratio of RMS of AE signal and temperatures recorded on the advancing and retreating side of the weld observed at point P3 (Region of interest). The ratio above 1 depicts higher amplitudes of AE signals or temperatures on the advancing side while ratio and reciprocally. While temperatures recorded welds T1, T2 and T4 had higher amplitude on the advancing side, for weld T3 an opposite trend was observed where temperature on the retreating side was higher.

The welding temperature is governed by shearing action and mass bulk movement of the heated plasticized material corresponding to the tool engagement. The effect of tool engagement on the shearing of the base material by the tool is highlighted in sections 4.4 & 4.5. The weld T3 performed at a lower tilt angle of 1.5° results in the increase of the tool engagement for the welds performed with lower RPM. The increase in the tool engagement also results in higher bulk movement of plasticized material towards the retreating side, resulting in higher temperature towards the retreating side of the weld. For weld T2 & T4, an opposite trend is observed and the increase in the material movement is supported by the tool tilt angle furthermore the temperature increases due to the heel plunge action of the tool. In Figure 94, welds T1, T2 and T4 resulted in a higher amplitude of RMS AE signals and temperature on the advancing

side of the weld, while weld T3 resulted in lower temperature on the retreating side. It was observed that the higher temperature on the retreating side cannot be correlated with the recorded RMS AE signal. Based on the results obtained the following observations can be made; the temperature observed for the FSW process on the advancing and retreating side of the weld is dependent on the amount of plasticized material and the movement of material around the tool; the weld temperature cannot be directly correlated AE signals obtained from the tool-workpiece interface.

4.9   Repeatability of continuous AE monitoring method

This section discusses the repeatability analysis of the continuous AE monitoring setup and highlights its potential for real-time application. The welds from each welding trial (listed in section 3.8) that had no defects were selected to check for repeatability of AE based monitoring method. Similar to previous sections, the data obtained from the AE sensors are analysed using PSD and spectrogram. The weld parameters for the repeated welds are mentioned in Table 26 below.

Weld Number	Repeated Weld Number	Tool RPM	Tool Traverse rate (mm/min)	Tool tilt angle	Material thickness (mm)	Weld Length (mm)	Material Type
R1	T2	800	550	1.5°	5	360	AA6082
R2	LOP1	500	300	1.5°	5	250	AA5083
R3	LOP5	800	300	1.5°	6	250	AA5083
R4	D1	1200	550	3°	5	250	AA6082

Table 26: Parameters for the repeated welds in the phase

Since the welds are repeated, the force experienced by the tool should be of a similar magnitude. To further aid the repeatability of the dedicated FSW machine the average axial and traverse forces during the welding phase are compared in Figure 95 below.
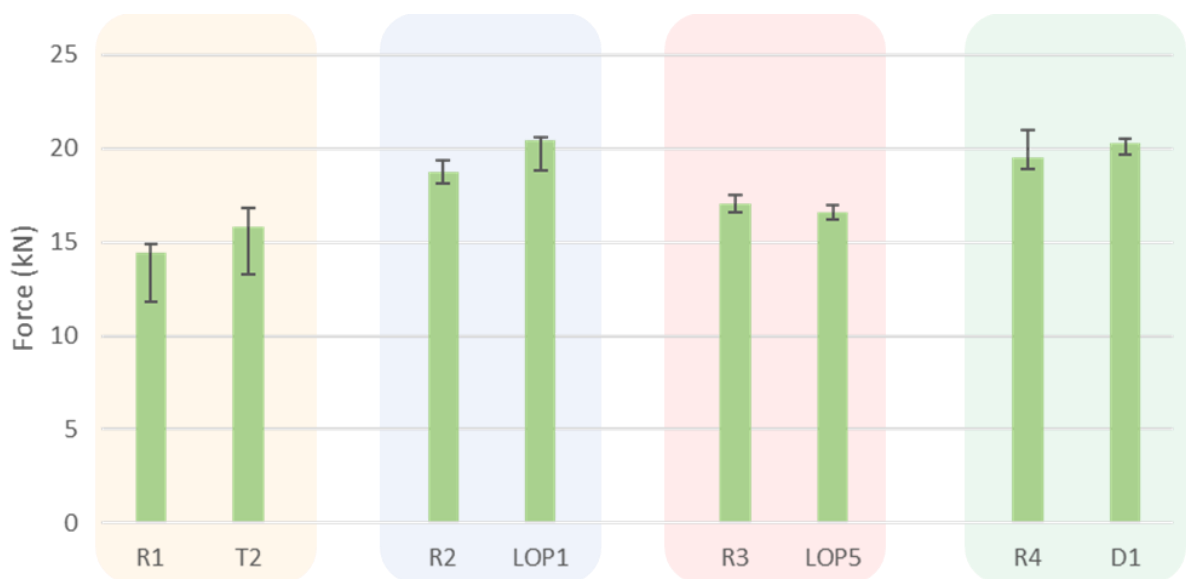
Figure 95: Average axial forces observed on the tool for repeated and previous welds

Figure 96 to Figure 99 compare the PSD plot obtained from the AE signals of sound welds discussed in the previous experimental phases and the repeated welds for this section. The y-axis represents logarithmic values of power spectral density with unit V^2/Hz and the x-axis represents the observed frequency in kHz. Similar to the PSD observed for welds D1 & D6 discussed in section 4.4.3, resonance peaks originating from the decoupler are observed in the PSD plots for the validation and original welds discussed in previous sections of this thesis. From the PSD the presence of the elemental frequency generated from repeated welds is confirmed.
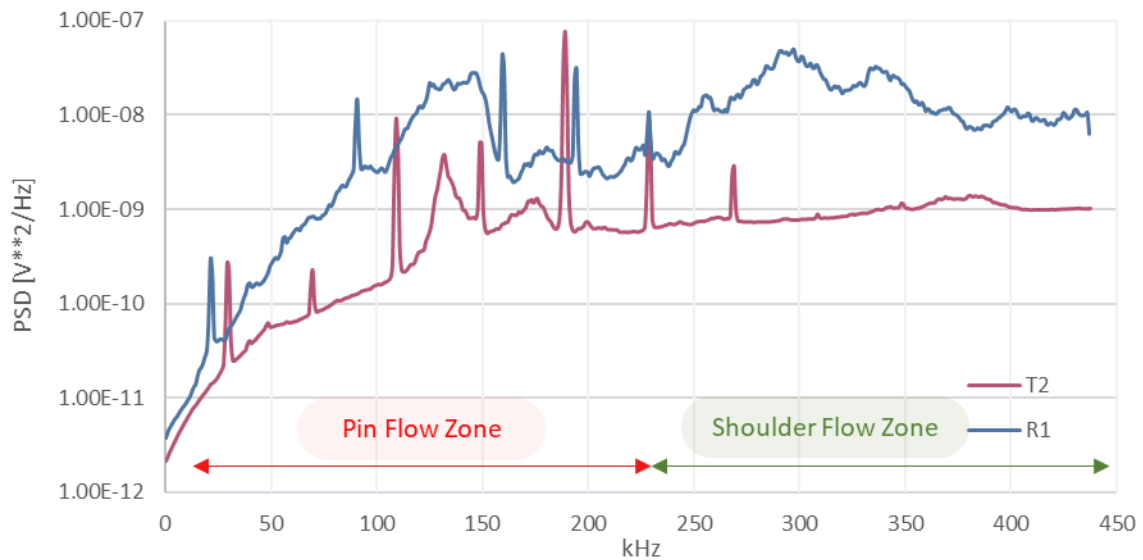
Figure 96: PSD plot obtained for weld T2 and the repeated weld R1
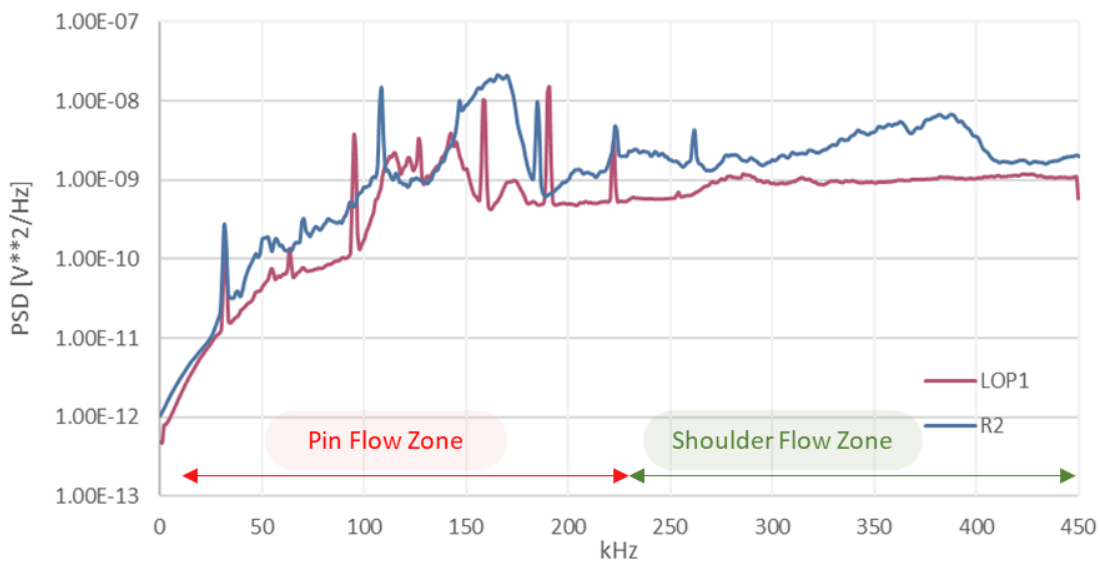
Figure 97: PSD plot obtained for weld LOP1 and the repeated weld R2
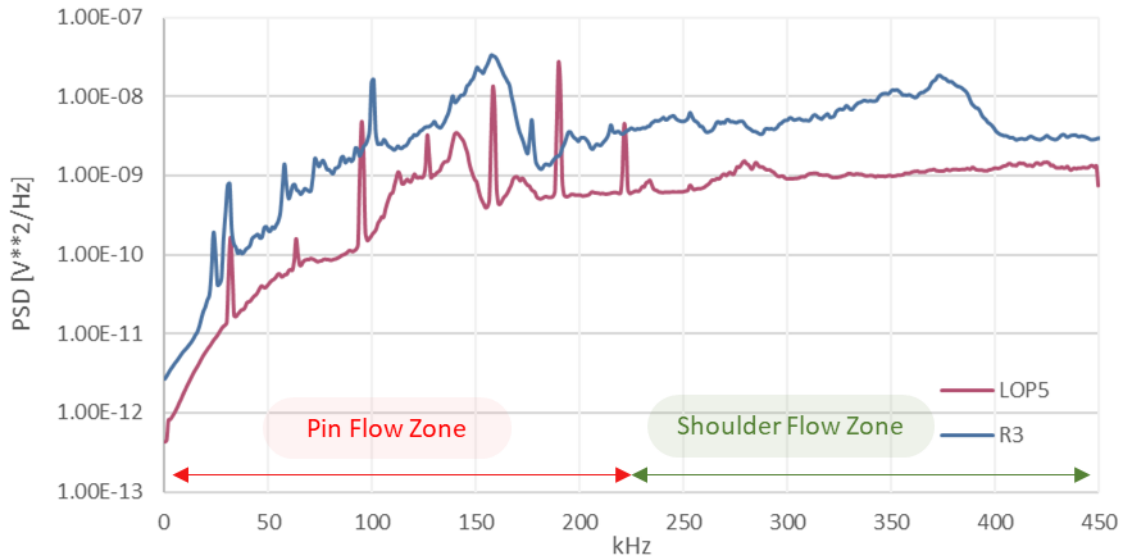
Figure 98: PSD plot obtained for weld LOP5 and the repeated weld R3
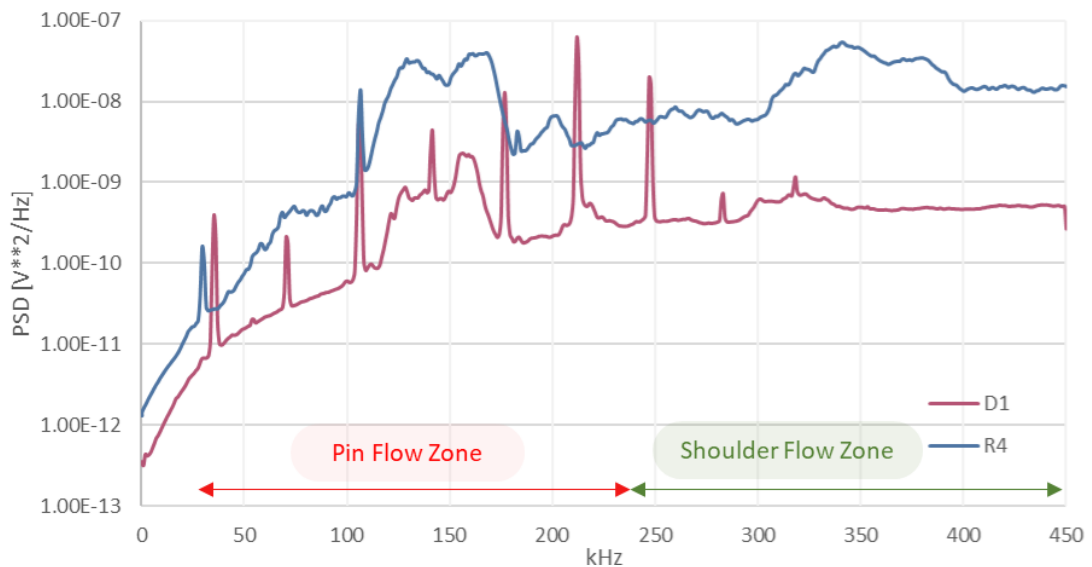
Figure 99: PSD plot obtained for weld D1 and the repeated weld R4

To analyse the effect of dry contact and couplant on the recorded acoustic emission for the FSW process, the welds R1, R2, R3 & R4 are performed using ultrasound couplant. Since the PSD plots define the signal's composition for a wide frequency bandwidth, the centroid of the spectrograms can be compared to determine the repeatability on the time scale. Utilizing Eq.(14) presented in section 4.3, the spectral centroid for the AE signal can be obtained from the spectrogram. Figure 100 to Figure 103 compares the standard deviation of spectral centroids plotted for a 5-second window of the welding phase for the welds discussed in this section.
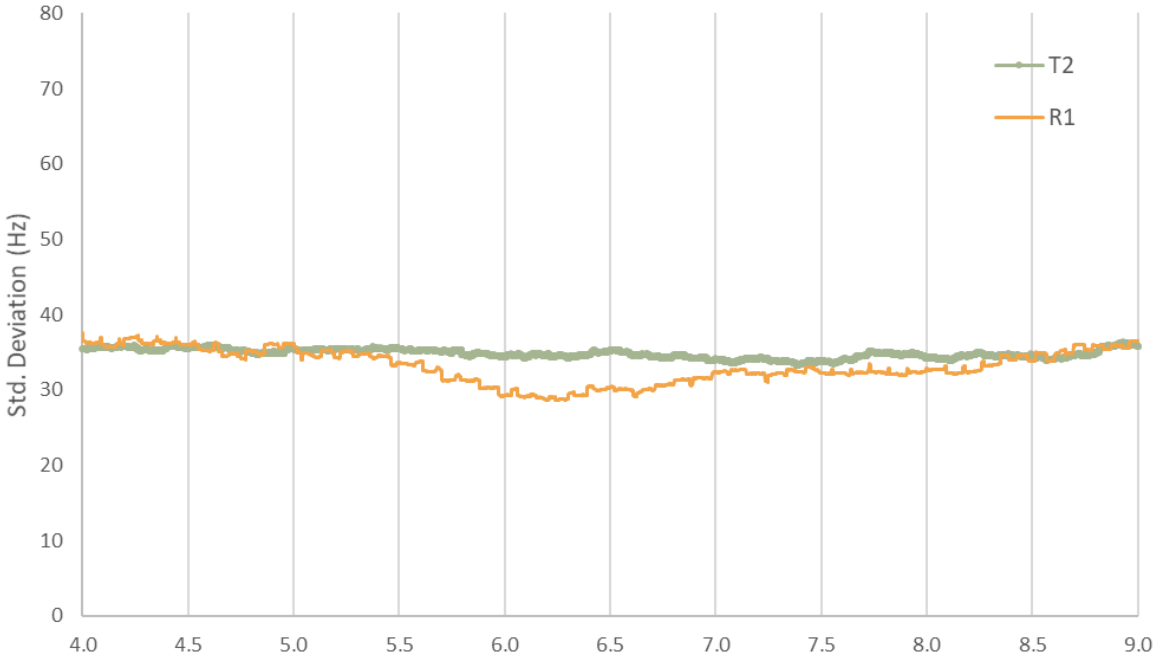
Figure 100: Spectral centroid plot for welding phase of weld T2 & R1
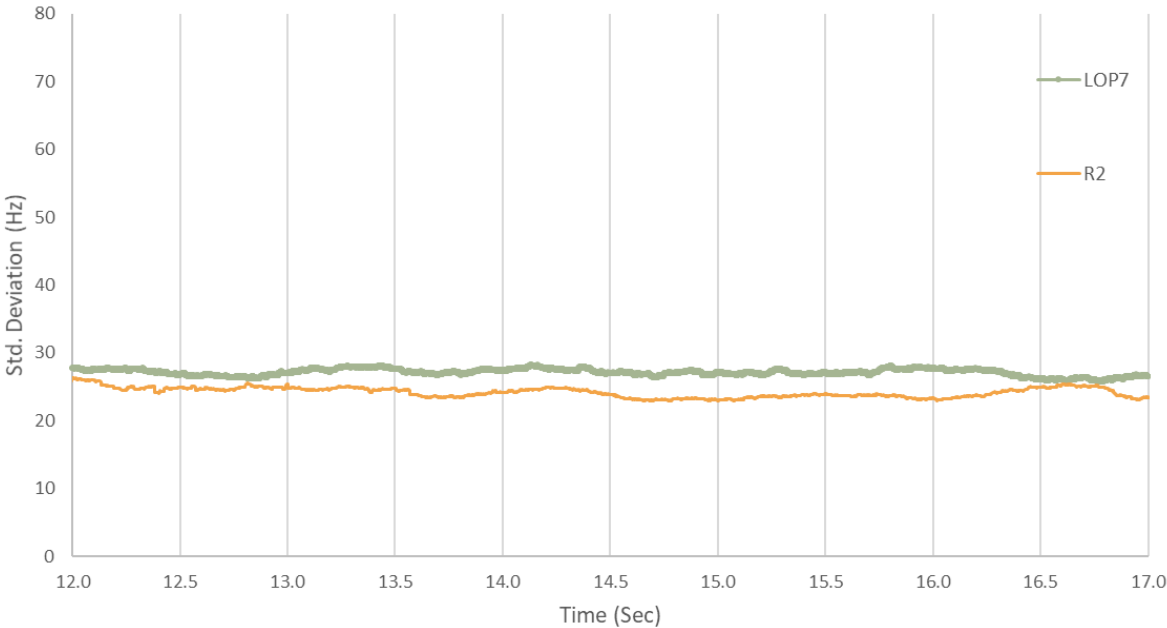
Figure 101: Spectral centroid plot for welding phase of weld LOP7 & R2
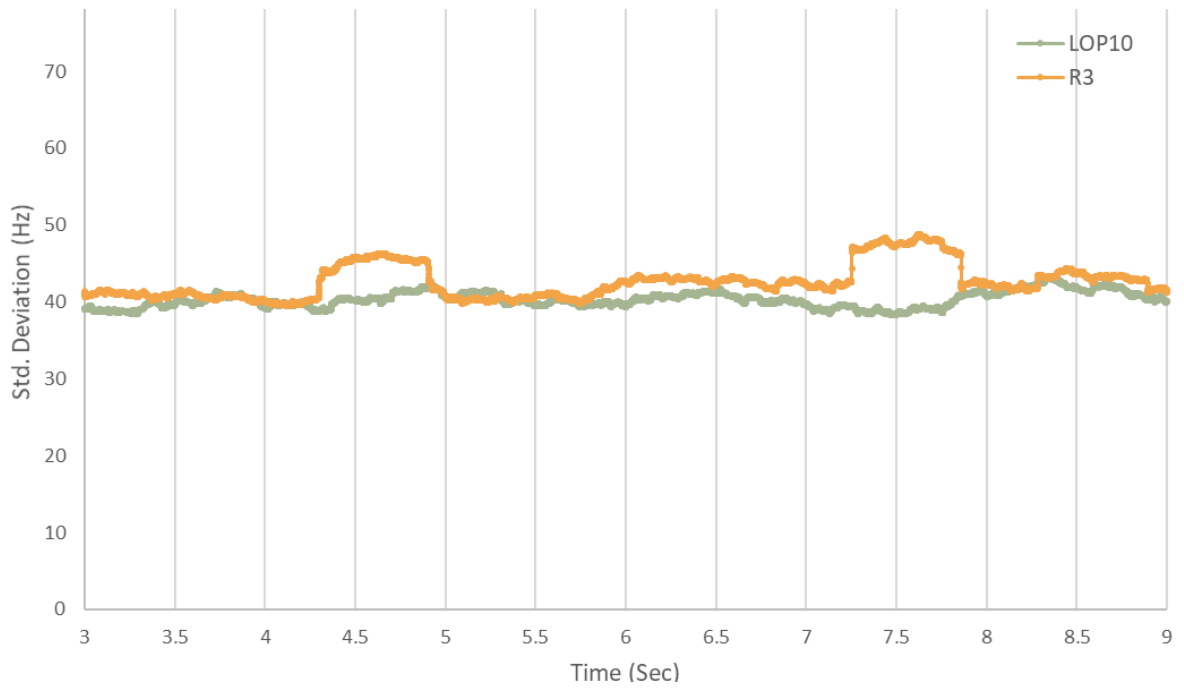
Figure 102: Spectral centroid plot for the welding phase of welds LOP10 & R3
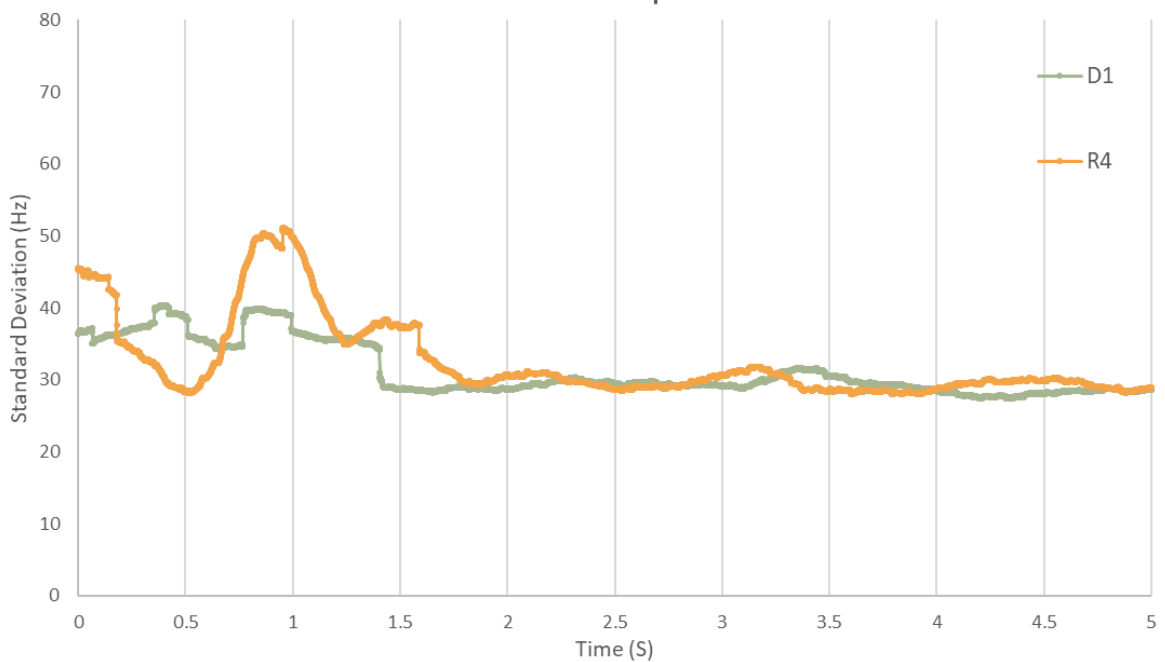
Figure 103: Spectral centroid plot for the welding phase of welds D1 and R4

From the PSD plots in Figure 96 to Figure 99, the repeated welds yielded a higher average amplitude of the power spectrum for the observed frequency range. This increase in amplitude is observed as a result of increased interaction between the welded plates and the measuring surface of the sensor due to the ultrasound gel couplant. In the case of dry contact, the micro air gaps presented at the interface of the

sensor and base metal reduce the amplitude of the generated shear waves. The peaks due to the electrical resonance of the decoupler yielded lesser profound peaks for the repeated welds (R1 to R4) while the welds discussed in the earlier sections of this thesis resulted in sharper peaks with higher amplitudes. As discussed in the earlier sections, the electric resonance peaks are observed as horizontal lines on the spectrogram and do not interfere with the AE observed for probe flow and shoulder flow. Since an increase in the amplitude is proportional along the observed frequencies, the repeatability analysis is further explored by comparing the spectral centroid of the monitored AE signal. Since the centroids are estimated with individual scales of different spectrograms, the approach of comparing the centroid further supports the repeatability analysis of the AE monitoring method. Using the Pearson correlation coefficient[132] defined in Eq.(16), the spectral centroid on a time scale can be compared to quantify the correlation. Where X_i and Y_i are the values in sample of both the dataset with $\bar{X}$ and $\bar{Y}$ as the mean of datasets. The correlation coefficient r compared for the spectral centroid of the AE signals from the discussed welds in Table 27.

$$r = \frac{\sum(X_i - \bar{X})(Y_i - \bar{Y})}{\sqrt{\sum(X_i - \bar{X})^2 \sum(Y_i - \bar{Y})^2}} \qquad [16]$$

Weld Name	Correlation coefficient
R1-T2	0.47
R2-LOP7	0.18
R3-LOP10	0.09
R4-D1	0.68

Table 27: Comparison of correlation coefficient of spectral centroids

From Figure 100 to Figure 103, it can be observed that the standard deviation of the spectral centroid for the original welds and the validation welds is comparable with a maximum variation of 7Hz observed in the case of material underpass. This is also reflected in the reduction of the correlation coefficient for welds R3-LOP10. The comparison of PSD and spectral centroids validates the repeatability of the continuous AE monitoring method. It can also be observed; that high amplitude and presence of

electrical resonance peaks do not affect the centroid of the individual spectrogram for original and repeated welds. In the abovementioned, the effect of the AE couplant is also highlighted which results in a higher amplitude of the characteristic frequency. It is concluded through the dry contact interface of the AE sensor the characteristic frequencies of the FSW process are not lost and the process can be effectively monitored by using wide-band AE sensors.

4.10 Summary of observations

This chapter of the thesis addressed the ability of continuous acoustic emission monitoring to detect the presence of defects in the FSW process. This chapter underlines the advantages of AE-based monitoring over force monitoring methods to detect FSW defects and flaws summarized in Table 28 below. It is concluded that AE based monitoring method is more sensitive to detecting defects and gives evidence for the application for online FSW monitoring.

Defect/Flaw	Force monitoring	Continuous AE monitoring	Observations
Presence of material disruption	Force monitoring of FSW can effectively detect the presence of material disruption limited to mass material disruption.	Continuous AE monitoring of the FSW process enables detection of the presence of mass material disruption and events of tool shoulder material underpass.	The observed frequency bandwidth determines the ability to detect the events of material disruption.
Lack of plunging pressure from tool shoulder	The lack of tool plunging pressure for different weld parameter combinations cannot be observed through force measurement.	Continuous AE monitoring enables detection of the lack of tool shoulder pressure by observing shifts in peak frequencies in the range of 250kHz to 450kHz	The detection of the shift in peaks is limited by the range of observed frequency.
Presence of sub-surface voids	Force monitoring for sub-surface void detection is limited by prior knowledge of force signature for a particular weld.	The sub-surface voids were detected through the observation of unique patterns in the spectrograms, enabling greater confidence in decision-making.	The unique pattern is observed from lower(50kHz) to higher (450kHz) which reduces the need for high bandwidth sensors.

| Lack of penetration of tool (LOP) | Welds performed with similar weld parameters for different plate thicknesses result in similar force signatures making LOP un-detectable through force monitoring | The LOP is detected by analysing the spread of frequencies in the spectrogram through spectral centroids during the welding phase. | The method is based on comparative waveform analysis of AE signal and is limited to a particular grade of aluminium (i.e.-AA5083-H11) It is also limited in terms of applicability as the method depends on prior knowledge of the percentage variance of the welds. |

Table 28: Summary of observations for results discussed in Chapter 4

5. Results of CNN classifiers

This section of the thesis expands on the results obtained during the training and testing of the proposed dual input CNN architectures discussed in the earlier sections of this chapter. For the testing of the models, the spectrograms and mel-spectrograms obtained from the AE of validation welds are used. Since the proposed architectures cannot be compared with original architectures in terms of size due to the dual input, the time taken to reach the highest accuracy is estimated and compared with the parent architecture (Discussed in section 5.6).

5.1 Exploration vs exploitation of training data

The coefficient of variance (COV) for the four classes of the training composing of mel-spectrogram are illustrated below in the Figure 104. The vertical axis represents the COV while the horizontal axis represents the individual spectrogram in the dataset.
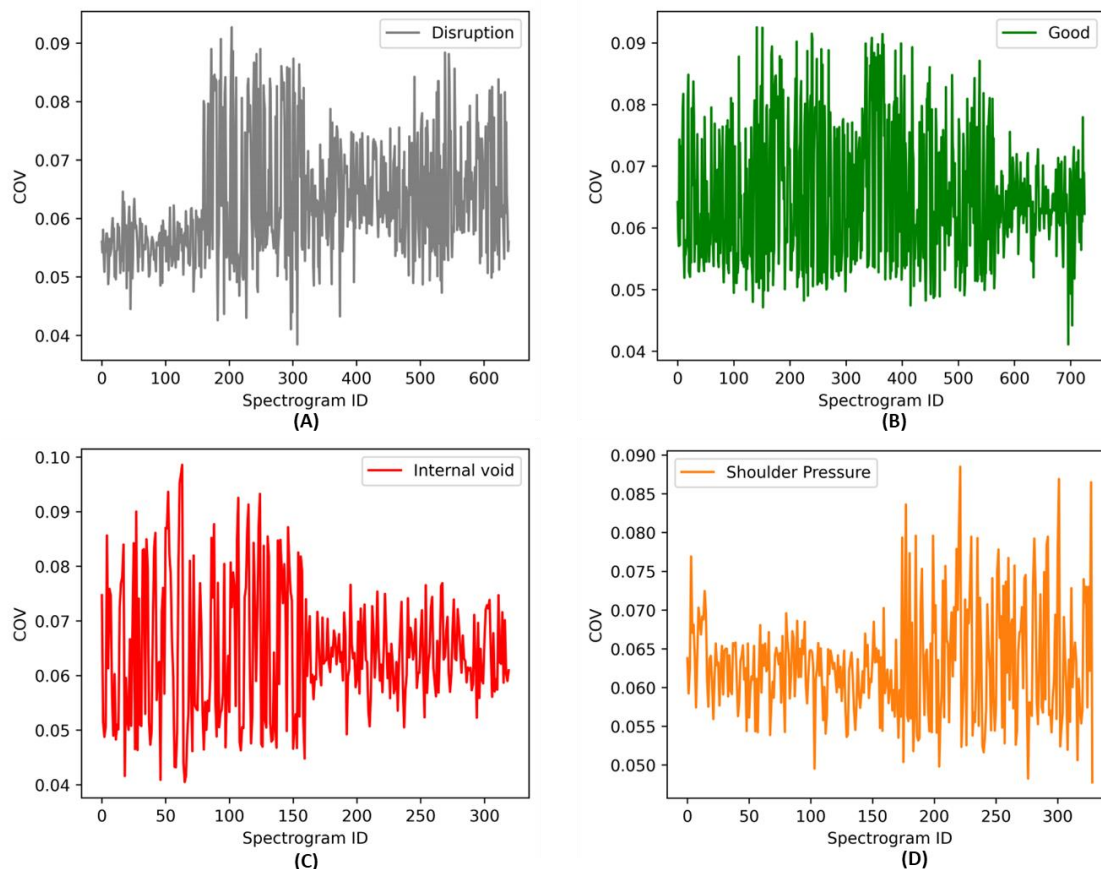
Figure 104: Coefficient of variance for (A) welds with disrupted material flow; (B) sound welds; (C) Welds with internal voids; (D) Welds with lacking forging/shoulder pressure

From the plots above the variance in the input dataset can be visualized for each category of the input data. The maximum variance was reported for welds with internal

void and least variance was reported for welds with reduced shoulder pressure in the Figure 104(C) and Figure 104(D). An average of 6% COV is reported for the combined input dataset which is marker of variability in the input dataset. It is also observed that no trend in the COV is observed throughout the input dataset. The abovementioned observations imply that through instating variance through the data augmentation method, a sufficient degree of exploratory data is introduced during the training process. It should also be highlighted that while the exploitation aspect of the dataset focuses on frequency recognition from the training data, the exploratory data is generated through the augmentation method. The performance of the proposed CNN architectures below highlights the effectiveness of the training data.

5.2 Binary classification using the VGG-16 inspired CNN architecture

The VGG-16-inspired classification model discussed in section 3.10.1 was trained using mel-spectrograms to classify the welds binarily into good and bad welds. The selection of welds for binary classification of the weld quality can be further explained in Table 29 below.

Good Welds	**Defective Welds**
No subsurface cavities	Sub-surface cavities
Complete penetration of the tool	Material disruption
No material disruption	Incomplete penetration of tool

Table 29: Selection criteria for binary weld quality classification

The training data consisting of a total of 3,918 labelled mel-spectrogram is divided into two categories with 2585 and 1333 mel-spectrograms in each category. For training the model the training and validation dataset is split into 85% and 15% while for the test dataset, welds other than the training dataset are selected. While loading the mel-spectrograms for training, a single channel of the image data was selected to reduce the computational cost of the model. The training process of the model can be visualized using the accuracy and loss plot in Figure 105. For the training, a batch size of 64 with 60 epochs was found to be optimum for a stable training process without overfitting the model.
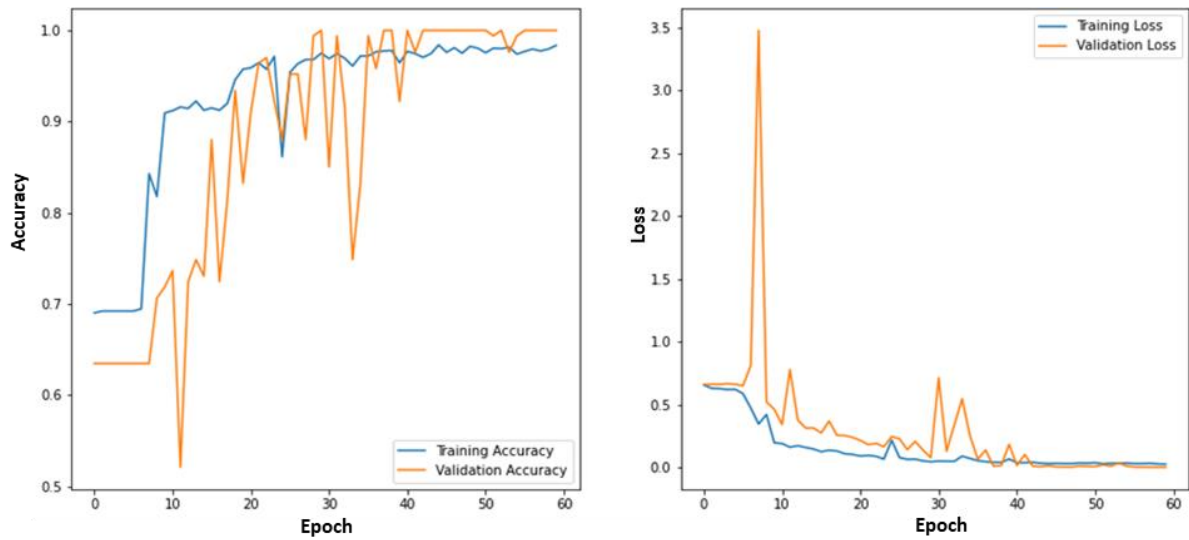
Figure 105: Training accuracy and loss plots for VGG-16 inspired model

The trained model was observed to have an accuracy of 98.5% and to estimate the accuracy of the trained model for unseen spectrograms, the classification from the test dataset is introduced to the model. The classification report of the model obtained from the test data is defined in Table 30 below.

	Precision	Recall	F1-score	Support
Good Weld	1	1	1	306
Bad Weld	1	1	1	533
Accuracy			1	839

Table 30: Classification report obtained for VGG-16-inspired CNN model

The proposed VGG-16-inspired network has 67% fewer trainable parameters compared to the conventional VGG-16 network. With the reduction in the number of trainable parameters, the time utilized for training and memory usage also reduces making the network ideal for training with spectrograms obtained from different cases of tool and workpiece material.

131

5.3   Sparse classifier using VGG-16 inspired CNN architecture

Section 3.10.1 also discusses the VGG-16-based sparse classification model for weld quality. The same architecture is extended to multiple outputs that are implemented for sparse classification specific to the type of defect and flaws. The sparse classification model utilises mel-spectrograms obtained from the welds discussed in section 3.8 of this thesis. The welds are classified into 4 labels; sound welds, generation of excess flash, presence of internal void and lack of tool shoulder pressure. With a batch size of 16 and the standard gradient descent (SGD) as the optimizer, the model is trained with a dataset of size of 1.4GB. The training process of the model can be visualized by using Figure 106 below.
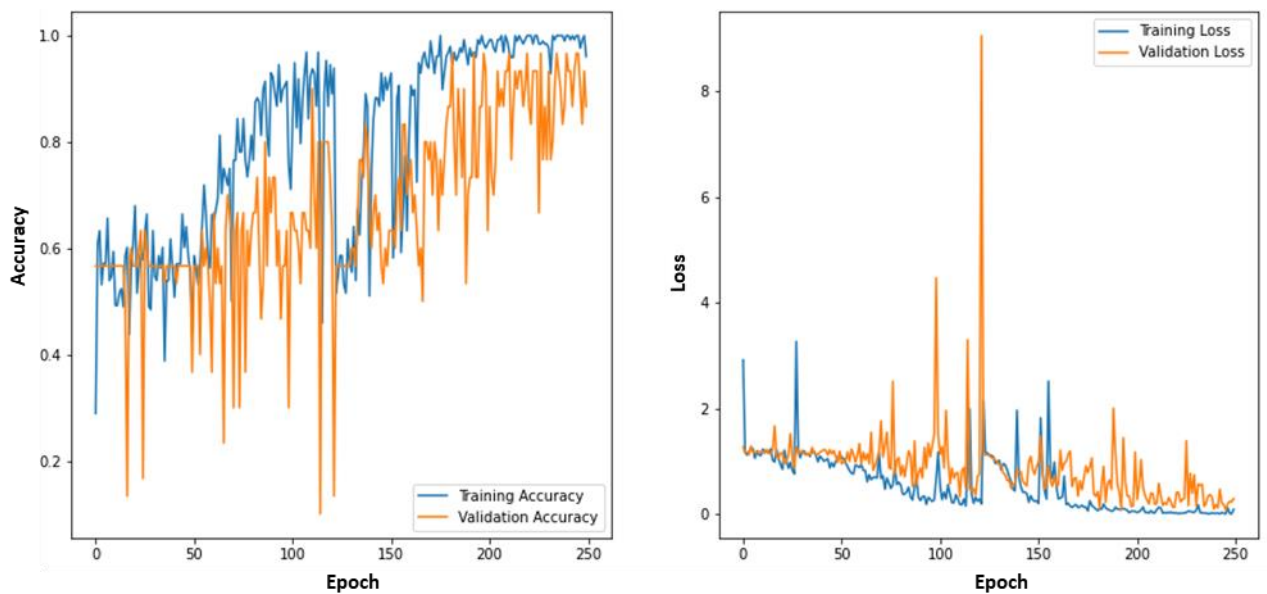
Figure 106: Training accuracy and loss plots for VGG-16 inspired model for sparse classification

	Precision	Recall	F1-score	Support
Excess Flash	0.5	1.0	0.67	1
Good	0	0	0	1
Internal Void	1	1	1	1
Shoulder Pressure	1	1	1	1

Table 31: Classification report obtained for VGG-16 inspired CNN model for sparse classification

SGD is found to be optimized to achieve accuracies of above 90% for the dataset and the hyperparameters. Unlike the binary classification, the training process visualized in Figure 106 is found to be more stable. The model is tested using the AE data collected from the validation welds discussed in section 4.7 and the sound welds in chapter 4. The accuracy of the model on the test data can be defined using the classification report. It is observed that the proposed VGG-16-inspired network can classify the welds with internal voids, lack of shoulder pressure and no defects with F1-score of 1, while a significant drop of 33% F1-score is observed while identifying welds with flash.

From the training process plots in Figure 106, it can be observed that the loss and accuracy are not stable, unlike the training of the binary classification model. This indicates a lack of confidence in the classification model. From Table 31 it can be observed that the proposed classification model in this section has difficulties in distinguishing sound welds from welds that generated excess flash due to high tool tilt angle. This lack of accuracy can be traced to the loss of the characteristic features from the mel-spectrogram generated by flash formation. This observation highlights the need for a hybrid input model with mel-spectrogams and spectrograms as spectrograms are more efficient in tracing the material disruption.

5.4   Sparse classifier using Inception-inspired CNN architecture

The typical Inception model is discussed in section 3.10.2 of this thesis which takes single image input. The proposed model illustrated in Figure 36 and Figure 37 utilizes hybrid input (i.e.- mel-spectrograms & Spectrograms) to extract the features by convolution.

With the observations from the sparse classification model in the earlier section, the proposed model in this section utilizes hybrid input from the mel-spectrogram and spectrogram to compensate for lost features from a single input model. The results obtained from the training process for the two proposed models (i.e.- version 1 & version 2) are illustrated in Figure 107 & Figure 108 below.
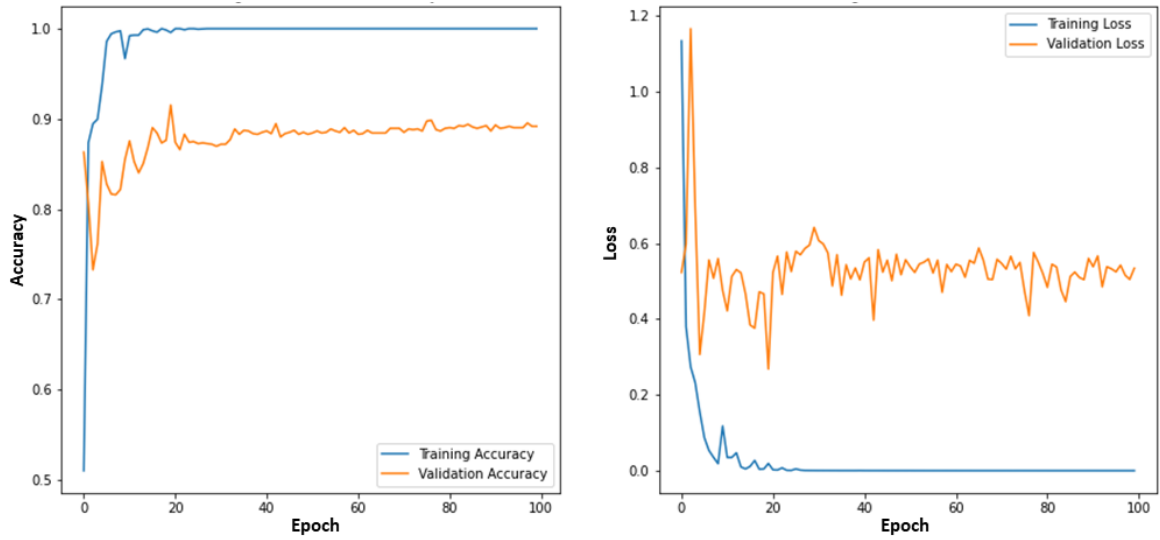
Figure 107: Training process of inception inspired sparse classifier version 1
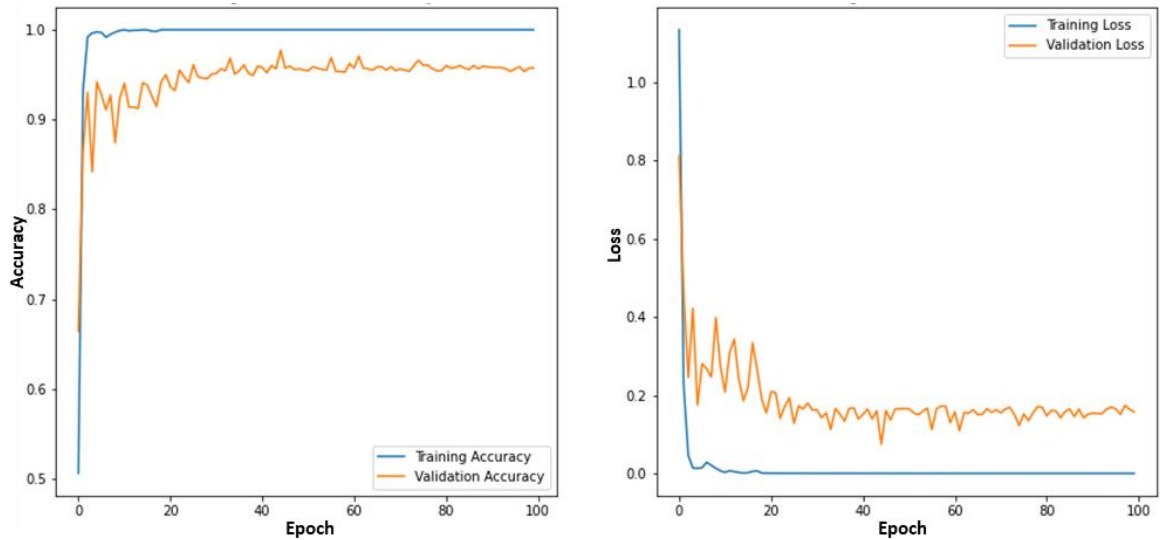
Figure 108: Training process of inception inspired sparse classifier version 2

To assess the proposed model performance, the confusion matrix for the true labels and the predicted labels is plotted in Figure 109 and Figure 110 below. The labels from 0 to 1 correspond to welds categorized in material disruption, sound weld, Subsurface void and lack of shoulder pressure respectively. The number of input spectrograms is measured by the bar scale on the right of the confusion matrix plot. Higher accuracy of the model can be visualized in the confusion matrix through minimal spread of classification.

134
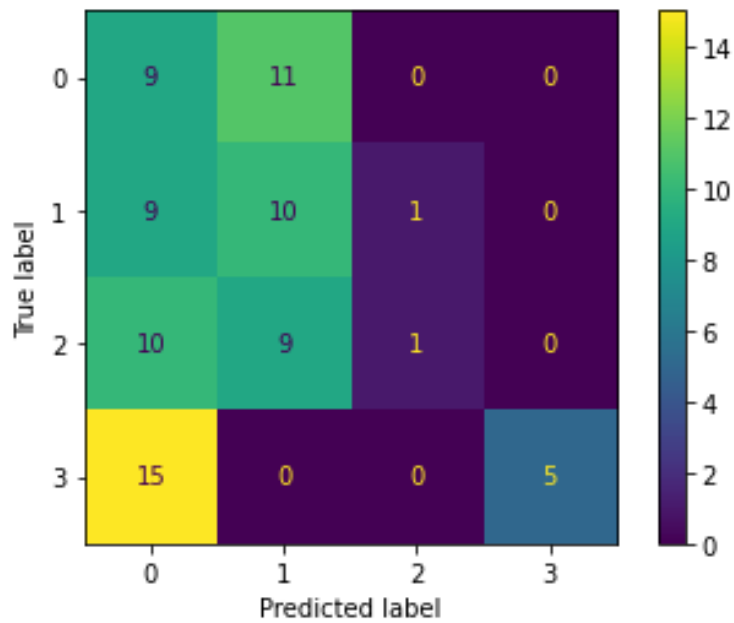
Figure 109: Confusion matrix obtained for inception-inspired sparse classifier version-1
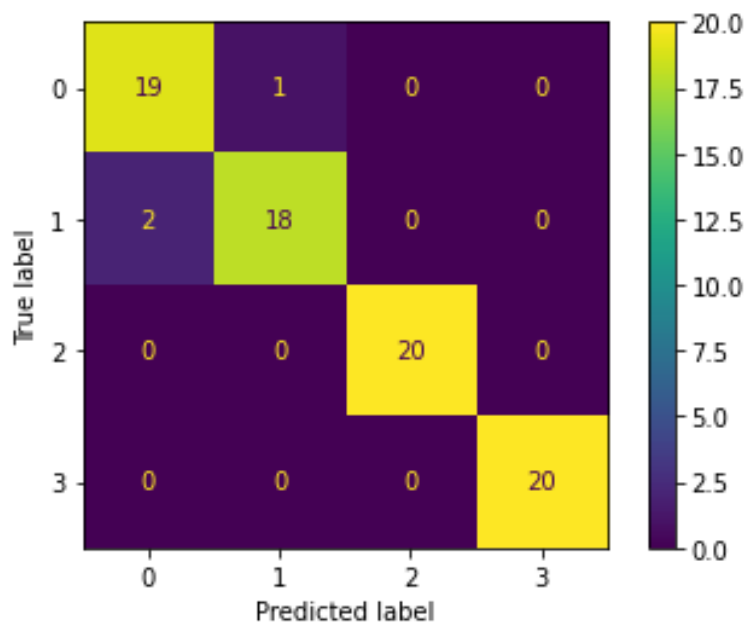
Figure 110: Confusion matrix obtained for inception-inspired sparse classifier version-2

From the observed confusion matrices for both proposed models, it is observed that version-1 of inception inception-inspired classifier has difficulties classifying the weld spectrograms with defects and flaws and classifies them wrongly into sound welds and welds with disruption. A similar instability is reflected in the training plots for accuracy and loss in Figure 107. The training plot for the second version of inception inception-inspired model in Figure 108 reflects a stable training process without any loss peaks due to overfitting or bad local events. From the classification report, it can be observed

that the model performed significantly better in distinguishing sound welds from welds with defects and flaws.

5.5   Sparse classifier using Resnet-inspired CNN architecture

Section 3.10.3 of this thesis discusses the typical residual network and the proposed residual learning model. The model used the same training data as the models discussed in the previous sections of this chapter. The training process for the model is visualized through the accuracy and the loss graphs in Figure 111. From the confusion matrix obtained from the test data for the proposed model in section 3.10.3, it was observed that the model performed significantly better with a reduction in the learning rate and an increase in the training epochs. A model trained with 60 epochs yielded a training accuracy of 89% while increasing the training epochs increased the training accuracy to 97%.
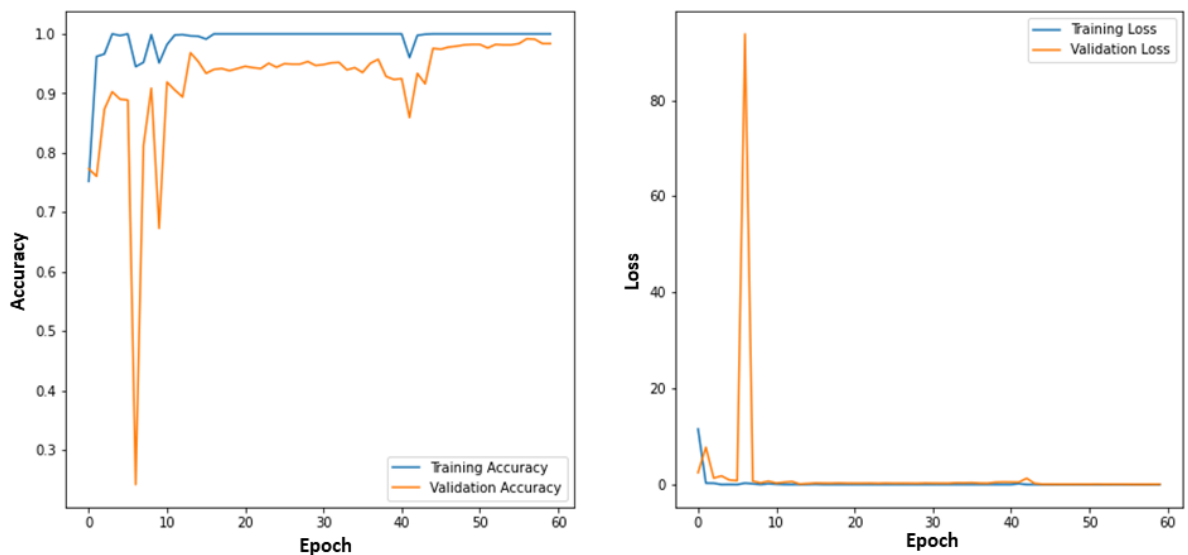
Figure 111: Training process of residual inspired sparse classifier
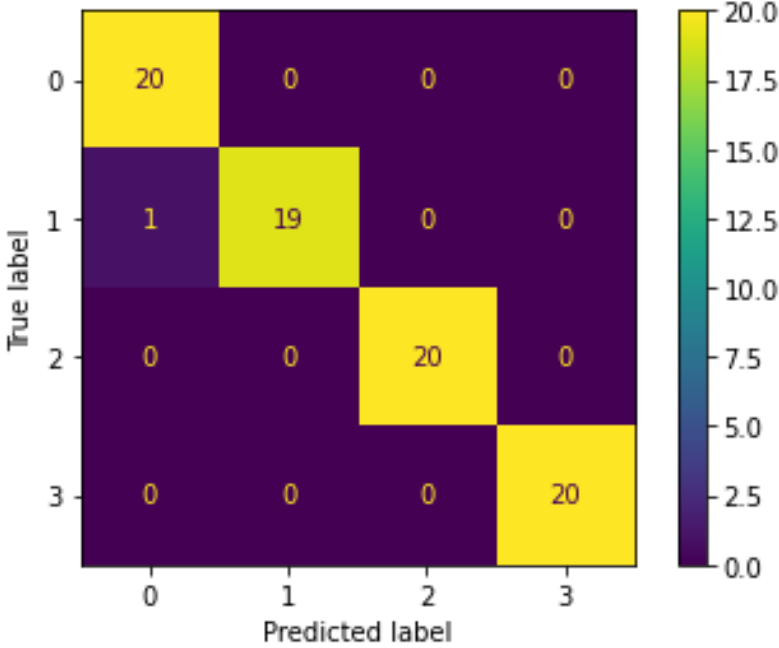
Figure 112: Confusion matrix obtained for residual learning-based model

The labels mentioned in the confusion matrix from 0 to 3 correspond to labels; material disruption, sound weld, subsurface void and lack of shoulder pressure respectively. It can be observed that the model performs better in terms of classifying welds between the presence of material disruption and sound welds.

5.6 Performance analysis of the proposed models

The earlier sections focus on the stability of the training process and the accuracy of the proposed models. Since the size of the proposed architecture cannot be compared to the parent architecture due to higher dual input increasing the overall size of the model, the performance of the proposed architecture is compared through training epoch and time consumed to achieve the maximum accuracy. The key observations for the proposed and parent architecture are presented in Table 32 below. It can be observed that the proposed parent architecture-inspired models have significantly fewer parameters utilizing lesser memory compared to parent architectures. It is also observed that the proposed models also yield higher accuracy compared to the parent architecture.

	No. of parameters	Max accuracy (Training)	Epoch/Time
VGG-16	Parent Architecture (23,206,276)	93.6%	60 / 105mins
	Proposed Architecture (19,303,044)	95%	60 / 35mins
Google le net/ Inception	Parent Architecture (23,552,708)	94%	60 / 44mins
	Proposed Architecture (18,868,268)	96%	60 / 22mins
Residual model	Parent Architecture (64,997,364)	Out of Memory	NA
	Proposed Architecture (9,997,508)	98%	60 / 34mins

Table 32: Performance analysis for the parent CNN and the proposed CNN architectures

5.7 Summary of observations

The results obtained from the trained model on the test data are discussed in sections 5.2 to 5.6 and are summarised in Table 33 below, highlighting the key features of the proposed architecture and the observations during the training and testing process. The observations from training and testing of the proposed CNN models outline the potential for online weld monitoring applications. Sparse classification accuracy of up to 98% is reported with the reduced model size making the proposed hybrid Resnet model an excellent model for AE-based weld classification system.

Parent architecture	Proposed architecture	Observation
VGG-16 Network	The proposed architecture utilizes 17% fewer trainable parameters offering 3% higher maximum validation accuracy achieved during the training process.	The loss and accuracy observed during the training process resulted in higher variance highlighting the instability of the process. The maximum accuracy achieved for binary and sparse classification are 99% and 94% respectively.
Google Le Network	The two proposed architectures are based on the Naive version and dimensional reduction version elemental blocks. The proposed dimensional reduction version offers a 20% lesser number of parameters to the parent architecture.	The loss and accuracy observed during the training process resulted in minimum variance and a stable training process. Two proposed architectures for naive and dimensional reduction elemental blocks resulted in a maximum accuracy of 90% and 96% respectively.
Residual Network	The original model could not be trained using the original 10-layer Resnet model due to lack of memory. The proposed model consisted of a lesser number of layers and filters resulting in an 80% lesser number of parameters.	The model achieved maximum accuracy of 98%. The proposed model reached the highest accuracy compared to the other proposed architectures with the same dataset.

Table 33: Summary of proposed models with observations

5.8 Proposed integration of AE and ML for FSW control system

The results obtained from the trained model highlight the potential for accurate classification of the weld quality through measuring acoustic emissions of the FSW process. This section underlines the potential of a close-loop monitoring system using CNN and AE signals. Chapter 4 of this thesis discusses the ability of the AE monitoring system to detect the presence of FSW defects and flaws while Chapter 5 highlights the ability of CNN to classify the welds corresponding to the type of defect.

Based on the observations from the last two chapters discussed in sections 4.10 & 5.7, an AE and ML integrated weld monitoring system is proposed as the building block of real time control system for the FSW process. The proposed integration consists of two phases focusing on data recording and processing illustrated in Figure 113. The first phase of the recording phase consists of the sensor setup, analogue to digital (AD) conversion and de-noising of the selected dataset for the desired time. Based on the observations from Chapter 4, the estimated time of 1.2 seconds is reported for the recording of the AE signal recorded over a duration of 2 seconds. The processing phase consists of visualization of AE signal through spectrograms, anomaly detection and prediction of optimized parameters. Chapter 5 of this thesis underlines the time consumed by the CNNs to analyse the spectrograms and identify the defects. Following the time observation, the estimated time for processing of the AE signal recorded for a window of 2 seconds can be projected as 1.5 seconds.
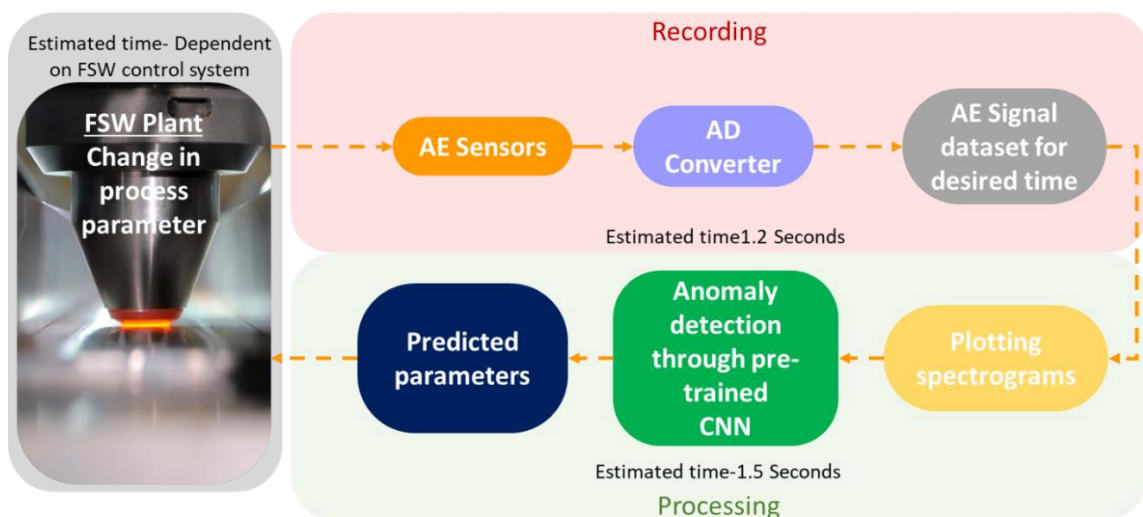
Figure 113: Proposed integration of AE monitoring & ML for FSW control system with processing times

The time consumed by the FSW plant to change the weld parameters is dependent on the type of control system. The total time consumed by the proposed integrated system is estimated to be 3 seconds considering signal recording and processing. In Chapter 4 the ability of the continuous AE monitoring method to detect the characteristic frequencies for the FSW process is highlighted. The time utilized for the generation of optimized parameters can be reduced by monitoring a narrower frequency bandwidth. Using the narrow frequency band sensor of the desired frequency range (obtained from cont. AE monitoring with wide band sensor) with the appropriately trained model, the time utilized by the first and second phases can be further reduced.

The average tool travel rate of the welds discussed in this thesis can be estimated to be 500mm/min. Considering the time expended by the proposed integrated system to generate the optimized weld parameters the tool would move a distance of 25mm till the optimized parameters are fed to the control system of the FSW plant at the given speed. Considering the nominal length of welds and the tool traverse speed the potential of the proposed weld monitoring method is highlighted through key points below.

- The methodology for the proposed integrated system is directed to be used for real-time monitoring of FSW to reduce the lead times for the welded parts and generation of waste material.
- Chapter 4 gives the preliminary evidence of the transferability of knowledge between different material grade 4. This highlights the potential applicability of monitoring the FSW process for different material grades of the same material.
- The evidence obtained from section Chapter 5 illustrates the ability to classify weld defects and flaws with high accuracy. Following a similar methodology, this system would enable the detection of welding defects and flaws along with the generation of corrective signals according to the type of defect or flaw to maintain the weld quality.
- The proposed integrated monitoring system would also enable the localization of defects and the ability for post-weld inspection if the corrective signal fails to maintain the weld quality.
- This thesis also presents an initial data management framework between the recording and processing phases which can be further improved and utilized to reduce the time consumption of the monitoring system.

6. Conclusions

The ability to manufacture complex parts is limited by the flexibility of conventional manufacturing systems and this thesis aims to address the key challenges faced by the FSW industry. The FSW process is a complex thermomechanical process which involves multiple intertwined phenomena. This thesis explores the key process parameters of the FSW process through AE monitoring. The work presented in this thesis illustrates the correlation between the AE signals and the material flow observed for the conventional FSW process. The presented work underlines the ability of AE monitoring to detect the presence of commonly occurring FSW defects and flaws. The key challenge faced by FSW is the inability to monitor the weld quality of FSW joints without post-weld inspections. This aim is achieved through the development of an online in-situ AE signal-based weld monitoring system. The thesis also highlights the advantages of the AE monitoring method over the conventional force monitoring method for weld quality assessment. To conclude, the findings of the study and the research questions (RQ) highlighted in section 1.3 are answered below.

RQ1: Can AE signals be correlated to FSW stages and observed forces?

Sections 4.3 and 4.4 outline the parametric and waveform analysis of the AE signals obtained from the welds performed with increasing tool RPM. The waveform analysis of the AE signal was performed by plotting the spectrogram from the recorded AE signals. The standard deviation of the axial force and spectral centroid of the spectrogram is compared to corelate the force and the AE signals. Based on the peaks observed from standard deviation plots, a good correlation between the datasets is observed. Furthermore, it is observed that the AE signals were sensitive to events of material underpass observed at the tool shoulder. The events of material underpass are also reported in sections 4.6 and 4.9. It is concluded that the results and observations from sections 4.3 and 4.4 of this thesis address RQ1 and the stages of the FSW process can be observed through AE-based monitoring. The abovementioned sections also provide evidence of higher sensitivity of cont. AE monitoring for FSW process events compared to the tool force monitoring method.

RQ2: How placement of the AE sensor affects the recorded AE signature of the FSW process?

Section 4.3 highlights the effect of sensor placement on the recorded AE signals of the FSW process. Through the parametric analysis of the AE signals obtained from the

welds it is observed that with increasing RPM, the RMS values of AE signals also increased. An opposite behaviour of AE signals was observed when the sensor was placed on the machine bed which confirms the phenomenon of AE signal damping caused by the viscous stir zone. The thesis also highlights how a lack of penetration defect can be effectively captured by changing the layout of the sensor setup.

Three combinations of AE sensor setup are discussed in section 2.9 of this thesis to detect the presence of different types of FSW defects and flaws. Section 4.4 gives evidence of the detection of sub-surface voids through the recorded events of high shearing using combination-1 of sensor setup. Section 4.5 is focused on the detection of AE frequencies originating from material flow around the FSW probe(50kHz to 250kHz) highlighting the ability to detect a lack of pressure from the FSW tool shoulder. Section 4.6 gives evidence of detection of lack of penetration through comparative analysis of percentage variance for a range of RPM observing the effect of damping by the increased stir zone by combination-3 of sensor setup. This phenomenon is also explored using parametric waveform analysis in Sub-Section 4.3.1.

The abovementioned observation from Chapter 4 supports the importance of AE sensor placement to capture different phenomena involved in defect formation. It is further deduced that the ability of the AE monitoring method to detect FSW defects is also dependent on the sampling rate of the data acquisition system.

RQ3: Can material flow disruption be measured through AE monitoring?

Sections 4.4 and 4.5 of this thesis discuss the methods of introducing artificial material disruption in the material flow around the tool. The material disruption discussed in section 4.4 is caused by the introduction of holes in the joint lines. It was observed that both force and AE signals were able to localize the location of the point of material disruption in the joint line. It was also highlighted that with a reduction in the observed frequency range, the capability of the AE signals to detect a lack of material flow around the tool also reduces. Furthermore, it was observed that the holes in the joint line lead to underfill due to the lack of material which is unacceptable to the FSW ISO standards. A periodic pattern of vertical lines was also observed at higher frequencies (100kHz to 400kHz) in the spectrograms correlated to the traces of flashes on the flash generated on the top side of the weld. From section 4.4 it can be concluded that the proposed AE monitoring method is sensitive to detect the change in material around the FSW tool due to its ability to monitor 1st degree process parameters. While section 4.4 outlines the effect of abrupt material disruption, section 4.5 highlights the material disruption

caused due to the lack of plunging pressure. Section 4.6 utilizes the AE sensor placement to measure the lack of penetration gives evidence of the capability of cont. monitoring method to measure partial penetration of the FSW tool.

RQ4: How sensitive is continuous AE monitoring to changes in process parameters for the FSW process?

The sensitivity of the AE monitoring method to detect changes in process parameters is widely discussed in chapter 4 of this thesis. Sections 4.3, 4.4 and 4.5 compare the advantages of AE-based monitoring over force monitoring. The ability of the AE monitoring method to detect material flow events like shoulder material underpass which are not observable through the existing force monitoring is reported in section 4.4. The event of the material underpass at the interface of the tool shoulder and workpiece is visualized through periodic vertical lines between 80kHz to 260kHz. This periodic behaviour is linked to the deposition of plasticized material ahead of the tool mentioned in Section 4.5. Furthermore, Sections 4.5 and 4.6 give evidence for the ability of the AE monitoring method to detect the presence of a lack of plunging pressure from the tool shoulder and lack of penetration during the FSW process. An 80kHz shift in frequency is reported between 250kHz to 400kHz for the weld with reduced tool shoulder engagement or pressure. It is also observed that Considering the evidence provided in Chapter 4, it is concluded that the proposed cont. AE monitoring method is sensitive to the changes in FSW process parameters and offers high potential for online weld monitoring.

RQ5: Can continuous AE monitoring detect the presence of FSW defects & flaws?

The type of defects and their acceptability according to the ISO standards are mentioned in section 2.8 of this thesis. Sections 4.4, 4.5 and 4.6. discuss the implementation of continuous acoustic emission monitoring to detect welding defects and flaws observed in the friction stir welding process. The ability of continuous AE monitoring methods to detect excess flash flaws and surface lack of fill defects caused by material disruption is confirmed in section 4.4.1. It is observed that the generation of flash is due to the accumulation of plasticized ahead of the tool which is moved to the side resulting in the generation of flash segments. This event is observed on the spectrogram through higher peaks between 50kHz-250kHz. Sections 4.4.2 and 4.7 of this thesis confirm and give evidence of the ability of continuous AE monitoring to detect the presence of internal cavity defects observed for the FSW process. It is

observed that the sub-surface cavities are formed due to the disrupted mixing of two flow zones due to reduced weld temperature at the tool probe. These events of high shearing are visualized through a spectrogram with high amplitude peaks ranging from 50kHz to more than 225kHz. The ability of the continuous AE monitoring method to detect the presence of a lack of penetration through parametric analysis is highlighted in section 4.6. It is observed that the proposed sensor setup (combination 3) was successful in detecting increased percentage variance for AE signals generated during the welding of plates with higher thickness.

Based on the evidence discussed in the above-mentioned sections, it is concluded FSW defects and flaws that can be effectively detected through cont. AE monitoring are limited by the intensity of the defects. As the generation of flash cannot be quantified, it is concluded that the flash generated due to a high tool tilt angle of 3° can be effectively monitored. For welds with the presence of internal voids, a minimum of 2.43mm wide voids can be detected effectively The FSW defects discussed in this thesis can be visualized through spectrograms obtained from the AE signals with an exception of LOP defect. The LOP defect is detected through comparative analysis of the deduced parameters of the spectrogram. It is concluded that the welds with 1mm LOP defect can be effectively detected using AE signals.

RQ6: How reproducible and reliable is the proposed ML-AE monitoring method?

An observed trend of AE signals for defects and flaws is mentioned while addressing the RQ3 and is reflected in the spectrograms plotted from the recorded data. Utilizing the ability of the convolutional neural network to distinguish the images, the spectrograms are classified binarily into good or bad welds and sparsely classified into types of defects. In this thesis, three CNN architectures (VGG-16, Inception/Le-Net and Residual Network) are considered. It is concluded that out of the three considered parent architectures, Resnet-inspired architecture resulted in the highest accuracy of 98%. Despite high accuracy, it is also highlighted that the trained models have significantly less accuracy when identifying the presence of weld flash. It is further concluded that the trained CNN models have a high potential to be a part of a real-time weld monitoring system further explained in section 5.8 focusing on the integration of AE monitoring and ML. For checking the reliability of the proposed system, the model was tested for the validation welds discussed in Section 4.9 and no loss in the accuracy was observed. To further support the robustness of the proposed monitoring method, the exploration vs exploitation aspect of the training process is discussed in section 5.1 of this thesis. It is concluded that a sufficient degree of exploratory aspect is introduced

through the data augmentation method while maintaining the characteristic features in the dataset to support the exploitation of the training data.

RQ7: How best might machine learning models be integrated with AE monitoring of the FSW process?

The conventional machine learning models presented in the literature are limited to the type of input data and require a large volume of pre-requisite data for making an inference. This thesis proposes CNNs with reduced size with high accuracy to classify the presence of FSW defects using AE signals. The CNNs are trained using mel-spectrograms and spectrograms to identify the defective welds. The results obtained from Chapter 5 of this thesis outline the performance of the proposed CNN models with the data augmentation methods. The proposed AE monitoring method along with data augmentation addresses the challenges of pre-requisite high-volume weld data increasing the potential for application for an online FSW weld monitoring system. As discussed in section 5.8, the proposed online weld monitoring system is an extension of a novel anomaly detection system for FSW. As previously mentioned, while addressing the RQ6, the proposed Residual network-inspired CNN model achieved an accuracy of 98% with a classification time of 1.5 seconds. The fast AE data acquisition system coupled with the proposed CNN offers high potential for the implementation of an online FSW weld monitoring system. The proposed monitoring system would also induce higher confidence in the decision-making process by the FSW machine operator mitigating the need for post-weld inspection.

RQ8: Can machine learning be used to aid weld quality-based decision making by FSW machine users?

The current state of FSW weld monitoring is limited by the type of control system and time-intensive force-based decision models. This delay contributes to the need for an offline FSW inspection process that increases the lead time of the welded part exponentially. Often the FSW machine operators are trained to identify flawed weld by looking at the top and bottom surface of the weld. However, the lack of penetration and subsurface voids cannot be detected through visual inspection. The proposed weld classification model can identify the presence of these defects by visualizing the spectrograms reducing the need for post-weld inspection. The use of CNNs also mitigates the need for prior knowledge of the AE process which further reduces the time consumed by the FSW machine user to assess the weld quality.

7. Future Work

Based on the findings of this study, future work in the direction of Industry 4.0 can be suggested. This study is focused on the implementation of cont. AE monitoring for welding two aluminium grades. To further explore the extent of the applicability of the proposed method for different materials and standardization, a welding database from a wide range of welding parameters with different tools and workpiece materials is required. To further establish the correlation between the AE monitoring and FSW process, the proposed FSW monitoring method can be extended for different variants of FSW and FS additive manufacturing processes.

The proposed cont. AE monitoring method utilized wide band AE sensors for determining the characteristic frequency of the FSW process. For the detailed analysis of the specific material flow zone, a combination of a wide-band sensor and a narrow-band sensor can be used as it would compensate for the loss of sensitivity observed by the wide-band sensors and enable to recording of the welds with longer durations.

The potential of online monitoring FSW tool wear can also be highlighted which would enable higher confidence in the weld quality while welding harder material like steel and titanium. As a main outcome of this thesis, the ability of the AE monitoring system to identify the flow zones is highlighted. While performing FSW on harder material the tool undergoes tool wear which can be traced with irregular stirring. The narrow band AE sensors with a suitable frequency range can be utilized for detailed monitoring focused FSW tool probe wear.

Since the proposed AE monitoring method monitors elastic waves generated by the tool from the plates, another approach of recording the AE signals from the FSW tool can also be explored. This approach would enable to a better correlation between the torque and the weld quality. The existing literature in section 2.8 highlights the superiority of torque monitoring over force monitoring and the approach for a multi-sensory system can be extended for the above two discussed locations for the AE sensors. The extended approach will enable the end user to have better confidence in the assessment of weld quality while welding harder material. Monitoring AE signals from the FSW tool will also enable 2nd-degree validation for the assessment of tool engagement. The limitations of the current data acquisition system are highlighted in section 1.4 of this thesis. To address the limitation of the maximum observable frequency of the AE signal, analogue to a digital converter with higher buffer memory should be selected. The current data acquisition process requires manual control and

data processing. It can be automated to get the AE signal for the desired time interval by using the existing Python's pico-python wrapper.

As highlighted in the existing literature discussed in section 2.9, AE signals are dependent on the heat input and thermal properties of the base material, a validation stage before the deployment of the proposed monitoring method discussed in section 5.8 should be further explored. The variance analysis of AE signals from the validation weld and exiting database would result in better confidence in the proposed monitoring system. The mechanical testing of the FSWed parts is widely accepted in all industries. The validation stage can be extended by the introduction of mechanical testing based on the ISO standards to further strengthen the confidence in the decision-making process before deployment of the online weld monitoring system.

The proposed deep neural network model in section 5.8 can be extended with recurrent reinforcement learning. The potential of exploration and exploitation aspect of the training process of the CNN can be further explored by extending the variability of the collected AE signals. The exploratory dataset should consist of welds performed with different tools and materials while the exploitation dataset should consist of minimum variance with high repeatability. The implementation of machine learning for the classification of FSW defects and flaws is limited to three basic CNNs. Using a similar methodology, the multi-sensory system-based ML model can be integrated with the FSW control system to have better confidence in the process. Section 5.8 proposes an AE and ML integrated system for real-time monitoring and control of the FSW process enabling automation based on 1st level of process parameter. As this study does not provide evidence for the efficiency of the proposed monitoring method for real-time application, further investigation is needed in terms of integration with the FSW control systems. It should also be highlighted that the proposed online weld monitoring method did not explore the latency estimation of the AD converter, FSW plant and other sub-systems. This issue of synchronization can be addressed by estimating the latency of each sub-system of the monitoring method. This would enable the monitoring system to localize the presence of defect or flaw to generate a corrective signal. The proposed weld classification system is limited to spectrograms as image-based input. The CNN models are widely used and known for multi-modal input, which can allow the usage of images and multi-sensory data to have better confidence in the decision-making process. It should also be noted that this increase in the amount of input data would require more efficient data processing capabilities. Exploiting the flexibility to incorporate multi-modal input will increase the cross-platform functionality and make the proposed monitoring system highly robust.

The recent developments in the domain of open-source single-board computers (SBC) (e.g.- NVIDIA Jetson Nano, ClockworkPi and Raspberry Pi) have enabled developers to run computationally intensive ML models on more economical alternative systems. The use of open-source SBC for the proposed weld monitoring system would further reduce the development and deployment cost with no restrictions in terms of interoperability. Due to the time limitation of the deployment phase of the pre-trained network online weld monitoring was not performed. It is advised to utilise the capabilities of the TinyML library for the deployment of a pre-trained network on SBC.

References

[1]   W. M. W. Thomas, E. D. Nicholas, J. C. Needham, M. G. Murch, P. Temple-Smith, and C. J. Dawes, "Friction stir welding process developments and variant techniques," *Google patents*, pp. 1–21, 1991, [Online]. Available: http://www.google.com/patents/US5460317%5Cn.

[2]   R. S. Mishra and Z. Y. Ma, "Friction stir welding and processing," *Mater. Sci. Eng. R Reports*, vol. 50, no. 1–2, pp. 1–78, 2005, doi: 10.1016/j.mser.2005.07.001.

[3]   WALTER POLT, "A little friction at Boing," vol. Volume 03, no. Issue 5, [Online]. Available: https://www.boeing.com/news/frontiers/archive/2004/september/i_tt.html.

[4]   "TWI Welding Technology used for Historic SpaceX Launch." https://www.twi-global.com/media-and-events/press-releases/2020/twi-technology-used-for-historic-spacex-launch.

[5]   S. Kallee, "FSW in Ship Building," 2023. https://www.alustir.com/english/fsw-ship-building/ (accessed Mar. 07, 2024).

[6]   J. M. Hoffman, "Car bodies first to be friction stir welded," 2003. https://www.machinedesign.com/archive/article/21816493/car-bodies-first-to-be-friction-stir-welded.

[7]   V. M. Magalhães, C. Leitão, and D. M. Rodrigues, "Friction stir welding industrialisation and research status," *Sci. Technol. Weld. Join.*, vol. 23, no. 5, pp. 400–409, 2018, doi: 10.1080/13621718.2017.1403110.

[8]   U. Dressler, G. Biallas, and U. Alfaro Mercado, "Friction stir welding of titanium alloy TiAl6V4 to aluminium alloy AA2024-T3," *Mater. Sci. Eng. A*, vol. 526, no. 1–2, pp. 113–117, 2009, doi: 10.1016/j.msea.2009.07.006.

[9]   D. E. Dilger, "Apple slims down iMac 40% with 'friction-stir welding' & ditching the disc drive," 2012. https://appleinsider.com/articles/12/10/24/apple-slims-down-imac-40-with-friction-stir-welding-ditching-the-disc-drive.

[10]   P. L. Threadgilll, A. J. Leonard, H. R. Shercliff, and P. J. Withers, "Friction stir welding of aluminium alloys," *Int. Mater. Rev.*, vol. 54, no. 2, pp. 49–93, 2009, doi: 10.1179/174328009X411136.

[11]   C. J. D. W.M. Thomas, E.D. Nicholas, J.C. Needham, M.G. Murch, P. Templesmith, "No Title," G.B. Patent Application No. 9125978.8, 1991.

[12]   S. Mandal, J. Rice, and A. A. Elmustafa, "Experimental and numerical investigation of the plunge stage in friction stir welding," *J. Mater. Process. Technol.*, vol. 203, no. 1–3, pp. 411–419, 2008, doi: 10.1016/j.jmatprotec.2007.10.067.

[13]   F. Marie, "Friction stir welding process using a device with a retractable pin with retraction of the retractable pin at the end of the welded path," CA2649767A1, 2007.

[14]   I. Zybin, K. Trukhanov, A. Tsarkov, and S. Kheylo, "Backing plate effect on temperature controlled FSW process," *MATEC Web Conf.*, vol. 224, 2018, doi: 10.1051/matecconf/201822401084.

[15]   J. L. Covington, "Experimental and Numerical Investigation of Tool Heating During

Friction Stir Welding," 2005.

[16]   V. Patel *et al.*, "High-speed friction stir welding in light weight battery trays for the EV industry," *Science and Technology of Welding and Joining*, vol. 27, no. 4. pp. 250–255, 2022, doi: 10.1080/13621718.2022.2045121.

[17]   M. Zhai, C. S. Wu, and H. Su, "Influence of tool tilt angle on heat transfer and material flow in friction stir welding," *J. Manuf. Process.*, vol. 59, no. July, pp. 98–112, 2020, doi: 10.1016/j.jmapro.2020.09.038.

[18]   R. Nandan, T. DebRoy, and H. K. D. H. Bhadeshia, "Recent advances in friction-stir welding - Process, weldment structure and properties," *Prog. Mater. Sci.*, vol. 53, no. 6, pp. 980–1023, 2008, doi: 10.1016/j.pmatsci.2008.05.001.

[19]   J. De Backer, "Thermoelectric method for temperature measurement in friction stir welding," no. September 2019, 2013, doi: 10.1179/1362171813Y.0000000135.

[20]   A. Meilinger and I. Torok, "the Importance of Friction Stir Welding Tool," *Prod. Process. Syst.*, vol. 6, no. 1, pp. 25–34, 2013.

[21]   Y. N. Zhang, X. Cao, S. Larose, and P. Wanjara, "Review of tools for friction stir welding and processing," *Can. Metall. Q.*, vol. 51, no. 3, pp. 250–261, Jul. 2012, doi: 10.1179/1879139512Y.0000000015.

[22]   C. I. Chang, C. J. Lee, and J. C. Huang, "Relationship between grain size and Zener – Holloman parameter during friction stir processing in AZ31 Mg alloys," vol. 51, pp. 509–514, 2004, doi: 10.1016/j.scriptamat.2004.05.043.

[23]   Y. S. Sato, M. Urata, and H. Kokawa, "Parameters controlling microstructure and hardness during friction-stir welding of precipitation-hardenable aluminum alloy 6063," *Metall. Mater. Trans. A*, vol. 33, no. 3, pp. 625–635, Mar. 2002, doi: 10.1007/s11661-002-0124-3.

[24]   R. P. Mahto, M. Rout, and S. K. Pal, "Mechanism of microstructure evolution and grain growth in friction stir welding of AA6061-T6 and AISI304 in air and water media," *Mater. Chem. Phys.*, vol. 273, p. 125081, Nov. 2021, doi: 10.1016/j.matchemphys.2021.125081.

[25]   K. N. Krishnan, "On the formation of onion rings in friction stir welds," *Mater. Sci. Eng. A*, vol. 327, no. 2, pp. 246–251, 2002, doi: 10.1016/S0921-5093(01)01474-5.

[26]   J. Mężyk and S. Kowieski, "The Application of Thermal Imaging Method," pp. 11–14, 2013.

[27]   A. Silva-Magalhães, J. De Backer, J. Martin, and G. Bolmsjö, "In-situ temperature measurement in friction stir welding of thick section aluminium alloys," *J. Manuf. Process.*, vol. 39, pp. 12–17, Mar. 2019, doi: 10.1016/j.jmapro.2019.02.001.

[28]   M. Maeda, H. Liu, H. Fujii, and T. Shibayanagi, "Temperature field in the vicinity of FSW-tool during friction stir welding of aluminium alloys," *Weld. World*, vol. 49, no. 3–4, pp. 69–75, 2005, doi: 10.1007/BF03266478.

[29]   A. C. F. Silva, J. De Backer, and G. Bolmsjö, "Temperature measurements during friction stir welding," *Int. J. Adv. Manuf. Technol.*, vol. 88, no. 9–12, pp. 2899–2908, 2017, doi: 10.1007/s00170-016-9007-4.

[30]   S. Grabmann, A. Zens, R. Marstatt, F. Haider, and M. F. Zaeh, "Temperature-controlled

friction stir welding process of Al-Cu joints with complex geometries," in *AIP Conference Proceedings*, 2019, vol. 2113, no. July, doi: 10.1063/1.5112568.

[31]   J. Backer, *Feedback Control of Robotic Friction Stir Welding*, vol. 2, no. 4. 2014.

[32]   Stephen Cater (TWI Ltd), "Friction Stir Welding of Steel: Microstructures and defects," 2020.

[33]   G. Liu, L. E. Murr, C. S. Niou, J. C. McClure, and F. R. Vega, "Microstructural aspects of the friction-stir welding of 6061-T6 aluminum," *Scr. Mater.*, vol. 37, no. 3, pp. 355–361, 1997, doi: 10.1016/S1359-6462(97)00093-6.

[34]   A. Ali, M. W. Brown, C. A. Rodopoulos, and S. Gardiner, "Characterization of 2024-T351 friction stir welding joints," *J. Fail. Anal. Prev.*, vol. 6, no. 4, pp. 83–96, 2006, doi: 10.1361/154770206X117559.

[35]   K. Kumar, S. V. Kailas, and T. S. Srivatsan, "Influence of tool geometry in friction stir welding," *Mater. Manuf. Process.*, vol. 23, no. 2, pp. 188–194, 2008, doi: 10.1080/10426910701774734.

[36]   H. Aghajani Derazkola, N. Kordani, and H. Aghajani Derazkola, "Effects of friction stir welding tool tilt angle on properties of Al-Mg-Si alloy T-joint," *CIRP J. Manuf. Sci. Technol.*, vol. 33, pp. 264–276, 2021, doi: 10.1016/j.cirpj.2021.03.015.

[37]   L. E. Murr, "A review of FSW research on dissimilar metal and alloy systems," *J. Mater. Eng. Perform.*, vol. 19, no. 8, pp. 1071–1089, 2010, doi: 10.1007/s11665-010-9598-0.

[38]   M. Sen, S. Shankar, and S. Chattopadhyaya, "Investigations into FSW joints of dissimilar aluminum alloys," *Mater. Today Proc.*, vol. 27, pp. 2455–2462, 2019, doi: 10.1016/j.matpr.2019.09.218.

[39]   P. Xue, B. L. Xiao, D. R. Ni, and Z. Y. Ma, "Enhanced mechanical properties of friction stir welded dissimilar Al-Cu joint by intermetallic compounds," *Mater. Sci. Eng. A*, vol. 527, no. 21–22, pp. 5723–5727, 2010, doi: 10.1016/j.msea.2010.05.061.

[40]   Y. G. Kim, H. Fujii, T. Tsumura, T. Komazaki, and K. Nakata, "Three defect types in friction stir welding of aluminum die casting alloy," *Mater. Sci. Eng. A*, vol. 415, no. 1–2, pp. 250–254, 2006, doi: 10.1016/j.msea.2005.09.072.

[41]   H. J. Liu *et al.*, "Weld appearance and microstructural characteristics of friction stir butt barrier welded joints of aluminium alloy to copper," *Sci. Technol. Weld. Join.*, vol. 17, no. 2, pp. 104–110, Feb. 2012, doi: 10.1179/1362171811Y.0000000086.

[42]   H. Fujii, L. Cui, M. Maeda, and K. Nogi, "Effect of tool shape on mechanical properties and microstructure of friction stir welded aluminum alloys," *Mater. Sci. Eng. A*, vol. 419, no. 1–2, pp. 25–31, Mar. 2006, doi: 10.1016/j.msea.2005.11.045.

[43]   M. F. X. Muthu and V. Jayabalan, "Tool travel speed effects on the microstructure of friction stir welded aluminum–copper joints," *J. Mater. Process. Technol.*, vol. 217, pp. 105–113, Mar. 2015, doi: 10.1016/j.jmatprotec.2014.11.007.

[44]   R. Sarrafi, A. H. Kokabi, M. A. Gharacheh, and B. Shalchi, "Evaluation of Microstructure and Mechanical Properties of Aluminum to Copper Friction Stir Butt Welds," in *Friction Stir Welding and Processing VI*, Hoboken, NJ, USA: John Wiley & Sons, Inc., 2011, pp. 253–264.

[45]   C. W. Tan, Z. G. Jiang, L. Q. Li, Y. B. Chen, and X. Y. Chen, "Microstructural evolution and

mechanical properties of dissimilar Al–Cu joints produced by friction stir welding," *Mater. Des.*, vol. 51, pp. 466–473, Oct. 2013, doi: 10.1016/j.matdes.2013.04.056.

[46]   W. S. Chang, S. R. Rajesh, C. K. Chun, and H. J. Kim, "Microstructure and Mechanical Properties of Hybrid Laser-Friction Stir Welding between AA6061-T6 Al Alloy and AZ31 Mg Alloy," *J. Mater. Sci. Technol.*, vol. 27, no. 3, pp. 199–204, 2011, doi: 10.1016/S1005-0302(11)60049-2.

[47]   A. Tamadon, D. J. Pons, K. Sued, and D. Clucas, "Internal Flow Behaviour and Microstructural Evolution of the Bobbin-FSW Welds: Thermomechanical Comparison between 1xxx and 3xxx Aluminium Grades," *Adv. Mater. Sci.*, vol. 21, no. 2, pp. 40–64, Jun. 2021, doi: 10.2478/adms-2021-0010.

[48]   M. Aissani, S. Gachi, F. Boubenider, and Y. Benkedda, "Design and optimization of friction stir welding tool," *Mater. Manuf. Process.*, vol. 25, no. 11, pp. 1199–1205, 2010, doi: 10.1080/10426910903536733.

[49]   P. Pankaj, A. Tiwari, P. Biswas, & A. G. Rao, and S. Pal, "Experimental studies on controlling of process parameters in dissimilar friction stir welding of DH36 shipbuilding steel-AISI 1008 steel," doi: 10.1007/s40194-020-00886-3/Published.

[50]   F. C. Liu, Y. Hovanski, M. P. Miles, C. D. Sorensen, and T. W. Nelson, "A review of friction stir welding of steels: Tool, material flow, microstructure, and properties," *Journal of Materials Science and Technology*, vol. 34, no. 1. pp. 39–57, 2018, doi: 10.1016/j.jmst.2017.10.024.

[51]   E. D. N. and W. M. T. Stephan W. Kallee, "Friction Stir Welding - Invention, Innovations and Applications," *8th Int. Conf. Joints Alum.*, 2001.

[52]   X. Chu, M. Yin, J. Gao, X. Wang, and Y. Wang, "Effects of Shoulder Geometry on Microstructures and Mechanical Properties of Probeless Friction Stir Spot Welded Aluminum 7075-T651 Sheets," *Metals (Basel).*, vol. 10, no. 12, p. 1605, Nov. 2020, doi: 10.3390/met10121605.

[53]   L. Trueba, G. Heredia, D. Rybicki, and L. B. Johannes, "Effect of tool shoulder features on defects and tensile properties of friction stir welded aluminum 6061-T6," *J. Mater. Process. Technol.*, vol. 219, pp. 271–277, 2015, doi: 10.1016/j.jmatprotec.2014.12.027.

[54]   C. Sorensen and T. Nelson, "Friction stir welding of ferrous and nickel alloys," *Frict. Stir Weld. Process.*, no. Ref 2, pp. 111–121, 2007.

[55]   W. M. Thomas, E. D. Nicholas, J. C. Needham, P. Temple-Smith, S. W. K. W. Kallee, and C. J. Dawes, "Friction Stir Welding," GB2306366A, 1996.

[56]   J. . Colligan, K.J. & Xu, J. & Pickens, "Welding tool and process parameter effects in friction stir welding of aluminum alloys," in *TMS Annual Meeting*, 2003, pp. 181–190.

[57]   E. Aldanondo, E. Arruti, A. Echeverria, and I. Hurtado, "Friction Stir Welding of Lap Joints Using New Al–Li Alloys for Stringer-Skin Joints," in *Friction Stir Welding and Processing X*, 2019, pp. 77–88.

[58]   M. Matsushita, Y. Kitani, and R. Ikeda, "Applicability of Friction Stir Welding (FSW) to Steels and Properties of the Welds," *JFE Tech. Rep.*, vol. 20, no. 20, pp. 133–140, 2015.

[59]   Y. Li, L. E. Murr, and J. C. McClure, "Solid-state flow visualization in the friction-stir welding of 2024 Al to 6061 Al," *Scr. Mater.*, vol. 40, no. 9, pp. 1041–1046, 1999, doi: 10.1016/S1359-6462(99)00062-7.

[60] Y. Li, L. E. Murr, and J. C. McClure, "Flow visualization and residual microstructures associated with the friction-stir welding of 2024 aluminum to 6061 aluminum," *Mater. Sci. Eng. A*, vol. 271, no. 1–2, pp. 213–223, 1999, doi: 10.1016/S0921-5093(99)00204-X.

[61] K. Colligan, "Material flow behavior during friction stir welding of aluminum," *Weld. J. (Miami, Fla)*, vol. 78, no. 7, pp. 229-s, 1999.

[62] J. A. Schneider and A. C. Nunes, "Characterization of plastic flow and resulting microtextures in a friction stir weld," *Metall. Mater. Trans. B Process Metall. Mater. Process. Sci.*, vol. 35, no. 4, pp. 777–783, 2004, doi: 10.1007/s11663-004-0018-4.

[63] C. Hamilton, S. Dymek, and M. Blicharski, "A model of material flow during friction stir welding," *Mater. Charact.*, vol. 59, no. 9, pp. 1206–1214, 2008, doi: 10.1016/j.matchar.2007.10.002.

[64] A. Baraka, G. Panoutsos, and S. Cater, "A real-time quality monitoring framework for steel friction stir welding using computational intelligence," *J. Manuf. Process.*, vol. 20, pp. 137–148, 2015, doi: 10.1016/j.jmapro.2015.09.001.

[65] P. Heurtier, M. J. Jones, C. Desrayaud, J. H. Driver, F. Montheillet, and D. Allehaux, "Mechanical and thermal modelling of Friction Stir Welding," vol. 171, pp. 348–357, 2006, doi: 10.1016/j.jmatprotec.2005.07.014.

[66] D. G. Andrade, C. Leitão, N. Dialami, M. Chiumenti, and D. M. Rodrigues, "Modelling torque and temperature in friction stir welding of aluminium alloys," *Int. J. Mech. Sci.*, vol. 182, no. May, 2020, doi: 10.1016/j.ijmecsci.2020.105725.

[67] T. A. Shehabeldeen *et al.*, "A Novel Method for Predicting Tensile Strength of Friction Stir Welded AA6061 Aluminium Alloy Joints Based on Hybrid Random Vector Functional Link and Henry Gas Solubility Optimization," *IEEE Access*, vol. 8, pp. 79896–79907, 2020, doi: 10.1109/ACCESS.2020.2990137.

[68] S. Guerdoux and L. Fourment, "A 3D numerical simulation of different phases of friction stir welding," *Model. Simul. Mater. Sci. Eng.*, vol. 17, no. 7, 2009, doi: 10.1088/0965-0393/17/7/075001.

[69] X. Deng and S. Xu, "Two-dimensional finite element simulation of material flow in the friction stir welding process," *J. Manuf. Process.*, vol. 6, no. 2, pp. 125–133, 2004, doi: 10.1016/S1526-6125(04)70066-3.

[70] T. V. Stotler and T. J. Trapp, "Friction stir welding travel axis load control method and apparatus," US7216793B2, 2004.

[71] W. R. Longhurst *et al.*, "Investigation of force-controlled friction stir welding for manufacturing and automation," *Proc. Inst. Mech. Eng. Part B J. Eng. Manuf.*, vol. 224, no. 6, pp. 937–949, 2010, doi: 10.1243/09544054JEM1709.

[72] M. Soron and I. Kalaykov, "A robot prototype for friction stir welding," *2006 IEEE Conf. Robot. Autom. Mechatronics*, 2006, doi: 10.1109/RAMECH.2006.252646.

[73] C. B. Smith, "Robotic friction stir welding using a standard industrial robot," *2nd Frict. Stir Weld. Int. Symp.*, 2000, [Online]. Available: http://www.frictionstirlink.com/publications/Pub062ndFSWSymposiumFSWSTDINDRobotpdf.pdf.

[74] N. F. Alkayem, B. Parida, and S. Pal, "Optimization of friction stir welding process

parameters using soft computing techniques," *Soft Comput.*, vol. 21, no. 23, pp. 7083–7098, 2017, doi: 10.1007/s00500-016-2251-6.

[75] W. R. Longhurst, A. M. Strauss, G. E. Cook, and P. A. Fleming, "Torque control of friction stir welding for manufacturing and automation," *Int. J. Adv. Manuf. Technol.*, vol. 51, no. 9–12, pp. 905–913, 2010, doi: 10.1007/s00170-010-2678-3.

[76] J. Qin, F. Léonard, and G. Abba, "Real-Time Trajectory Compensation in Robotic Friction Stir Welding Using State Estimators," *IEEE Trans. Control Syst. Technol.*, vol. 24, no. 6, pp. 2207–2214, 2016, doi: 10.1109/TCST.2016.2536482.

[77] J. De Backer and G. Bolmsjö, "Deflection model for robotic friction stir welding," *Ind. Rob.*, vol. 41, no. 4, pp. 365–372, 2014, doi: 10.1108/IR-01-2014-0301.

[78] J. Shi, Y. Wang, G. Zhang, and H. Ding, "Optimal design of 3-DOF PKM module for friction stir welding," *Int. J. Adv. Manuf. Technol.*, vol. 66, no. 9–12, pp. 1879–1889, Jun. 2013, doi: 10.1007/s00170-012-4467-7.

[79] Q. Li, W. Wu, J. Xiang, H. Li, and C. Wu, "A hybrid robot for friction stir welding," *Proc. Inst. Mech. Eng. Part C J. Mech. Eng. Sci.*, vol. 229, no. 14, pp. 2639–2650, 2015, doi: 10.1177/0954406214562848.

[80] A. Adriana and G. Rodriguez, "Multiscale modelling for optimal process operating windows in Friction Stir Welding," University of Sheffield, 2014.

[81] IIW, "Friction stir welding — Aluminium — Part 5: Quality and inspection requirements," *ISO 25239-52020*, p. 12, 2020, [Online]. Available: https://www.iso.org/ics/25.160.10.html.

[82] H. Takahara, Y. Motoyama, M. Tsujikawa, S. Oki, S. W. Chung, and K. Higashi, "Allowance of Deviation and Gap in Butt Joint on Friction Stir Welding," *Adv. Mater. Res.*, vol. 15–17, pp. 375–380, Feb. 2006, doi: 10.4028/www.scientific.net/AMR.15-17.375.

[83] Y. Imani and M. Guillot, "Tolerating for Joint Fit-Up Issues Using Welding Parameters in Friction Stir Welding of Aa6061-T6 At Right," *ResearchGate*, no. September, pp. 1–6, 2014.

[84] Y. Yang, P. Kalya, R. G. Landers, and K. Krishnamurthy, "Automatic gap detection in friction stir butt welding operations," *Int. J. Mach. Tools Manuf.*, vol. 48, no. 10, pp. 1161–1169, 2008, doi: 10.1016/j.ijmachtools.2008.01.007.

[85] P. A. Fleming *et al.*, "Misalignment detection and enabling of seam tracking for friction stir welding," *Sci. Technol. Weld. Join.*, vol. 14, no. 1, pp. 93–96, 2009, doi: 10.1179/136217108X372568.

[86] T. Jene, G. Dobmann, G. Wagner, and D. Eifler, "Monitoring of the friction stir welding process to describe parameter effects on joint quality," *Weld. World*, vol. 52, no. 9–10, pp. 47–53, 2008, doi: 10.1007/BF03266668.

[87] P. J. Ramulu, R. G. Narayanan, S. V. Kailas, and J. Reddy, "Internal defect and process parameter analysis during friction stir welding of Al 6061 sheets," *Int. J. Adv. Manuf. Technol.*, vol. 65, no. 9–12, pp. 1515–1528, 2013, doi: 10.1007/s00170-012-4276-z.

[88] U. Kumar *et al.*, "Defect identification in friction stir welding using discrete wavelet analysis," *Adv. Eng. Softw.*, vol. 85, pp. 43–50, 2015, doi: 10.1016/j.advengsoft.2015.02.001.

[89]   S. Kumari *et al.*, "Defect identification in friction stir welding using continuous wavelet transform," *J. Intell. Manuf.*, vol. 30, no. 2, pp. 483–494, 2019, doi: 10.1007/s10845-016-1259-1.

[90]   A. Shrivastava, M. Zinn, N. A. Duffie, N. J. Ferrier, C. B. Smith, and F. E. Pfefferkorn, "Force measurement-based discontinuity detection during friction stir welding," *J. Manuf. Process.*, vol. 26, pp. 113–121, 2017, doi: 10.1016/j.jmapro.2017.01.007.

[91]   D. J. Franke, M. R. Zinn, and F. E. Pfefferkorn, "Intermittent Flow of Material and Force-Based Defect Detection During Friction Stir Welding of Aluminum Alloys," 2019, pp. 149–160.

[92]   K. M. Holford, "Acoustic Emission–Basic Principles and Future Directions," *Strain*, vol. 36, no. 2, pp. 51–54, May 2000, doi: 10.1111/j.1475-1305.2000.tb01173.x.

[93]   D. Ozevin, "MEMS acoustic emission sensors," *Appl. Sci.*, vol. 10, p. 8966, 2020.

[94]   Christian U. Grosse (Department of Non-destructive Testing, M. O. (Graduate S. of S. & T. Techniques, and Monitoring), and Kumamoto University), *Acoustic Emission Testing*. Berlin, Heidelberg: Springer Berlin Heidelberg, 2008.

[95]   V. Soundararajan, H. Atharifar, and R. Kovacevic, "Monitoring and processing the acoustic emission signals from the friction-stir-welding process," *Proc. Inst. Mech. Eng. Part B J. Eng. Manuf.*, vol. 220, no. 10, pp. 1673–1685, Oct. 2006, doi: 10.1243/09544054JEM586.

[96]   E. Jiménez-Macías, A. Sánchez-Roca, H. Carvajal-Fals, J. Blanco-Fernández, and E. Martínez-Cámara, "Wavelets application in prediction of friction stir welding parameters of alloy joints from vibroacoustic ANN-based model," *Abstr. Appl. Anal.*, vol. 2014, 2014, doi: 10.1155/2014/728564.

[97]   C. Chen, R. Kovacevic, and D. Jandgric, "Wavelet transform analysis of acoustic emission in monitoring friction stir welding of 6061 aluminum," *Int. J. Mach. Tools Manuf.*, vol. 43, no. 13, pp. 1383–1390, 2003, doi: 10.1016/S0890-6955(03)00130-5.

[98]   S. Subramaniam, S. Narayanan, and A. S. Denis, "Acoustic emission-based monitoring approach for friction stir welding of aluminum alloy AA6063-T6 with different tool pin profiles," *Proc. Inst. Mech. Eng. Part B J. Eng. Manuf.*, vol. 227, no. 3, pp. 407–416, 2013, doi: 10.1177/0954405412472673.

[99]   O. Simeone, "A Brief Introduction to Machine Learning for Engineers," *Found. Trends® Signal Process.*, vol. 12, no. 3–4, pp. 200–431, 2018, doi: 10.1561/2000000102.

[100]   D. H. Hubel and T. N. Wiesel, "Receptive fields and functional architecture of monkey striate cortex," *J. Physiol.*, vol. 195, no. 1, pp. 215–243, Mar. 1968, doi: 10.1113/jphysiol.1968.sp008455.

[101]   K. Fukushima, "Neocognitron: A self-organizing neural network model for a mechanism of pattern recognition unaffected by shift in position," *Biol. Cybern.*, vol. 36, no. 4, pp. 193–202, Apr. 1980, doi: 10.1007/BF00344251.

[102]   Y. LeCun *et al.*, "Backpropagation Applied to Handwritten Zip Code Recognition," *Neural Comput.*, vol. 1, no. 4, pp. 541–551, Dec. 1989, doi: 10.1162/neco.1989.1.4.541.

[103]   X. Wu, Y. Liu, X. Zhou, and A. Mou, "Automatic Identification of Tool Wear Based on Convolutional Neural Network in Face Milling Process," *Sensors*, vol. 19, no. 18, p. 3817, Sep. 2019, doi: 10.3390/s19183817.

[104] A. Kothuru, S. P. Nooka, and R. Liu, "Application of deep visualization in CNN-based tool condition monitoring for end milling," *Procedia Manuf.*, vol. 34, pp. 995–1004, 2019, doi: 10.1016/j.promfg.2019.06.096.

[105] H. Ney, "On the Probabilistic Interpretation of Neural Network Classifiers and Discriminative Training Criteria," *IEEE Trans. Pattern Anal. Mach. Intell.*, vol. 17, no. 2, pp. 107–119, 1995, doi: 10.1109/34.368176.

[106] E. Boldsaikhan, E. M. Corwin, A. M. Logar, and W. J. Arbegast, "The use of neural network and discrete Fourier transform for real-time evaluation of friction stir welding," *Appl. Soft Comput. J.*, vol. 11, no. 8, pp. 4839–4846, 2011, doi: 10.1016/j.asoc.2011.06.017.

[107] B. Das, S. Pal, and S. Bag, "Weld quality prediction in friction stir welding using wavelet analysis," *Int. J. Adv. Manuf. Technol.*, vol. 89, no. 1–4, pp. 711–725, 2017, doi: 10.1007/s00170-016-9140-0.

[108] N. N. Bhat, K. Kumari, S. Dutta, S. K. Pal, and S. Pal, "Friction stir weld classification by applying wavelet analysis and support vector machine on weld surface images," *J. Manuf. Process.*, vol. 20, pp. 274–281, Oct. 2015, doi: 10.1016/j.jmapro.2015.07.002.

[109] V. Murthy, K. Ullegaddi, B. Mahesh, and B. M. Rajaprakash, "Application of Image Processing and Acoustic Emission Technique in Monitoring of Friction Stir Welding Process," *Mater. Today Proc.*, vol. 4, no. 8, pp. 9186–9195, 2017, doi: 10.1016/j.matpr.2017.07.276.

[110] Q. Zhang, M. Zhang, T. Chen, Z. Sun, Y. Ma, and B. Yu, "Recent advances in convolutional neural network acceleration," *Neurocomputing*, vol. 323, pp. 37–51, 2019, doi: 10.1016/j.neucom.2018.09.038.

[111] K. Simonyan and A. Zisserman, "Very deep convolutional networks for large-scale image recognition," *3rd Int. Conf. Learn. Represent. ICLR 2015 - Conf. Track Proc.*, pp. 1–14, 2015.

[112] "Going deeper with convolutions." p. 500, [Online]. Available: arxiv:1409.4842v1 [cs.CV] 17 Sep 2014.

[113] Z. Cheng, H. Sun, M. Takeuchi, and J. Katto, "Deep Residual Learning for Image Compression." 2019, [Online]. Available: http://arxiv.org/abs/1906.09731.

[114] Y. Lu, C. Ma, Y. Lu, J. Lu, and L. Ying, "A Mean-field Analysis of Deep ResNet and Beyond: Towards Provable Optimization Via Overparameterization From Depth," Mar. 2020, doi: arXiv:2003.05508v2.

[115] S. Metals, "6082 Aluminium Technical Datasheet," 2023. https://www.smithmetal.com/pdf/aluminium/6xxx/6082.pdf (accessed Jan. 08, 2024).

[116] S. Metals, "5083 Aluminium Technical Datasheet," 2023. https://www.smithmetal.com/pdf/aluminium/5xxx/5083.pdf (accessed Jan. 08, 2024).

[117] TWI, "FSW TRI-FLUTE MX PROBE," p. 1, 2016.

[118] TWI, "FSW TOOL 15 DIA. 7 DEGREE CONCAVE SHOULDER," 2016.

[119] Vallen Systeme GmbH, "AE-Sensor Data Sheet VS900-M," 2019. [Online]. Available: https://www.vallen.de/sensors/broad-band-sensors/vs900-m/.

[120] R. Oshana, "Overview of Digital Signal Processing Algorithms," in *DSP Software*

Development Techniques for Embedded and Real-Time Systems, Elsevier, 2006, pp. 59–121.

[121] TC Direct, "Fibreglass Insulated Flat Twin Thermocouple Cable (480°C)," 2024. https://www.tcdirect.co.uk/product-2-180-21/Welded-Tip-PFA-Thermocouple#180_21_2 (accessed Jan. 08, 2024).

[122] D. O'Shaughnessy, *Speech Communications: Human and Machine, 2nd Edition*, 2nd ed. John Wiley & Sons, Inc., 1999.

[123] B. McFee *et al.*, "librosa: Audio and Music Signal Analysis in Python," *Proc. 14th Python Sci. Conf.*, no. Scipy, pp. 18–24, 2015, doi: 10.25080/majora-7b98e3ed-003.

[124] G. Perdikaris, *Computer Controlled Systems*. Springer Science & Business Media, 1991.

[125] E. T. Whittaker, "XVIII.—On the Functions which are represented by the Expansions of the Interpolation-Theory," *Proc. R. Soc. Edinburgh*, vol. 35, no. 0033, pp. 181–194, 1915, doi: 10.1017/s0370164600017806.

[126] S. V. Stehman, "Selecting and interpreting measures of thematic classification accuracy," *Remote Sens. Environ.*, vol. 62, no. 1, pp. 77–89, Oct. 1997, doi: 10.1016/S0034-4257(97)00083-7.

[127] D. Shen, G. Wu, and H.-I. Suk, "Deep Learning in Medical Image Analysis," *Annu. Rev. Biomed. Eng.*, vol. 19, no. 1, pp. 221–248, Jun. 2017, doi: 10.1146/annurev-bioeng-071516-044442.

[128] K. R. Prilianti, T. H. P. Brotosudarmo, S. Anam, and A. Suryanto, "Performance comparison of the convolutional neural network optimizer for photosynthetic pigments prediction on plant digital image," 2019, p. 020020, doi: 10.1063/1.5094284.

[129] J. Rabi, T. Balusamy, and R. Raj Jawahar, "Analysis of vibration signal responses on pre induced tunnel defects in friction stir welding using wavelet transform and empirical mode decomposition," *Def. Technol.*, vol. 15, no. 6, pp. 885–896, 2019, doi: 10.1016/j.dt.2019.05.014.

[130] A. Klapuri and M. Davy, Eds., *Signal Processing Methods for Music Transcription*. Boston, MA: Springer US, 2006.

[131] D. Ambrosio *et al.*, "On the potential applications of acoustic emission in friction stir welding," *J. Manuf. Process.*, vol. 75, no. January, pp. 461–475, 2022, doi: 10.1016/j.jmapro.2022.01.012.

[132] D. H. Jones, "Book Review: Statistical Methods, 8th Edition George W. Snedecor and William G. Cochran Ames: Iowa State University Press, 1989. xix + 491 pp," *J. Educ. Stat.*, vol. 19, no. 3, pp. 304–307, Sep. 1994, doi: 10.3102/10769986019003304.

Appendices

Appendix 1: Data Augmentation Scripts

<u>Weld_Data_Gen.py</u>

```python
from multiprocessing import Process,  Pipe
from audaug import augmen
import numpy as np
import pandas as pd
import glob
from scipy.signal import savgol_filter
from skimage import util
import os
import matplotlib.pyplot as plt
"""
Note:   Change the outpath and the label list according to the weld
data category
        Check for the Weld number @ weld
"""

#----------- Start of functions---------#


#labels=['P5_W2','W5 600rpm 1000mmmin','P7_W1']# Internal Void
#labels=['27042022_W2','27042022_W3','27042022_W4']# Shoulder Pressure
#labels=['adv_ret_bad','adv_ret_bad_multiple', 'W4 800rpm 1000mmmin']#
Disruption
#labels=['adv_ret_good','Plate1000rpm','Plate800rpm','Plate1200rpm','2
7042022_W1','6xxx W6', '11082022 W1','11082022 W3','11082022
W4','11082022 W5','11082022 W6','11082022 W7']#Good

#labels=['P6_W1']
labels=['27042022_W3','27042022_W4']

fn=0
input_d=[]
tinput_d=[]
out_d=[]
predict_a=[]
sr=900000
rate=sr

# Column 1 = Channel A
# Column 2 = Channel B
wel=0  # weld number in the file name
dir_path= 'C:\python code data\Acoustic Data'
for label in labels:
    path=os.path.join(dir_path,label)
    files= glob.glob(path+'/*.csv')
    L=[]
    for f in files:
        temp_df=pd.read_csv(f)
        L.append(temp_df)


    df= pd.concat(L,axis=0)
    print(df.shape)
    df.head
    dat_ch1=(df[['Channel A']])
```

159

```python
    #dat_ch2=(df[['Channel B']])

    dat_ch1 = np.array(dat_ch1)
    dat_ch1 =dat_ch1 [4:,]
    dat_ch1 =dat_ch1 .ravel()
    dat_ch1_cln=list()
    for elm in dat_ch1:
        try:
            float(elm)
            dat_ch1_cln.append(elm)
        except ValueError as e:
            er=(e)

    """dat_ch2 = np.array(dat_ch2)
    dat_ch2 =dat_ch2 [4:,]
    dat_ch2 =dat_ch1 .ravel()
    dat_ch2_cln=list()
    for elm in dat_ch2:
        try:
            float(elm)
            dat_ch2_cln.append(elm)
        except ValueError as e:
            er=e
    """
    dataf1=np.array(dat_ch1_cln)
    dataf1 = dataf1.astype('float32')
    datam=savgol_filter(dataf1,513,2)
    dataf1=dataf1-datam
    pre_emphasis = 0.98
    emphasized_signal = np.append(dataf1[0], dataf1[1:] - pre_emphasis
* dataf1[:-1])
    dataf1=emphasized_signal
    dataf1 = dataf1[~np.isnan(dataf1)]
    data_rms=np.sqrt(np.mean(dataf1**2))

    """dataf2=np.array(dat_ch2_cln)
    dataf2 = dataf2.astype('float32')
    datam2=savgol_filter(dataf2,513,2)
    dataf2=dataf2-datam2
    pre_emphasis = 0.98
    emphasized_signal2 = np.append(dataf2[0], dataf2[1:] -
pre_emphasis * dataf2[:-1])
    dataf2=emphasized_signal2
    dataf2 = dataf2[~np.isnan(dataf2)]
    data_rms2=np.sqrt(np.mean(dataf2**2))"""

    wel=wel+1
    sr=900000

#outpath="C:\\Users\\mathurk1\\Documents\\Spect\\Model_train\\Internal
Void"       #C:\\Users\\mathurk1\\Documents\\Model_train

#outpath="C:\\Users\\mathurk1\\Documents\\Spect\\Model_train\\Shoulder
pressure"

#outpath="C:\\Users\\mathurk1\\Documents\\Spect\\Model_train\\Disrupti
on"

#outpath="C:\\Users\\mathurk1\\Documents\\Spect\\Model_train\\Good"
```

```python
#outpath_2="C:\\Users\\mathurk1\\Documents\\MelSpect\\Model_train\\Internal Void"  #C:\\Users\\mathurk1\\Documents\\Model_train

#outpath_2="C:\\Users\\mathurk1\\Documents\\MelSpect\\Model_train\\Shoulder pressure"

#outpath_2="C:\\Users\\mathurk1\\Documents\\MelSpect\\Model_train\\Disruption"

#outpath_2="C:\\Users\\mathurk1\\Documents\\MelSpect\\Model_train\\Good"

    outpath="C:\\Users\\mathurk1\\Documents\\CNN Data\\Spect\\Model__test\\Shoulder Pressure"
    outpath_2="C:\\Users\\mathurk1\\Documents\\CNN Data\\MelSpect\\Model__test\\Shoulder Pressure"
    if __name__=='__main__':
        parent_conn,child_conn= Pipe()
        p= Process(target=augmen, args=(dataf1, outpath, outpath_2, sr, wel))
        p.start()
```

Audaug.py

```python
from multiprocessing import Process, Pipe
from skimage import util
from mpl_toolkits.axes_grid1 import make_axes_locatable
import numpy as np
import random
import matplotlib.pyplot as plt

from os import path
import librosa
import librosa.display


# Adding white noise
def WN(signal, noise_perc):
    noise = np.random.normal(0, signal.std(), signal.size)
    aug_signal= signal+noise*noise_perc
    aug_signal=aug_signal.astype(type(signal[0]))
    return aug_signal
def random_gain(signal, max_f):
    gain_rate = random.uniform(1, max_f)
    augmented_signal = signal * gain_rate
    return augmented_signal

def augmen(dataf,outpath,outpath_2,sr,wel):
    fn=0
    #Pitch scaling for the data
    '''
    #Training dataset formation'

    for sc in np.linspace(1.0 ,5.0, num=10):
        dataf_pitch=librosa.effects.pitch_shift(dataf,sr,n_steps=sc)
        for max_f in np.linspace(1.0, 4.0, num=2):
            dataf_pitch_rg=random_gain(dataf_pitch, max_f)
            for wn in np.linspace(0.1, 1, num=10):
                dataf_pitch_wn= WN (dataf_pitch_rg,wn)
                rate=sr
                '''
    """
    #Validation Dataset formation
    for sc in np.linspace(0.2 ,0.6, num=3):
        dataf_pitch=librosa.effects.pitch_shift(dataf,sr,n_steps=sc)
        for max_f in np.linspace(10.0, 12.0, num=3):
            dataf_pitch_rg=random_gain(dataf_pitch, max_f)
            for wn in np.linspace(0.1, 0.6, num=3):
                dataf_pitch_wn= WN (dataf_pitch_rg,wn)
                rate=sr
                """

    #Test Dataset formation
    for sc in np.linspace(0.2 ,1.8, num=3):
        dataf_pitch=librosa.effects.pitch_shift(dataf,sr,n_steps=sc)
        for max_f in np.linspace(10.0, 20.0, num=4):
            dataf_pitch_rg=random_gain(dataf_pitch, max_f)
            for wn in np.linspace(0.1, 0.8, num=3):
                dataf_pitch_wn= WN (dataf_pitch_rg,wn)
                rate=sr

                #-------------------- Spectrogram-----------------
-----#
```

```python
            fn=fn+1
            l=len(dataf_pitch_wn)/rate #seconds for 1MS/s sampling
rate
                #slicing
            W = 2048
            slices = util.view_as_windows(dataf_pitch_wn,
window_shape=(W,), step=800)
                #windowing
            win = np.hanning(W + 1)[:-1]
            slices = slices * win
            slices = slices.T
            print('Shape of slices`:', slices.shape)
            spectrum = np.fft.fft(slices, axis=0)[:W // 2 + 1:-1]
            spectrum = np.abs(spectrum)
            S = np.abs(spectrum)
            S = 20 * np.log10(S / np.max(S))


            # Plots

            f, ax = plt.subplots(figsize=(14, 6),dpi=120)
            im1=ax.imshow(S, origin='lower', cmap='jet',
extent=(0, l, 0, rate / 2 / 1000))
            ax.axis('off')
            ax.axis('tight')
            plt.savefig(path.join(outpath,
"Spect_{}_{}.png".format(wel,fn)),bbox_inches='tight')
            plt.show()



            #----------------------Mel Spectrogram---------------
--------#

            mel_spect = librosa.feature.melspectrogram(S=S)
            log_mel_spect = librosa.amplitude_to_db(mel_spect,
ref=np.max)
            f, ax = plt.subplots(figsize=(14, 6),dpi=120)
            im1=ax.imshow(log_mel_spect, origin='lower',
cmap='jet', extent=(0, l, 0, rate / 2 / 1000))
            ax.axis('off')
            ax.axis('tight')
            plt.savefig(path.join(outpath_2,
"Mel_Spect_{}_{}.png".format(wel,fn)),bbox_inches='tight')
            plt.show()
```

Appendix 2: Proposed CNN architectures

VGG-16 inspired architecture for binary classification

```python
import numpy as np
import matplotlib.pyplot as plt
import os

from tensorflow import keras
from tensorflow.keras.preprocessing.image import ImageDataGenerator
from tensorflow.keras.models import Sequential
from tensorflow.keras.layers import Dense, Dropout, Activation,
Flatten
from tensorflow.keras.layers import Conv2D, MaxPooling2D
from sklearn.metrics import classification_report, confusion_matrix


from tensorflow.compat.v1 import ConfigProto
from tensorflow.compat.v1 import InteractiveSession
config = ConfigProto()
config.gpu_options.allow_growth = True
session = InteractiveSession(config=config)


data_dir1 = "C:\\python code data\\Acoustic_train"
data_dir2 = "C:\\python code data\\Acoustic_val"
data_dir3 = "C:\\python code data\\Acoustic_test"

epoch = 150
batch_size = 8

image_gen=ImageDataGenerator(zoom_range
=.1,rescale=1/255,validation_split=0.2)
train_dat=image_gen.flow_from_directory(directory=data_dir1,color_mode
='rgb',shuffle=True,target_size=(200,450),subset="training",class_mode
='sparse')
val_dat=image_gen.flow_from_directory(directory=data_dir2,color_mode='
rgb',shuffle=True,target_size=(200,450),subset="validation",class_mode
='categorical')

batch_1_img = train_dat[0]
for i in range(0,2):
    img = batch_1_img[0][i]
    lab = batch_1_img[1][i]
    plt.imshow(img)
    plt.title(lab)
    plt.axis('off')
    plt.show()


model = Sequential()

model.add(Conv2D(16,(3,3),padding="same",
activation="relu",kernel_initializer='glorot_normal',
input_shape=[200,450,3]))
model.add(MaxPooling2D((2,2), strides=(2,2)))
model.add(Conv2D(64, (3,3),
padding="same",kernel_initializer='glorot_normal', activation="relu"))
model.add(Conv2D(64, (3,3),
padding="same",kernel_initializer='glorot_normal', activation="relu"))
```

```python
model.add(MaxPooling2D((2,2), strides=(2,2)))
model.add(Conv2D(124, (3,3),
padding="same",kernel_initializer='glorot_normal', activation="relu"))
model.add(Conv2D(124, (3,3),
padding="same",kernel_initializer='glorot_normal', activation="relu"))
model.add(Conv2D(124, (3,3),
padding="same",kernel_initializer='glorot_normal', activation="relu"))
model.add(MaxPooling2D((2,2), strides=(2,2)))

model.add(Flatten())

model.add(Dense(256,activation="relu"))
model.add(Dense(128,activation="relu"))
model.add(Dense(64,activation="relu"))
model.add(keras.layers.Dropout(0.3))
model.add(Dense(2, activation="softmax"))

model.summary()
opt = keras.optimizers.SGD(learning_rate=0.0095)
model.compile(optimizer = opt , loss = 'categorical_crossentropy',
metrics = ['accuracy'])
#callback=keras.callbacks.EarlyStopping(monitor='val_loss',restore_bes
t_weights=True)
history = model.fit(train_dat ,epochs = epoch ,batch_size=batch_size,
validation_data=(val_dat),steps_per_epoch=len(train_dat)/batch_size)#,
callbacks=callback

acc = history.history['accuracy']
val_acc = history.history['val_accuracy']
loss = history.history['loss']
val_loss = history.history['val_loss']
epochs_range = range(epoch)

plt.figure(figsize=(15, 15))
plt.subplot(2, 2, 1)
plt.plot(epochs_range, acc, label='Training Accuracy')
plt.plot(epochs_range, val_acc, label='Validation Accuracy')
plt.legend(loc='lower right')
plt.title('Training and Validation Accuracy')

plt.subplot(2, 2, 2)
plt.plot(epochs_range, loss, label='Training Loss')
plt.plot(epochs_range, val_loss, label='Validation Loss')
plt.legend(loc='upper right')
plt.title('Training and Validation Loss')
plt.show()

model.save("C:\\Users\\mathurk1\\Documents\\Models\\CNNver1
model"+str(epoch)+" epoch")

#Testing the Model
test_model=keras.models.load_model("C:\\Users\\mathurk1\\Documents\\Mo
dels\\CNNver1 model"+str(epoch)+" epoch")

img_gen_test=ImageDataGenerator(rescale=1/255,validation_split=0.2)
test_dat=img_gen_test.flow_from_directory(directory=data_dir3,shuffle=
False,color_mode='rgb',target_size=(200,450),
class_mode='categorical')

'''
result = test_model.predict(test_dat)
```

```python
'''
#Confution Matrix and Classification Report
Y_pred = test_model.predict_generator(test_dat)
y_pred = np.argmax(Y_pred, axis=1)
print('Confusion Matrix')
print(confusion_matrix(test_dat.classes, y_pred))
print('Classification Report')
target_names = ["Good Weld", "Bad Weld"]
print(classification_report(test_dat.classes, y_pred,
target_names=target_names))
```

VGG-16 inspired architecture for sparse classification

```python
"""
Past Run Note- Shuffle at data prepration stage and at compilation

Max efficiency achieved - 98%

Batch Size 03112022- 32- Acc 99%
"""

import matplotlib.pyplot as plt
import os
from tensorflow import keras
from sklearn.model_selection import train_test_split
from sklearn.utils import shuffle
from tensorflow.keras.models import Model
from tensorflow.keras.preprocessing.image import ImageDataGenerator
from tensorflow.keras.layers import Dense, Dropout, Activation,
Flatten
from tensorflow.keras.layers import Conv2D, Input, MaxPooling2D,
LeakyReLU
from tensorflow.keras.layers import Concatenate, add
from tensorflow.keras.models import Sequential
from pandas import read_csv
import numpy as np
from sklearn.metrics import classification_report,
confusion_matrix,accuracy_score

from tensorflow.compat.v1 import ConfigProto
from tensorflow.compat.v1 import InteractiveSession
config = ConfigProto()
config.gpu_options.allow_growth = True
session = InteractiveSession(config=config)


epoch = 60
batch_size =32

data_dir1 = "C:\\python code data\\MelSpect\\Model_train"
data_dir2 = "C:\\python code data\\MelSpect\\Model_val"
data_dir3 = "C:\\python code data\\MelSpect\\Model_test"
data_dir4 = "C:\\python code data\\Spect\\Model_train"
data_dir5 = "C:\\python code data\\Spect\\Model_val"
data_dir6 = "C:\\python code data\\Spect\\Model_test"

image_gen=ImageDataGenerator(rescale=1/255)
train_dat=image_gen.flow_from_directory(directory=data_dir1,color_mode
='rgb',shuffle=False,target_size=(100,180),class_mode='categorical',ba
tch_size=3015)
val_dat=image_gen.flow_from_directory(directory=data_dir2,color_mode='
rgb',shuffle=False,target_size=(100,180),class_mode='categorical',batc
h_size=3015)
x1_train, y1_train=train_dat.next()
x1_val,y1_val=val_dat.next()

batch_1_img = train_dat[0]
for i in range(0,2):
    img = batch_1_img[0][i]
    lab = batch_1_img[1][i]
    plt.imshow(img)
    plt.title(lab)
```

```python
    plt.axis('off')
    plt.show()

train_dat1=image_gen.flow_from_directory(directory=data_dir4,color_mod
e='rgb',shuffle=False,target_size=(100,180),class_mode='categorical',b
atch_size=3015)
val_dat1=image_gen.flow_from_directory(directory=data_dir5,color_mode=
'rgb',shuffle=False,target_size=(100,180),class_mode='categorical',bat
ch_size=3015)
x2_train, y2_train=train_dat.next()
x2_val,y2_val=val_dat.next()

x1,x2,y1,y2=shuffle(x1_train, x2_train, y1_train, y2_train)
x_train_comp = np.stack((x1, x2), axis=4)
x_train, x_test, y_train, y_test = train_test_split(x_train_comp, y1,
test_size = 0.15, random_state=666)

# take them apart
x1_train = x_train[:,:,:,:,0]
x1_test = x_test[:,:,:,:,0]

x2_train = x_train[:,:,:,:,1]
x2_test = x_test[:,:,:,:,1]

def conv_layer(inp_img):
  model = Conv2D(12, (3, 3), padding='same')(inp_img)
  model = LeakyReLU(alpha=0.1)(model)
  model = Conv2D(12, (3, 3), padding='same')(model)
  model = LeakyReLU(alpha=0.1)(model)
  model = Conv2D(12, (3, 3), padding='same')(model)
  model = LeakyReLU(alpha=0.1)(model)
  model = MaxPooling2D((1,1 ),padding='same')(model)

  model = Conv2D(36, (3, 3), padding='same')(model)
  model = LeakyReLU(alpha=0.1)(model)
  model = Conv2D(36, (3, 3), padding='same')(model)
  model = LeakyReLU(alpha=0.1)(model)
  model = MaxPooling2D((3, 3),padding='same')(model)

  model = Conv2D(60, (3, 3), padding='same')(model)
  model = LeakyReLU(alpha=0.1)(model)
  model = Dropout(0.3)(model)




  return model

def fcc_module(layer_in):
    flt=Flatten()(layer_in)
    drop=keras.layers.Dropout(0.2)(flt)
    fcc1= Dense(256,activation='relu')(drop)

    fcc2=Dense(4, activation='softmax')(fcc1)
    return (fcc2)

MelSpect= Input(shape=(100,180,1))
MelConv= conv_layer(MelSpect)

Spect= Input(shape=(100,180,1))
SpectConv= conv_layer(Spect)
```

```python
convolute= Concatenate(axis=-1)([MelConv,SpectConv])

layer=fcc_module(convolute)

model= Model(inputs=[MelSpect, Spect], outputs=layer)

model.summary()
opt = keras.optimizers.SGD(learning_rate=0.0076)
model.compile(optimizer = opt , loss = 'categorical_crossentropy',
metrics = ['accuracy'])
#callback=keras.callbacks.EarlyStopping(monitor='val_loss',restore_bes
t_weights=True)
history = model.fit([x1_train,x2_train],y_train,epochs = epoch
,batch_size=batch_size, validation_data=([x1_val, x2_val], y1_val),
shuffle=True)

acc = history.history['accuracy']
val_acc = history.history['val_accuracy']
loss = history.history['loss']
val_loss = history.history['val_loss']
epochs_range = range(epoch)

plt.figure(figsize=(15, 15))
plt.subplot(2, 2, 1)
plt.plot(epochs_range, acc, label='Training Accuracy')
plt.plot(epochs_range, val_acc, label='Validation Accuracy')
plt.legend(loc='lower right')
plt.title('Training and Validation Accuracy')

plt.subplot(2, 2, 2)
plt.plot(epochs_range, loss, label='Training Loss')
plt.plot(epochs_range, val_loss, label='Validation Loss')
plt.legend(loc='upper right')
plt.title('Training and Validation Loss')
plt.show()


#model.save("C:\\Users\\mathurk1\\Documents\\Models\\2910_Hybrid_V2
model"+str(epoch)+" epoch")

test_model=keras.models.load_model("C:\\Users\\mathurk1\\Documents\\Mo
dels\\2910_Hybrid mode epoch")

test_dat=image_gen.flow_from_directory(directory=data_dir3,color_mode=
'grayscale',shuffle=False,target_size=(100,180),class_mode='categorica
l',batch_size=3200)
x1_test, y1_test=test_dat.next()

test_dat1=image_gen.flow_from_directory(directory=data_dir6,color_mode
='grayscale',shuffle=False,target_size=(100,180),class_mode='categoric
al',batch_size=3200)
x2_test, y2_test=test_dat1.next()
y1_test=np.argmax(y1_test,axis=1)
#y_test=np.argmax(y_test,axis=1)
result = test_model.predict([x1_test,x2_test])
result = np.argmax(result, axis=1)


accuracy = accuracy_score(y_true=y1_test, y_pred=result)
'''
```

```python
print('Confusion Matrix')
print(confusion_matrix(test_dat.classes, result))
print('Classification Report')
target_names = ["Disruption","Good","Internal Void","Shoulder
Pressure"]
print(classification_report(test_dat.classes, result,
target_names=target_names))

#Confution Matrix and Classification Report
Y_pred = test_model.predict_generator(test_dat)
y_pred = np.argmax(Y_pred, axis=1)
print('Confusion Matrix')
print(confusion_matrix(test_dat.classes, y_pred))
print('Classification Report')
target_names = ["Disruption","Good","Internal Void","Shoulder
Pressure"]
print(classification_report(test_dat.classes, y_pred,
target_names=target_names))
'''
```

Inception inspired architecture for sparse classification

```python
"""
Past Run Note- Shuffle at data preparation stage and at compilation

Max efficiency achieved - %

Batch Size 04112022- - Acc %
"""

import matplotlib.pyplot as plt
import os
import tensorflow as tf
from tensorflow import keras
from sklearn.model_selection import train_test_split
from sklearn.utils import shuffle
from tensorflow.keras.models import Model
from tensorflow.keras.preprocessing.image import ImageDataGenerator
from tensorflow.keras.layers import Dense, Dropout, Activation,
Flatten
from tensorflow.keras.layers import Conv2D, Input, MaxPool2D,
LeakyReLU
from tensorflow.keras.layers import Concatenate, add
from tensorflow.keras.models import Sequential
from pandas import read_csv
import numpy as np
from sklearn.metrics import classification_report,
confusion_matrix,accuracy_score

from tensorflow.compat.v1 import ConfigProto
from tensorflow.compat.v1 import InteractiveSession
config = ConfigProto()
config.gpu_options.allow_growth = True
session = InteractiveSession(config=config)


epoch = 100
batch_size =4

data_dir1 = "E:\\CNN Data\\MelSpect\\Model__train"
data_dir2 = "E:\\CNN Data\\MelSpect\\Model__val"
data_dir3 = "E:\\CNN Data\\MelSpect\\Model__test"
data_dir4 = "E:\\CNN Data\\Spect\\Model__train"
data_dir5 = "E:\\CNN Data\\Spect\\Model__val"
data_dir6 = "E:\\CNN Data\\Spect\\Model__test"

image_gen=ImageDataGenerator(rescale=1/255)
train_dat=image_gen.flow_from_directory(directory=data_dir1,color_mode
='rgb',shuffle=False,target_size=(100,120),class_mode='categorical',ba
tch_size=3381)
val_dat=image_gen.flow_from_directory(directory=data_dir2,color_mode='
rgb',shuffle=False,target_size=(100,120),class_mode='categorical',batc
h_size=1358)
x1_train, y1_train=train_dat.next()
x1_val,y1_val=val_dat.next()

batch_1_img = train_dat[0]
for i in range(0,2):
    img = batch_1_img[0][i]
    lab = batch_1_img[1][i]
    plt.imshow(img)
```

```python
    plt.title(lab)
    plt.axis('off')
    plt.show()

train_dat1=image_gen.flow_from_directory(directory=data_dir4,color_mod
e='rgb',shuffle=False,target_size=(100,120),class_mode='categorical',b
atch_size=3381)
val_dat1=image_gen.flow_from_directory(directory=data_dir5,color_mode=
'rgb',shuffle=False,target_size=(100,120),class_mode='categorical',bat
ch_size=1358)
x2_train, y2_train=train_dat.next()
x2_val,y2_val=val_dat.next()

x1,x2,y1,y2=shuffle(x1_train, x2_train, y1_train, y2_train)
x_train_comp = np.stack((x1, x2), axis=4)
x_train, x_test, y_train, y_test = train_test_split(x_train_comp, y1,
test_size = 0.01, random_state=666)

# take them apart
x1_train = x_train[:,:,:,:,0]
x1_test = x_test[:,:,:,:,0]

x2_train = x_train[:,:,:,:,1]
x2_test = x_test[:,:,:,:,1]

def conv_layer(inp_img,f1,f2,f3,f4):
    conv1 = Conv2D(f1, (1,1), padding='same',
activation='relu')(inp_img)
    conv2= Conv2D(f2, (1,1), padding='same',
activation='relu')(inp_img)
    conv3 = Conv2D(f3, (1,1), padding='same',
activation='relu')(inp_img)
    pool = MaxPool2D((3,3), strides=(1,1), padding='same')(inp_img)
    conv_pool = Conv2D(f4, (1,1), padding='same',
activation='relu')(pool)
    # concatenate filters, assumes filters/channels last
    layer_out = Concatenate(axis=-1)([conv1, conv2, conv3, conv_pool])

    return layer_out




def fcc_module(layer_in):
    flt=Flatten()(layer_in)
    drop=keras.layers.Dropout(0.2)(flt)
    fcc1= Dense(256,activation='relu')(drop)

    fcc2=Dense(4, activation='softmax')(fcc1)
    return (fcc2)

MelSpect= Input(shape=(100,120,1))

Spect= Input(shape=(100,120,1))

concat= Concatenate(axis=-1)([MelSpect,MelSpect])

Conv_concat1=conv_layer(concat,16,8,16,16)
Conv_concat2=conv_layer(Conv_concat1,8,32,8,8)
layer=fcc_module(Conv_concat2)
```

```python
model= Model(inputs=[MelSpect, Spect], outputs=layer)

model.summary()
opt = keras.optimizers.SGD(learning_rate=0.007)
model.compile(optimizer = opt , loss = 'categorical_crossentropy',
metrics = ['accuracy'])
#callback=keras.callbacks.EarlyStopping(monitor='val_loss',restore_bes
t_weights=True)
history = model.fit([x1_train,x2_train],y_train,epochs = epoch
,batch_size=batch_size, validation_data=([x1_val, x2_val],
y1_val),shuffle=True)

acc = history.history['accuracy']
val_acc = history.history['val_accuracy']
loss = history.history['loss']
val_loss = history.history['val_loss']
epochs_range = range(epoch)

plt.figure(figsize=(15, 15))
plt.subplot(2, 2, 1)
plt.plot(epochs_range, acc, label='Training Accuracy')
plt.plot(epochs_range, val_acc, label='Validation Accuracy')
plt.legend(loc='lower right')
plt.title('Training and Validation Accuracy')

plt.subplot(2, 2, 2)
plt.plot(epochs_range, loss, label='Training Loss')
plt.plot(epochs_range, val_loss, label='Validation Loss')
plt.legend(loc='upper right')
plt.title('Training and Validation Loss')
plt.show()


#model.save("E:\\CNN results\\T1-07072023\\Models\\070723_Hybrid_V2
model"+str(epoch)+" epoch")

#test_model=keras.models.load_model("E:\\CNN results\\T1-
07072023\\Models\\070723_Hybrid_V2 model100 epoch")
'''
test_dat=image_gen.flow_from_directory(directory=data_dir3,color_mode=
'grayscale',shuffle=False,target_size=(100,180),class_mode='categorica
l',batch_size=3200)
x1_test, y1_test=test_dat.next()

test_dat1=image_gen.flow_from_directory(directory=data_dir6,color_mode
='grayscale',shuffle=False,target_size=(100,180),class_mode='categoric
al',batch_size=3200)
x2_test, y2_test=test_dat1.next()
y1_test=np.argmax(y1_test,axis=1)
#y_test=np.argmax(y_test,axis=1)
result = test_model.predict([x1_test,x2_test])
result = np.argmax(result, axis=1)


accuracy = accuracy_score(y_true=y1_test, y_pred=result)

print('Confusion Matrix')
print(confusion_matrix(test_dat.classes, result))
print('Classification Report')
target_names = ["Disruption","Good","Internal Void","Shoulder
Pressure"]
```

```python
print(classification_report(test_dat.classes, result,
target_names=target_names))

#Confution Matrix and Classification Report
Y_pred = test_model.predict_generator(test_dat)
y_pred = np.argmax(Y_pred, axis=1)
print('Confusion Matrix')
print(confusion_matrix(test_dat.classes, y_pred))
print('Classification Report')
target_names = ["Disruption","Good","Internal Void","Shoulder
Pressure"]
print(classification_report(test_dat.classes, y_pred,
target_names=target_names))
'''
```

<u>Resnet inspired architecture for sparse classification</u>

```python
import matplotlib.pyplot as plt
import os
import tensorflow as tf
from typing import List
from tensorflow import keras
from sklearn.model_selection import train_test_split
from sklearn.utils import shuffle
from tensorflow.keras.models import Model
from tensorflow.keras.preprocessing.image import ImageDataGenerator
from tensorflow.keras.layers import Dense, Dropout, Activation,
Flatten, add, BatchNormalization, AveragePooling2D
from tensorflow.keras.layers import Conv2D, Input, MaxPool2D,
LeakyReLU
from tensorflow.keras.layers import Concatenate
from tensorflow.keras.initializers import glorot_uniform
from tensorflow.keras.models import Sequential
from pandas import read_csv
import numpy as np
from sklearn.metrics import classification_report,
confusion_matrix,accuracy_score

from tensorflow.compat.v1 import ConfigProto
from tensorflow.compat.v1 import InteractiveSession
config = ConfigProto()
config.gpu_options.allow_growth = True
session = InteractiveSession(config=config)


epoch = 60
batch_size =8

data_dir1 = "E:\\CNN Data\\MelSpect\\Model__train"
data_dir2 = "E:\\CNN Data\\MelSpect\\Model__val"
data_dir3 = "E:\\CNN Data\\MelSpect\\Model__test"
data_dir4 = "E:\\CNN Data\\Spect\\Model__train"
data_dir5 = "E:\\CNN Data\\Spect\\Model__val"
data_dir6 = "E:\\CNN Data\\Spect\\Model__test"

image_gen=ImageDataGenerator(rescale=1/255)
train_dat=image_gen.flow_from_directory(directory=data_dir1,color_mode
='grayscale',shuffle=False,target_size=(100,150),class_mode='categoric
al',batch_size=3381)
val_dat=image_gen.flow_from_directory(directory=data_dir2,color_mode='
grayscale',shuffle=False,target_size=(100,150),class_mode='categorical
',batch_size=1358)
x1_train, y1_train=train_dat.next()
x1_val,y1_val=val_dat.next()

batch_1_img = train_dat[0]
for i in range(0,2):
    img = batch_1_img[0][i]
    lab = batch_1_img[1][i]
    plt.imshow(img)
    plt.title(lab)
    plt.axis('off')
    plt.show()
```

175

```python
train_dat1=image_gen.flow_from_directory(directory=data_dir4,color_mod
e='grayscale',shuffle=False,target_size=(100,150),class_mode='categori
cal',batch_size=3381)
val_dat1=image_gen.flow_from_directory(directory=data_dir5,color_mode=
'grayscale',shuffle=False,target_size=(100,150),class_mode='categorica
l',batch_size=1358)
x2_train, y2_train=train_dat.next()
x2_val,y2_val=val_dat.next()

x1,x2,y1,y2=shuffle(x1_train, x2_train, y1_train, y2_train)
x_train_comp = np.stack((x1, x2), axis=4)
x_train, x_test, y_train, y_test = train_test_split(x_train_comp, y1,
test_size = 0.01, random_state=666)

# take them apart
x1_train = x_train[:,:,:,:,0]
x1_test = x_test[:,:,:,:,0]

x2_train = x_train[:,:,:,:,1]
x2_test = x_test[:,:,:,:,1]

def conv_layer(inp_img,f1 ):
    merge_input = inp_img
     # check if the number of filters needs to be increase, assumes
channels last format
    #if inp_img.shape[-1] != f1:
    merge_input = Conv2D(f1, (1,1), padding='same',
kernel_initializer='he_normal')(inp_img)
    # conv1
    conv1 = Conv2D(f1, (3,3), padding='same',
kernel_initializer='he_normal')(inp_img)
    conv1 = BatchNormalization(axis=1)(conv1)
    conv1 =  Activation('relu')(conv1)
    conv2 = Conv2D(f1, (3,3), padding='same',
kernel_initializer='he_normal')(conv1)
    conv2 = BatchNormalization(axis=1)(conv2)
    conv2 =  Activation('relu')(conv2)
    conv3 = Conv2D(f1, (3,3), padding='same',
kernel_initializer='he_normal')(conv2)
    conv3 = BatchNormalization(axis=1)(conv3)
    # add filters, assumes filters/channels last
    layer_out = add([conv2, merge_input])
    # activation function
    layer_out = Activation('relu')(layer_out)

    return layer_out




def fcc_module(layer_in):
    flt=Flatten()(layer_in)
    drop=keras.layers.Dropout(0.2)(flt)
    #fcc1= Dense(256,activation='relu')(drop)

    fcc2=Dense(4, activation='softmax')(drop)
    return (fcc2)

MelSpect= Input(shape=(100,150,1))

Spect= Input(shape=(100,150,1))
```

```python
concat= Concatenate(axis=-1)([MelSpect,MelSpect])
X= Conv2D(64, (3,3), padding='same', activation='relu',
kernel_initializer='he_normal')(concat)
X=AveragePooling2D((3,3), strides=(1,1), padding='same')(X)
Conv_concat=conv_layer(X,16)
Conv_concat=conv_layer(Conv_concat,16)
Conv_concat=conv_layer(Conv_concat,16)
Conv_concat=conv_layer(Conv_concat,32)
Conv_concat=conv_layer(Conv_concat,32)
Conv_concat=conv_layer(Conv_concat,32)
Conv_concat=conv_layer(Conv_concat,64)


layer=fcc_module(Conv_concat)

model= Model(inputs=[MelSpect, Spect], outputs=layer)

model.summary()
opt = keras.optimizers.Adam(learning_rate=0.00023)
model.compile(optimizer = opt , loss = 'categorical_crossentropy',
metrics = ['accuracy'])
#callback=keras.callbacks.EarlyStopping(monitor='val_loss',restore_bes
t_weights=True)
history = model.fit([x1_train,x2_train],y_train,epochs = epoch
,batch_size=batch_size, validation_data=([x1_val, x2_val],
y1_val),shuffle=True)

acc = history.history['accuracy']
val_acc = history.history['val_accuracy']
loss = history.history['loss']
val_loss = history.history['val_loss']
epochs_range = range(epoch)

plt.figure(figsize=(15, 15))
plt.subplot(2, 2, 1)
plt.plot(epochs_range, acc, label='Training Accuracy')
plt.plot(epochs_range, val_acc, label='Validation Accuracy')
plt.legend(loc='lower right')
plt.title('Training and Validation Accuracy')

plt.subplot(2, 2, 2)
plt.plot(epochs_range, loss, label='Training Loss')
plt.plot(epochs_range, val_loss, label='Validation Loss')
plt.legend(loc='upper right')
plt.title('Training and Validation Loss')
plt.show()


#model.save("E:\\CNN results\\V3.2-
12082023\\Models\\12082023_Hybrid_V3 model"+str(epoch)+" epoch")

#test_model=keras.models.load_model("E:\\CNN results\\T1-
07072023\\Models\\070723_Hybrid_V2 mode epoch")
```